Synthesis and Ion Transport Behavior of Polymeric Single-Ion Conductors for Electrical Energy Storage

By

Ryan L. Weber

A dissertation submitted in partial fulfillment of

the requirements for the degree of

Doctor of Philosophy

(Chemistry)

at the

UNIVERSITY OF WISCONSIN-MADISON

2013

Date of final oral examination: 6/24/2013

The dissertation is approved by the following members of the Final Oral Committee:

Mahesh K. Mahanthappa, Associate Professor, Chemistry
Arun Yethiraj, Professor, Chemistry
Mark D. Ediger, Professor, Chemistry
Randall H. Goldsmith, Assistant Professor, Chemistry
David M. Lynn, Professor, Chemical and Biological Engineering

PREFACE

Chapter 1 is an overview of the current state of research in polymeric single-ion conductors focusing on systems relevant to polymer electrolytes for electrochemical devices. Chapter 2 concerns the synthesis and characterization of polymerized ionic liquid homopolymers with an emphasis on structure-property relationships as they relate to the thermal and ion-conducting properties of single-ion conductors. Dr. Yuesheng Ye and Professor Yossef A. Elabd in the Department of Chemical and Biological Engineering at Drexel University performed all conductivity measurements described in the chapter. Professor Michael A. Hickner in the Department of Materials Science and Engineering at The Pennsylvania State University obtained water-uptake data on the hydrophilic polymerized ionic liquids. Steven M. Banik in the Department of Chemistry at the University of Wisconsin – Madison assisted with synthesis of the alkoxyamine initiator. The majority of this work was previously published in the *Journal of Polymer Science, Part B: Polymer Physics*, **2011,** *49* (18), 1287-1296. Copyright 2011 Wiley Periodical, Inc. (DOI: 10.1002/polb.22319) Chapter 3 describes the investigation of morphology-conductivity relationships in polymerized ionic liquid block copolymers. Dr. Yuesheng Ye and Professor Yossef A. Elabd in the Department of Chemical and Biological Engineering at Drexel University performed all conductivity measurements described in the chapter. Dr. Andrew L. Schmitt and Steven M. Banik in the Department of Chemistry at the University of Wisconsin – Madison obtained transmission electron micrograph seen in Figure 3.4 and assisted with synthesis of the alkoxyamine initiator, respectively. The majority of this chapter was previously published in *Macromolecules* **2011,** *44* (14), 5727-5735. Copyright 2011 American Chemical

Society. (DOI: 10.1021/ma201067h) Chapter 4 details the synthesis and electrochemical characterization of a new polymeric lithium single-ion conductor for use as an electrolyte in lithium ion batteries. Joseph C. Yeager and Professor Robert J. Hamers in the Department of Chemistry at the University of Wisconsin – Madison performed electrochemical impedance spectroscopy and cyclic voltammetry measurements described in this chapter. The polymers described and the methods to make them were the subject of U.S. Patent Application 13/796155 filed March 12, 2013. Chapter 5 describes the synthesis and characterization of a series of crosslinked lithium single-ion conducting polymer gels with a focus on the relationship between rheological and ion-transporting properties. Frank W. Speetjens II and Dominic V. Perroni in the Department of Chemistry at the University of Wisconsin – Madison performed rheology measurements and infrared spectroscopy on the crosslinked polymer gels, respectively.

ACKNOWLEDGEMENTS

This thesis came to fruition through the generous help of countless people. I am truly grateful to the many friends, family members, and colleagues who helped me along the way. I have enjoyed the guidance of mentors, the aide of colleagues, the levity of friends, and the love and support of family. I greatly appreciate all the help that I have received and I acknowledge many of those individuals here.

First, I want to thank my wonderful wife and best friend, Angie. Her continuous love and generous support in all aspects of my life have given me the strength and courage to pursue my goals. I thank her for her support and understanding over the past several months as I labored to make this document a reality. Angie is a constant source of love and inspiration in my life and I cannot thank her enough for all she has done to help me. I look forward to continuing our journey together as we continue on from Madison.

I also want to thank my parents Robert and Ruth Weber for always supporting me and believing in me. Ever since I was young they told me that I could accomplish anything no matter how difficult the task. Without their encouragement in my youth and today, I would not have achieved so much. I sincerely thank them for the countless ways they have supported me over the years.

I especially want to thank my advisor, Professor Mahesh Mahanthappa. Mahesh's passion for science was evident to me from the first time I stepped into his office on my visit to the University of Wisconsin – Madison. I knew from that day that I wanted to join Mahesh's group and to learn as much as I could from him. He has been an exceptional friend and mentor

over these past five years and I thank him for all of the skills he has fostered in me that will be invaluable in my future. His encouragement and help have resulted in many new opportunities that I would not have otherwise had. I thank Mahesh for his extraordinary mentorship and his infectious passion for chemistry that have driven me to become the scientist I am today.

During my time in graduate school, the Mahanthappa group was a second family to me. I want to thank all of the members of the Mahanthappa group both past and present for being such wonderful friends and colleagues who made these past five years so enjoyable. It was an honor and a pleasure working with them all. I joined the Mahanthappa group in 2008 alongside Greg Sorenson and Milton Repollet-Pedrosa. I thank both of these gentlemen for being supportive lab mates and excellent friends. Since both of us were in the organic division, Greg and I shared many of the trials and triumphs of teaching, classes, exams, second year reports, research proposals and the quest to write a thesis. I thank him for his help, commiseration, and friendship through these challenges. I thank Steven Banik for helping me make it through my first two years as a graduate student by providing me with much-appreciated humor and fun. Although Beau Monnot was only in the Mahanthappa group a relatively short time, his impact on the group and on me was profound. I thank Beau for his constant humor and friendship as well as for leading many a Friday afternoon trek to the Terrace. I thank Dominic Perroni for being a great friend and colleague whose energy and personality are infectious. I thank Adam Schmitt for being a good friend and for always being willing to help in any way he can. I also thank Frank Speetjens for his friendship and for sharing in the excitement of doing polymer chemistry. I thank Wansoo Chang for his friendship and for sharing in my endeavors of working on materials for lithium ion batteries. Finally, I thank Dr. Andrew Schmitt for his friendship, his help with

analytical techniques beyond my experience, and his encouragement of my scientific abilities. Just as I had many mentors who helped me along the way, I was given the opportunity to mentor two outstanding undergraduate students. I thank Carlos Báez and Harry Robertson for their hard work and for making my time as their mentor so enjoyable.

In addition to the Mahanthappa group, I also want to thank my many friends, colleagues, and classmates within the Department of Chemistry at the University of Wisconsin – Madison. In particular, I want to thank J. P. Gerdt and Alex Nolan for sharing in the struggles of classes and teaching and sharing a monthly lunch with Greg and me. I would also like to thank Liz Tyson and the rest of the Yoon group for always being willing to share chemicals and advice on syntheses.

Much of my thesis work was made possible through the help of some extraordinary collaborators. My sincerest thanks to Professor Yossef Elabd and Dr. Yuesheng Ye at Drexel University and Professor Michael Hickner at The Pennsylvania State University for helping me obtain the data for my first publications. I would also like to thank Professor Robert Hamers and Joseph Yeager at UW-Madison for helping me make a push into the world of lithium ion battery materials research. I especially thank Joe for his constant willingness to discuss research and for helping me understand cyclic voltammetry and electrochemical impedance spectroscopy. Much of the data presented in this thesis was made possible with the extraordinary help of these collaborators.

My journey to become a scientist started much earlier than my time at the University of Wisconsin – Madison. At Theodore Roosevelt High School in Kent, OH, I was blessed with some of the most passionate science teachers one could ask for. I would like to thank my high

school physics teacher Dr. Jon Secaur for fostering my passion for science during these formative years. I also want to thank my high school chemistry teacher, Dr. Mitch Lambert for introducing me to the fascinating world of chemistry.

At Kent State University I was fortunate that Professor Robert Twieg reached out and accepted me into his research group. He introduced me to the world of chemistry research that I have come to love and encouraged me to expand my knowledge to grow into an independent scientist. I sincerely thank him for all of his support. I thank all of the members of the Twieg group with whom I coincided for helping me along my journey. Specifically, I want to thank my friend Dr. Zhikuan Lu for teaching me so many of the lab skills that I have used nearly every day since those first days in the lab. I also want to thank my office mate during those years in the Twieg group, Dr. Melati Khairuddean, for always being so helpful and supportive.

As I progressed through college I had the opportunity to spend a summer at Stanford University in Professor Robert Waymouth's group. I thank Bob for welcoming me into his group and for introducing me to the world of polymer chemistry, which has had a profound impact on my scientific career. I also thank Dr. Matt Kiesewetter for being an outstanding mentor during my time in the Waymouth group.

Outside of my life in chemistry I have enjoyed the love and support of many friends and family members who have helped me to grow into the person I am today. I thank my brother Joseph, my sister-in-law Allison, and my nephew, Bobby for their love and support. I thank my grandparents Robert (*d*. 1999) and Patricia Andrews and Richard (*d*. 2008) and Joan Weber for so much love and encouragement. Over the past several years, I have been welcomed into a new family, and I would like to thank my mother- and father-in-law Barb and Dave Conant for their

support. I also want to thank my many wonderful friends that have stood by me through so many years, particularly Michael Dietz, Trevor Williams, Christopher Battles, and Christopher Myers.

Finally, I would like to thank the members of my thesis committee, Professors Mark Ediger, David Lynn, Randy Goldsmith, and Arun Yethiraj. I greatly appreciate their feedback and guidance.

I offer my sincerest thanks to all of you who have helped and guided me over the years. I am truly appreciative of all of your unwavering support that has made this thesis a reality.

FINANCIAL SUPPORT

We gratefully acknowledge financial support from the University of Wisconsin–Madison, a National Science Foundation Graduate Research Fellowship awarded to Ryan L. Weber, an NSF CAREER Award (DMR-0748503) awarded to Professor Mahesh K. Mahanthappa, and a National Science Foundation - American Competitiveness in Chemistry Postdoctoral Fellowship (CHE-1041975) awarded to Dr. Andrew L. Schmitt that funded the purchase of the Metrohm Autolab instrument. SAXS data was acquired at the Advanced Photon Source DuPont-Northwestern-Dow Collaborative Access Team beamline (Sector 5), which is supported by E. I. DuPont de Nemours & Co., the Dow Chemical Company, the State of Illinois, and the U.S. Department of Energy, Office of Basic Energy Sciences (Contract No. DE-AC02-06CH11357). This research made extensive use of UW-Madison MRSEC/NSEC core characterization facilities (DMR-0520527 and DMR-0425880) as well as Department of Chemistry core characterization facilities partially supported by the National Science Foundation (CHE-9629688, CHE-0342998, CHE-9974839, CHE-1048642, CHE-9208463) and the National Institute of Health (1-S10-RR08389-01)

TABLE OF CONTENTS

LIST OF FIGURES

LIST OF SCHEMES

LIST OF TABLES

CHAPTER 1

AN OVEREVIEW OF NON-PROTONIC POLYMERIC SINGLE-ION CONDUCTORS

1.1 Introduction

In view of the current unprecedented rate of global energy consumption, one of the greatest challenges facing society in the 21st century will be the development and implementation of clean and renewable sources of energy on a global scale. The imminent depletion of fossil fuels and the emerging threat of global climate change renders this task of paramount importance.[1] Energy sources such as solar power and wind power are promising alternatives to fossil fuels; however, they must overcome numerous challenges before they may be widely adopted for large-scale energy production.[2] One such challenge is that both solar and wind are intermittent sources of energy, meaning that they cannot continuously produce energy. For example, solar panels cannot produce energy at night or in cloudy weather, when solar radiation is inaccessible. Therefore, widespread use of these alternative energy sources requires the development of viable, large scale energy storage devices such as batteries and fuel cells.[3] Not only are these technologies necessary for large scale grid storage, but they are also imperative for smaller scale applications such as portable electronics and transportation (e.g., automobiles, aircraft). The development of high-performance batteries and fuel cells for both large-scale and small-scale applications is a task of great significance.[4,5]

While current battery and fuel cell technologies exist, they are not yet ready to meet the demands of a renewable energy-based society. Developing better materials for batteries and fuel

cells, particularly new electrolyte materials, is an area of active and interdisciplinary research in the scientific community. While each technology demands different stability criteria for the electrolyte materials used in the electrochemical cell (e.g., electrochemical stability, chemical stability, mechanical robustness), they all share a common purpose. The material must selectively conduct a particular ion between electrodes, while electronically insulating the electrodes from one another to avoid a short circuit. In fuel cells, the ions of interest for transport are either protons or hydroxide ions depending on the pH of cell operation,[6,7] whereas for lithium batteries, lithium ions must be transported.[8] The ion of interest in electrolytes for batteries and fuel cells must be balanced by a charge compensating counterion, which has historically been accomplished by the use of salts such as KOH for alkaline fuel cells or $LiPF_6$ for lithium ion batteries. However, in each of these cases only a single-ion of interest (e.g., OH^-, Li^+) must be transported between electrodes for the cell to function, whereas the motion of other ions (e.g., K^+, PF_6^-) is unproductive. To maximize the motion of a particular ion, the balancing counterion may be covalently tethered to a solid support in order to immobilize it, leaving only the ion of interest mobile. One method of immobilizing the counterion is to covalently tether it to a polymeric chain, creating what is known as a polymeric single-ion conductor. Since the polymer chains are ideally large and entangled, the counterions are effectively immobilized, thus maximizing the motion of the particular ion of interest. Studies have demonstrated the gains that may be achieved by using these polymeric electrolytes in electrochemical devices.[7,9] The following sections detail such studies to provide an overview of the current state of research in polymeric single-ion conductors.

1.2 Applications for Polymeric Single-Ion Conductors and Scope of this Review

Polymeric single-ion conductors may be classified by the particular technological applications for which they are used. The major classes of single-ion conductors include proton-conducting polymers, hydroxide-conducting polymers (HCPs), polymerized ionic liquids (POILs), and polymeric lithium single-ion conductors (PLSICs). This chapter presents an overview of the different classes of polymeric single-ion conductors and their applications in terms of electrochemical devices.

Proton-conducting polymers have direct applications as proton exchange membranes in acidic fuel cells.[10] In acidic fuel cells, the fuel (e.g., hydrogen, methanol) is oxidized by a catalyst at the anode to yield protons and electrons with the electrons flowing through an external circuit and protons travelling through a membrane. At the cathode, another catalyst reduces protons, electrons, and oxygen to yield water. A key component of these systems is the proton exchange membrane that allows the free flow of protons from anode to cathode, while minimizing fuel crossover that is detrimental to the cell. The most well-known proton exchange membrane is Nafion®, produced by DuPont, which is comprised of a fluorinated backbone decorated with fluoro-sulfonic acid side chains (Figure 1.1.a).[11] This polymer has remained the prototypical proton-conducting polymer since its invention in the 1960s. When hydrated, Nafion® adopts a supramolecular structure consisting of crystallites of fluorinated backbone and channels of water surrounded by sulfonic acid groups (Figure1.1.b).[12] These channels of water give rise to the exceptional proton conductivity of Nafion®, as the water becomes structured by the sulfonic acid groups allowing for so-called Grötthuss transport of protons in addition to conventional diffusion transport. In Grötthuss transport, water and hydronium ions are organized

into “water wires” and a re-shuffling of hydrogen bonds allows for very fast transport of protons along these channels. Despite the success of Nafion®, it has several drawbacks that have prompted researchers to pursue new polymeric materials for use as proton conducting polymers. The use of polymers bearing hydrated acidic groups, protic ionic liquids, and amphoteric moieties are among a few of the approaches being employed to develop next-generation proton-conducting polymers. Further discussion of such efforts is outside of the scope of this overview; however, these materials have recently been reviewed by others.[6,10,13-18]

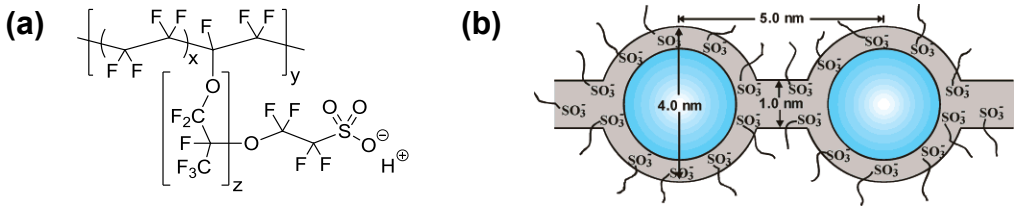

Figure 1.1. (a) The chemical structure of Nafion® and (b) the proposed water-channel structure adopted by hydrated Nafion®. Image adapted from Reference 11.

Hydroxide-conducting polymers (HCPs) are useful as hydroxide exchange membranes in alkaline fuel cells.[19,20] Alkaline fuel cells operate analogously to acidic fuel cells, yet several aspects of their function render them more technologically viable.[7] Diagrams of acidic and alkaline fuel cells are shown in Figure 1.2. Cheaper catalysts may be used for alkaline fuel cells (Ag, Ni) than in acidic fuel cells (Pt, Pd) making cells cheaper to produce, although the cheaper catalysts are more susceptible to poisoning by contaminants in the fuel. Redox reactions are more facile in an alkaline environment, allowing cells to run at lower temperatures (< 100 °C). This renders alkaline fuel cells more practical and mitigates issues associated with water management above its boiling point. Finally, the flow of hydroxide ions through the membrane

opposes the so-called "electro-osmotic drag" that is responsible for fuel crossover, which degrades performance of the cell. A key component in alkaline fuel cells is the hydroxide exchange membrane that separates the electrodes and shuttles hydroxide ions from cathode to anode. The use of polymeric hydroxide conductors is preferred over aqueous electrolytes comprised of metal hydroxides, as metal hydroxides (NaOH, KOH) may react with CO_2 found in the fuel stream to form metal carbonates (Na_2CO_3, K_2CO_3). These carbonate salts typically precipitate from solution and block active catalyst sites, thus degrading fuel cell performance.[7,21] Historically, HCPs have been based on polymers bearing tetra(alkyl)ammonium groups bearing a hydroxide counterion. These polymers mitigate problems associated with carbonate precipitation; however, their chemical stabilities in alkaline environments are suboptimal. To circumvent these problems associated with polymer degradation, current research is focused on developing HCPs with backbones and cationic moieties that are more chemically stable in the corrosive environment of alkaline fuel cells. An overview of some current research in this area will be presented in the Section 1.3.

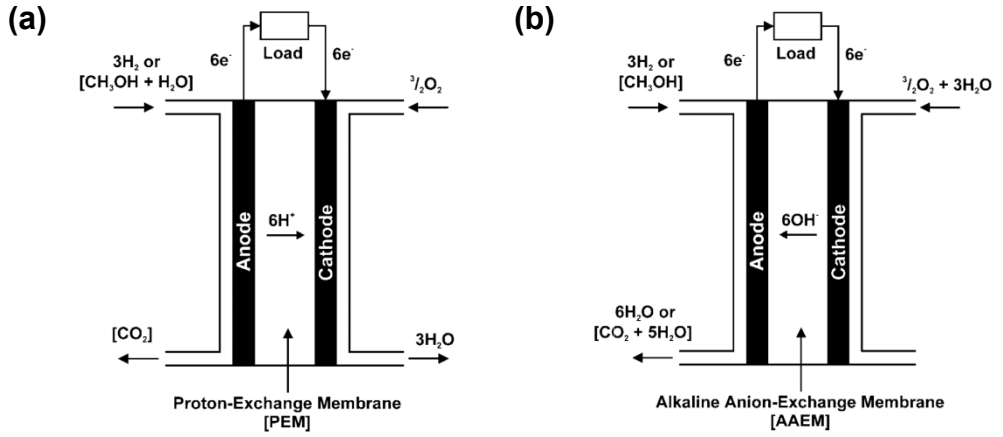

Figure 1.2. Diagrams of acidic and alkaline fuel cells. (a) An acidic fuel cell utilizing a proton exchange membrane and (b) an alkaline fuel cell utilizing a hydroxide exchange membrane. Images adapted from Reference 19.

Polymerized ionic liquids (POILs) are polymers derived from the enchainment of polymerizable small molecule ionic liquids. By analogy to small molecule ionic liquids, POILs exhibit useful properties such as low flammabilities, negligible vapor pressures, chemical, thermal, and electrochemical stabilities, as well as high ionic conductivities.[22] As a consequence of these favorable attributes, POILs have found use in wide-ranging applications including catalysis,[23,24] nanomaterials synthesis,[25] gas separations media,[26-29] microwave absorbing materials,[30] electrochemical transducers,[31] and gene delivery,[32,33] as well as polymer electrolytes for battery and fuel cell applications.[22,34-36] While POILs may be comprised of a plethora of different possible combinations of cation and anion structures, typical POILs contain polymer-bound cationic groups such as ammoniums, imidazoliums, or phosphoniums with counteranions including halides, tetrafluoroborate, hexafluorophosphate, or bis(trifluoromethanesulfonylimide) (TFSI).[37] A few examples of POIL structures are shown in Figure 1.3. While POILs are

potentially useful electrolytes for electrochemical devices,[22,34-36] their use as single-ion conductors is limited due to the fact that the mobile ions in these systems must be selected from the group of cations and anions mentioned above (e.g., ammonium, halide) that are not directly relevant in these applications. Instead, POILs are typically used as high-dielectric polymer matrices that promote transport of other ions such as lithium. Despite their limited applications as single-ion conductors in electrochemical devices, POILs serve as an excellent platform for fundamental studies of structure-property relationships in single-ion conductors due to their ease of synthesis and widely tunable physiochemical properties. These fundamental studies may then be translated to other technologically relevant systems (i.e., HCPs, PLSICs). An overview of the studies of structure-property relationships in polymerized ionic liquids as they relate to ion conduction will be presented in Section 1.4.

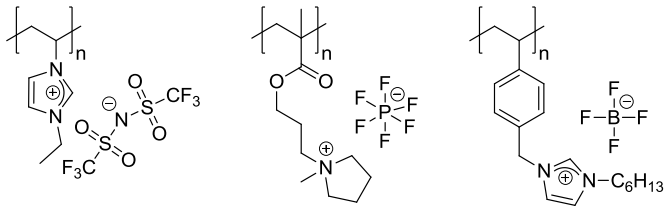

Figure 1.3. Some representative structures of polymerized ionic liquids (POILs).

The final class of single-ion conductors to be discussed herein are polymeric lithium single-ion conductors (PLSICs), which are technologically useful as electrolytes in both conventional lithium ion batteries as well as next-generation lithium-sulfur and lithium-air batteries.[38] During discharge of a lithium ion battery, lithium ions de-intercalate from the anode (commonly graphite), traverse an electrolyte, and then intercalate into the cathode (commonly $LiMO_2$, where M = Co, Mn) with concurrent shuttling of electrons through an external circuit

from anode to cathode as shown in Figure 1.4.[4] The charging cycle reverses the process described for battery discharge. The electrolyte is an integral aspect of the lithium ion battery.[8] Commercial batteries rely on a mixture of a liquid electrolyte (typically, ethylene carbonate and diethyl carbonate) with a dissolved lithium salt such as lithium hexafluorophosphate. The electrolyte fills the pores of a separator comprised of a porous polymer (e.g., polyethylene, carboxymethylcellulose) that physically separates the electrodes and prevents the battery from shorting. There are numerous problems associated with this type of electrolyte that manifest in limited cycle life, limited cell potential, limited charging rate, and possible catastrophic failure.[39] To address these issues, polymeric electrolytes such as poly(ethylene oxide) containing dissolved lithium salts may be used. However, such materials still have what is known as low lithium ion transference numbers ($t_{\mathrm{Li+}}$):

$$t_{\mathrm{Li+}} = \frac{I_{Li+}}{I_{total}} = \frac{I_{Li+}}{I_{anion}+I_{Li+}} \qquad (1.1)$$

where $I_{\mathrm{Li+}}$ is the current due to lithium ion motion and I_{total} is the total current due to the motion of both Li^+ ions and the charge compensating counteranions.[38,40] Lithium salts in organic carbonates or in poly(ethylene oxide) have lithium transference numbers on the order of 0.2–0.4, meaning that only about 20 – 40% of the current in the cell is actually carried by lithium ions, which is detrimental to the performance of the battery.[9,41,42] To mitigate this problem, a polymeric lithium single-ion conductor may be used as the electrolyte to maximize the performance of the electrolyte component of the battery. An overview of the current research on PLSICs will be presented in Section 1.5.

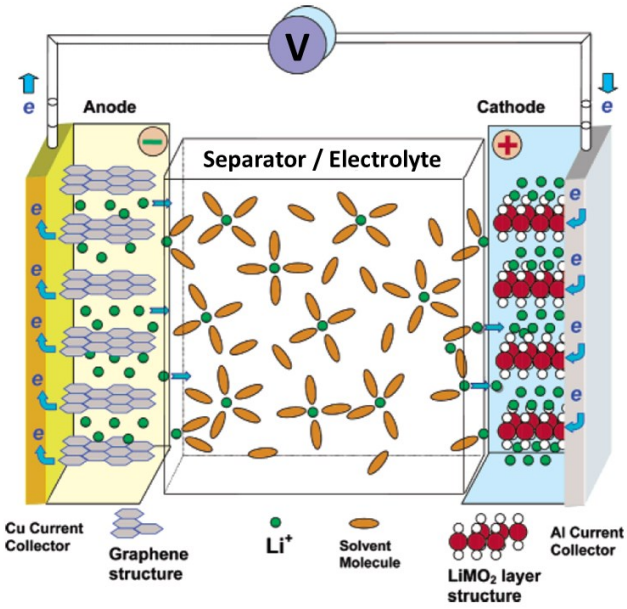

Figure 1.4. Diagram of a lithium ion battery displaying a discharge cycle. Lithium ions de-intercalate from the anode, traverse an electrolyte, and then intercalate into the cathode with concurrent shuttling of electrons through an external circuit from anode to cathode. Image adapted from Reference 8.

A theme that emerges across all of these classes of single-ion conductors is that ion transport is governed by one of two conduction mechanisms.[43] In systems where an exogenous, low molecular weight solvent (e.g., water, organic carbonates) is used to swell the polymer matrix, ion transport is governed by a solvent-mediated bulk transport mechanism. Ion conductivity in such system obeys Arrhenius-type behavior consistent with bulk diffusion of the ions. In systems devoid of small-molecule solvents, ion conduction is mediated by the polymer segmental dynamics. In other words, ion transport is directly coupled to the motion of polymer chains. Ionic conductivities in the latter systems follow Vogel-Fulcher-Tammann (VFT) behavior consistent with polymer segmental motion. As single-ion conducting materials are

explored throughout this overview, they will be classified according to this dichotomy of solvent-assisted Arrhenius behavior versus polymer chain-mediated VFT behavior.

The purpose of this chapter is not to provide a complete and comprehensive review of this vast and growing field of polymeric single-ion conductors, but instead, to present an overview of the current state of research on various aforementioned classes of polymeric single-ion conductors. For many of the technologically-relevant hydroxide-conducting polymers and polymeric lithium single-ion conductors presented below, we report the absolute values of ionic conductivity (σ) found for optimized materials, as these numbers indicate the relative merit of these materials as potential electrolytes. For the polymerized ionic liquids, we do not report the absolute values of conductivity and instead comment on the reported trends. While absolute values of conductivity are a useful reference within a single study or for multiple studies from a single research group, we caution against direct comparison of absolute conductivities between multiple studies and therefore only report the order of magnitude for ion conduction. Conductivity measurements are highly dependent on the exact conditions and geometry of the experimental setup (e.g., blocking *vs.* non-blocking electrodes, two-probe *vs.* four-probe, AC *vs.* DC). Since there is no universally accepted protocol for these measurements, each research group develops its own techniques to measure conductivity and rarely calibrates the cell using a standard material such as Nafion® or standardized KCl (*aq*) solutions.[44] Unless otherwise noted, all conductivities are reported at room temperature (298 ± 5 K).

1.3 Hydroxide-Conducting Polymers (HCPs)

1.3.1 Challenges Facing Hydroxide-Conducting Polymers

As introduced in Section 1.2, alkaline fuel cells represent an important and viable opportunity for the clean conversion of chemical energy into electrical energy. Alkaline fuel cells may operate on numerous types of fuels including $H_2(g)$ as well as alcohol fuels such as methanol and ethanol. They are also substantially less prone to the problems that prevent acidic fuel cells from becoming widely adopted energy production devices. The greater facility of the redox kinetics of fuel oxidation in the alkaline environment allows alkaline fuel cells to operate at lower temperatures (~ 60-80 °C) with less precious metal catalysts (e.g., Ag, Ni). The reversed electro-osmotic drag due to shuttling of hydroxide ions from cathode to anode reduces fuel crossover which can poison the oxidation catalyst and degrade cell performance.

One of the largest barriers facing the widespread adoption of alkaline fuel cells is the development of robust hydroxide exchange membranes. Electrochemical stability is not a major concern in these materials, as alkaline fuel cells operate at potentials ≤ 1.25 V that depend on the fuel used. A major liability of alkaline fuel cells is the highly caustic alkaline environment that tends to degrade most potential hydroxide exchange membranes. Therefore, research in developing high-performance hydroxide exchange membranes in recent years has largely focused on polymeric materials that can withstand the highly corrosive alkaline environments. Since organic polymers degrade through numerous different pathways, advances have been made by exploring different tethered cationic moieties and different polymer backbone architectures. We present an overview of these studies below.

Since alkaline fuel cells operate in hydrated environments, all of the hydroxide ion conductivities reported below were obtained under humidified conditions. These hydrophilic polymers uptake a substantial amount of water, causing the hydroxide ions associated with the polymers to be well-hydrated, and so they exhibit bulk, solvent-assisted transport. Thus, the temperature-dependent ion transport exhibits Arrhenius-type behavior.

1.3.3 Cationic Groups in Hydroxide-Conducting Polymers

Much of the current research in hydroxide-conducting polymers (HCPs) has focused on changing the nature of the cationic group to increase its stability in alkaline conductions. The most common degradation pathways for HCPs involve either direct nucleophilic displacement of the cationic group or Hoffman elimination (Figure 1.5).[19,45] Quaternary ammonium groups have historically been the most common ionic group; however, they are prone to degradation by these mechanisms, particularly when they are located in a benzylic position. Instead, cationic groups such as imidazoliums, guanidiniums, phosphoniums, inorganic cations, and ammoniums that block particular degradation pathways have been investigated for next generation HCPs.

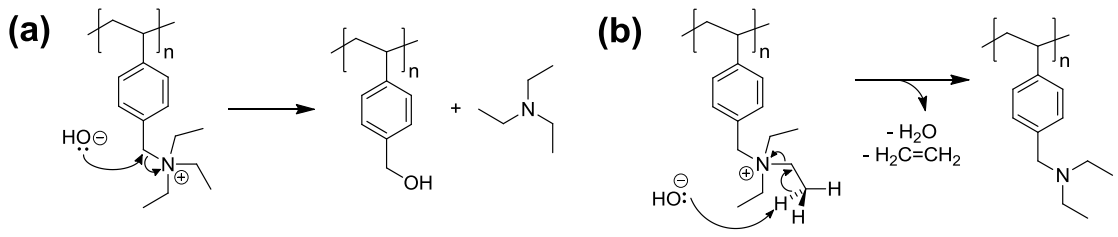

Figure 1.5. Common degradation pathways for hydroxide-conducting polymers including (a) direct nucleophilic displacement and (b) Hoffman elimination.

Despite the questionable alkaline stability of benzylic tri(alkyl)ammonium functional groups in HCPs, they remain one of the most widely used cationic groups due to their synthetic accessibility. Facile nucleophilic substitution of a benzylic halide with a variety of commercially available tertiary amines and subsequent anion exchange furnishes a HCP with benzylic ammonium cationic groups (Figure 1.6). Attendant with the synthetic ease for obtaining these polymers is the facile degradation by either Hoffman elimination if protons β to nitrogen are present, or by nucleophilic substitution by hydroxide at the electrophilic benzylic position. Despite this drawback, numerous recent reports of such polymers have appeared in the literature that exhibit high hydroxide conductivities (~ 10^{-3} – 10^{-1} S cm^{-1}).[46-55]

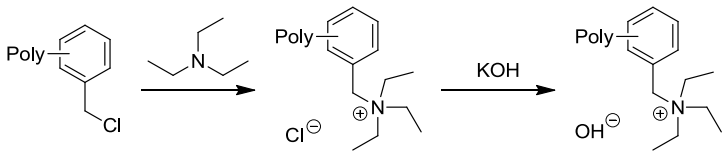

Figure 1.6. Synthesis of a benzylic ammonium hydroxide-conducting polymer by reaction of a pendant benzyl chloride with a tertiary amine and subsequent anion exchange with hydroxide.

The alkaline stabilities of ammonium-bearing polymers may be enhanced by modifying the structure of the linker tethering the ammonium group to the polymer backbone. Non-benzylic ammonium cations have been used as a more alkaline-stable alternative to the benzylic analogues, while maintaining hydroxide conductivities (~ 10^{-3} – 10^{-2} S cm^{-1}).[56,57] By removing the ammonium moiety from the electrophilic benzylic position, the likelihood of degradation by nucleophilic displacement is diminished; however, Hoffman elimination is still viable if β-protons on the N-alkyl substituents are present. Greater enhancement in alkaline stability is

observed for polymers bearing non-benzylic ammonium cations that block Hoffman elimination. Several recent reports by Coates and coworkers described highly conductive (~ 10^{-2} – 10^{-1} S cm^{-1}) polymers bearing trimethylammonium groups that are tethered to the polymer backbone via alkyl chains that lack β-protons, thereby preventing Hoffman elimination (Figure 1.7).[58-60] While they do not comment directly on the alkaline stabilities of these polymers, their inability to degrade by Hoffman elimination is expected to substantially increase their stabilities.

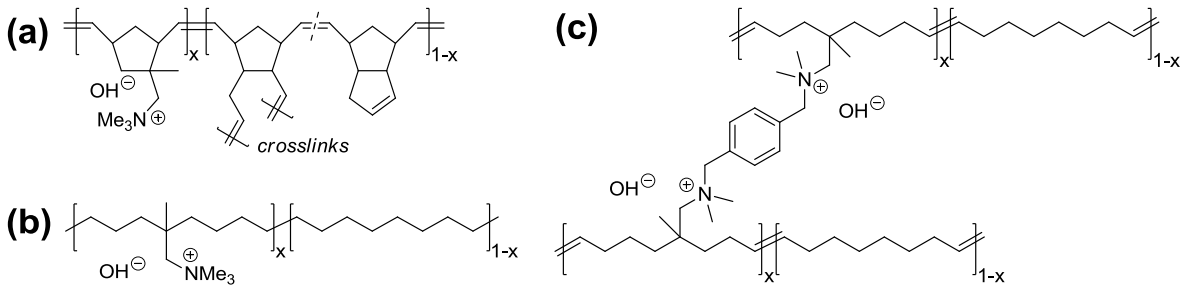

Figure 1.7. Hydroxide-conducting polymers resistant to degradation by Hoffman elimination due to the absence of β-protons on the N-alkyl substituents.[58-60]

Alkylimidazoliums have recently been explored as alternatives to ammonium cationic groups, giving rise to HCPs with high hydroxide conductivities (σ ~ 10^{-3} – 10^{-1} S cm^{-1}).[61-63] Although some reports claim that the aromatic nature of the imidazolium cation imparts stability in alkaline environments,[64] numerous recent reports have indicated otherwise. Both nucleophilic substitution and Hoffman elimination are still viable, especially for benzylic imidazoliums. Reports by the groups of Hickner[65] and Varcoe[66] demonstrated the severely diminished ionic conductivities of benzylic alkylimidazolium polymers compared to analogous trimethylammonium polymers upon exposure to alkaline environments at elevated temperatures that simulate alkaline fuel cell operating conditions. ^{1}H NMR studies of alkylimidazolium HCPs

by Elabd and coworkers elucidated one mechanism of degradation for such polymers.[67] At high pH and temperature, they observed the formation of a formamide species from the ring-opening of the imidazolium species (Figure 1.8.a). These studies suggest that alkylimidazolium polymers are unsuitable for use as HCPs for alkaline fuel cell membranes. An additional degradation route available to imidazolium groups is deprotonation of the relatively acidic C-2 proton in the imidazolium ring to form a reactive N-heterocyclic carbene. Some groups have reported 2-methylimidazolium-based structures that guard against this possible decomposition mechanism with retention of high conductivities (~ 10^{-2} S cm^{-1}).[68,69] A recent report by Varcoe and coworkers investigated the relative alkaline stabilities of HCPs containing pendant benzyl trimethylammonium, 1-benzyl-3-methylimidazolium, or 1-benzyl-2,3-dimethylimidazolium (Figure 1.8.b) cationic groups.[70] While all three polymers had similar initial conductivities (~ 10^{-2} S cm^{-1}), they found that aging the membranes in 1 M KOH at 60 °C resulted in greatly diminished conductivities for both imidazolium-based polymers. However, the 1-benzyl-2,3-dimethylimidazolium polymer did show better retention of conductivity relative to the 1-benzyl-3-methylimidazolium polymer.

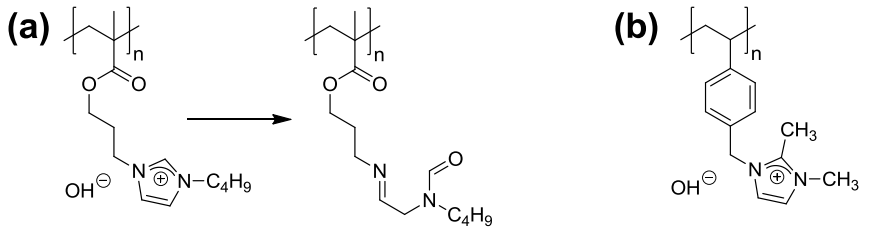

Figure 1.8. (a) Degradation of an unstable imidazolium-based hydroxide-conducting polymer[67] and (b) a hydroxide-conducing polymer containing 1-benzyl-2,3-dimethylimidazolium cationic groups exhibiting enhanced alkaline stability.[70]

Recent reports of HCPs with phosphonium-based cationic groups have shown promise for this class of materials. Yan and coworkers reported both soluble and crosslinked polymers bearing quaternary arylphosphoniums that exhibited high hydroxide conductivities (~ 10^{-2} S cm^{-1}) and excellent resistance to degradation in alkaline environments (Figure 1.9.a).[71,72] Similarly, tetrakis(dialkylamino)phosphonium-containing polymers described by Coates and coworkers exhibited both high conductivities (~ 10^{-2} S cm^{-1}) and alkaline stabilities (Figure 1.9.b).[73] In contrast to these more decorated cationic phosphonium moieties, simple tetraalkylphosphonium cations exhibit poor alkaline stabilities. Elabd and coworkers reported a series of HCPs based on a perfluorinated Nafion® scaffold with varying cationic moieties including linear, cyclic, and bicyclic amines, as well as a trimethylphosphonium.[74] Despite high initial hydroxide conductivities for all polymers studied (~ 10^{-3} – 10^{-2} S cm^{-1}) only the phosphonium-based polymer degraded under alkaline conditions (1 M KOH, 80 °C) as evidenced by a loss of conductivity and disintegration of the film, whereas similar ammonium-based polymers retained conductivity and remained intact. Similar results were observed by Ramani and coworkers for poly(arylene ether sulfones) functionalized with different ammonium cations or a trimethylphosphonium cation.[75] In this study they showed that the major decomposition pathway for the phosphonium polymer proceeds via facile formation of a phosphonium ylide as seen in Wittig reactions.

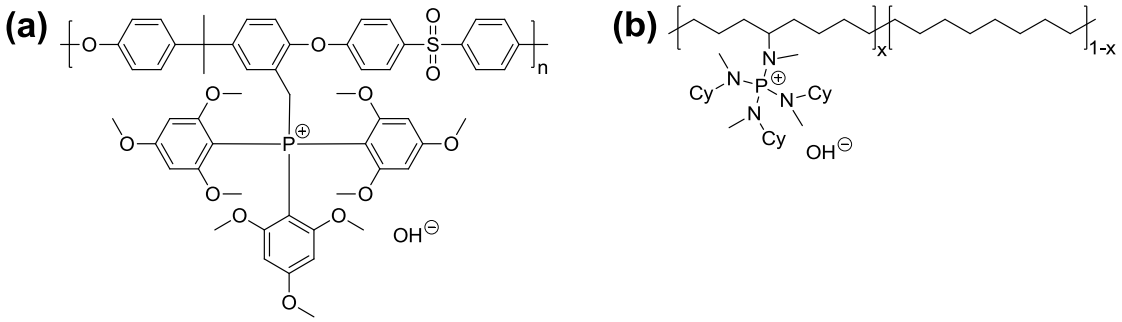

Figure 1.9. (a) A quaternary arylphosphonium hydroxide-conducting polymer[71] and (b) a tetrakis(dialkylamino)phosphonium hydroxide-conducting polymer.[73]

Other systems are emerging that show promise as HCPs due to their high conductivities and alkaline stabilities. Guanidinium cations represent one particular cationic platform for enabling alkaline-stable HCPs. Several recent examples of HCPs utilizing pendant guanidinium cationic groups have exhibited high hydroxide conductivities (~ 10^{-2} – 10^{-1} S cm^{-1}) while resisting degradation under alkaline conditions.[76-78] One of the more exotic polymeric cations used for a HCP is based on the inorganic cation bis(terpyridine)ruthenium(II) reported by Tew and coworkers.[79] These polymers exhibited hydroxide conductivities comparable to more traditional quaternary ammonium polymers (~ 10^{-2} S cm^{-1}). Although the use of ruthenium precludes this particular polymer from widespread commercial application, similar systems utilizing cheaper transition metal centers may be potential candidates for future HCPs.

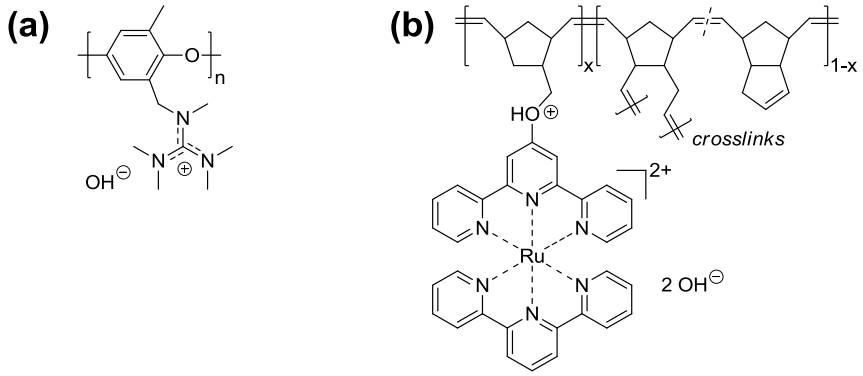

Figure 1.10. (a) A poly(arylene ether) hydroxide-conducting polymer with guanidinium cations[78] and (b) a hydroxide-conducting polymer containing bis(terpyridine) ruthenium(II) cations.[79]

It is evident from the above examples that a wide variety of structures may be used as cationic moieties in HCPs. As a consequence of the demanding alkaline environments to which these materials are subjected, much care must be taken to design materials that mitigate potential degradation pathways. By engaging in this endeavor, chemists will be able to advance the technology of alkaline fuel cells by designing materials with both high hydroxide ion conductivities and long-term functioning stabilities.

1.3.2 Polymer Backbones in Hydroxide-Conducting Polymers

While the alkaline stability of a polymeric HCP is highly dependent on the structure of cationic groups as detailed above, the chemical stability of the polymeric scaffold plays a large role in overall polymer stability. A diverse assortment of polymeric backbones that can withstand the harsh chemical conditions of an alkaline fuel cell have been explored as scaffolds for HCPs, including widely used poly(arylene ether sulfones), Nafion®-like fluoropolymers, synthetically

accessible vinyl polymers, poly(ethers), and purely hydrocarbon backbones. While a limited number of studies have directly probed the alkaline stabilities of these different polymer structures, we discuss their merits here.

Ever since the initial report of the alkaline stability of poly(arylene ether sulfone) by Quellmalz and coworkers, much attention has been focused on developing HCPs based on this polymer backbone (Figure 1.11.a).[80] There have been numerous reports of highly hydroxide-conductive (~ 10^{-2} S cm^{-1}) poly(arylene ether sulfones) bearing a wide assortment of cationic groups including ammoniums,[50,52-55,75] imidazoliums,[65,68] phosphoniums,[71,72] and guanidiniums.[76,77] Although it is generally accepted that poly(arylene ether sulfones) exhibit exceptional alkaline stabilities, a recent study by Hickner and coworkers suggests otherwise.[81] In this study they investigated the alkaline stabilities of various polymer scaffolds bearing trimethylammonium groups, finding that HCPs based on poly(arylene ether sulfones) exhibited surprisingly low stabilities in alkaline environments. Further investigation is needed to determine the long-term stability of this polymer backbone for use in alkaline fuel cells.

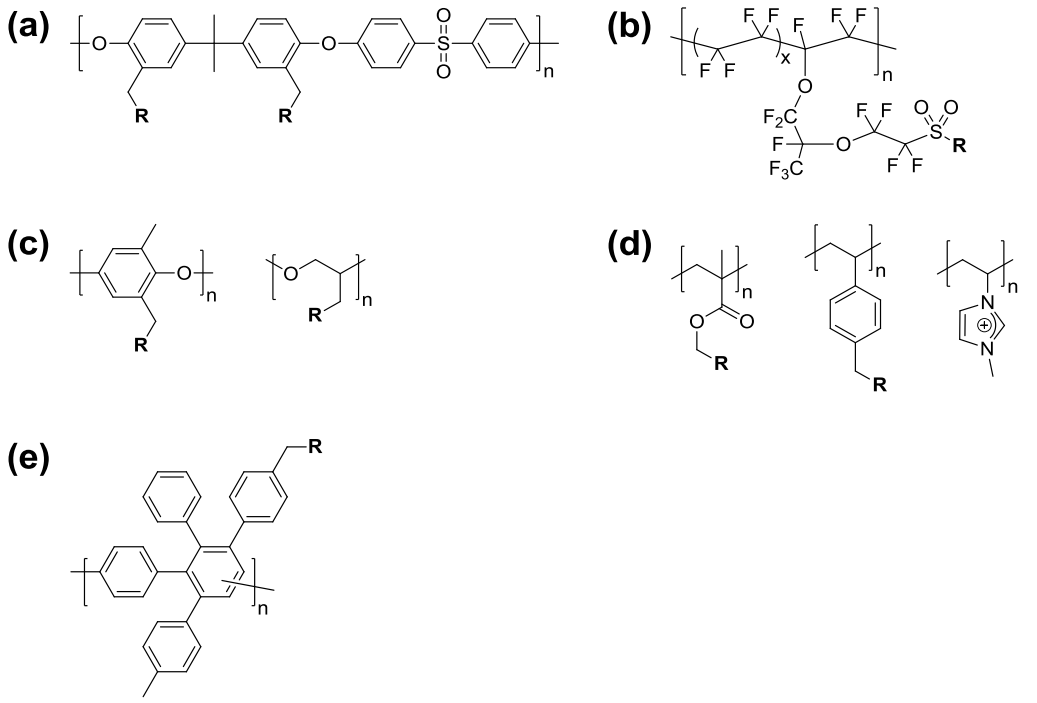

Figure 1.11. A variety of polymer backbone scaffolds used for hydroxide-conducting polymers. R represents a cationic moiety. Structures include (a) poly(arylene ether sulfones), (b) perfluorinated backbones based on Nafion®, (c) polyethers, (d) vinyl polymers including (meth)acrylates, styrenics, and poly(1-vinyl-3-alkylimidazoliums), and (e) poly(phenylenes).

In polymeric structures that mimic Nafion®, Varcoe, Slade and coworkers developed HCPs through radiation-induced grafting of vinylbenzyl chloride chains onto a fluoropolymer backbone with subsequent quaternization and ion exchange ($\sigma \sim 10^{-3}$ S cm^{-1}).[49] Through a series of studies, they demonstrated that radiation-grafting to backbones comprised of a mixture of fluorinated and non-fluorinated units (i.e., poly(ethylene-*co*-tetrafluoroethylene)) produces more robust films than systems based on fully fluorinated backbones (i.e., poly(tetrafluoroethylene-*co*-hexafluoropropylene)). Several studies by Elabd and coworkers described chemical modification

of commercially available fluorinated proton exchange polymers such as Nafion® to obtain highly conductive (~ 10^{-3} S cm^{-1}) and chemically stable HCPs (Figure 1.11.b).[57,74] Due to the chemical inertness of these fluorinated backbones, they provide a promising scaffold for alkaline fuel cell electrolyte membranes.

Polyethers are another class of relatively unexplored polymer scaffolds that exhibit promise as HCPs (Figure 1.11.c). Although polyethers are ubiquitous in lithium ion battery electrolytes (See Section 1.5), there are few reports of alkaline exchange membranes based on this versatile platform. Guo et al. functionalized an alkylene polyether, poly(epichlorohydrin) with ammonium groups to yield a highly conductive (~ 10^{-2} S cm^{-1}) material that remained stable under alkaline conditions.[56] Alternatively, Lin et al. synthesized a poly(arylene ether) with guanidinium cations that also exhibited high conductivity (~ 10^{-1} S cm^{-1}) and excellent alkaline stability.[78] Although there are very limited examples of HCPs based on this scaffold, these results suggest further study of their utility is warranted.

The facile synthesis of vinyl polymers derived from styrenes and (meth)acrylates by free-radical methods prompted numerous studies of HCPs based on these versatile platforms (Figure 1.11.d). Few reports of acrylate- or methacrylate-based HCPs have been published due to the lability of the ester bond to hydrolysis under alkaline conditions. Elabd and coworkers reported one such polymer in which they detailed the degradation of the imidazolium-containing polymer under basic conditions (σ ~ 10^{-2} S cm^{-1}) (Figure 1.8.a).[67] Several reports of materials based on poly(1-vinyl-3-alkylimidazoliums) have suggested that these polymers show alkaline stability, despite allegations that alkylimidazoliums are inherently unstable under such conditions (σ ~ 10^{-2} S cm^{-1}).[61,62,69] The stability of these systems is presumably due to the non-benzylic nature of

the alkylimidazolium group. Styrenic polymers are gaining interest as a promising scaffold for HCPs. Several recent reports have demonstrated their facile synthesis, high hydroxide conductivities (~ 10^{-2} S cm^{-1}), and alkaline chemical stabilities.[46,47,63,64] A study by Hickner and coworkers suggested that styrenic polymers are the most alkaline-stable platform among many of the commonly studied polymer backbones for HCPs.[81] The stability of styrenic polymers coupled with their facile syntheses positions them as a leading contender for stable polymeric electrolytes for alkaline fuel cells.

The questionable alkaline stabilities of poly(arylene ether sulfones) and other heteroatomic polymer backbones prompted investigations of HCPs based on purely hydrocarbon polymer scaffolds. Hibbs and coworkers developed a poly(phenylene) based HCP with pendant ammonium groups that showed good retention of hydroxide conductivity (~ 10^{-1} S cm^{-1}) and mechanical properties after exposure to strongly alkaline conditions over extended time periods (Figure 1.11.e).[48] In an effort to expand the library of HCPs with more alkaline-stable backbones, Coates and coworkers recently reported several examples of HCPs with hydrocarbon backbones synthesized by ring-opening metathesis polymerization (ROMP) (Figure 1.7). Through this route they developed both crosslinked membranes as well as linear, solvent-processable polymers with hydrocarbon backbones that are resistant to decomposition in the corrosive alkaline environments (σ ~ 10^{-2} – 10^{-1} S cm^{-1}).[58-60] Although such materials are in their infancy and further studies are required to determine their ultimate utility, these polymers are interesting electrolyte candidates for next-generation alkaline fuel cells.

1.3.4 Hydroxide-Conducting Block Copolymers

The high levels of hydration required to achieve sufficient conductivities in HCPs seemingly necessitates a trade-off between conductivity and polymer mechanical properties. Microphase-separated hydroxide conducting block copolymers provide an enticing opportunity to develop mechanically robust materials that also exhibit facile hydroxide conduction. These are hybrid materials with one block comprising a HCP, such as those described above, and another block that provides structural integrity to the material. Despite a recent perspective by Elabd and Hickner suggesting the utility of microphase-separated block copolymers for energy applications, particularly as electrolyte membranes for fuel cells, relatively few reports of such materials have appeared in the literature.[82] Cavicchi and coworkers reported the synthesis of a poly(styrene-*b*-vinylbenzyl-triethylammonium hydroxide-*b*-styrene) triblock copolymer by reversible-addition fragmentation-chain transfer (RAFT) polymerization that exhibited high ionic conductivity (Figure 1.12.a).[83] Structurally similar diblock copolymers were synthesized by Coughlin and coworkers and used to investigate the role of morphology on hydroxide conductivity.[84] They found that increasing hydration of the hydroxide-conducting block decreased deleterious effects of morphological grain boundaries on the hydroxide conductivities (~ 10^{-2} S cm^{-1}). HCPs based on the functionalization of styrene-hydrogenated isoprene block copolymers exhibited high conductivities (~ 10^{-3} S cm^{-1}) while minimizing the methanol permeability of the membrane, which is technologically important for methanol fuel cells (Figure 1.12.b).[85] These promising results motivate further work in the study of hydroxide-conducting block copolymers.

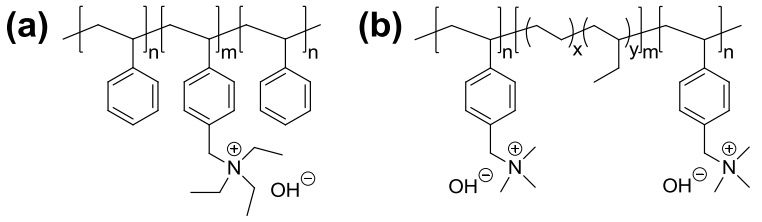

Figure 1.12. Hydroxide-conducting block copolymers containing styrenic ammonium ionic blocks with (a) poly(styrene) structural blocks[83] and (b) a hydrogenated isoprene structural block.[85]

1.4 Polymerized Ionic Liquids (POILs)

1.4.1 Polymerized Ionic Liquids as Model Single-Ion Conductors

Polymerized ionic liquids (POILs) are a class of materials with wide ranging applications, not least of which is their ability to act as ion-conducting media. POILs provide a versatile platform to explore structure-conductivity relationships without careful consideration of the strict demands of chemical stability (hydroxide-conducting polymers) or electrochemical stability (polymeric lithium single-ion conductors). Numerous studies of POILs have established design criteria for developing polymeric single-ion conductors with high ionic mobilities. Investigations of the nature of the polymer backbone, the precise identity and placement of ionic groups, and the incorporation of non-ionic groups have furnished insight into the effects of polymer structure on the ionic conductivity of POILs. The following studies demonstrate the sensitive dependence of ionic conductivity on the many possible variations in POIL structure.

In the following studies of POILs, a dichotomy between solvated and solvent-free ion conduction mechanisms is apparent. In non-solvated POILs (Subsection 1.4.2), ion motion is mediated by the segmental dynamics of the polymer chains, as described by the Vogel-Fulcher-

Tammann model. In contrast, solvated POILs (Subsection 1.4.3) exhibit a solvent-assisted ion transport mechanism, so that ionic conductivity depends on the solvent content and exhibits Arrhenius behavior.

1.4.2 Non-Solvated Polymerized Ionic Liquids

Over the past fifteen years, numerous fundamental studies of POILs with varying structures have probed different aspects of structure-property relationships as they relate to ion conduction. The results of these studies may have short-term implications for the development of electromechanical actuators and other devices. In the long term, these studies may provide important insights into the molecular design of polymer electrolytes for next-generation fuel cells and lithium ion batteries.

The ionic conductivity of a POIL is generally much lower than that of its parent ionic liquid monomer. Ohno and coworkers found that the ionic conductivity of 1-vinyl-3-ethylimidazolium TFSI dropped by 3 orders of magnitude upon polymerization even though the polymer retained a low T_g (Figure 1.13.a).[86] Although the large magnitude of the decrease may be attributed to a number of effects, the immobilization of cationic species upon polymerization should inherently lower the measured ionic conductivity of the polymer relative to the ionic liquid monomer. This is analogous to the transference number of the monomer versus the polymer related to Equation 1.1. Gibson, Colby and coworkers confirmed this in their studies of imidazolium acrylate POILs by dynamic relaxation spectroscopy (DRS) (Figure 1.14.a). Through an electrode polarization model of the DRS data, they were able to determine both the number and mobility of conducting ions in the polymer, finding that the percentage of mobile

ions was lower for the POILs relative to the respective monomers due to immobilization of the cations upon polymerization.[87]

In an effort to mitigate this drop in conductivity due to enchainment of ionic liquid monomers upon polymerization, Ohno and coworkers studied the effects of adding flexible linkers between the polymer backbone and the tethered ionic group. For acrylate- and methacrylate-based POILs, they found that alkyl- and ethylene glycol oligomer-based linkers between the polymer backbone and the imidazolium cation minimized the drop in ionic conductivity upon polymerization. Moreover, longer linkers were more effective in doing so than the shorter spacers (Figure 1.13.c).[88,89] Notably, these studies found that the conductivities of polymers with alkyl spacers were slightly higher than those with ethylene glycol spacers, presumably due to interaction of the ether oxygens with the carrier ions that impeded ion motion. In a similar study, Shaplov et al. found that ionic conductivities increased with the length of the alkyl spacer between the polymer backbone and the imidazolium cationic group due to flexibility of the side chain (Figure 1.13.c).[90]

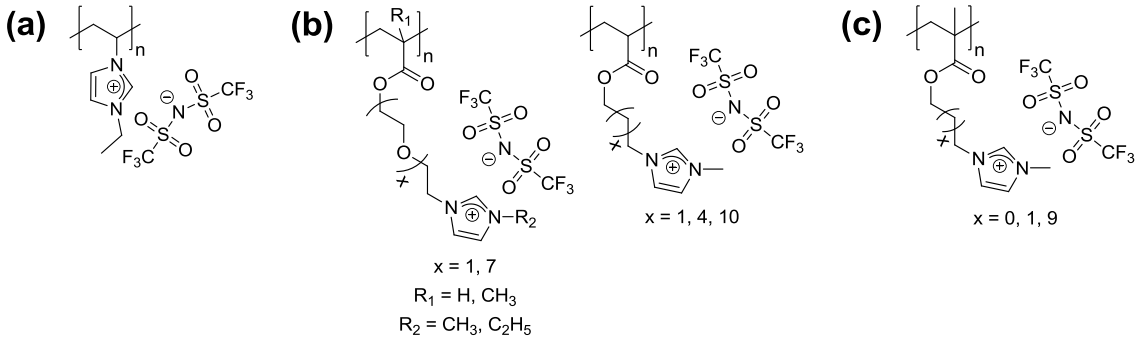

Figure 1.13. Polymerized ionic liquids used to study the effects of polymerization and the nature/length of the nonionic linker on ionic conductivity. (a) Poly(1-viny-3-ethylimidazolium TFSI),[86] (b) acrylate and methacrylate imidazolium POILs with alkyl and oligo(ethylene glycol) nonionic spacers,[88,89] and (c) methacrylate imidazolium POILs with alkyl nonionic spacers.[90]

Just as the linker between the ionic moiety and the polymer backbone has a significant effect on the ionic conductivities of POILs, so do the other non-ionic substituents attached to the ionic group. By studying alkylimidazolium acrylate POILs with varying structures, Gibson, Colby and coworkers found that changing the pendant imidazolium substituent from a butyl group to a diethyleneoxy group enhances ionic conductivity, which is contrary to the aforementioned observations by Ohno and coworkers for linkers (Figure 1.14.a).[87] They argued that since the ether chain was not tethered between the imidazolium group and the polymer chain, it actually promotes ion pair dissociation and thus leads to a larger fraction of mobile charge carriers. In a subsequent study of imidazolium acrylates with *n*-butyl *vs.* *n*-dodecyl imidazolium substituents, they found that the polymers with dodecyl tails form larger ionic aggregates due to association of the hydrophobic chains (Figure 1.14.a).[91] This manifested itself in a lower static dielectric constant and therefore a slightly lower ionic conductivity compared to

the polymers with the butyl tails. In contrast, studies by Long and coworkers on 1-vinyl-3-alkylimidazolium POILs showed that the length of alkyl substituent on the imidazolium ring had relatively little influence on the ionic conductivities in these materials (Figure 1.14.b).[92] However, they also found that introducing a hydroxyl group at the end of the alkyl chain significantly increased the measured conductivity (Figure 1.14.b).[93] While the addition of the hydroxyl group decreased T_g of the POIL, the T_g-independent conductivities of a series of POILs showed that the increase in dielectric constant and dispersion of ionic aggregates caused by the hydroxyl group enhanced ionic conductivities as well. In a related study, Winey and coworkers used x-ray scattering to determine the nanoscale morphology of 1-vinyl-3-alkylimidazolium homopolymers and correlated the backbone-to-backbone distance, the side chain-to-side chain distance, and the anion-to-anion distance to the ionic conductivities for a variety of polymer structures (Figure 1.14.b).[94] They found that while ionic conductivity was dominated by T_g effects, there were contributions to conductivity from the backbone-to-backbone distance that dictates the distance required for ion hopping. Specifically, they found that increasing the size of the imidazolium alkyl substituent decreased T_g (increasing conductivity), while also increasing intermolecular separation, which inhibited ion hopping thus decreasing conductivity.

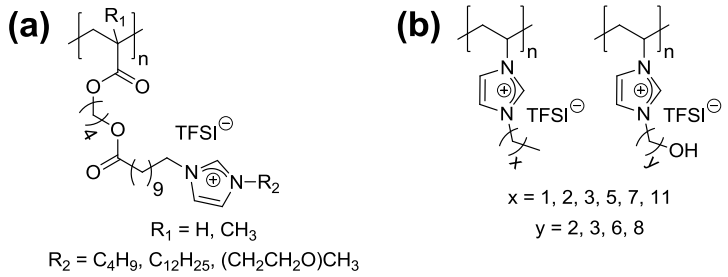

Figure 1.14. Polymerized ionic liquids used to study the effects of pendant nonionic groups on ionic conductivity. (a) Acrylate and methacrylate POILs with alkyl or oxyethylene nonionic tails,[87,91] and (b) 1-vinyl-3-alkylimidazolium POILs with alkyl- or hydroxyalkyl-tails.[92-94]

The precise identity of the ionic groups tethered to the polymer chain also significantly influences the ion conducting properties of POILs. Shaplov et al. reported the free radical polymerization of a series of methacrylate-based ionic liquid monomers with TFSI anions and varied cation structures (Figure 1.15.a).[90] They found that POILs having methylimidazolium cations were generally more conductive than the structurally analogous POILs with trimethylammonium cations. Although they were unable to homopolymerize a monomer bearing two trimethylammonium groups, they found that crosslinked copolymers of this monomer with ethylene glycol-dimethacrylate showed nearly identical conductivities as the analogous copolymer in which the ionic monomer had only one trimethylammonium group, suggesting that the ionic density per monomer unit had little effect on conductivity. While the above studies probe the effects of changing a single tethered ion, Ohno and coworkers investigated the consequences of tethering both ions to the polymer chain to form zwitterionic POILs (Figure 1.15.b). They showed that polymerized zwitterionic imidazolium sulfonamides exhibited severely diminished ionic conductivities due to the lack of mobile carrier ions and that

reasonable values of ionic conductivity were only achieved upon addition of exogenous LiTFSI salt.[95]

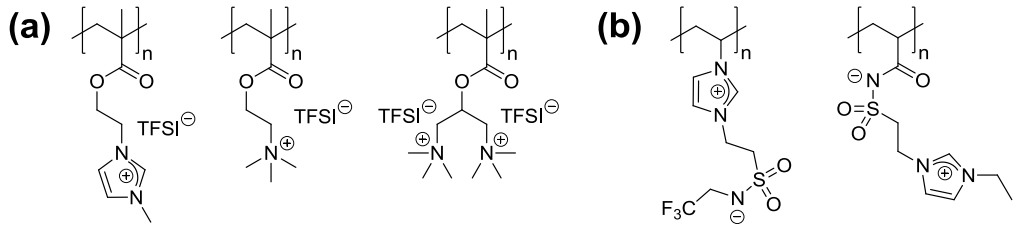

Figure 1.15. Polymerized ionic liquids studied to determine the effect of tethered cation on ionic conductivity. (a) methacrylate POILs with different tethered cationic groups[90] and (b) zwitterionic POILs.[95]

Since POILs can be viewed as synthetically accessible models of both hydroxide-conducting polymers based on polycations and polymeric lithium single-ion conductors based on polyanions, structure-conductivity relationships in POILs comprised of polycations with mobile anions and a polyanions with mobile cations have been investigated. Shaplov, et al. investigated methacrylate polymers with tethered imidazolium and pyrrolidinium cations with mobile TFSI counter-anions and compared them to analogous polymers with tethered sulfonate anions and mobile imidazolium or pyrrolidinium counter-cations (Figure 1.16.a).[96] While they found that the ionic conductivities for the polycations was marginally higher than for the polyanions, this is likely due to differences in ion pair dissociation between cation/TFSI and sulfonate/cation. Interestingly, they found that copolymerization of anionic and cationic monomers resulted in enhanced conductivities due to the formation of tethered ion pairs with attendant liberation of small molecule ionic liquids responsible for the increased conductivities. Although this study suggests minor differences between the ion conducting properties of polycations *vs.* polyanions,

a similar study by Ohno and coworkers suggests that conductivity is independent of whether the cation or the anion is tethered. They found that conductivity primarily depends on the polymer T_g as governed by the linker between the backbone and the tethered ionic group (Figure 1.16.b).[97] These studies suggest that the conductivities do not substantially depend on which ion is tethered to the polymeric backbone in these POILs. These studies form a strong foundation for the extension of these structure-property relationships to the other classes of technologically relevant hydroxide-conducting polymers and polymeric lithium single-ion conductors.

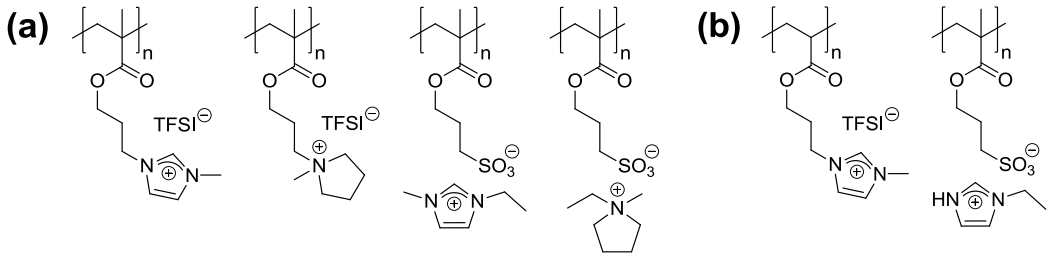

Figure 1.16. Polymerized ionic liquids studied to investigate the differences in ionic conductivity between polyanions and polycations. (a) Polycationic methacrylate POILs with imidazolium or pyrrolidinium cations and polyanionic methacrylate POILs with sulfonate anions[96] and (b) polycationic acrylate POIL with imidazolium cations and polyanionic methacrylate POIL with sulfonate anions.[97]

One common theme that emerges from a number of studies on POILs seen already is that ionic conductivity depends sensitively on the polymer segmental dynamics, with lower T_g polymers exhibiting higher conductivities. Numerous studies have indicated that the structure of the mobile counterion has a large effect on the segmental dynamics and therefore the ionic conductivities of POILs. Elabd and coworkers showed that partially exchanging tetrafluoroborate anions for TFSI anions in imidazolium methacrylate POILs furnished a polymer with a

depressed T_g and enhanced ionic conductivity (Figure 1.17.a).[98] Numerous subsequent studies of POILs with varying backbone architectures exemplify the effect that different counterions has on the T_g's, and therefore the ionic conductivities, of polymerized ionic liquids. Elabd and coworkers described a series of methacrylate imidazolium-based POILs (Figure 1.17.a),[99] Mahanthappa and coworkers reported a series of styrenic imidazolium-based POILs (Figure 1.17.b),[43] and Long and coworkers described a series of 1-vinyl-3-butylimidazolium-based POILs (Figure 1.17.c),[92] each bearing BF_4^-, PF_6^-, triflate, or TFSI anions. Each of these studies demonstrated the plasticizing effect that large, bulky anions such as TFSI has on the polymer, resulting in a lower T_g and enhanced ionic conductivity. Surprisingly, the studies of the methacrylate and styrenic POILs show that the T_g-independent conductivities of POILs with TFSI anions are actually lower than for POILS with BF_4 and PF_6 anions, suggesting that other factors such as anion size and symmetry play a role in determining ionic conductivity. These factors are discussed in further detail in Chapter 2. The strong dependence of ionic conductivities of POILs on the polymer segmental dynamics observed throughout many of these studies indicates a conduction mechanism where ion motion is intimately coupled with polymer chain motion according to the VTF model.

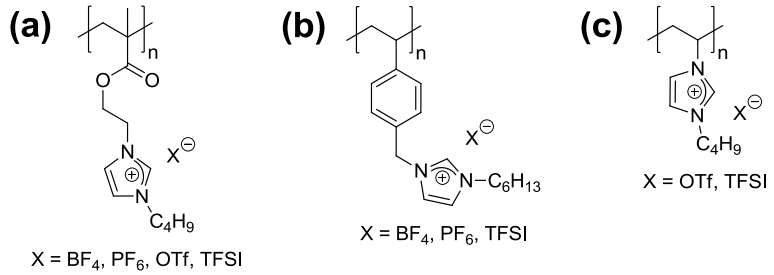

Figure 1.17. Polymerized ionic liquids used to study the effect of anion structure on glass transition temperature and ionic conductivity. (a) Methacrylic imidazolium POILs,[98,99] (b) styrenic imidazolium POILs,[43] and (c) 1-vinyl-3-butylimidazolium POILs.[92]

1.4.3 Hydrophilic Polymerized Ionic Liquids

Hydrophilic polymerized ionic liquids, particularly those bearing mobile hydroxide anions, have been the target of a large number of studies due to their implications for the design of advanced electrolytes for alkaline fuel cells, and both lithium-air and zinc-air batteries. The former application requires that these materials exhibit high conductivities under highly variable relative humidity conditions. In contrast to the non-solvated POILS wherein ionic conductivity depends on polymer segmental dynamics as described by the VTF model, hydrophilic POILs typically conduct ions through the available solvent.

Elabd and coworkers recently showed that established ion conducting polymers such as Nafion®, which is used extensively in proton conduction, may be modified through simple chemistries to yield robust and highly conductive materials.[57] More explicitly, they showed that reaction of Nafion® with dimethylpiperazine to form a cationic sulfonamide moiety and subsequent ion exchange furnished a material that conducts ions such as Cl^-, HCO_3^-, CO_3^-, and

OH^- while retaining the favorable water-uptake and nanostructured morphology of parent Nafion®. Similarly, Herring and coworkers converted a perfluorinated sulfonic acid ionomer into an ammonium-containing anion conductor that exhibited ionic conductivity that depended highly on the structure and hydration of the cationic groups. Variable temperature conductivity measurements revealed an Arrhenius behavior of ion conduction.[100]

A fundamental study of structure-property relationships for hydrophilic POILs was published by our group in which we demonstrate that ion conduction occurs by a fundamentally different mechanism in hydrated hydrophilic POILs than in anhydrous hydrophobic POILs.[43] By studying a series of hydrophilic poly(vinylbenzyl(alkyl)imidazolium chloride) homopolymers, we showed that ionic conductivities increased for polymers that were more highly hydrated and that ion conduction obeyed Arrhenius behavior (Figure 1.18.a). From these observations, we asserted that the key parameter for optimizing ionic conductivity for hydrated POILs is the choice of structures that maximize ion hydration or polymer hydrophilicity. Details of this study comprise the major topic of Chapter 2. A related study by Hickner and coworkers on POIL triblock copolymers randomly functionalized with ammonium groups also established that ionic conductivity in hydrated polymers is dictated by the concentration of ionic groups and the level of hydration: highly hydrated polymers bearing highly dissociated ion pairs exhibited the highest conductivities (Figure 1.18.b).[101] In their comparisons of these anion-conducting polymers to analogous proton-conducting polymers, they demonstrated that the conductivities were the same in both cases when normalized by the dilute solution diffusivity of the respective ions (i.e., H^+ *vs.* OH^-). In a related vein, Balsara and coworkers reported similar results in hydrophilic styrenic POIL block copolymers with either ammonium or imidazolium cationic groups (Figure

1.18.c).[102] At a given block copolymer composition exhibiting the same nanoscale morphology, the ionic conductivities for polymers with either cationic group were similar since they had comparable degrees of hydration. Therefore, ion conduction depends sensitively on the level of hydration of the hydrophilic POIL.

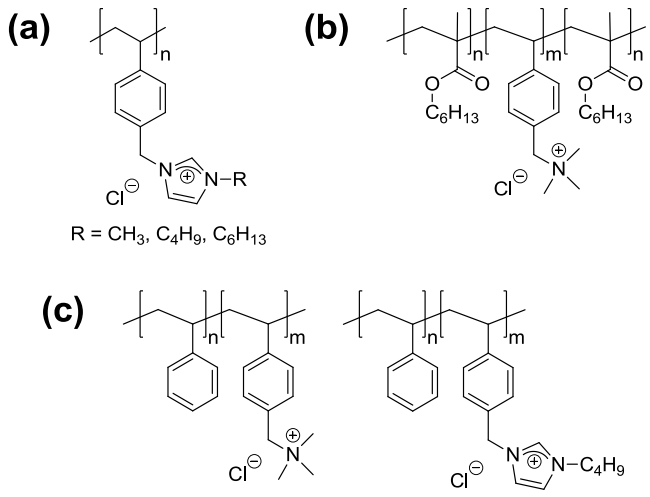

Figure 1.18. Hydrophilic polymerized ionic liquids studied to determine the effect of hydration on ionic conductivity. (a) Styrenic imidazolium POILs,[43] (b) POIL triblock copolymer with hydrophobic methacrylate blocks and styrenic ammonium ionic blocks,[101] and (c) styrenic POIL block copolymers with ammonium or imidazolium cations.[102]

1.4.4 Nanostructured Polymerized Ionic Liquids

All of the aforementioned studies of both hydrophilic and hydrophobic POILs indicate that the highest conductivities are only achieved when these materials exhibit liquid-like characteristics, namely, low T_g's or high hydration states. The liquid-like nature of these highly conductive materials diminishes their utility in many device applications, where mechanically

robust, solid-like materials are required. Microphase separated POIL-containing block copolymers provide a promising avenue for the development of mechanically robust, nanostructured materials in which the ionic POIL domains form contiguous paths for ion conduction through an insulating, mechanically robust matrix phase.

Several reports of nanostructured ionic liquid block copolymers have appeared in recent years, including our pioneering fundamental study of morphology-conductivity relationships in poly(styrene-*b*-vinylbenzyl(alkyl)imidazolium) block copolymers (Figure 1.19.a).[103] Using PS-POIL block copolymers that self-assembled into lamellae, cylinders, and coexistence of these two phases, we showed that ionic conductivity depends sensitively on the nanoscale morphology. Although the conductivity of a polymer exhibiting lamellar morphology was roughly consistent with the volume fraction and geometric constraints associated with randomly oriented polydomains, samples exhibiting cylindrical morphologies had severely diminished conductivities that we attributed to morphological defects resulting in "dead-end" conducting channels. This study is described in detail in Chapter 3.

In a related study, Elabd and coworkers[104] compared methacrylate-based imidazolium microphase-separated block copolymers with analogous disordered random copolymers at similar compositions to determine the effect of nanoscale morphology on ionic conductivity (Figure 1.19.b). At all compositions, they found that the ionic conductivities increased by approximately two orders of magnitude for the nanostructured block copolymer. This result suggests that the local concentration of ions in a microdomain enhances conductivity.

Long and coworkers reported on triblock copolymers in which the center, ion-conducting block was a low T_g random copolymer containing varying amounts of polymerized ionic liquid

units (Figure 1.19.c). They found that these microphase separated block copolymers exhibited increased conductivities with increasing incorporation of ionic liquid monomer in the POIL block.[105]

Wang and coworkers described a series of triblock copolymers in which a fluorinated center block is flanked by two methacrylate-POIL end blocks (Figure 1.19.d). Surprisingly, they found that these block copolymers do not microphase separate due to the miscibility of the POIL blocks with the fluorinated blocks. In accord with the studies presented above, they saw increased conductivities for POILs with counterions that lower the T_g of the polymer. Consequently, ionic conductivity was strongly correlated with polymer segmental dynamics as evidenced by data fitting to the VFT model.[106]

While the microphase separated materials presented thus far have been based on block copolymers, Gibson and coworkers reported that a series of segmented imidazolium polyesters that undergo crystallization-induced microphase separation (Figure 1.19.e). In polymers with larger linear alkyl spacers between imidazolium units, they found evidence for semicrystalline order that caused aggregation of ionic groups into weakly ordered lamellae with enhanced ionic conductivities relative to analogous amorphous polymers.[107]

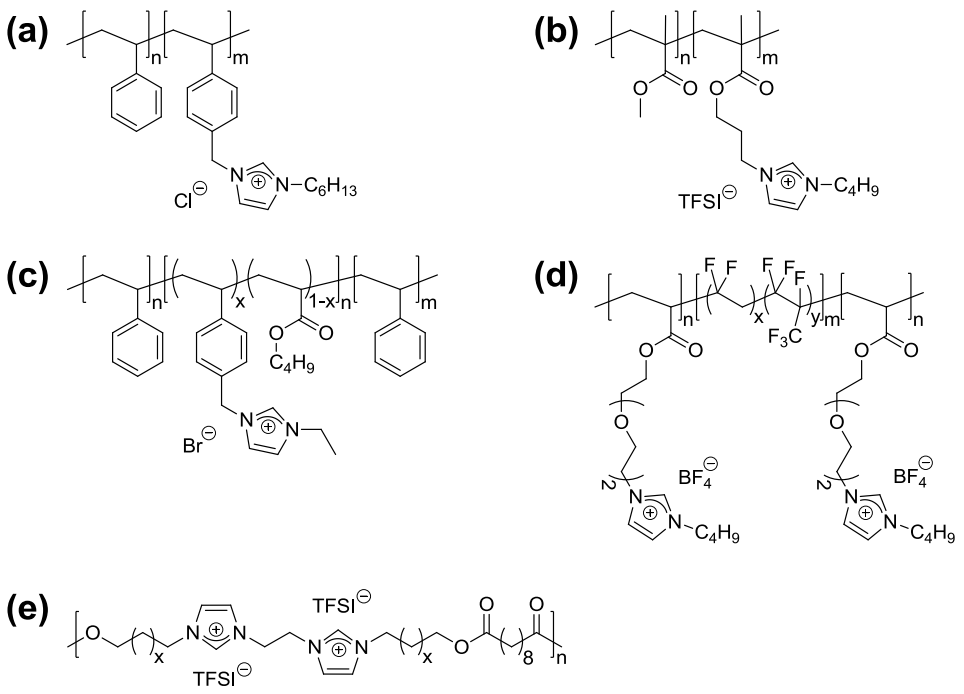

Figure 1.19. Polymerized ionic liquid block copolymers for studying morphology-conductivity relationships. (a) Styrenic imidazolium POIL diblock copolymers,[103] (b) methacrylic imidazolium POIL random and diblock copolymers,[104] (c) POIL triblock copolymers with a mix of charged and uncharged units in the center block,[105] (d) POIL triblock copolymers with a fluorinated nonionic center block,[106] and (e) segmented polyester POILs.[107]

1.5 Polymeric Lithium Single-Ion Conductors (PLSICs)

1.5.1 Challenges Facing Lithium Single-Ion Conductors

Rechargeable lithium ion batteries are ubiquitous in today's high-tech society. Nearly every cellular phone, laptop, and tablet PC draws power from a lithium ion battery. As discussed in the introduction to this chapter, advances in the chemistry and engineering of lithium ion batteries are necessary to push this technology from small portable electronics applications into

larger scale applications for electric vehicles and large-scale electrical grid storage for intermittent, renewable energy sources.[3] As advances next-generation battery anodes and cathodes continues to push lithium ion batteries to higher voltages and larger capacities, new electrolyte materials must be developed to support these advanced batteries.[39]

Currently, most commercial lithium-ion battery electrolytes are comprised of binary lithium salts dissolved in organic solvents such as alkyl carbonates. However, these systems suffer from two major safety issues that may lead to catastrophic failure of the battery: (1) possible leakage of inherently flammable liquid electrolytes, and (2) dendrite formation upon repeated charge/discharge cycling that leads to short circuiting of the battery.[108] Alternatively, solid polymer and polymer gel electrolytes have garnered much attention in recent years due to their favorable attributes, including reduced flammability and increased mechanical strength that may lead to safer batteries.[8] Since the initial discovery by Wright and coworkers that lithium salts dissolved in poly(ethylene oxide) (PEO) exhibited high ionic conductivities, much research on polymeric electrolyte materials has focused on optimizing these macromolecular solutions.[109-111] Although these materials have met some successes, they continue to suffer from several limitations, including a limited electrochemical window (< 4 V *vs.* Li/Li^+), limited lithium ion conductivities, and limited lithium ion mobilities relative to their charge compensating anions stemming from strong chelation of the lithium ions by the polyether matrix.[4] This chelation substantially decreases the lithium ion transference number (t_{Li+}), which is the fraction of current carried by lithium as opposed to other ions in the system as described by Equation 1.1. In both organic carbonate solutions and in PEO-based systems, $t_{Li+} \sim 0.2\text{-}0.4$. This low t_{Li+} causes performance losses in the battery due to electrolyte concentration polarization that decreases the

voltage window experienced by the electrodes.[41,112,113] By covalently tethering the anionic species to a polymer chain with a charge-balancing lithium counterion, thus forming a polymeric lithium single-ion conductor (PLSIC), the transference number approaches unity, which results in greatly enhanced electrolyte and battery performance.

Next-generation lithium ion batteries for large scale applications require high-performance electrolytes that are both safe and functional. Key figures of merit for a lithium ion battery electrolyte include high lithium ion conductivity, high t_{Li+}, and a wide electrochemical window (up to 5 V) so that higher power output and safer function may be achieved. The preferred method of modulating these parameters in a PLSIC is to carefully choose the anionic moiety that is tethered to the polymeric scaffold.[38] The nature of the anion as well as the dielectric constant of the surrounding medium (e.g., polymer backbone, solvent) greatly affect the dissociation of lithium ions from the tethered anions, thus directly influencing the mobility of the lithium ions. Concurrently, the nature of the anion plays a major role in determining the electrochemical window in which the PLSIC may operate. This parameter is also affected by the nature of the polymeric backbone as well as other additives.

Several studies by Ohno and coworkers highlighted the importance of having highly dissociated ion pairs in order to obtain highly conductive electrolytes. Through their studies of a series of α,ω-telechelic poly(ethylene oxides) having charged end groups with various charge compensating counterions, they were able to correlate ionic conductivity to the extent of ion pair dissociation[114-116] (Figure 1.20). They demonstrated that the conductivities of a series of polyether salts containing constant sulfonamide end groups with different alkali metal cations increased in the order $\sigma_{Cs+} > \sigma_{Rb+} > \sigma_{K+} > \sigma_{Na+} > \sigma_{Li+}$ (Figure 1.20.a). Thus, larger cations gave

rise to higher conductivities than smaller cations due to their increased extent of dissociation. Since the target application for these materials is lithium ion batteries, changing the identity of the cation is not productive, as lithium ions must be used. Therefore, they explored a range of different anion structures such as carboxylates, sulfonates, and sulfonamides, finding that lithium sulfonamides exhibited the highest conductivity (~ $10^{-4.5}$ S cm^{-1}) and lithium carboxylates exhibited the lowest conductivity (~ $10^{-5.5}$ S cm^{-1}), as would be expected from their relative degrees of ion pair dissociation.

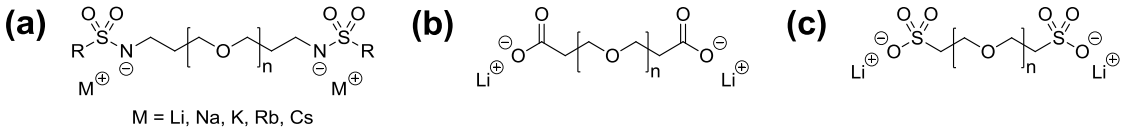

Figure 1.20. Polymeric lithium single-ion conductors comprised of poly(ethylene oxide) with ionic end groups used to probe the effect of ion pair structure on lithium conductivity. End groups consist of (a) sulfonamides, (b) carboxylates, and (c) sulfonates.[114-116]

The following subsections review the different anion chemistries that have been investigated for PLSICs. Numerous structures ranging from relatively simple carboxylates and sulfonates to more exotic sulfonamides, sulfonylimides, and borates have been implemented into PLSICs toward the discovery of highly conductive and electrochemically stable polymeric electrolytes with a high lithium ion transference number for use in lithium ion batteries.

1.5.2 Lithium Carboxylates

Although the extent of ion pair dissociation of lithium carboxylates is relatively low, many of the earliest reports of PLSICs are based on lithium methacrylates due to their synthetic accessibility. Kobayashi, et al. prepared random copolymers of lithium methacrylate and oligo(ethylene oxide) methacrylate to yield lithium single-ion conductors[117,118] (Figure 1.21.a). While increasing the percentage of lithium methacrylate in the polymer improved conductivity due to a higher lithium ion concentration, the increased concentration of ionic species in the polymer raised the T_g of the material, which lowered its conductivity. Therefore, balancing these two competing factors maximized the observed lithium ion conductivity. Further analysis of these polymers revealed that they exhibited a lithium transference number of unity and displayed VFT behavior due to the coupling of ion motion and polymer segmental dynamics. Kim and Park reported structurally similar random copolymers in which the carboxylate moiety was separated from the polymer backbone by an alkyl branch[119,120] (Figure 1.21.b). Although they hypothesized that the increased flexibility of this chain would enhance ionic conductivity relative to the values observed by Kobayashi, the reported lithium ion conductivities were similar ($\sim 10^{-7}$ S cm^{-1}). FTIR spectroscopic analyses of these polymers indicated significant lithium-carboxylate ion pairing, indicative of low degrees of ion pair dissociation. Poor dissociation of the lithium-carboxylate ion pair resulted in a small number of mobile lithium ions capable of transferring charge.

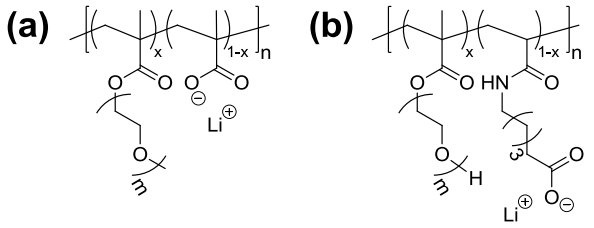

Figure 1.21. Lithium carboxylate random copolymers studied as polymeric lithium single-ion conductors. (a) Lithium methacrylate random copolymers[117,118] and (b) methacrylate/acrylamide random copolymers incorporating pendant lithium carboxylates.[119,120]

In an attempt to maximize the number of mobile lithium ions in lithium carboxylate single-ion conductors, Mayes and coworkers developed several microphase separated copolymer systems that exhibited enhanced ion dissociation, and consequently enhanced lithium ion conductivities.[113,121] They found that the placement of lithium methacrylate (LiMA) units within a copolymer of lauryl methacrylate (LMA) and poly(ethylene oxide) methacrylate (PEOM) had a profound effect on ionic conductivity. Polymer architectures that physically separated the LiMA units from the ion-conducting PEOM units such as in poly(LMA-*b*-LiMA-*b*-PEOM) (Figure 1.22.a) and poly((LMA-*ran*-LiMA)-*b*-PEOM) (Figure 1.22.b) exhibited lithium conductivities that were one to two orders of magnitude higher than for polymer architectures where the LiMA units were incorporated into the ion-conducting PEOM units such as poly(LMA-*b*-(LiMA-*ran*-PEOM)) (Figure 1.22.c). They proposed that separating the LiMA units from the high dielectric, ion-conducting PEOM domains forced the lithium carboxylates to dissociate so that the lithium ions migrate to the PEOM domains. In a subsequent study of polymers comprised of LiMA and a poly(propylene oxide) methacrylate monomer bearing a heptadecyl end-cap they demonstrated

that the aggregation of the hydrophobic heptacdecyl tails drove the formation of ion channels that enhanced lithium ion conductivity[122] (Figure 1.22.d). Finally, in a series of LiMA-PEOM copolymers incorporating a poly(dimethylsiloxane) methacrylate block, Mayes and coworkers showed that microphase separation into ion-conducting channels alone was not sufficient to obtain high conductivity[123] (Figure 1.22.e). Doping the polymer with the Lewis acid BF_3, which promotes the dissociation of lithium ions from the methacrylate units, significantly enhanced lithium ion conductivity while maintaining lithium single-ion conducting behavior ($t_{Li+} \approx 1$). Additionally, they demonstrated that this polymer performed well in full cell battery tests.[124]

Although Mayes and coworkers were successful in obtaining highly lithium conductive block copolymers, their work highlights the sensitive dependence of lithium ion conductivity on the polymer functionality and molecular architecture. The importance of these considerations is exemplified by poly(styrene-*b*-lithium methacrylate) block copolymers reported by Floudas and coworkers that exhibited severely diminished lithium ion conductivities ($< 10^{-11}$ S cm^{-1} at 110 °C) presumably due to poor lithium ion dissociation[125] (Figure 1.22.f).

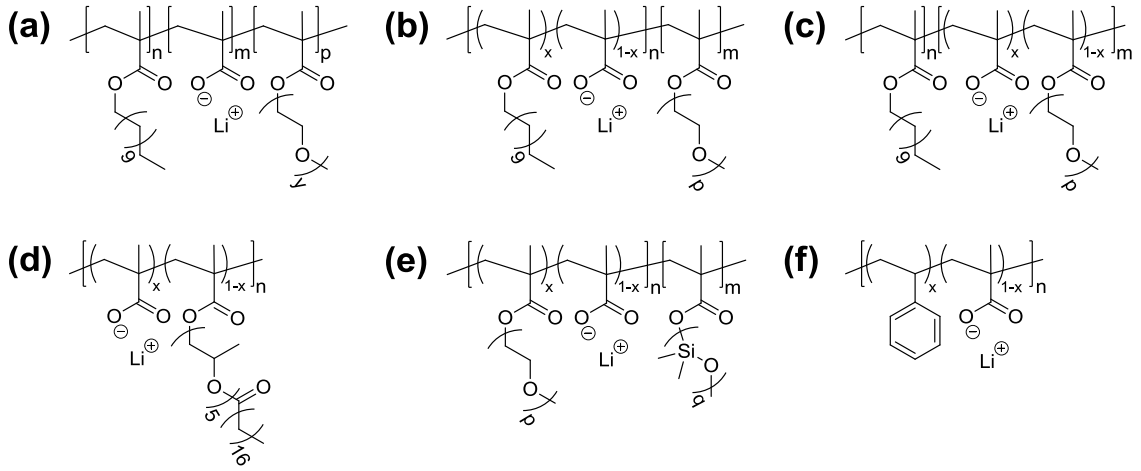

Figure 1.22. Lithium single-ion conducting block copolymers containing lithium carboxylates exemplifying the effect of polymer architecture on ionic conductivity. (a) poly(LMA-*b*-LiMA-*b*-PEOM),[113] (b) poly((LMA-*ran*-LiMA)-*b*-PEOM),[113] (c) poly(LMA-*b*-(LiMA-*ran*-PEOM)),[113] (d) lithium methacrylate random copolymers incorporating propylene oxide segments with heptadecyl tails,[122] (e) lithium methacrylate copolymers incorporating poly(dimethyl siloxane branches),[123] and (f) poly(S-*b*-LiMA).[125]

In spite of the development of highly lithium conductive PLSICs based on lithium carboxylates, the utility of these materials for commercial battery applications is uncertain due to the questionable reductive stability of the ester linkages in these methacrylate-based polymers. While Mayes and coworkers demonstrated the oxidative stability of their materials up to potentials of ~ 6 V *vs.* Li/Li^+, they did not report on their reductive stability. Since a lithium ion battery experiences an electrochemical potential range from highly reductive to highly oxidative, ideal materials must be stable across all conditions in order to exhibit high performance and cycling lifetime.

1.5.3 Lithium Sulfonates, Sulfonamides, and Sulfonylimides

PLSICs based on lithium sulfonates, sulfonamides, and sulfonylimides address some of the noted concerns regarding reductive instability and poor ion pair dissociation found in lithium carboxylate PLSICs. One class of single-ion conducting polymers is based on arylsulfonates tethered by polyether linkers. Colby, Runt, Winey and coworkers studied polyesters derived from sulfonate-bearing isophthalates and α,ω-dihydroxy telechelic poly(ethylene oxide). The conductivities of these materials simply depended on the polymer T_g, as would be expected for a solvent-free PLSIC[126] (Figure 1.23.a). Further study of these materials revealed evidence for the formation of ionic aggregates or clusters. Introducing the lower dielectric polyether poly(tetramethylene oxide) into the system promoted the formation of these clusters.[127,128] Maranas and coworkers subsequently studied similar polymers by neutron scattering and found that the formation of ionic aggregates did not impede ion motion, as previously believed.[129,130] They proposed that the long-chain ionic aggregates formed in these systems may allow for facile ion motion through fast rearrangement of the ionic clusters, a conclusion that they supported with molecular dynamics simulations.[131] While these systems provide interesting insights into the physical phenomena governing ion motion in single-ion conductors, their ionic conductivities are relatively low, precluding them from use as lithium ion battery electrolytes.

In contrast to the aforementioned arylsulfonate polymers in which the ion pairs are proximal to the polymer backbone, other polymeric systems were developed with a spacer between the backbone and the ion pair in an attempt to maximize ionic conductivity. Zhang et al. described a crosslinked methacrylate-based polymer containing both poly(ethylene oxide) methacrylate and pendant lithium sulfonate monomer units[132] (Figure 1.23.b). While

conductivity was still relatively low, they proved that this polymer exhibits lithium single-ion conducting behavior as evidenced by a near unity lithium transference number. Kerr and coworkers reported on similar non-crosslinked systems based on acrylates (Figure 1.23.c). While the conductivity of the neat polymer was relatively low, they showed that it could be increased by three orders of magnitude upon the addition of 50 wt% of the solvent propylene carbonate / ethylmethyl carbonate (1:1 v/v). Cycling of this polymer in a symmetric Li/Li cell demonstrated the lithium single-ion conducting nature of the polymer as evidenced by a lack of electrode polarization.[133]

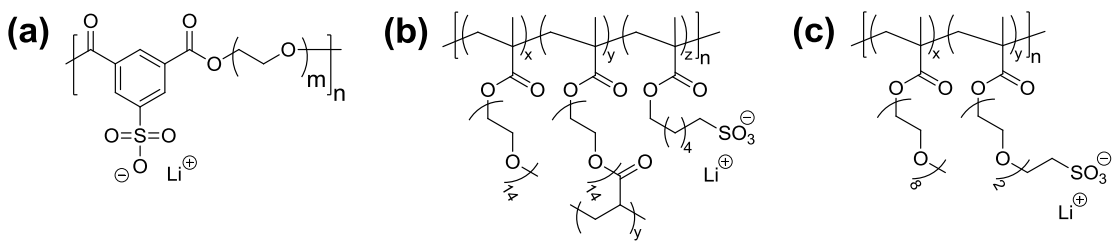

Figure 1.23. Lithium sulfonate-containing polymeric lithium single-ion conductors based on conventional polymer backbones. (a) polyesters containing lithium arylsulfonates,[126-131] (b) crosslinked poly(methacrylate) containing pendant lithium sulfonates,[132] and (c) linear poly(methacrylate) containing pendant lithium sulfonates.[133]

The reductive lability of the ester linkages in the PLSICs described above minimized potential utility of these materials in actual lithium ion batteries. After cycling the symmetric Li/Li cell to failure using their acrylate-based single-ion conductor, Kerr and coworkers analyzed the polymer electrolyte and concluded that failure was caused by decomposition of the ester

linkages on the reductive lithium electrodes.[133] These studies indicate that reductively unstable ester functionalities should be avoided in the design of electrochemically stable PLSICS.

Some unconventional polymeric backbones and nanoparticle hybrid systems bearing lithium sulfonate ionic groups have been employed as lithium single-ion conductors. Independent reports by Doyle et al.[134] and Liu et al.[135] described the conversion of Nafion® or a comparable perfluorinated sulfonic acid ionomer to a lithium sulfonate-based lithium single-ion conductor (Figure 1.24.a). Upon swelling these materials with organic carbonate solvents, they reported excellent room temperature lithium ion conductivities (~ 10^{-3} S cm^{-1}) as well as long cycle lifetimes in battery full cell tests. These are intriguing materials; however, the cost of perfluorinated ionomers is still prohibitively high. Tada et al. reported the synthesis of a poly(phosphazene) backbone containing pendant lithium sulfonate moieties tethered through ethylene glycol segments[136] (Figure 1.24.b). They compared the lithium conductivity of this polymer with the conductivity of an analogous non-ionic polymer containing a binary lithium salt and found that while both had similar conductivities, the single-ion conductor maintained its conductivity under constant potential over time, whereas the conductivity of the binary salt diminished due to polarization effects. Although they did not report on the electrochemical stability of their materials, phosphazenes are known to be relatively electrochemically stable and have the added feature of acting as flame retardants.[137] Silica nanoparticles decorated with lithium sulfonate groups have also been demonstrated as lithium single-ion conductors[138] (Figure 1.24.c). Archer and coworkers showed that such materials exhibited modest lithium ion conductivities that could be increased by the addition of solvents (propylene carbonate, tetraglyme), or by complexation of the sulfonate groups with BF_3 to promote ion pair

dissociation.[139] They further demonstrated that the nanoparticle system exhibited excellent electrochemical stabilities ranging from -0.3 – 6 V *vs.* Li/Li^+ for the sulfonate-decorated nanoparticles, whereas the electrochemical window narrows slightly for the materials complexed with BF_3.

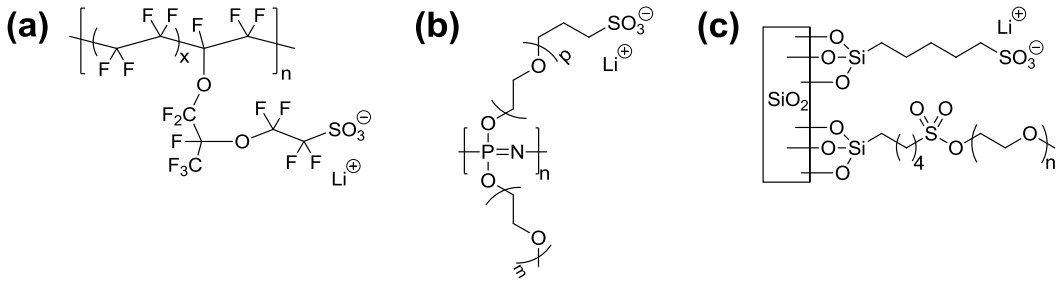

Figure 1.24. Lithium single-ion conductors comprised of non-conventional polymer backbones and inorganic hybrid systems. Lithium single-ion conductors based on (a) Nafion®,[134,135] (b) poly(phosphazene),[136] and (c) silica nanoparticles.[139]

While these examples demonstrate that sulfonate-containing lithium single-ion conductors can exhibit acceptable levels of lithium ion conductivity, evidence suggests that the dissociation of ion pairs may be enhanced by changing from a sulfonate anion to a sulfonamide or sulfonylimide anion. Endo and coworkers reported the synthesis of lithium sulfonate and lithium sulfonylimide-containing network lithium single-ion conductors synthesized by amine-hardening epoxy chemistry[140,141] (Figure 1.25.a,b). By changing from a sulfonate-containing network to a sulfonylimide-containing network, they observed an increase in conductivity of almost an order of magnitude (~ 10^{-7} S cm^{-1} to ~ 10^{-6} S cm^{-1}). They were able to obtain even larger gains in ionic conductivity by swelling the network with propylene carbonate to yield gels in which both the sulfonate and sulfonylimide networks had similar conductivity (~ 10^{-5} S cm^{-1}).

Shriver and coworkers described a linear comb polymer based on a polysiloxane backbone with a combination of sulfonamide-containing side chains and poly(ethylene oxide) side chains[142] (Figure 1.25.c). They measured conductivities similar to those of Endo in the range of 10^{-6} S cm^{-1}. While neither Endo nor Shriver commented on the electrochemical stability of their respective polymer systems, one anticipates relatively wide electrochemical stability windows based on the chemical functionalities used in these polymers.

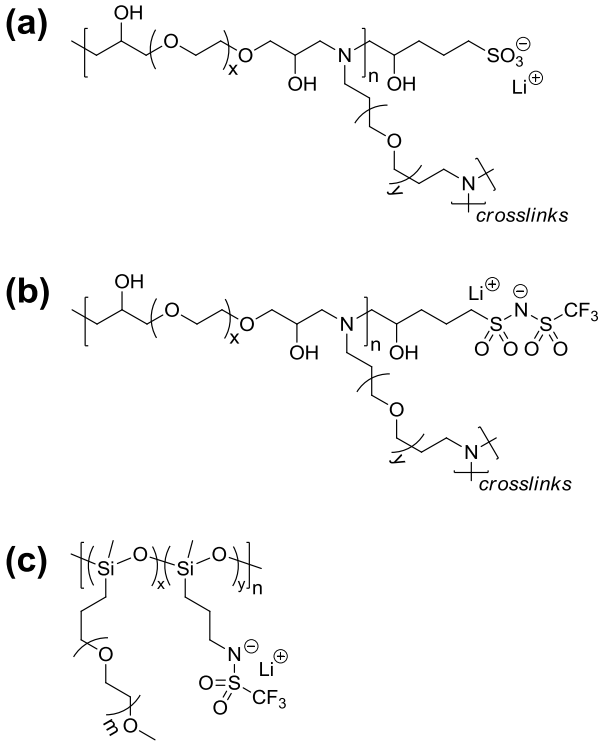

Figure 1.25. Polymeric lithium single-ion conductors containing lithium sulfonate, lithium sulfonamide, and lithium sulfonylimide ionic groups. (a) Lithium sulfonate-containing epoxy networks,[140] (b) lithium sulfonylimide-containing epoxy networks,[141] and (c) linear lithium sulfonamide-containing polymers with a poly(siloxane) backbone.[142]

Recently, Armand and coworkers described the facile synthesis of a PLSIC based on a polystyrene backbone with lithium sulfonylimide ionic groups[143] (Figure 1.26.a). Although this material exhibited a glass transition temperature in excess of 150 °C, precluding measurement of room temperature lithium ion conductivity, they found that a blend of this polymer with poly(ethylene oxide) exhibited a moderately useful lithium ion conductivity (~ 10^{-6} S cm^{-1} at 45 °C). In a subsequent report, they described the synthesis of block copolymers of this sulfonylimide-decorated polystyrene with poly(ethylene oxide)[144] (Figure 1.26.b). By optimizing the ratio of the different blocks, they were able to obtain conductivities on the order of 10^{-6} S cm^{-1} at 45 °C. Additionally, they demonstrated that these polymers were oxidatively stable in excess of 5 V (*vs.* Li/Li^+), which is better than the oxidative stability of nonionic PS-*b*-PEO-*b*-PS containing LiTFSI. This polymer represents an interesting class of materials that warrants further investigation.

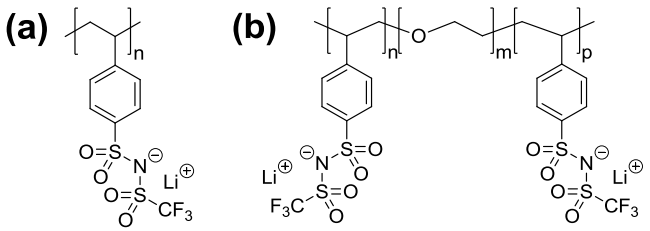

Figure 1.26. Styrenic polymeric lithium single-ion conductors incorporating sulfonylimide anionic groups. (a) Styrenic lithium sulfonylimide homopolymer[143] and (b) styrenic lithium sulfonylimide block copolymer with a poly(ethylene oxide) block.[144]

A major issue precluding the use of LiTFSI and its polymeric salt analogues in lithium ion batteries is their ability to corrode aluminum, which is commonly used as a current collector

in lithium ion battery cathodes.[145] This major limitation coupled with the often tedious synthesis of polymers incorporating sulfonamides and sulfonylimides renders the likelihood that these polymeric electrolytes will find application in lithium batteries quite low.

1.5.4 Lithium Borates

In spite of the synthetic accessibility of PLSICs based on lithium carboxylates and the enhanced ionic conductivities of polymers containing lithium sulfonate and sulfonylimides, lithium single-ion conductors based on lithium borates have also garnered substantial attention. The high degree of ionic dissociation, which leads to high lithium ion conductivities and electrochemical stability of many of these materials, renders this class of PLSICs intriguing potential electrolyte materials for lithium ion batteries.

Fujinami and coworkers reported the synthesis of liquid lithium borate salts containing two oligomeric ethylene oxide chains and either two triflate or two perfluorinated phenolate groups to promote lithium dissociation[146] (Figure 1.27.a,b). Although these salts exhibited conductivities up to $10^{-4.5}$ S cm^{-1} at 30 °C and were stable to 4.1 V, their transference numbers were significantly less than unity, presumably due to the relatively low molecular weight of the anionic species. To overcome this limitation, they synthesized polymeric analogues that maintained the oligo(ethylene oxide) chains, while linking the borate groups to the polymer backbone through perfluorinated ester linkages[147] (Figure 1.27.c). Upon optimization of the relative lengths of ethylene oxide units and by blending with PEO homopolymer, they obtained modest lithium ion conductivities (~ 10^{-6} S cm^{-1}).

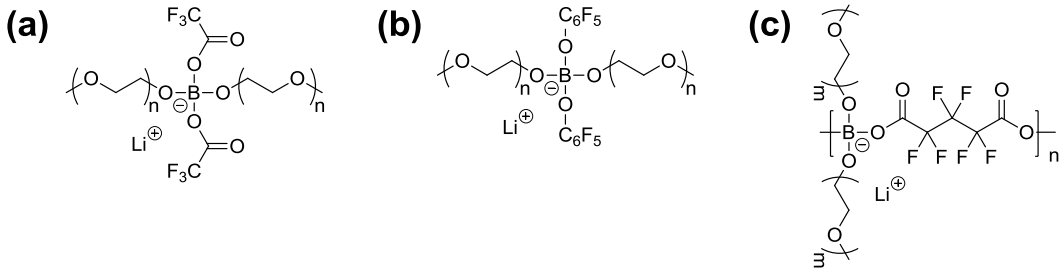

Figure 1.27. Attempts to obtain lithium single-ion conductors using (a,b) liquid lithium borate salts with poly(ethylene oxide) chains[146] and (c) an analogous polymerized material.[147]

Ohno and coworkers described two alternate syntheses of mesitylborate-containing polymers bridged by poly(ethylene oxide) units (Figure 1.28a,b).[148,149] Depending on their synthetic route, they were able to install either aryl groups or alkoxide groups on the borate to yield a range of polymers with modest conductivities (~ 10^{-5} to $10^{-6.5}$ S cm^{-1} at 25 °C) and $t_{Li+} \approx$ 0.8, depending on the substituent. Although they did not explicitly comment on the lower than expected transference number, the relatively low molecular weight of the polymers likely results in a nontrivial amount of counterproductive anion motion. Using a similar synthetic approach, Angell and coworkers reported a series of borate polymers that they modified using a range of lithium salts.[150] For lithium salts with more weakly basic anions such as TFSI and triflate, the borate polymer acts as an "anion trap" that inhibits anion motion but does not completely immobilize it. If they instead treated the polymer with lithium salts bearing more strongly basic anions such as cyanide or thiocyanate, these anions bound tightly to the borate, effectively immobilizing them to give true lithium single-ion conductors. They observed enhanced conductivities for the "anion trapped" salts over the single-ion conductors (~ 10^{-4} S cm^{-1} for

LiTFSI *vs.* ~ $10^{-5.5}$ S cm^{-1} for LiCN); however, the higher conductivity came at the expense of a lower transference number. These polymers are electrochemically stable up to 4.5 V *vs.* Li/Li^+.

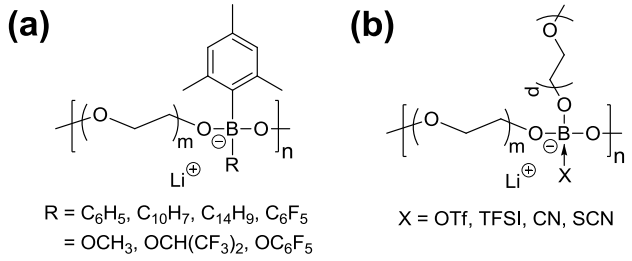

Figure 1.28. Lithium borate containing single-ion conductors. (a) mesitylborate-containing polymers[148,149] and (b) lithium borate single-ion conductors and "anion-trapping" polymers.[150]

Colby and coworkers recently reported the synthesis of a novel lithium single-ion conductor comprised of a polysiloxane backbone bearing a mixture of pendant lithium tetra(aryl)borate moieties and pendant cyclic carbonates to aid in dissociation of the lithium salts[151] (Figure 1.29). They found that tethering the tetra(aryl)borate via a diethylene glycol linker enhanced conductivity relative to an alkyl linker, while perfluorinating the aryl groups on the tetra(aryl)borate also enhanced ion dissociation resulting in higher conductivity. Because there is a trade-off between ion carrier density and T_g of the polymer, the materials contained relatively low lithium ion concentrations that result in modest overall lithium ion conductivities (~ 10^{-7} S cm^{-1}).

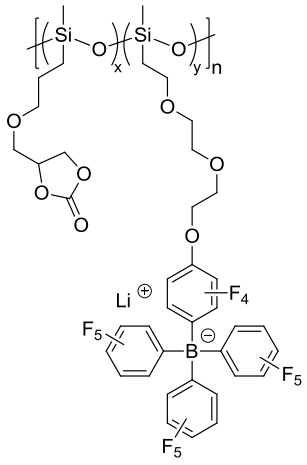

Figure 1.29. A lithium tetra(aryl)borate containing polymeric lithium single-ion conductor.[151]

Angell and coworkers reported the synthesis of new lithium salts, lithium bis(oxolato)borate (LiBOB) (Figure 1.30.a) and lithium bis(malonato)borate (LiBMB) (Figure 1.30.b) that exhibited exceptional thermal and electrochemical stabilities as well as high lithium conductivities in polar media.[152] In an effort develop PLSICs that possess these favorable attributes, Angell and coworkers synthesized poly(mono(oxolato)borate) (polyMOB) (Figure 1.30.c) and poly(mono(malonato)borate) (polyMMB) (Figure 1.30.d) containing poly(ethylene oxide) linkers.[153,154] While they optimized these materials to obtain high conductivities (~ 10^{-5} S cm^{-1} for polyMOB and ~ 10^{-6} S cm^{-1} for polyMMB), they noted that their synthetic method left nontrivial amounts of LiBOB salt in the polyMOB that could not be removed. The presence of LiBOB in this material decreased the lithium ion transference number due to the mobile BOB anions. In spite of the presence of the LiBOB salt impurity, they demonstrated that these materials are electrochemically stable in excess of 4.5 V *vs.* Li/Li^+, and that their conductivities could be increased by two orders of magnitude upon the addition of organic carbonate

plasticizers (~ 10^{-3} S cm^{-1}).[155] They also synthesized an analogous polymer containing bis(oxolato)phosphate moieties (Figure 1.30.e) that displayed moderate lithium conductivities (~ 10^{-6} S cm^{-1}), which is a rare example of a phosphate-based lithium single-ion conductor.[156]

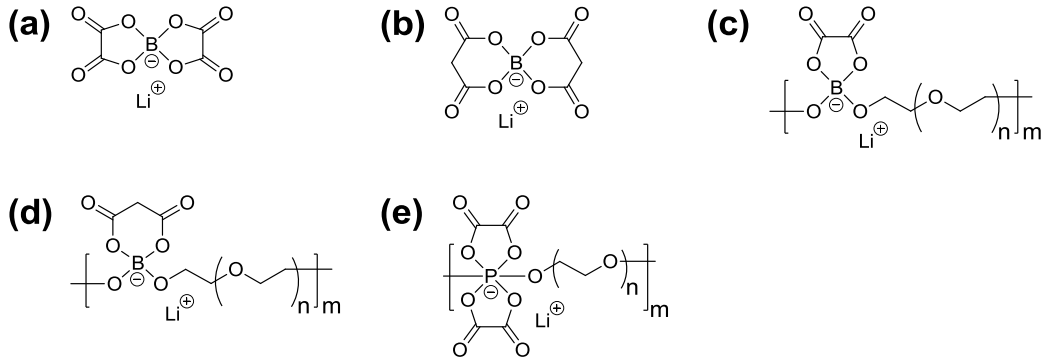

Figure 1.30. (a) Lithium bis(oxolato)borate, (b) lithium bis(malonato)borate, and polymeric lithium single-ion conductors mimicking their structures including (c) poly(mono(oxolato)borate),[153-155] (d) poly(mono(malonato)borate),[153-155] and (e) a bis(oxolato)phosphate containing polymer.[156]

In a similar effort to synthesize PLSICs that mimic the structure of LiBOB, Zhu et al. functionalized common polymer scaffolds such as poly(acrylic acid) (Figure 1.31.a) and poly(vinyl alcohol) (Figure 1.31.b) in order to obtain such structures.[157,158] In these reports, they claimed to obtain linear polymer incorporating lithium borate species along the backbone of the polymers. However, the molecular structures of these the materials are difficult to discern due to their limited characterization. Regardless, they obtained polymers that exhibited room temperature conductivities on the order of 10^{-6} S cm^{-1} governed by Arrhenius behavior due to plasticization with propylene carbonate. They claimed that the polymers exhibit electrochemical stabilities in excess of 6 V *vs.* Li/Li^+.

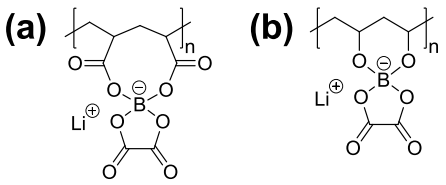

Figure 1.31. Lithium bis(oxolato)borate-based polymeric lithium single-ion conductors synthesized by functionalization of (a) poly(acrylic acid)[157] and (b) poly(vinyl alcohol).[158]

While the above examples by Angell and Zhu both incorporate LiBOB-like moieties into a PLSIC relied on poorly defined chemistries, several reports by Kerr and coworkers employed efficient reactions to install LiBMB groups into polymer matrices. Initial reports described the synthesis of a comb polymer based on an acrylate backbone bearing poly(ethylene oxide) branches[159,160] (Figure 1.32.a). The termini of some of these branches contained vinyl groups to which a silane-bearing LiBMB salt were attached through Pt-catalyzed hydrosilylation to yield a crosslinked lithium single-ion conductor containing LiBMB. Although the dry lithium ion conductivities were relatively low for these materials (~10^{-8} S cm^{-1}), presumably due to low lithium ion incorporation, addition of a carbonate solvent dramatically increased conductivities into a useful range. They demonstrated the lithium single-ion conducting nature of this material by polarization tests in a Li/Li half-cell, although potential fluctuations were observed that ultimately resulted in failure of the cell. Post-mortem analysis of the electrolyte revealed that failure was due to reductive decomposition of acrylate ester groups on the highly reducing lithium surface. As seen in previous studies, the use of esters in lithium ion battery electrolytes is a liability that is detrimental to the longevity of the material. To remedy this instability, they reported an improved poly(ether) network lithium single-ion conductor that exhibited the same

high t_{Li+}, with mitigated reductive instability and enhanced lithium conductivities (~ 10^{-6} S cm^{-1} for the dry polymer)[161,162] (Figure 1.32.b). The lithium ion conductivities were optimized by swelling the network polymers in carbonate solvents. For the most tightly crosslinked network, an increase in conductivity of one order of magnitude was realized, whereas for the least crosslinked network, conductivity rose by two orders of magnitude relative to the unsolvated polymer electrolyte. Finally, they demonstrated the potential utility of this material as an electrolyte for lithium ion batteries by performing full-cell tests to prove that the polymer exhibits sufficient conductivity and longevity upon cycling.

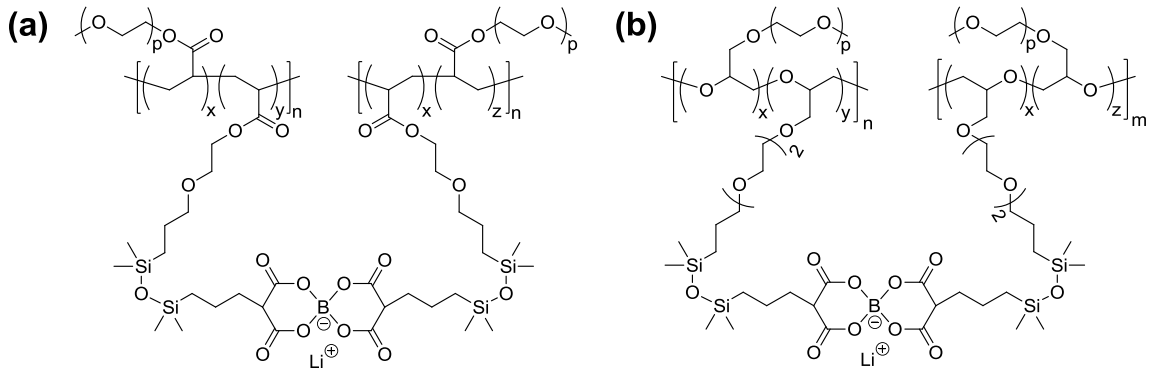

Figure 1.32. Crosslinked lithium bis(malonato) borate containing lithium single-ion conducting network comb polymers with (a) polyacrylate backbones[159,160] and (b) polyether backbones.[161,162]

Inspired by the work of Angell and Kerr, we developed PLSICs incorporating LiBMB moieties. Using acyclic diene metathesis polymerization, we obtained a linear polymer that exhibits high lithium ion conductivity (~ 10^{-5} S cm^{-1}) in propylene carbonate solution. This polymer also forms an unusually stable solid-electrolyte interphase layer that remains stable over the electrochemical window 0.05–8.0 V *vs.* Li/Li^+ (Figure 1.33.a). These studies are the subject

of Chapter 4. Expanding on this work, we prepared polymer network gel lithium single-ion conductors via crosslinking thiol-ene polymerization in order to investigate the dependence of crosslink density on ionic conductivity therein (Figure 1.33.b). We found that the gels exhibited lithium ion conductivities ~ 10^{-6} S cm^{-1} that depend weakly on gel crosslink density. This work is described in detail in Chapter 5.

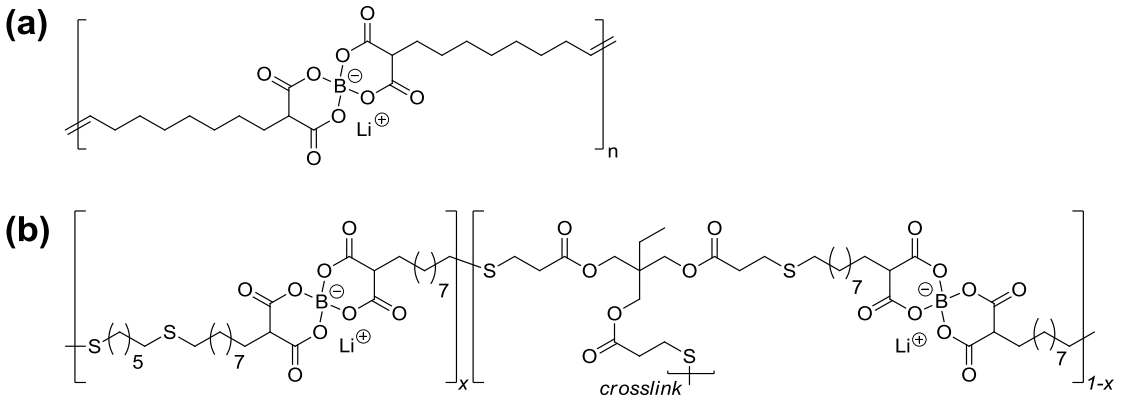

Figure 1.33. (a) Linear and (b) crosslinked lithium bis(malonato)borate containing polymeric lithium single-ion conductors.

1.6 References

(1) Salameh, M. G. *Appl. Energy* **2003**, *75*, 33.

(2) de Vries, B. J. M.; van Vuuren, D. P.; Hoogwijk, M. M. *Energy Policy* **2007**, *35*, 2590.

(3) Dunn, B.; Kamath, H.; Tarascon, J. M. *Science* **2011**, *334*, 928.

(4) Etacheri, V.; Marom, R.; Elazari, R.; Salitra, G.; Aurbach, D. *Energy Environ. Sci.* **2011**, *4*, 3243.

(5) Steele, B. C. H.; Heinzel, A. *Nature* **2001**, *414*, 345.

(6) Peighambardoust, S. J.; Rowshanzamir, S.; Amjadi, M. *Int. J. Hydrogen Energy* **2010**, *35*, 9349.

(7) Merle, G.; Wessling, M.; Nijmeijer, K. *J. Membr. Sci.* **2011**, *377*, 1.

(8) Xu, K. *Chem. Rev.* **2004**, *104*, 4303.

(9) Thomas, K. E.; Sloop, S. E.; Kerr, J. B.; Newman, J. *J. Power Sources* **2000**, *89*, 132.

(10) Zhang, H. W.; Shen, P. K. *Chem. Soc. Rev.* **2012**, *41*, 2382.

(11) Mauritz, K. A.; Moore, R. B. *Chem. Rev.* **2004**, *104*, 4535.

(12) Schmidt-Rohr, K.; Chen, Q. *Nat. Mater.* **2007**, *7*, 75.

(13) Zhang, H.; Shen, P. K. *Chem. Rev.* **2012**, *112*, 2780.

(14) Park, M. J.; Kim, S. Y. *J. Polym. Sci., Part B: Polym. Phys.* **2013**, *51*, 481.

(15) Wu, L.; Zhang, Z. H.; Ran, J.; Zhou, D.; Li, C. R.; Xu, T. W. *Phys. Chem. Chem. Phys.* **2013**, *15*, 4870.

(16) Kirt, A. P.; Brandon, W. R. In *Polymers for Energy Storage and Delivery: Polyelectrolytes for Batteries and Fuel Cells*; American Chemical Society: 2012; Vol. 1096, p 147.

(17) DeLuca, N. W.; Elabd, Y. A. *J. Polym. Sci., Part B: Polym. Phys.* **2006**, *44*, 2201.

(18) Neburchilov, V.; Martin, J.; Wang, H. J.; Zhang, J. J. *J. Power Sources* **2007**, *169*, 221.

(19) Varcoe, J. R.; Slade, R. C. T. *Fuel Cells* **2005**, *5*, 187.

(20) McLean, G. F.; Niet, T.; Prince-Richard, S.; Djilali, N. *Int. J. Hydrogen Energy* **2002**, *27*, 507.

(21) Couture, G.; Alaaeddine, A.; Boschet, F.; Ameduri, B. *Prog. Polym. Sci.* **2011**, *36*, 1521.

(22) Green, O.; Grubjesic, S.; Lee, S.; Firestone, M. *Polym. Rev.* **2009**, *49*, 339.

(23) Kim, J.-H.; Kim, J.-W.; Shokouhimehr, M.; Lee, Y.-S. *J. Org. Chem.* **2005**, *70*, 6714.

(24) Yang, X.; Fei, Z.; Zhao, D.; Ang, W. H.; Li, Y.; Dyson, P. J. *Inorg. Chem.* **2008**, *47*, 3292.

(25) Yuan, J. Y.; Giordano, C.; Antonietti, M. *Chem. Mater.* **2010**, *22*, 5003.

(26) Bara, J. E.; Camper, D. E.; Gin, D. L.; Noble, R. D. *Acc. Chem. Res.* **2010**, *43*, 152.

(27) Bara, J. E.; Noble, R. D.; Gin, D. L. *Ind. Eng. Chem. Res.* **2009**, *48*, 4607.

(28) Tang, J. B.; Shen, Y. Q.; Radosz, M.; Sun, W. L. *Ind. Eng. Chem. Res.* **2009**, *48*, 9113.

(29) Tang, J.; Tang, H.; Sun, W.; Plancher, H.; Radosz, M.; Shen, Y. *Chem. Commun.* **2005**, 3325.

(30) Tang, J.; Radosz, M.; Shen, Y. *Macromolecules* **2008**, *41*, 493.

(31) Green, M. D.; Wang, D.; Hemp, S. T.; Choi, J.-H.; Winey, K. I.; Heflin, J. R.; Long, T. E. *Polymer* **2012**, *53*, 3677.

(32) Allen, M. H.; Day, K. N.; Hemp, S. T.; Long, T. E. *Macromol. Chem. Phys.* **2013**, *214*, 797.

(33) Hemp, S. T.; Allen, M. H., Jr.; Green, M. D.; Long, T. E. *Biomacromolecules* **2012**, *13*, 231.

(34) Armand, M.; Endres, F.; MacFarlane, D. R.; Ohno, H.; Scrosati, B. *Nat. Mater.* **2009**, *8*, 621.

(35) Qiu, B.; Lin, B.; Yan, F. *Polym. Int.* **2013**, *62*, 335.

(36) Ye, Y.-S.; Rick, J.; Hwang, B.-J. *J. Mater. Chem. A* **2013**, *1*, 2719.

(37) Mecerreyes, D. *Prog. Polym. Sci.* **2011**, *36*, 1629.

(38) Kerr, J. B. In *Lithium Batteries: Science and Technology*; Nazri, G., Pistoia, G., Eds.; Kluwer Academic Publishers: Boston, 2004, p 574.

(39) Xu, K.; von Cresce, A. *J. Mater. Chem.* **2011**, *21*, 9849.

(40) Bin, W.; Chun, F. *Adv. Mater. Res.* **2012**, *535-537*, 2092.

(41) Doyle, M.; Fuller, T. F.; Newman, J. *Electrochim. Acta* **1994**, *39*, 2073.

(42) Hayamizu, K.; Aihara, Y.; Arai, S.; Martinez, C. G. *J. Phys. Chem. B* **1999**, *103*, 519.

(43) Weber, R. L.; Ye, Y. S.; Banik, S. M.; Elabd, Y. A.; Hickner, M. A.; Mahanthappa, M. K. *J. Polym. Sci., Part B: Polym. Phys.* **2011**, *49*, 1287.

(44) Lee, C. H.; Park, H. B.; Lee, Y. M.; Lee, R. D. *Ind. Eng. Chem. Res.* **2005**, *44*, 7617.

(45) Long, H.; Kim, K.; Pivovar, B. S. *J. Phys. Chem. C* **2012**, *116*, 9419.

(46) Xu, H.; Fang, J.; Guo, M.; Lu, X.; Wei, X.; Tu, S. *J. Membr. Sci.* **2010**, *354*, 206.

(47) Luo, Y.; Guo, J.; Liu, Y.; Shao, Q.; Wang, C.; Chu, D. *J. Membr. Sci.* **2012**, *423-424*, 209.

(48) Hibbs, M. R.; Fujimoto, C. H.; Cornelius, C. J. *Macromolecules* **2009**, *42*, 8316.

(49) Varcoe, J. R.; Slade, R. C. T.; Yee, E. L. H.; Poynton, S. D.; Driscoll, D. J.; Apperley, D. C. *Chem. Mater.* **2007**, *19*, 2686.

(50) Hibbs, M. R.; Hickner, M. A.; Alam, T. M.; McIntyre, S. K.; Fujimoto, C. H.; Cornelius, C. J. *Chem. Mater.* **2008**, *20*, 2566.

(51) Pan, J.; Lu, S. F.; Li, Y.; Huang, A. B.; Zhuang, L.; Lu, J. T. *Adv. Funct. Mater.* **2010**, *20*, 312.

(52) Yan, J.; Hickner, M. A. *Macromolecules* **2010**, *43*, 2349.

(53) Li, X.; Yu, Y.; Liu, Q.; Meng, Y. *ACS Appl. Mater. Interfaces* **2012**.

(54) Ni, J.; Zhao, C.; Zhang, G.; Zhang, Y.; Wang, J.; Ma, W.; Liu, Z.; Na, H. *Chem. Commun.* **2011**.

(55) Wang, J.; Wang, J.; Li, S.; Zhang, S. *J. Membr. Sci.* **2011**, *368*, 246.

(56) Guo, T. Y.; Zeng, Q. H.; Zhao, C. H.; Liu, Q. L.; Zhu, A. M.; Broadwell, I. *J. Membr. Sci.* **2011**, *371*, 268.

(57) Salerno, H. L. S.; Beyer, F. L.; Elabd, Y. A. *J. Polym. Sci., Part B: Polym. Phys.* **2012**, *50*, 552.

(58) Clark, T. J.; Robertson, N. J.; Kostalik IV, H. A.; Lobkovsky, E. B.; Mutolo, P. F.; Abruña, H. D.; Coates, G. W. *J. Am. Chem. Soc.* **2009**, *131*, 12888.

(59) Robertson, N. J.; Kostalik IV, H. A.; Clark, T. J.; Mutolo, P. F.; Abruña, H. D.; Coates, G. W. *J. Am. Chem. Soc.* **2010**, *132*, 3400.

(60) Kostalik IV, H. A.; Clark, T. J.; Robertson, N. J.; Mutolo, P. F.; Longo, J. M.; Abruña, H. D.; Coates, G. W. *Macromolecules* **2010**, *43*, 7147.

(61) Guo, M.; Fang, J.; Xu, H.; Li, W.; Lu, X.; Lan, C.; Li, K. *J. Membr. Sci.* **2010**, *362*, 97.

(62) Lin, B.; Qiu, L.; Lu, J.; Yan, F. *Chem. Mater.* **2010**, *22*, 6718.

(63) Li, W.; Fang, J.; Lv, M.; Chen, C.; Chi, X.; Yang, Y.; Zhang, Y. *J. Mater. Chem.* **2011**, *21*, 11340.

(64) Qiu, B.; Lin, B.; Qiu, L.; Yan, F. *J. Mater. Chem.* **2012**, *22*, 1040.

(65) Chen, D.; Hickner, M. A. *ACS Appl. Mater. Interfaces* **2012**, *4*, 5775.

(66) Deavin, O. I.; Murphy, S.; Ong, A. L.; Poynton, S. D.; Zeng, R.; Herman, H.; Varcoe, J. R. *Energy Environ. Sci.* **2012**, *5*, 8584.

(67) Ye, Y.; Elabd, Y. A. *Macromolecules* **2011**, *44*, 8494.

(68) Lin, B.; Qiu, L.; Qiu, B.; Peng, Y.; Yan, F. *Macromolecules* **2011**, *44*, 9642.

(69) Qiu, B.; Lin, B.; Si, Z.; Qiu, L.; Chu, F.; Zhao, J.; Yan, F. *J. Power Sources* **2012**, *217*, 329.

(70) Page, O. M. M.; Poynton, S. D.; Murphy, S.; Lien Ong, A.; Hillman, D. M.; Hancock, C. A.; Hale, M. G.; Apperley, D. C.; Varcoe, J. R. *RSC Advances* **2013**, *3*, 579.

(71) Gu, S.; Cai, R.; Luo, T.; Chen, Z.; Sun, M.; Liu, Y.; He, G.; Yan, Y. *Angew. Chem. Int. Ed.* **2009**, *48*, 6499.

(72) Gu, S.; Cai, R.; Yan, Y. *Chem. Commun.* **2011**, *47*, 2856.

(73) Noonan, K. J.; Hugar, K. M.; Kostalik IV, H. A.; Lobkovsky, E. B.; Abruna, H. D.; Coates, G. W. *J. Am. Chem. Soc.* **2012**, *134*, 18161.

(74) Salerno, H. L. S.; Elabd, Y. A. *J. Appl. Polym. Sci.* **2013**, *127*, 298.

(75) Arges, C. G.; Parrondo, J.; Johnson, G.; Nadhan, A.; Ramani, V. *J. Mater. Chem.* **2012**, *22*, 3733.

(76) Wang, J.; Li, S.; Zhang, S. *Macromolecules* **2010**, *43*, 3890.

(77) Zhang, Q.; Li, S.; Zhang, S. *Chem. Commun.* **2010**, *46*, 7495.

(78) Lin, X.; Wu, L.; Liu, Y.; Ong, A. L.; Poynton, S. D.; Varcoe, J. R.; Xu, T. *J. Power Sources* **2012**, *217*, 373.

(79) Zha, Y.; Disabb-Miller, M. L.; Johnson, Z. D.; Hickner, M. A.; Tew, G. N. *J. Am. Chem. Soc.* **2012**, *134*, 4493.

(80) Zschocke, P.; Quellmalz, D. *J. Membr. Sci.* **1985**, *22*, 325.

(81) Nuñez, S. A.; Hickner, M. A. *ACS Macro Letters* **2013**, *2*, 49.

(82) Elabd, Y. A.; Hickner, M. A. *Macromolecules* **2011**, *44*, 1.

(83) Liu, Y.; Cavicchi, K. A.; Mausar, J.; Decker, B. *PMSE Prepr.* **2009**, *100*, 448.

(84) Tsai, T.-H.; Maes, A. M.; Vandiver, M. A.; Versek, C.; Seifert, S.; Tuominen, M.; Liberatore, M. W.; Herring, A. M.; Coughlin, E. B. *J. Polym. Sci., Part B: Polym. Phys.* **2012**, 10.1002/polb.23170.

(85) Zeng, Q. H.; Liu, Q. L.; Broadwell, I.; Zhu, A. M.; Xiong, Y.; Tu, X. P. *J. Membr. Sci.* **2010**, *349*, 237.

(86) Ohno, H.; Ito, K. *Chem. Lett.* **1998**, 751.

(87) Lee, M.; Choi, U. H.; Colby, R. H.; Gibson, H. W. *Chem. Mater.* **2010**, *22*, 5814.

(88) Yoshizawa, M.; Ohno, H. *Chem. Lett.* **1999**, 889.

(89) Yoshizawa, M.; Ohno, H. *Electrochim. Acta* **2001**, *46*, 1723.

(90) Shaplov, A. S.; Lozinskaya, E. I.; Ponkratov, D. O.; Malyshkina, I. A.; Vidal, F.; Aubert, P.-H.; Okatova, O. g. V.; Pavlov, G. M.; Komarova, L. I.; Wandrey, C.; Vygodskii, Y. S. *Electrochim. Acta* **2011**, *57*, 74.

(91) Choi, U. H.; Lee, M.; Wang, S.; Liu, W.; Winey, K. I.; Gibson, H. W.; Colby, R. H. *Macromolecules* **2012**, *45*, 3974.

(92) Green, M. D.; Salas-de la Cruz, D.; Ye, Y.; Layman, J. M.; Elabd, Y. A.; Winey, K. I.; Long, T. E. *Macromol. Chem. Phys.* **2011**, *212*, 2522.

(93) Allen, M. H.; Wang, S.; Hemp, S. T.; Chen, Y.; Madsen, L. A.; Winey, K. I.; Long, T. E. *Macromolecules* **2013**, *46*, 3037.

(94) Salas-de la Cruz, D.; Green, M. D.; Ye, Y.; Elabd, Y. A.; Long, T. E.; Winey, K. I. *J. Polym. Sci., Part B: Polym. Phys.* **2012**, *50*, 338.

(95) Yoshizawa, M.; Hirao, M.; Ito-Akita, K.; Ohno, H. *J. Mater. Chem.* **2001**, *11*, 1057.

(96) Shaplov, A. S.; Vlasov, P. S.; Lozinskaya, E. I.; Ponkratov, D. O.; Malyshkina, I. A.; Vidal, F.; Okatova, O. V.; Pavlov, G. M.; Wandrey, C.; Bhide, A.; Schönhoff, M.; Vygodskii, Y. S. *Macromolecules* **2011**, *44*, 9792.

(97) Ohno, H.; Yoshizawa, M.; Ogihara, W. *Electrochim. Acta* **2004**, *50*, 255.

(98) Chen, H.; Choi, J.-H.; Salas-de la Cruz, D.; Winey, K. I.; Elabd, Y. A. *Macromolecules* **2009**, *42*, 4809.

(99) Ye, Y.; Elabd, Y. A. *Polymer* **2011**, *52*, 1309.

(100) Vandiver, M. A.; Horan, J. L.; Yang, Y.; Tansey, E. T.; Seifert, S.; Liberatore, M. W.; Herring, A. M. *J. Polym. Sci., Part B: Polym. Phys.* **2012**, DOI: 10.1002/polb.23171.

(101) Disabb-Miller, M. L.; Johnson, Z. D.; Hickner, M. A. *Macromolecules* **2013**, *46*, 949.

(102) Sudre, G.; Inceoglu, S.; Cotanda, P.; Balsara, N. P. *Macromolecules* **2013**, *46*, 1519.

(103) Weber, R. L.; Ye, Y. S.; Schmitt, A. L.; Banik, S. M.; Elabd, Y. A.; Mahanthappa, M. K. *Macromolecules* **2011**, *44*, 5727.

(104) Ye, Y.; Choi, J.-H.; Winey, K. I.; Elabd, Y. A. *Macromolecules* **2012**, *45*, 7027.

(105) Green, M. D.; Choi, J.-H.; Winey, K. I.; Long, T. E. *Macromolecules* **2012**, *45*, 4749.

(106) Chanthad, C.; Masser, K. A.; Xu, K.; Runt, J.; Wang, Q. *J. Mater. Chem.* **2012**, *22*, 341.

(107) Lee, M.; Choi, U. H.; Salas-de la Cruz, D.; Mittal, A.; Winey, K. I.; Colby, R. H.; Gibson, H. W. *Adv. Funct. Mater.* **2011**, *21*, 708.

(108) Bandhauer, T. M.; Garimella, S.; Fuller, T. F. *J. Electrochem. Soc.* **2011**, *158*, R1.

(109) Wanakule, N. S.; Panday, A.; Mullin, S. A.; Gann, E.; Hexemer, A.; Balsara, N. P. *Macromolecules* **2009**, *42*, 5642.

(110) Young, W. S.; Epps, T. H. *Macromolecules* **2009**, *42*, 2672.

(111) Fenton, D. E.; Parker, J. M.; Wright, P. V. *Polymer* **1973**, *14*, 589.

(112) Ghosh, A.; Wang, C.; Kofinas, P. *J. Electrochem. Soc.* **2010**, *157*, A846.

(113) Ryu, S.-W.; Trapa, P. E.; Olugebefola, S. C.; Gonzalez-Leon, J. A.; Sadoway, D. R.; Mayes, A. M. *J. Electrochem. Soc.* **2005**, *152*, A158.

(114) Ito, K.; Nishina, N.; Tominaga, Y.; Ohno, H. *Solid State Ionics* **1996**, *86-8*, 325.

(115) Tominaga, Y.; Ito, K.; Ohno, H. *Polymer* **1997**, *38*, 1949.

(116) Ito, K.; Ohno, H. *Electrochim. Acta* **1998**, *43*, 1247.

(117) Kobayashi, N.; Uchiyama, M.; Tsuchida, E. *Solid State Ionics* **1985**, *17*, 307.

(118) Tsuchida, E.; Kobayashi, N.; Ohno, H. *Macromolecules* **1988**, *21*, 96.

(119) Kim, H. T.; Park, J. K. *Polym. Bull.* **1996**, *36*, 427.

(120) Kim, H. T.; Park, J. K. *Solid State Ionics* **1997**, *98*, 237.

(121) Sadoway, D. R.; Huang, B. Y.; Trapa, P. E.; Soo, P. P.; Bannerjee, P.; Mayes, A. M. *J. Power Sources* **2001**, *97-8*, 621.

(122) Ryu, S. W.; Mayes, A. M. *Polymer* **2008**, *49*, 2268.

(123) Trapa, P. E.; Acar, M. H.; Sadoway, D. R.; Mayes, A. M. *J. Electrochem. Soc.* **2005**, *152*, A2281.

(124) Trapa, P. E.; Reyes, A. B.; Das Gupta, R. S.; Mayes, A. M.; Sadoway, D. R. *J. Electrochem. Soc.* **2006**, *153*, A1098.

(125) Ioannou, E. F.; Mountrichas, G.; Pispas, S.; Kamitsos, E. I.; Floudas, G. *Macromolecules* **2008**, *41*, 6183.

(126) Dou, S. C.; Zhang, S. H.; Klein, R. J.; Runt, J.; Colby, R. H. *Chem. Mater.* **2006**, *18*, 4288.

(127) Wang, W.; Liu, W.; Tudryn, G. J.; Colby, R. H.; Winey, K. I. *Macromolecules* **2010**, *43*, 4223.

(128) Tudryn, G. J.; O'Reilly, M. V.; Dou, S.; King, D. R.; Winey, K. I.; Runt, J.; Colby, R. H. *Macromolecules* **2012**, *45*, 3962.

(129) Sinha, K.; Maranas, J. K. *Macromolecules* **2011**, *44*, 5381.

(130) Sinha, K.; Wang, W.; Winey, K. I.; Maranas, J. K. *Macromolecules* **2012**, *45*, 4354.

(131) Lin, K.-J.; Maranas, J. K. *Macromolecules* **2012**, *45*, 6230.

(132) Zhang, S. S.; Wan, G. X. *J. Appl. Polym. Sci.* **1993**, *48*, 405.

(133) Sun, X.; Hou, J.; Kerr, J. *Electrochim. Acta* **2005**, *50*, 1139.

(134) Doyle, M.; Lewittes, M. E.; Roelofs, M. G.; Perusich, S. A. *J. Phys. Chem. B* **2001**, *105*, 9387.

(135) Liu, Y.; Cai, Z.; Tan, L.; Li, L. *Energy Environ. Sci.* **2012**, *5*, 9007.

(136) Tada, Y.; Sato, M.; Takeno, N.; Nakacho, Y.; Shigehara, K. *Chem. Mater.* **1994**, *6*, 27.

(137) Xu, K.; Ding, M. S.; Zhang, S.; Allen, J. L.; Jow, T. R. *J. Electrochem. Soc.* **2002**, *149*, A622.

(138) Zhang, H.; Zhang, X.; Shiue, E.; Fedkiw, P. S. *J. Power Sources* **2008**, *177*, 561.

(139) Schaefer, J. L.; Yanga, D. A.; Archer, L. A. *Chem. Mater.* **2013**, *25*, 834.

(140) Matsumoto, K.; Endo, T. *J. Polym. Sci., Part A: Polym. Chem.* **2010**, *48*, 3113.

(141) Matsumoto, K.; Endo, T. *J. Polym. Sci., Part A: Polym. Chem.* **2011**, *49*, 1874.

(142) Siska, D. P.; Shriver, D. F. *Chem. Mater.* **2001**, *13*, 4698.

(143) Meziane, R.; Bonnet, J.-P.; Courty, M.; Djellab, K.; Armand, M. *Electrochim. Acta* **2011**, *57*, 14.

(144) Bouchet, R.; Maria, S.; Meziane, R.; Aboulaich, A.; Lienafa, L.; Bonnet, J.-P.; Phan, T. N. T.; Bertin, D.; Gigmes, D.; Devaux, D.; Denoyel, R.; Armand, M. *Nat. Mater.* **2013**, *12*, 452.

(145) Krause, L. J.; Lamanna, W.; Summerfield, J.; Engle, M.; Korba, G.; Loch, R.; Atanasoski, R. *J. Power Sources* **1997**, *68*, 320.

(146) Tao, R.; Miyamoto, D.; Aoki, T.; Fujinami, T. *J. Power Sources* **2004**, *135*, 267.

(147) Aoki, T.; Konno, A.; Fujinami, T. *Electrochim. Acta* **2004**, *50*, 301.

(148) Matsumi, N.; Sugai, K.; Ohno, H. *Macromolecules* **2003**, *36*, 2321.

(149) Matsumi, N.; Sugai, K.; Sakamoto, K.; Mizumo, T.; Ohno, H. *Macromolecules* **2005**, *38*, 4951.

(150) Xu, W.; Sun, X. G.; Angell, C. A. *Electrochim. Acta* **2003**, *48*, 2255.

(151) Liang, S. W.; Choi, U. H.; Liu, W. J.; Runt, J.; Colby, R. H. *Chem. Mater.* **2012**, *24*, 2316.

(152) Xu, W.; Angell, C. A. *Electrochem. Solid-State Lett.* **2001**, *4*, E1.

(153) Xu, W.; Williams, M. D.; Angell, C. A. *Chem. Mater.* **2002**, *14*, 401.

(154) Xu, W.; Angell, C. A. *Solid State Ionics* **2002**, *147*, 295.

(155) Xu, W.; Angell, C. A. *Electrochim. Acta* **2003**, *48*, 2029.

(156) Sun, X.; Angell, C. A. *Solid State Ionics* **2004**, *175*, 743.

(157) Zhu, Y. S.; Gao, X. W.; Wang, X. J.; Hou, Y. Y.; Liu, L. L.; Wu, Y. P. *Electrochem. Commun.* **2012**, *22*, 29.

(158) Zhu, Y. S.; Wang, X. J.; Hou, Y. Y.; Gao, X. W.; Liu, L. L.; Wu, Y. P.; Shimizu, M. *Electrochim. Acta* **2013**, *87*, 113.

(159) Sun, X.; Liu, G.; Xie, J.; Han, Y.; Kerr, J. B. *Solid State Ionics* **2004**, *175*, 713.

(160) Sun, X. G.; Reeder, C. L.; Kerr, J. B. *Macromolecules* **2004**, *37*, 2219.

(161) Sun, X. G.; Kerr, J. B.; Reeder, C. L.; Liu, G.; Han, Y. B. *Macromolecules* **2004**, *37*, 5133.

(162) Sun, X. G.; Kerr, J. B. *Macromolecules* **2006**, *39*, 362.

CHAPTER 2

THERMAL AND ION TRANSPORT PROPERTIES OF HYDROPHILIC AND HYDROPHOBIC POLYMERIZED STYRENIC IMIDAZOLIUM IONIC LIQUIDS

2.1 Introduction

Polymerized ionic liquids (POILs) have emerged as an interesting class of materials with potentially wide-ranging applications including uses in catalysis,[1,2] nanomaterials synthesis,[3] gas separations media,[4-7] and as polymer electrolytes for battery and fuel cell applications.[8-11] As a consequence of the low flammability, low vapor pressure, chemical and thermal stability, and widely tunable physical properties associated with small molecule ionic liquids, POILs offer an enticing opportunity to develop processable solid polymeric electrolytes that circumvent electrolyte leakage issues encountered with small-molecule liquid electrolytes and ionic liquid swollen polymer networks ("ion gels").[12-15] POILs in which cationic moieties are anchored to the polymer backbone with free and mobile counterions are classified as "single ion conductors," specifically, anion conductors. The properties of such single ion conductors differ greatly from ion gels by virtue of the immobilization of one ion along the polymer backbone. Single anion conductors comprise a class of materials of growing importance because of their utility as polymer electrolytes for advanced electrical energy storage and conversion devices (*e.g.*, fuel cells and advanced battery technologies).[16,17]

Although a wide variety of poly(sulfones),[18-21] crosslinked ionic liquid resins,[22-27] radiation-grafted fluoropolymers, [28-30] and well-defined linear polymers[31-37] have been

investigated as potential fuel cell and battery polymer electrolytes, linear POILs based on well-known imidazolium ionic liquids have received only modest attention. Recent work from the groups of Ohno,[38-40] Colby,[41] and Elabd and coworkers[42,43] have investigated the temperature-dependent ionic conductivities of POIL homopolymers and copolymers derived from acrylate- and methacrylate-based imidazolium ionic liquids with varying chemical structures and counterions. These studies suggested that the ionic conductivities in this class of POILs depend mainly upon glass transition temperatures (T_g) of the polymers, which reflect the segmental motions of the polymer backbones. Syntheses of styrenic POIL homopolymers, random copolymers, and block copolymers bearing quaternary ammonium or imidazolium functionalities have been reported,[6,32,33,44-46] however, only a few reports of their ionic conductivities have appeared.[32,33,46] Ready synthetic access to styrenic imidazolium POILs bearing various anions ($TFSI^-$, OH^-, CO_3^{2-}, I^-) coupled with their anticipated thermal stabilities motivate fundamental studies of their temperature-dependent ionic conductivities towards new polymeric single ion conductors for applications in electrochemical devices. Systematic studies of this type as a function of both the monomer and mobile counterion structures at constant average chain length were previously unreported prior to our publishing on the work described in the present chapter. Concurrent with our work, Elabd and coworkers reported on the effect that the POIL counterion plays in determining the thermal and ion conducting properties of hydrophobic methacrylate POILs at a constant chain length.[47] Shortly thereafter, Long and coworkers reported similar results for 1-vinyl-3-alkylimidazolium POILs with varied counterions and alkyl substituents, however the polymers did not have a constant average chain length.[48]

In this study, we describe the modular synthesis and physical characterization of styrenic POILs derived from post-synthetic modification of a relatively narrow dispersity poly(4-vinylbenzyl chloride) produced by nitroxide-mediated polymerization (NMP). Reactions of this prepolymer with *N*-methylimidazole, *N*-butylimidazole, and *N*-hexylimidazole yield a homologous series of hydrophilic poly(4-vinylbenzyl alkylimidazolium chloride) (PVBn(alkyl)ImCl with alkyl = $-CH_3$ (Me), $-C_4H_9$ (Bu), and $-C_6H_{13}$ (Hex)) homopolymers with a constant average degree of polymerization. Salt metathesis reactions of the PVBnHexImCl homopolymer provide access to a series of hydrophobic PVBnHexImX (X = tetrafluoroborate (BF_4^-), hexafluorophosphate (PF_6^-), or bis(trifluoromethanesulfonyl)imide ($TFSI^-$)) polymerized ionic liquids. These two series of hydrophilic POILs with variable alkyl chains and hydrophobic POILs with variable counterions enable formulation of systematic correlations between anchored cation structure, mobile anion structure, thermal stability, and glass transition temperatures of these materials at constant average degree of polymerization. The humidity- and temperature-dependent ionic conductivities of the hydrophilic ionic liquid homopolymers are shown to exhibit Arrhenius-type behavior consistent with decreased coupling of the ionic conductivity from polymer segmental motions. The dry temperature-dependent ionic conductivities of the hydrophobic homopolymers are related to trends in POIL T_g, indicating that the conductivity largely depends on the polymer segmental motion, however, other factors such as counterion size and symmetry also contribute. Vogel-Fulcher-Tammann (VFT) analyses indicate that the conductivities of the styrenic POILs are intrinsically lower than those of recently reported methacrylate-based POILs with identical counterions,[43] which we attribute to the lower ion concentrations in the materials reported here.

2.2 Experimental

Materials. All chemicals were purchased from Sigma-Aldrich Chemical Company (Milwaukee, WI, USA) and were used as received unless otherwise noted. Copper(I) bromide was purified according to the literature.[49] 4-Vinylbenzyl chloride was purified by passage through silica gel using hexanes as an eluent followed by concentration *in vacuo*. *N*-methylimidazole, *N*-butylimidazole, and *N,N,N',N'',N''*-pentamethyldiethylenetriamine were distilled under reduced pressure. *N*-Hexylimidazole was synthesized by a slight modification of a literature procedure in which ethanol was used as a solvent instead of 1-propanol.[50] 2,2,5-Trimethyl-4-phenyl-3-azahexane 3-nitroxide (TIPNO) was prepared according to a previously reported literature procedure.[51]

NMR Spectroscopy. ^{1}H NMR spectra were recorded on a Varian Mercury Plus or Bruker AC+ 300 spectrometer and were referenced relative to tetramethylsilane (in $CDCl_3$) or the residual protiated solvent peak (in DMSO-d_6) in the samples. ^{1}H NMR spectra for all compounds are provided in Appendix 1.

Elemental Analysis. Elemental analyses were conducted at Atlantic Microlab, Inc. (Norcross, GA, USA) using standard combustion analysis for carbon, hydrogen, and nitrogen content, and flask combustion followed by ion chromatography to quantify fluorine and chlorine contents.

Size Exclusion Chromatography (SEC). SEC analyses were performed using a Visctoek GPCMax Tetradetector system using refractive index (RI), two-angle light scattering (7° and 90°), differential viscometric, and UV-Vis detection. Separations employed two Polymer Laboratories (Amherst, MA) Resipore columns (250 mm x 4.6 mm) using a THF eluent at a flow

rate of 1.0 mL min^{-1}. The refractive index increment for poly(4-vinylbenzyl chloride) was determined to be dn/dc = 0.127 L g^{-1} at 40 °C, by linearly fitting the RI detector response as a function of polymer solution concentration for a single polymer sample. This value was used to calculate the absolute M_n for poly(4-vinylbenzyl chloride) using the light scattering detector. The reported polydispersity indices (M_w/M_n) were derived from a conventional poly(styrene) calibration curve constructed using 10 narrow molecular weight distribution standards having M_n = 580-377400 g mol^{-1} (Polymer Laboratories, Amherst, MA).

Thermogravimetric Analysis (TGA). Thermal stabilities of the POILs were measured on a TA Instruments Q500 Thermogravimetric Analyzer using a ramp rate of 10 °C min^{-1} under a $N_2(g)$ purge (50 mL min^{-1}) over a temperature range of 25-500 °C.

Differential Scanning Calorimetry (DSC). Glass transition temperatures (T_g) were measured using a TA Instruments Q100 modulated differential scanning calorimeter under nitrogen atmosphere. The thermal history of samples hermetically sealed in aluminum pans was erased by heating to 220 °C for three minutes and cooling to 25 °C. Second heating curves recorded over a temperature range of -50 °C to 220 °C using a heating ramp rate of 5 °C min^{-1} were used to determine T_g.

Electrochemical Impedance Spectroscopy (EIS). The ionic conductivities of the polymerized ionic liquids (POILs) were measured using electrochemical impedance spectroscopy (EIS) (Solartron, 1260 impedance analyzer, 1287 electrochemical interface, Zplot software) over a frequency range of 1 Hz to 10^6 Hz at 200 mV. POIL films with thickness ranging between 80 and 200 μm were prepared by solution casting on a glass slide (5 mm × 40 mm) under ambient conditions. The hydrophobic and hydrophilic POILs were cast from

acetonitrile and deionized water, respectively, as a 10 wt% polymer solution. After solvent casting, the POIL films were annealed under vacuum at $T = T_g + 20$ °C for 24 h after which they were stored in a desiccator. The conductivities of the POIL films were measured using four-parallel electrodes (four-point method) in a custom-made Teflon-coated stainless steel cell, which was placed in an environmental chamber (Tenney, BTRS model) to control both temperature and humidity. An alternating current was applied to the outer electrodes and the real impedance or resistance, R, was measured between the two inner reference electrodes. The resistance was determined from a high x-intercept of the semi-circle regression of the Nyquist plot. Conductivity was calculated by using the following equation: $\sigma = L/AR$, where L and A are the distance between two inner electrodes and the cross sectional area of the polymer film ($A=Wl$; W is the film width and l is the film thickness), respectively. The thickness of each polymer film was measured with a Mitutoyo digital micrometer (± 0.001 mm) before measuring the conductivity. Samples were allowed to equilibrate for 2 h at each measurement condition followed by at least 6 measurements at that condition. The values reported are an average of these steady-state measurements.

Water Uptake and Hydration Number. Water uptake of the hydrophilic POILs was measured as a function of relative humidity at 30 ºC using a TA Instruments (New Castle, Delaware) Q5000SA dynamic vapor sorption analyzer. The relative humidity steps and equilibration times were the same those used in EIS experiments. Hydration number, λ (mol H_2O/mol anion), was calculated from the following equation:

$$\lambda = \left(\frac{\text{mass}_{RH} - \text{mass}_{dry}}{18.01} \right) \left(\frac{1000}{\text{mass}_{dry} \cdot \text{IEC}} \right) \qquad (2.1)$$

where $mass_{RH}$ is the sample mass at a given RH, $mass_{dry}$ is the dry mass of the sample, and IEC is the ion exchange capacity of the sample in milliequivalents of anion per gram of polymer.

Synthesis of 2,2,5-Trimethyl-3-(2-oxyethyl isobutryl)-4-phenyl-3-azahexane (1). Copper(I) bromide (0.12 g, 0.85 mmol) and copper(0) powder (3.24 g, 51.1 mmol) were placed in a 100 mL Schlenk flask under nitrogen. Ethyl α-bromoisobutyrate (3.37 g, 17.0 mmol), TIPNO (2.50 g, 11.3 mmol), *N*,*N*,*N*',*N*'',*N*''-pentamethyldiethylenetriamine (0.14 g, 0.85 mmol), and *N,N*-dimethylformamide (DMF) (40 mL) were combined in a second dry 100 mL Schlenk tube and freeze-thaw degassed four times. Under a flush of nitrogen, the latter solution was cannula transferred onto the copper mixture to yield a dark green solution. This solution was vigorously stirred at 40 °C for 60 minutes, during which time it turned dark blue, and then it was stirred overnight at 22 °C. The solution was then filtered through a plug of neutral alumina, which was subsequently washed with ethyl acetate (250 mL) and the combined eluent was concentrated on a rotary evaporator at 40 °C. The resulting crude product purified by silica gel column chromatography (10 cm x 5 cm diameter) using hexanes/ethyl acetate (30:1 v/v) to furnish the alkoxyamine as a yellow/orange viscous liquid. Yield: 3.41 g (90% yield). ^{1}H NMR (300 MHz, $CDCl_3$, 22°C): δ (ppm) 7.63–7.16 (m, 5 H, -Ar-*H*, both diastereomers), 4.28 – 4.06 (m, 2H, O-C*H*$_2$-CH_3, both diastereomers), 3.70 (d, $J_{H\text{-}H}^{3}$ = 10.8 Hz, 1H, N-C*H*, minor diastereomer), 3.42 (d, $J_{H\text{-}H}^{3}$ = 10.8 Hz, 1H, N-C*H*, major diastereomer), 2.48–2.34 (m, 1H, C*H*$(CH_3)_2$, minor diastereomer), 1.90–1.76 (m, 1H, C*H*$(CH_3)_2$, major diastereomer), 1.62 (s, 3H, C(C*H*$_3)_2$, major diastereomer, rotamer A), 1.59 (s, 3H, C(C*H*$_3)_2$, minor diastereomer, rotamer A), 1.55 (s, 3H, C(C*H*$_3)_2$, major diastereomer, rotamer B), 1.48 (s, 3H, C(C*H*$_3)_2$, minor diastereomer, rotamer B), 1.31 (t, $J_{H\text{-}H}^{3}$ = 7.2 Hz, 3H, O-CH_2-C*H*$_3$, minor diastereomer), 1.28 (t, $J_{H\text{-}H}^{3}$ = 7.2 Hz,

3H, O-CH_2-CH_3, major diastereomer), 1.24 (d, $J_{H\text{-}H}^3$ = 6.2 Hz, 3H, CH(CH_3)$_2$, minor diastereomer, rotamer A), 1.16 (d, $J_{H\text{-}H}^3$ = 6.2 Hz, 3H, CH(CH_3)$_2$, major diastereomer, rotamer A), 0.93 (s, 9H, C(CH_3)$_3$, major diastereomer), 0.81 (s, 9H, C(CH_3)$_3$, minor diastereomer), 0.72 (d, $J_{H\text{-}H}^3$ = 6.8 Hz, 3H, CH(CH_3)$_2$, minor diastereomer, rotamer B), 0.39 (d, $J_{H\text{-}H}^3$ = 6.8 Hz, 3H, CH(CH_3)$_2$, major diastereomer, rotamer B). The ^{1}H NMR spectrum is provided in Appendix 1 (Figure A1.1). ^{13}C NMR (75 MHz, $CDCl_3$, 22°C): δ (ppm, all diastereomers and rotamers) 175.26, 175.03, 142.04, 140.62, 131.01, 130.26, 127.35, 127.11, 126.50, 126.10, 81.86, 79.57, 73.74, 72.42, 60.57, 60.32, 30.75, 30.18, 28.23, 27.29, 25.97, 25.23, 24.59, 22.83, 22.66, 22.55, 22.06, 21.88, 20.97, 13.94. ESI-MS: calcd. for $C_{20}H_{33}NO_3$ $[M+Na]^+$ 358.2, found 358.3.

Poly(4-vinylbenzyl chloride) (PVBCl). Freshly purified 4-vinylbenzyl choride (23.0 g, 151 mmol), **1** (0.505g, 1.51 mmol), and xylenes (15.25 mL) were sealed in a 100 mL pear-shaped flask and subjected to five freeze-thaw degassing cycles, after which the flask contents were placed under N_2(*g*). The flask was placed in an oil bath thermostatted at 125 °C for 31 minutes, after which it was chilled in dry ice/isopropanol for 10 minutes before exposure to air. The polymerization reaction was diluted with dichloromethane (50 mL), and twice precipitated into methanol (1 L). Yield: 14.6 g (63% conversion). ^{1}H NMR (300 MHz, $CDCl_3$, 22°C): δ (ppm) 7.35–6.82 (m, 2H, Ar-*H meta*), 6.80–6.17 (m, 2H, Ar-*H ortho*), 4.51 (s, 2H, CH_2-Cl), 2.46–1.11 (m, 3H, CH_2-C*H*-Ar). The ^{1}H NMR spectrum is provided in Appendix 1 (Figure A1.2.a). SEC (THF, 40 °C): M_n = 15.9 kg mol^{-1} (SEC-LS), M_w/M_n = 1.34.

Synthesis of PVBnMeImCl homopolymer. Poly(4-vinlbenzyl chloride) (1.5 g, 0.094 mmol) and *N*-methylimidazole (2.5 g, 30.9 mmol) were dissolved in *N,N*-dimethylformamide (20 mL) and heated to 80 °C for 12 h, during which time a solid precipitated from the reaction

mixture. The supernatant liquid was decanted and the solid was triturated with acetone (25 mL) for 3 h before isolation by vacuum filtration and vacuum drying at 22 °C. In order to remove traces of *N*-methylimidazole, the polymer was dissolved in methanol, precipitated into acetone, and dried *in vacuo*. Yield: 1.21 g (52 % yield). ^{1}H NMR (300 MHz, DMSO-d_6, 22°C): δ (ppm) 10.46 – 9.75 (1H, N=C*H*-N), 8.38 – 7.66 (2H, N-C*H*=C*H*-N) 7.63 – 6.98 (2H, Ar-*H meta*), 6.86 – 5.98 (2H, Ar-*H ortho*), 5.93 – 5.19 (2H, C-CH_2-N), 4.15 – 3.59 (3H, N-CH_3), 2.16 – 0.31 (3H, CH_2-C*H*-Ar). The ^{1}H NMR spectrum is provided in Appendix 1 (Figure A1.2.b).

Synthesis of PVBnBuImCl homopolymer. The synthesis of PVBnBuImCl follows that of PVBnMeImCl, except that the traces of *N*-butylimidazole were removed by dissolution of the polymer in 2-propanol and precipitation into diethyl ether. Yield: 1.11 g (41 % yield). ^{1}H NMR (300 MHz, DMSO-d_6, 22°C): δ (ppm) 10.72 – 9.85 (1H, N=C*H*-N), 8.51 – 7.72 (2H, N-C*H*=C*H*-N) 7.72 – 6.96 (2H, Ar-*H meta*), 6.79 – 5.89 (2H, Ar-*H ortho*), 5.89 – 4.95 (2H, C-CH_2-N), 4.50 – 3.86 (2H, N-CH_2-CH$_2$-), 2.18 – 0.31 (CH_2-C*H*-Ar and –CH_2-CH_2-CH_3). The ^{1}H NMR spectrum is provided in Appendix 1 (Figure A1.2.c).

Synthesis of PVBnHexImCl homopolymer. PVBCl (8.0 g, 0.50 mmol) and 1-hexylimidazole (16.1 g, 105.8 mmol) were reacted in $CHCl_3$ (50 mL) at 55 °C for 24 hours. The reaction mixture was then diluted with $CHCl_3$ (50 mL), and the polymer was precipitated into rapidly stirred hexanes (2 L). The isolated polymer was dried and precipitated sequentially from $CHCl_3$ (150 mL) into hexanes (2 L) and from $CHCl_3$ in diethyl ether (2 L) to remove excess *N*-hexylimidazole, before vacuum drying. This material was carried on to subsequent ion-metathesis reactions. Yield: 14.8 g (93 % yield).

In order to remove traces of *N*-hexylimidazole and to obtain analytically pure PVBnHexImCl, a sample of the polymer was dissolved in a minimum amount of methanol, precipitated into cold acetone, and dried *in vacuo*. Residual acetone was removed by triturating the polymer in hexanes for two hours followed by vacuum drying at 55 °C. ^{1}H NMR (300 MHz, DMSO-d_6, 22°C): δ (ppm) 10.77 – 9.85 (1H, N=C*H*-N), 8.53 – 7.72 (2H, N-C*H*=C*H*-N), 7.69 – 6.88 (2H, Ar-*H meta*), 6.83 – 5.88 (2H, Ar-*H ortho*), 5.88 – 4.83 (2H, C-CH_2-N), 4.50 – 3.83 (2H, N-CH_2-CH$_2$-), 2.11 – 0.31 (14H, CH_2-C*H*-Ar and –CH_2-CH_2-CH_2-CH_2-CH_3). The ^{1}H NMR spectrum is provided in Appendix 1 (Figure A1.2.d).

Synthesis of of PVBnHexImPF$_6$. In a 100 mL Schlenk tube, PVBnHexImCl (2.0 g, 0.063 mmol), NaPF$_6$ (3.56 g, 21.2 mmol), and *N,N*-dimethylformamide (20 mL) were mixed to give a cloudy solution. The solution was stirred at ambient temperature for 48 hours. The polymer was precipitated into deionized water (300 mL) then isolated on a glass frit. The polymer was redissolved in minimum acetone and then precipitated again from water, isolated, and dried *in vacuo* at 55 °C. Yield: 2.41 g (89 % yield). ^{1}H NMR (300 MHz, DMSO-d_6, 22°C): δ (ppm) 9.33–9.00 (1H, N=C*H*-N), 7.99–7.30 (2H, N-C*H*=C*H*-N), 7.30–6.74 (2H, Ar-*H meta*), 6.74–5.93 (2H, Ar-*H ortho*), 5.50–4.80 (2H, C-CH_2-N), 4.30–3.85 (2H, N-CH_2-CH$_2$-), 2.18–0.41 (14H, CH_2-C*H*-Ar and –CH_2-CH_2-CH_2-CH_2-CH_3). The ^{1}H NMR spectrum is provided in Appendix 1 (Figure A1.2.e). *Anal*. Calc.: C, 52.17; H, 6.08; N, 6.76; F, 27.51; Cl, 0.00. Found: C, 51.95; H, 5.95; N, 6.61; F, 27.65; Cl, 0.0.

Synthesis of PVBnHexImBF$_4$. PVBnHexImBF$_4$ was produced by a similar salt metathesis procedure to that used to produce PVBnImHexPF$_6$ using NaBF$_4$. Yield: 1.93 g (83 % yield). ^{1}H NMR (300 MHz, DMSO-d_6, 22°C): δ (ppm) 9.30–9.00 (1H, N=C*H*-N), 7.95–7.32

(2H, N-C*H*=C*H*-N) 7.32–6.74 (2H, Ar-*H meta*), 6.74–5.96 (2H, Ar-*H ortho*), 5.52–4.80 (2H, C-CH_2-N), 4.30–3.82 (2H, N-CH_2-CH$_2$-), 2.18–0.43 (14H, CH_2-C*H*-Ar and –CH_2-CH_2-CH_2-CH_2-CH_3). The ^{1}H NMR spectrum is provided in Appendix 1 (Figure A1.2.f). *Anal.* Calc.: C, 60.69; H, 7.07; N, 7.86; F, 21.33; Cl, 0.00. Found: C, 60.71; H, 7.01; N, 7.68; F, 21.09; Cl, 0.0.

Synthesis of PVBnHexImTFSI. PVBnImHexCl (2.0 g, 0.063 mmol), lithium bis(trifluoromethane sulfonyl)imide (LiTFSI) (2.42 g, 22.0 mmol), and *N,N*-dimethylformamide (20 mL) were reacted at ambient temperature for 48 h. The polymer was precipitated into stirring deionized water (300 mL) to give a sticky polymer that was dried *in vacuo.* The polymer was redissolved in a minimum amount of THF and precipitated by adding methanol/water (1:1 v/v) dropwise to the polymer solution. After stirring for several minutes, the supernatant liquid was decanted, the polymer dried *in vacuo*. This precipitation process was repeated twice more (until a qualitative flame test of the polymer no longer indicated the presence of lithium), and the final polymer was dried *in vacuo* at 55 °C. Yield: 2.43 g (67 % yield). ^{1}H NMR (300 MHz, DMSO-d_6, 22°C): δ (ppm) 9.33–9.06 (1H, N=C*H*-N), 7.99–7.26 (2H, N-C*H*=C*H*-N), 7.26–6.69 (2H, Ar-*H meta*), 6.69–5.92 (2H, Ar-*H ortho*), 5.55–4.80 (2H, C-CH_2-N), 4.31–3.88 (2H, N-CH_2-CH$_2$-), 2.15–0.43 (14H, CH_2-C*H*-Ar and –CH_2-CH_2-CH_2-CH_2-CH_3). The ^{1}H NMR spectrum is provided in Appendix 1 (Figure A1.2.g). *Anal.* Calc.: C, 43.71; H, 4.58; N, 7.65; F, 20.74; Cl, 0.00. Found: C, 44.76; H, 4.49; N, 7.55; F, 21.11; Cl, 0.0.

2.3 Results & Discussion

2.3.1 POIL Syntheses.

Polymerized imidazolium ionic liquid homopolymers with variable structures may be produced by: (1) direct polymerization of an ionic liquid monomer (Scheme 2.1.a), or (2) exhaustive post-synthetic functionalization of a prepolymer (Scheme 2.1.b). The first method typically suffers from tedious synthesis and purification of IL monomers that render large-scale production of the pure monomers difficult and expensive. Furthermore, isolation of the pure polymerized ionic liquid and subsequent characterization of its molecular weight and molecular weight distribution are major challenges encountered in this synthetic approach.[4,6,40,42,45,52-56] On the other hand, the second method facilitates the modular synthesis of a homologous series of POILs at constant average degree of polymerization and molecular weight distribution with varied structures and functionalities, thus enabling development of systematic correlations between POIL chemical structures and physical properties. Stancik *et al.* initially reported post-synthetic nucleophilic substitution reactions of poly(4-vinylbenzyl chloride) (PVBCl) homopolymer segments in styrenic block copolymers made by nitroxide-mediated polymerizations to produce block copolymers containing PVBnMeImX blocks (X = Cl, BF_4).[44] This work demonstrates that relatively narrow dispersity POIL homopolymers, block copolymers, and complex architectures may be readily synthesized using controlled/living polymerization techniques. Numerous groups have recently utilized similar approaches to functionalize various polymer scaffolds with cationic moieties to form POILs as potential new polymer electrolytes for energy storage and conversion applications.[18-20,24,28,33,57,58]

Scheme 2.1. POIL synthesis by (a) direct polymerization of an ionic liquid monomer, or (b) exhaustive post-synthetic polymer functionalization of a parent prepolymer.

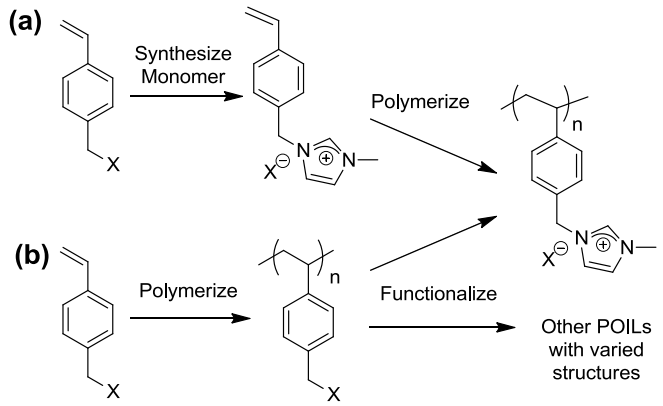

We prepared a homologous series of POIL homopolymers by functionalization of a single, relatively narrow dispersity PVBCl homopolymer by analogy to the work of Stancik *et al*. (Scheme 2.2). Alkoxyamine **1** was synthesized in high yields by atom transfer radical coupling of ethyl 2-bromoisobutyrate and TIPNO radical using *N,N*-dimethylformamide (DMF) as the optimized solvent. Consistent with previous reports of the NMP of 4-vinylbenzyl chloride using (2,2,6,6-tetramethylpiperidin-1-yl)oxyl (TEMPO)-based alkoxyamines,[59-61] we found that **1** modestly controls its rapid polymerization at 125 °C (> 60 % conversion after 30 minutes) in presence of xylenes as a diluent to slow the polymerization rate. Thus a single master-batch of PVBCl homopolymer with absolute M_n = 15.9 kg mol^{-1} and M_w/M_n = 1.34 was produced. Although the overall control of the polymerization is less than that typically observed for styrene, the molecular weight dispersity of PVBCl prepared herein is substantially narrower than in previous accounts of nitroxide-mediated polymerizations of 4-vinylbenzyl chloride,[59-61] furnishing access to nitroxyl-chain end functionalized polymers by this technique. Exhaustive reaction of PVBCl with excess *N*-alkylimidazole in either $CHCl_3$ at 55 °C or DMF at 80 °C over

12-24 h yields the desired PVBn(alkyl)ImCl homopolymers (alkyl = CH_3 (Me), -C_4H_9 (Bu), and -C_6H_{13} (Hex)), as demonstrated by a shift in the ^{1}H NMR signals associated with the –C*H*$_2$Cl functionalities of the starting PVBCl to those attributed to the –C*H*$_2$(alkyl)ImCl functionalities (Figure A1.2). In the syntheses of PVBnMeImCl and PVBnBuImCl, we noted that the functionalization reactions proceeded to completion despite the extremely poor solubility of these POIL homopolymers in the reaction solvent.

Scheme 2.2. Syntheses of PVBn(alkyl)ImCl homopolymers from a common polymer precursor.

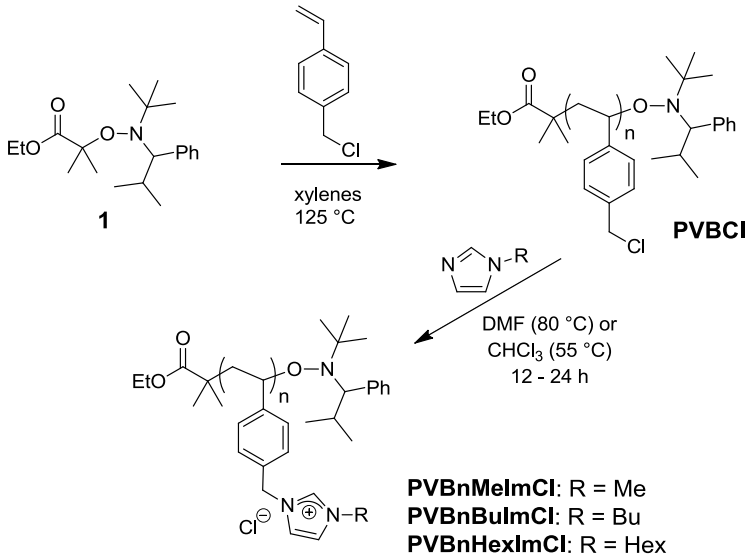

To study counterion effects on the physical properties and the ionic conductivities of POILs, the chloride counterions of PVBnHexImCl were exchanged to yield a homologous series of hydrophobic materials containing weakly coordinating counterions. Salt metathesis reactions of PVBnHexImCl using $NaBF_4$, $NaPF_6$, or LiTFSI in DMF yield the desired POILs (Scheme 2.3). Although the PVBnHexImCl is relatively hygroscopic, the POILs bearing BF_4^-, PF_6^-, and

$TFSI^-$ anions resisted substantial water uptake and were generally more soluble in organic solvents. Combustion/ion chromatography analyses along with C/H/N/F elemental analyses establish that the salt metathesis reactions proceed to complete conversion and confirm the absence of residual salts in these samples.

In addition to the salt metatheses to furnish the hydrophobic POILs, we attempted to exchange the chloride counterions for hydroxide in order to obtain a hydroxide conducting polymer that would function as a polymer electrolyte for alkaline fuel cells. Typically, hydroxide exchange is performed in a heterogeneous fashion in which block copolymers or other water-insoluble monoliths of polymer are soaked in aqueous metal hydroxide solutions followed by rinsing in deionized water to remove exogenous salt.[31,62] In our case, PVBnHexImCl is water-soluble, so a homogeneous solution reaction was necessary to attempt to exchange chloride counterions for hydroxides. Several attempts to metathesize PVBnHexImTFSI with sodium hydroxide or potassium hydroxide under varying conditions resulted in polymers that were insoluble in a range of NMR solvents, preventing us from analyzing the products of the reactions. Despite our lack of success in obtaining styrenic-based imidazolium POILs with hydroxide counterions, Elabd and coworkers recently established a protocol that allows for the metathesis of bromide counterions for hydroxide ions in methacrylate-based imidazolium POILs, although they observe significant decomposition of the imidazolium ring upon strongly basic conditions or at elevated temperature.[63]

Scheme 2.3. Salt metathesis syntheses of PVBn(Hex)ImX (X = PF_6, BF_4, and TFSI).

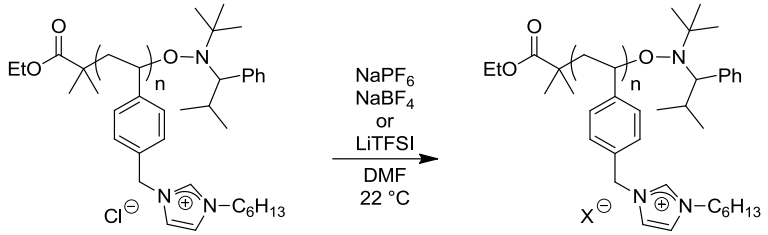

PVBnHexImCl

PVBnHexImPF$_6$
PVBnHexImBF$_4$
PVBnHexImTFSI

2.3.2 Thermal Analyses of POIL Homopolymers.

Thermogravimetric analyses (TGA) demonstrate that POIL thermal stability depends sensitively on the structure of the anion (Table 2.1) as previously observed by Mecerreyes[55] and Brennecke.[64] The hydrophilic PVBn(alkyl)ImCl materials exhibit a slight weight loss (< 5%) below 100 °C (Figure 2.1), which we attribute to water loss from these hygroscopic materials. After accounting for this water loss, we observe that the onset of decomposition (temperature at which 5% weight loss is observed) ranges from 222 - 245 °C with a second decomposition event consistently occurring at ~400 °C. In sharp contrast to these results, the onset of decomposition for the PVBnHexImX occurs at 291, 295, and 345 °C for X = BF_4^-, PF_6^-, and $TFSI^-$, respectively (Figure 2.2). Testament to the hydrophobicity of these materials is the fact that no weight loss is observed below 100 °C, indicating that these materials do not appreciably absorb moisture. The TGA profiles for the hydrophobic POILs mirror results reported previously by Shen and co-workers for PVBnBuImBF_4 synthesized by atom transfer radical polymerization.[57]

Table 2.1. Thermal Characteristics of POIL Homopolymers.

Sample	T_g (°C) [a]	T_{decomp} (°C) [b]
PVBnMeImCl	180	222, 320, 393
PVBnBuImCl	119	245, 408
PVBnHexImCl	109	233, 405
PVBnHexImPF_6	87	295, 385
PVBnHexImBF_4	79	291, 395
PVBnHexImTFSI	9	345

[a] determined from the average values observed on second and third heating by DSC.
[b] Temperature at which 5% weight loss is observed as determined by TGA for each observed decomposition event.

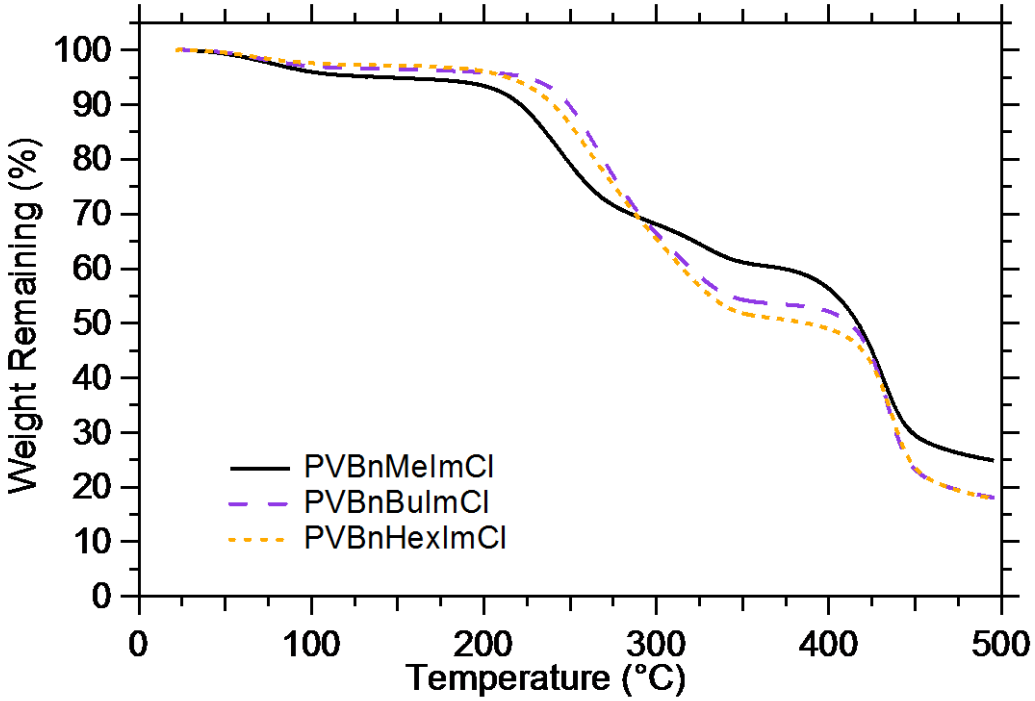

Figure 2.1. TGA profiles for the PVBn(alkyl)ImCl POILs that demonstrate two decomposition events.

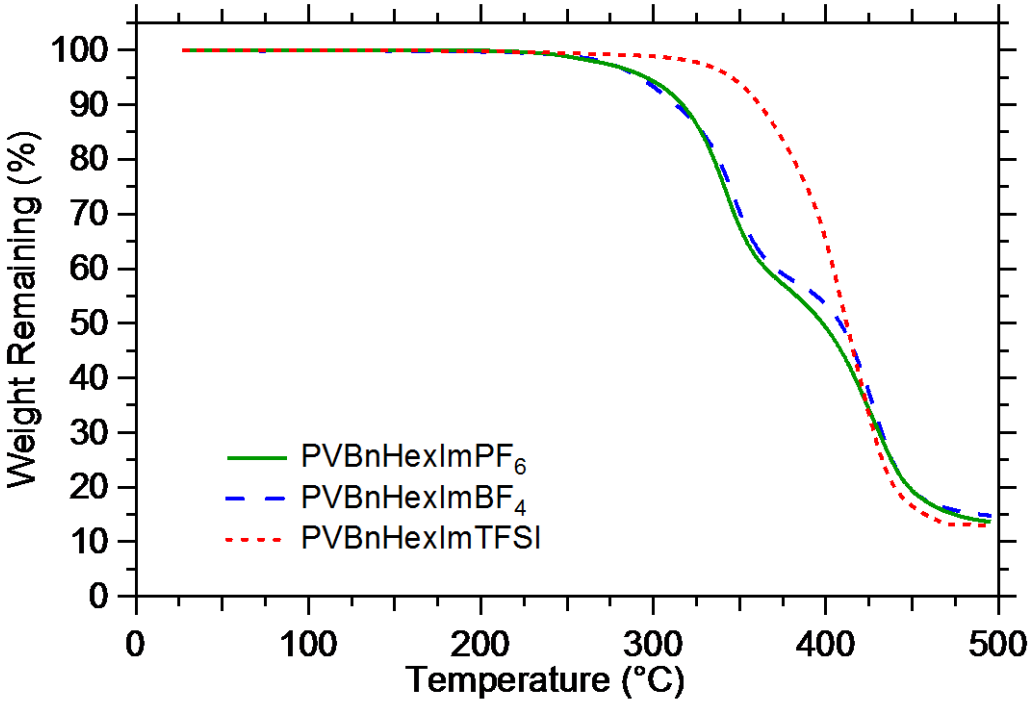

Figure 2.2. TGA profiles for the series of PVBnHexImX (X = BF_4, PF_6, and TFSI) polymers that exhibit enhanced thermal stability.

The relatively poor thermal stability of the PVBn(alkyl)ImCl polymers and their narrow range of thermal decomposition temperatures derive from a common degradation pathway inherent to the benzyl(alkyl)imidazolium chloride functionality. Three possible decomposition pathways are available to benzyl(alkyl)imidazolium chloride ionic liquids:[65] (i) Hofmann elimination to yield an *N*-benzylic imidazole, a terminal olefin, and HCl (Scheme 2.4.a), (ii) deprotonation of the imidazolium ring to form an *N*-heterocyclic carbene and HCl (Scheme 2.4.b), and (iii) nucleophilic displacement of the alkylimidazole by Cl^- to revert to PVBCl (Scheme 2.4.c). Given that all of the PVBn(alkyl)ImCl undergo decomposition at similar temperatures, we rule out Hofmann elimination because it is not a viable mechanism for PVBnMeImCl. Deprotonation of the imidazolium ring at the 2-position also seems unlikely

given the weak basicity of the Cl^- counterion. Given the nucleophilic character of Cl^- and the presence of a good *N*-alkylimidazole leaving group at the benzylic position that is activated for S_N2 displacement, we assert that the decomposition occurs by nucleophilic displacement of the *N*-alkylimidazole.[66] TGA data for these POILs support this assertion, because the first decomposition event for the Me-, Bu-, and Hex-substituted polymers results in weight loss percentages of 35%, 45%, and 50%, respectively. Assuming that decomposition occurs exclusively by S_N2 displacement and subsequent volatilization of the *N*-alkylimidazole, one predicts weight losses of 35%, 45%, and 47% that agree reasonably well with the observed values within experimental error. POILs with weakly coordinating BF_4^-, PF_6^-, and $TFSI^-$ counterions decompose by alternate pathways,[65,67] rendering them far more stable. For the observed two-step decomposition of BF_4 and PF_6-containing polymers, the first decomposition event likely corresponds to the anion-mediated mechanism described by the groups of Kumai[65] and Witkamp[67] for small molecule ionic liquids, followed by degradation of the poly(styrene) backbone. The PVBnHexImTFSI is so stable that only one decomposition event was observed, consistent with decomposition of the poly(styrene) backbone.[68]

Scheme 2.4. Potential decomposition pathways available to PVBn(alkyl)ImCl homopolymers: (*a*) Hoffman elimination; (*b*) *N*-heterocyclic carbene formation; and (*c*) nucleophilic substitution to revert to the chlorinated prepolymer.

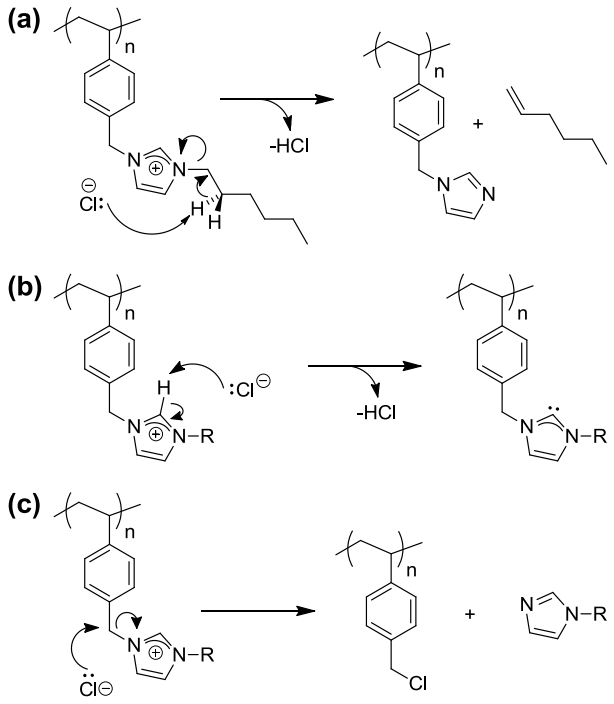

The post-synthetic functionalization route to POIL homopolymers with constant average degrees of polymerization enables deconvolution of the effects of cation and anion structure on the glass transition temperatures (T_g) for these materials, without having to account for molecular weight effects on T_g. On the basis of differential scanning calorimetry (DSC) analyses (Figure 2.3), we found that the POIL T_g's depend sensitively on both the counterion and the alkyl chain length (Table 2.1). In the PVBn(alkyl)ImCl series, the homopolymer T_g consistently decreases with increasing alkyl chain length because of the internal plasticization of the polymer by these longer alkyl chains. In the case of the PVBnHexImX homopolymer series, the T_g decreases in the order $Cl^- > PF_6^- > BF_4^- > TFSI^-$. These results are consistent with results by Shen and co-workers,

in which they observed similar trends in PVBn(alkyl)ImBF_4 and PVBnBuImX homopolymers synthesized by uncontrolled free radical polymerizations of ionic liquid monomers.[45] They reasoned that POIL anions act as plasticizers, and that larger anions plasticize polymers to larger extents. Ye and Elabd have also recently reported similar T_g trends as a function of counterion in methacrylate-based POILs, in which they attribute the substantial plasticization observed in the TFSI-based POILs to the low symmetry, charge delocalization, and flexibility of this fluorinated anion.[43]

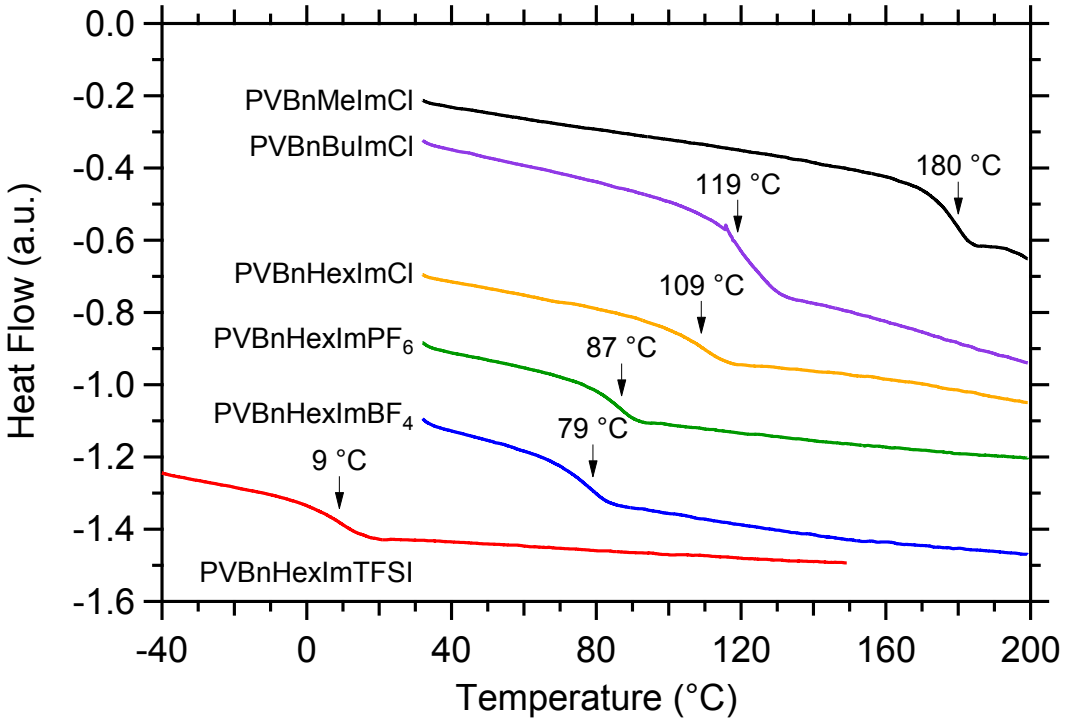

Figure 2.3. DSC heating curves for the homologous PVBn(alkyl)ImCl (alkyl = methyl, butyl, and hexyl) homopolymers and for the PVBnHexImX homopolymers (X = BF_4^-, PF_6^-, and $TFSI^-$) demonstrating a consistent decrease in T_g with increasing alkyl chain length and increasing counterion size.

2.3.3 Ionic Conductivity.

Figure 2.4.a shows the measured ionic conductivities of the hydrophobic styrenic POILs (PVBnHexImX; X = $TFSI^-$, BF_4^-, PF_6^-) as a function of temperature under a dry condition (RH ≤ 10%). Ionic conductivity increases by 2-3 orders of magnitude as temperature increases from 80 to 150 °C for all of the hydrophobic POILs. The observed conductivity of the POIL with $TFSI^-$ anions is also several orders of magnitude greater than that of the POILs with BF_4^- and PF_6^- anions, indicating a substantial dependence of conductivity on the identity of the counterion. These differences in conductivity are less significant at higher temperatures, where the conductivities only vary over approximately one order of magnitude. The apparent differences in conductivity appear to be predominately dictated by differences in the glass transition temperature, T_g, and the underlying temperature-dependent segmental motion of the polymer chain, whereby ion transport is facilitated by polymers exhibiting faster segmental motions. Specifically, the $TFSI^-$ anions in PVBnHexImTFSI (T_g = 9 °C) have a more significant plasticizing effect on the parent polymer leading to a much lower T_g as compared to $PVBnHexImBF_4$ (T_g = 79 °C) and $PVBnHexImPF_6$ (T_g = 87 °C). Ye and Elabd recently reported similar trends in their work with methacrylate-based POILs.[43]

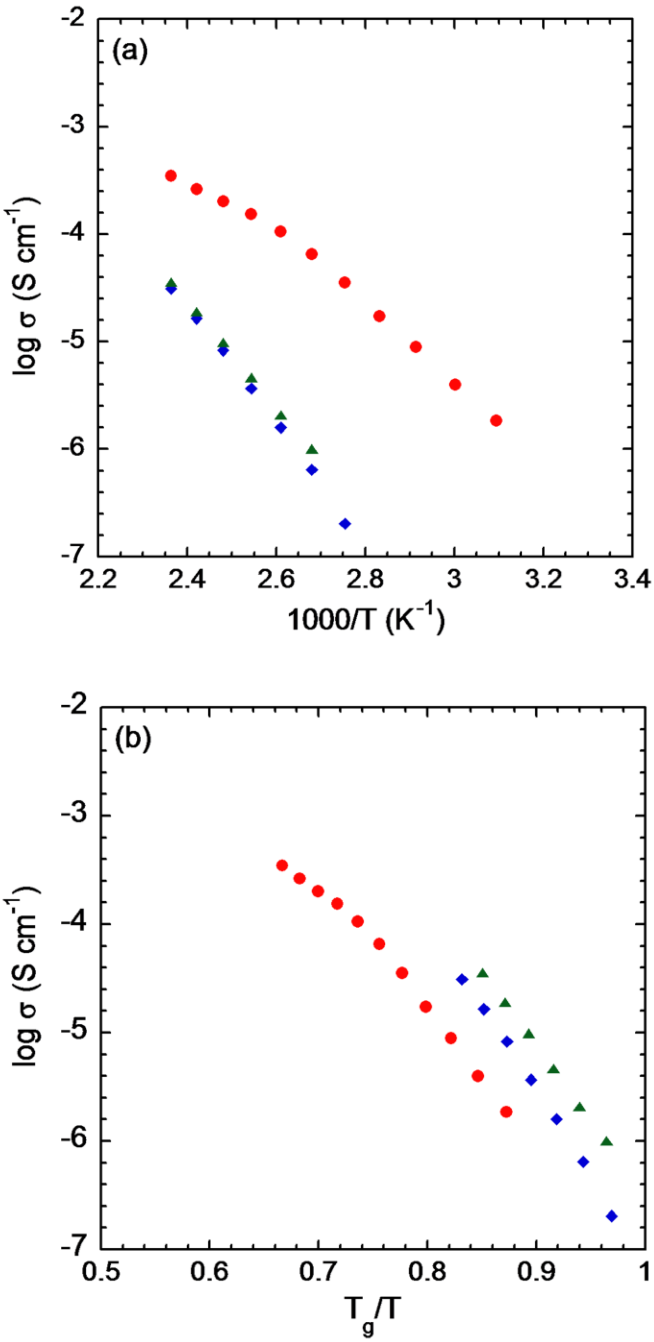

Figure 2.4. (a) Temperature-dependent and (b) Tg-independent ionic conductivity of hydrophobic styrenic POILs, PVBnHexImX; X = $TFSI^-$ (●), BF_4^- (◆), PF_6^- (▲).

Figure 2.4.b shows the T_g-independent conductivity, where conductivity is plotted versus the normalized temperature T_g/T, to deconvolute the effects of T_g and molecular structure that influence ionic conductivity. Interestingly, the conductivites associated with POILs having different anions do not collapse onto a single master curve, suggesting that other factors influence ion conductivity in these systems. The data shown in Figure 2.4.b indicates that POILs containing BF_4^- and PF_6^- anions exhibit comparable conductivities that are intrinsically higher than that of materials containing $TFSI^-$ counterions. Thus, ion size and symmetry may play a secondary role in governing the intrinsic ionic conductivities of POIL homopolymers.

Figure 2.5 compares the results of this study on styrenic POILs with methacrylate-based POILs (PMEBImX) in work by Ye and Elabd.[43] Note that the T_gs of the methacrylate-based POILs, PMEBImX, are 7, 85, and 94 °C, for X = $TFSI^-$, BF_4^-, and PF_6^-, respectively. In the methacrylate series, the apparent ionic conductivity increases in the order $BF_4^- < PF_6^- < TFSI^-$ suggesting a strong correlation between conductivity and T_g. For each anion, the T_g-independent conductivities for the methacrylate-based POILs are approximately half an order of magnitude higher than the styrenic POILs in this study.

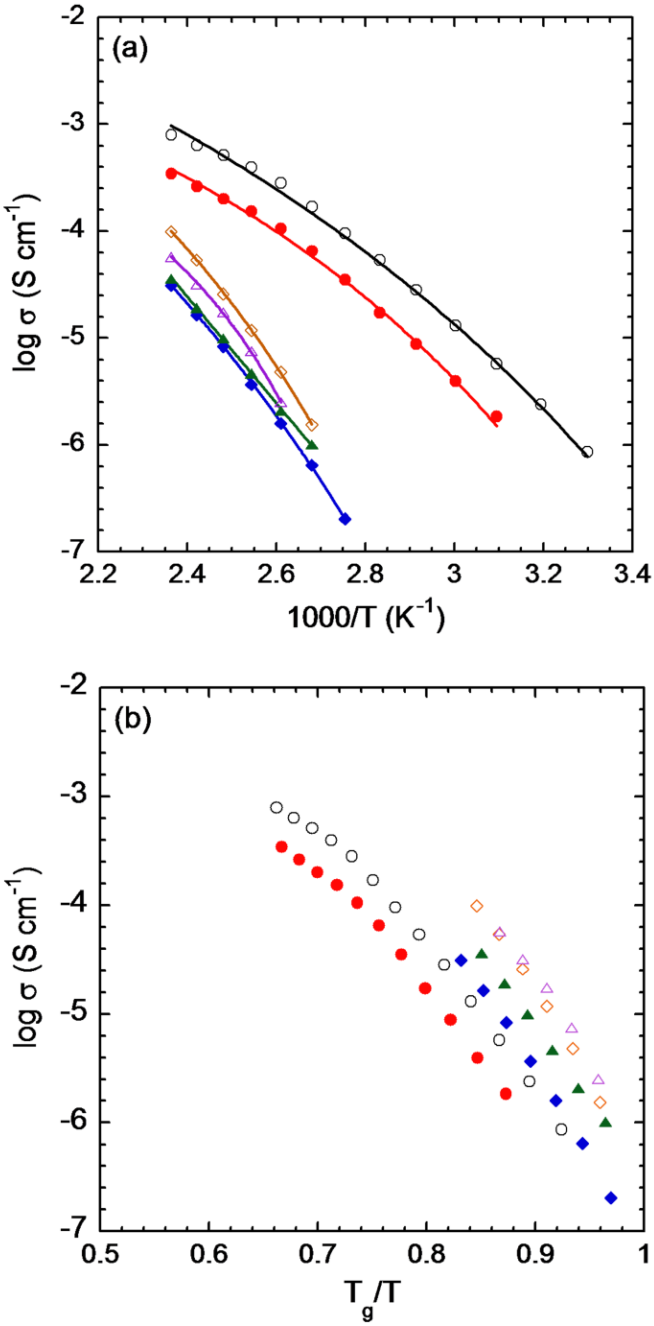

Figure 2.5. (a) Temperature-dependent and (b) Tg-independent ionic conductivity of hydrophobic styrenic POILs: PVBnHexImX; X = $TFSI^-$ (●), BF_4^- (◆), PF_6^- (▲) and hydrophobic methacrylate-based POILs, PMEBImX; X^- = $TFSI^-$ (○), BF_4^- (◇), PF_6^- (△). Lines represent regression to VFT equation. (Eq. 2.2)

To understand this result, the temperature-dependent ionic conductivity data were quantitatively analyzed using the Vogel-Fulcher-Tammann (VFT) equation[69-71]:

$$\sigma(T) = \sigma_\infty \exp\left(-\frac{B}{T - T_0}\right) \qquad (2.2)$$

In Eq (2.2), σ_∞ (S cm^{-1}) is the infinite temperature conductivity, B (K) is the VFT activation energy, and T_0 (K) is the Vogel temperature that physically represents the temperature at which ion motion ceases. A non-linear regression of the temperature-dependent conductivity data to Eq (2.2) results in three fitting parameters (σ_∞, B, T_0). Alternatively, Eq (2.2) can be recast into the following form:

$$\sigma(T) = \sigma(T_r) \exp\left(-B\left(\frac{1}{T - T_0} - \frac{1}{T_r - T_0}\right)\right) \qquad (2.3)$$

where σ (T_r) is an experimentally measured conductivity at a reference temperature, T_r, thus reducing the number of fitting parameters from three to two (B, T_0).[43] Therefore, the temperature-dependent conductivity was regressed according to Eq (2.3) (Figure 2.5.a). Table 2.2 lists the VFT fitting parameters for the TFSI-containing styrenic POIL (PVBnHexImTFSI) and methacrylate-based POIL (PMEBImTFSI); due to the limited temperature range over which the ionic conductivity could be measured for the PVBnHexImBF_4 and PVBnHexImPF_6, we could not reliably regress these data to obtain VFT fitting parameters with high confidence. From these data (Table 2.2), we see that the infinite temperature conductivity, σ_∞, for the methacrylate-based POIL is one order of magnitude higher than for the styrenic POIL. As the VFT conductivity equation is a form of the Nernst-Einstein equation that includes contributions from the VFT viscosity equation, the Stokes-Einstein equation, and the Einstein diffusion equation, σ_∞ is a

product of the valence charge or charge on the mobile ions, charge concentration, and ion mobility at infinite temperature. In other words, σ_∞ provides an estimate of the impact of charge concentration on the temperature-independent conductivity. Thus the higher T_g-independent conductivities of the methacrylate-based POILs may be attributed to the differences in ion concentration between the polymers (Figure 2.5.b), because the volume occupied by a methacrylate unit is much smaller than that occupied by a styrene unit[72] and we are comparing polymers bearing the same alkylimidazolium substituent and the same counterion. On the basis of this argument, we hypothesize that low T_g POILs with high ion concentration are desirable to achieve the highest ionic conductivity.

In comparison to previously reported "ion gels", the materials described in this study exhibit lower conductivities by at least one order of magnitude. Lodge and coworkers recently reported ion gels comprised of 10-50 wt% poly(styrene-*b*-methyl methacrylate-*b*-styrene) PS-*b*-PMMA-*b*-PS in an ionic liquid that display conductivities in the range of 3 x 10^{-5} to 3 x 10^{-2} S cm^{-1} over a temperature range of 30 – 200 °C.[13] Elabd and coworkers also prepared materials containing 50-70 wt% PS-*b*-PMMA polymers in ionic liquid that have ionic conductivities in the range 3 x 10^{-6} to 2 x 10^{-3} S cm^{-1} over a temperature range of 30 to 150 °C.[15] Both of these previous examples of ion gels contain both free anions and cations that contribute to the overall conductivity, While our materials exhibit somewhat lower conductivities in the range of 2 x 10^{-7} to 4 x 10^{-4} S cm^{-1} over a temperature range of 50 to 150 °C, they are "single ion conductors" with transference numbers for the anion equal to unity. These types of materials with only a single mobile ionic species are useful models for solid electrolytes used in fuel cell and battery technologies.

Table 2.2. VFT equation regression values of temperature-dependent conductivity data for $TFSI^-$ POILs.

POIL	T_g (K)	T_r (K)	$\sigma(T_r)$ (S cm^{-1})	σ_∞ (S cm^{-1})	B (K)	T_0 (K)	T_g-T_0 (K)	Min. SSE[a]
PVBnHexImTFSI	282	333	3.97 x10^{-6}	0.14	1211	217	65	2.0 x 10^{-2}
PMEBImTFSI	280	333	1.31 x10^{-6}	1.39	1759	181	99	3.0 x 10^{-2}

[a] Minimum of the sum of squares error for two fitting parameters (B, T_0) over the data set ($T_g > T_0 > 0$), where only one minimum was observed.

We also examined the ionic conductivity of the series of hydrophilic PVBn(alkyl)ImCl POILs. As opposed to the aforementioned hydrophobic POILs for which ion mobility depends mainly upon segmental dynamics of the polymer chains, one expects the ion mobility in solvated hydrophilic POILs to depend on the water content which enables solvent-assisted transport. Examples of both solvent-free and solvent-assisted transport mechanisms have been observed in salt-poly(ethylene oxide)[73] and water-Nafion®[74] polymer electrolyte systems, respectively.

Figure 2.6 shows the humidity-dependent conductivity for the styrenic hydrophilic POILs, PVBnMeImCl, PVBnBuImCl, PVBnHexImCl, as function of alkyl chain length at a fixed temperature (30 °C). The observed conductivity increases by up to three orders of magnitude with increasing relative humidity (RH) from 30% to 90% RH for all hydrophilic POILs studied. Furthermore, the conductivity of these hydrophilic POILs at high RH is orders of magnitude higher than the hydrophobic POILs (*c.f.*, Figure 2.4.a) , which cannot be explained by considering the size of Cl^- versus $TFSI^-$, BF_4^- or PF_6^-. The hydration numbers of the PVBnMeImCl, PVBnBuImCl, PVBnHexImCl decreased with increasing alkyl chain length (Figure 2.6.b), which agrees with observations of the water-uptake for alkylimidazolium ionic

liquids.[67,75,76] The hydration numbers are instructive in this case because they take into account the water content of the sample on a per ion basis. PVBnMeImCl, the POIL with the shortest alkyl chain and greatest hydration number, exhibits a higher conductivity than the two POILs bearing longer alkyl chains over the entire range of relative humidities. The conductivities and hydration numbers of PVBnBuImCl and PVBnHexImCl are, however, similar and demonstrate that hydration plays an important role in the humidity-dependent conductivity in these materials. Despite the small hydration number differences between all three samples, the conductivity is much higher for PVBnMeImCl. On the basis of the previously observed alkyl chain length-dependent microphase separation of small molecule ionic liquids,[77-79] we speculate that the alkyl substituent may affect the formation of ion conducting pathways through the material. The relatively hydrophobic butyl and hexyl substituents may drive the formation of morphologies that impede ion motion to a more significant degree than could be expected based on the water uptake of the samples.

We note that the difference in conductivity between shorter and longer alkyl chain POILs is less significant at higher humidities, where the ions in all samples are highly hydrated and able to rapidly diffuse throughout the material. Also, the conductivity-humidity trend differs from the classical power-law dependent conductivity-humidity relationship predicted by percolation theory that is observed in phase-segregated polyelectrolytes such as Nafion®, likely due to the high ion exchange capacity of these POILs.[74]

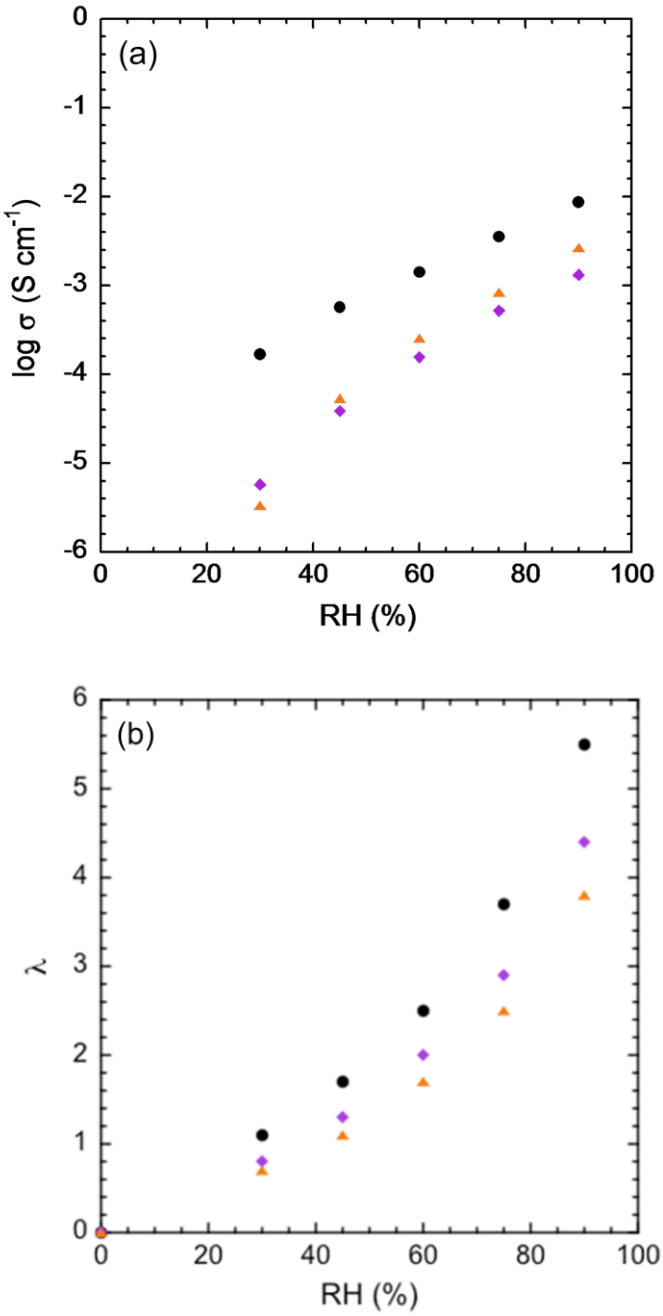

Figure 2.6. (a) Humidity-dependent ionic conductivity and (b) solubility isotherms at 30 °C for hydrophilic POILS: PVBnMeImCl (●), PVBnBuImCl (◆), PVBnHexImCl (▲),: PVBnMeImCl (●), PVBnBuImCl (◆), PVBnHexImCl (▲).

To further probe the differences in ion transport properties between hydrophobic and hydrophilic POILs, we investigated the effect of temperature on ionic conductivity. Figure 2.7 shows the temperature-dependent ionic conductivity for the hydrophilic POILs at 90% RH. Overall, the conductivity is orders of magnitude higher than the hydrophobic POILs (*c.f.*, Figure 2.4.a) over the temperature range 30-80 °C. The chloride ion conductivity in the hydrophilic POILs approaches ~0.10 S cm^{-1} at 80 °C and 90% RH, a value comparable to the proton conductivity observed in Nafion® under comparable conditions.[80] Additionally, the difference in conductivity between POILs bearing shorter and longer alkyl substituents is even less significant at 80 °C that at lower temperatures.

This temperature-dependent ionic conductivity follows an Arrhenius behavior similar to other hydrated polymer electrolytes exhibiting water-assisted transport (e.g., Nafion®). The Arrhenius activation energies determined for PVBnMeImCl, PVBnBuImCl, and PVBnHexImCl are 36.2 kJ mol^{-1}, 53.0 kJ mol^{-1} and 55.6 kJ mol^{-1}, respectively. Because of the observed Arrhenius behavior of these materials, ion transport in hydrated hydrophilic POILs must occur by a different mechanism than in the hydrophobic POILs that exhibit VFT behavior. In contrast the temperature-dependent ionic conductivity of hydrophobic POILs, the ionic conductivity of hydrophilic POILs depends sensitively on the level of hydration.

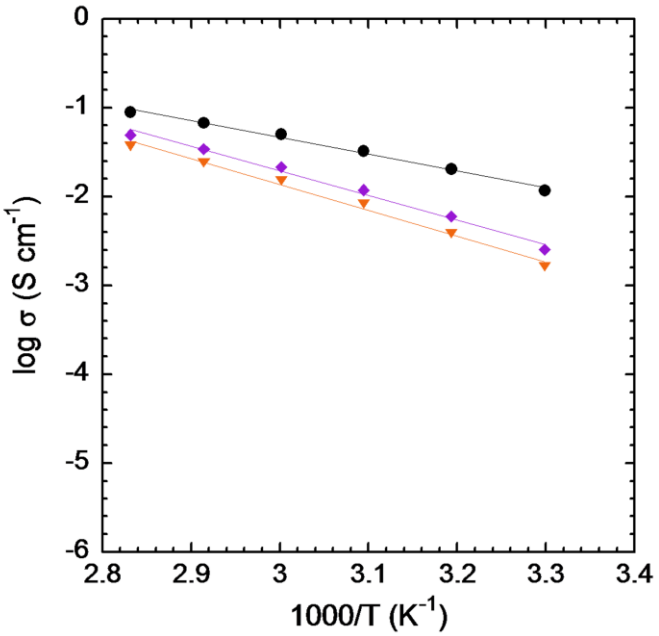

Figure 2.7. Temperature-dependent ionic conductivity (90% RH) of hydrophilic POILs: PVBnMeImCl (●), PVBnBuImCl (◆), PVBnHexImCl (▲). Solid lines represent a regression to the Arrhenius equation.

2.4 Conclusions

We have described the synthesis, thermal characterization, and ionic conductivity of a series of relatively narrow dispersity styrenic imidazolium polymerized ionic liquid homopolymers with varying counterions at constant average degree of polymerization. Post-synthetic modification of narrow dispersity poly(4-vinylbenzyl chloride) using a range of alkylimidazoles followed by salt metathesis furnished both a series of hydrophilic POILs with Cl^- counterions and varying imidazolium alkyl substituents, and a series of hydrophobic POILs with constant hexylimidazolium cations and varying hydrophobic counterions ($TFSI^-$, BF_4^-, and PF_6^-). Thermal analyses of the POILs showed decreasing glass transition temperatures for POILs

with longer alkylimidazolium substituents and for POILs with larger, more dissociated counterions. Thermal decomposition for POILs with chloride counterions proceeded via benzylic nucleophilic substitution by Cl^- at relatively low temperatures, whereas this pathway was suppressed for the POILs with weakly coordinating anions rendering them more thermally stable. Hydrated hydrophilic POILs exhibited high ionic conductivity that follows Arrhenius behavior, consistent with water-facilitated transport of ions in which ionic conductivity correlates with POIL hydration number and alkyl chain length. For hydrophobic POILs, ionic conductivity depended largely on POIL T_g, although T_g-independent plots of ionic conductivity suggested that the size and symmetry of counterions affected conductivity as well. A comparison of regressed values for the VFT equation for styrenic POILs and methacrylate-based POILs with the same counterions suggested that ionic conductivity also depends on ion concentration. The structure-property relationships established for POILs through this work will be applied to the synthesis of nanostructured POIL block copolymers, which is the subject of Chapter 3.

2.5 References

(1) Kim, J.-H.; Kim, J.-W.; Shokouhimehr, M.; Lee, Y.-S. *J. Org. Chem.* **2005**, *70*, 6714.

(2) Yang, X.; Fei, Z.; Zhao, D.; Ang, W. H.; Li, Y.; Dyson, P. J. *Inorg. Chem.* **2008**, *47*, 3292.

(3) Yuan, J. Y.; Giordano, C.; Antonietti, M. *Chem. Mater.* **2010**, *22*, 5003.

(4) Bara, J. E.; Camper, D. E.; Gin, D. L.; Noble, R. D. *Acc. Chem. Res.* **2010**, *43*, 152.

(5) Bara, J. E.; Noble, R. D.; Gin, D. L. *Ind. Eng. Chem. Res.* **2009**, *48*, 4607.

(6) Tang, J. B.; Shen, Y. Q.; Radosz, M.; Sun, W. L. *Ind. Eng. Chem. Res.* **2009**, *48*, 9113.

(7) Tang, J.; Tang, H.; Sun, W.; Plancher, H.; Radosz, M.; Shen, Y. *Chem. Commun.* **2005**, 3325.

(8) Green, O.; Grubjesic, S.; Lee, S.; Firestone, M. *Polym. Rev.* **2009**, *49*, 339.

(9) Armand, M.; Endres, F.; MacFarlane, D. R.; Ohno, H.; Scrosati, B. *Nat. Mater.* **2009**, *8*, 621.

(10) Qiu, B.; Lin, B.; Yan, F. *Polym. Int.* **2013**, *62*, 335.

(11) Ye, Y.-S.; Rick, J.; Hwang, B.-J. *J. Mater. Chem. A* **2013**, *1*, 2719.

(12) Lodge, T. P. *Science* **2008**, *321*, 50.

(13) Zhang, S.; Lee, K. H.; Frisbie, C. D.; Lodge, T. P. *Macromolecules* **2011**, *44*, 940.

(14) Gu, Y.; Lodge, T. P. *Macromolecules* **2011**, *44*, 1732.

(15) Gwee, L.; Choi, J.-H.; Winey, K. I.; Elabd, Y. A. *Polymer* **2010**, *51*, 5516.

(16) Kreuer, K. D.; Paddison, S. J.; Spohr, E.; Schuster, M. *Chem. Rev.* **2004**, *104*, 4637.

(17) Sun, X. G.; Reeder, C. L.; Kerr, J. B. *Macromolecules* **2004**, *37*, 2219.

(18) Yan, J.; Hickner, M. A. *Macromolecules* **2010**, *43*, 2349.

(19) Gu, S.; Cai, R.; Luo, T.; Chen, Z.; Sun, M.; Liu, Y.; He, G.; Yan, Y. *Angew. Chem. Int. Ed.* **2009**, *48*, 6499.

(20) Wang, J.; Li, S.; Zhang, S. *Macromolecules* **2010**, *43*, 3890.

(21) Gu, S.; Cai, R.; Yan, Y. *Chem. Commun.* **2011**, *47*, 2856.

(22) Clark, T. J.; Robertson, N. J.; Kostalik IV, H. A.; Lobkovsky, E. B.; Mutolo, P. F.; Abruña, H. D.; Coates, G. W. *J. Am. Chem. Soc.* **2009**, *131*, 12888.

(23) Robertson, N. J.; Kostalik IV, H. A.; Clark, T. J.; Mutolo, P. F.; Abruña, H. D.; Coates, G. W. *J. Am. Chem. Soc.* **2010**, *132*, 3400.

(24) Varcoe, J. R.; Slade, R. C. T.; Lam How Yee, E. *Chem. Commun.* **2006**, 1428.

(25) Sun, X. G.; Kerr, J. B. *Macromolecules* **2006**, *39*, 362.

(26) Matsumoto, K.; Endo, T. *Macromolecules* **2009**, *42*, 4580.

(27) Matsumoto, K.; Endo, T. *J. Polym. Sci., Part A: Polym. Chem.* **2010**, *48*, 3113.

(28) Danks, T. N.; Slade, R. C. T.; Varcoe, J. R. *J. Mater. Chem.* **2003**, *13*, 712.

(29) Varcoe, J.; Slade, R. *Electrochem. Commun.* **2006**, *8*, 839.

(30) Liu, H.; Yang, S.; Wang, S.; Fang, J.; Jiang, L.; Sun, G. *J. Membr. Sci.* **2011**, *369*, 277.

(31) Kostalik IV, H. A.; Clark, T. J.; Robertson, N. J.; Mutolo, P. F.; Longo, J. M.; Abruña, H. D.; Coates, G. W. *Macromolecules* **2010**, *43*, 7147.

(32) Vinodh, R.; Ilakkiya, A.; Elamathi, S.; Sangeetha, D. *Mater. Sci. Eng., B* **2010**, *167*, 43.

(33) Xu, H.; Fang, J.; Guo, M.; Lu, X.; Wei, X.; Tu, S. *J. Membr. Sci.* **2010**, *354*, 206.

(34) Dou, S. C.; Zhang, S. H.; Klein, R. J.; Runt, J.; Colby, R. H. *Chem. Mater.* **2006**, *18*, 4288.

(35) Sun, X.; Angell, C. A. *Solid State Ionics* **2004**, *175*, 743.

(36) Yoshizawa, M.; Hirao, M.; Ito-Akita, K.; Ohno, H. *J. Mater. Chem.* **2001**, *11*, 1057.

(37) Lee, M.; Choi, U. H.; Salas-de la Cruz, D.; Mittal, A.; Winey, K. I.; Colby, R. H.; Gibson, H. W. *Adv. Funct. Mater.* **2011**, *21*, 708.

(38) Hoshino, K.; Yoshio, M.; Mukai, T.; Kishimoto, K.; Ohno, H.; Kato, T. *J. Polym. Sci., Part A: Polym. Chem.* **2003**, *41*, 3486.

(39) Ohno, H. *Electrochim. Acta* **2001**, *46*, 1407.

(40) Yoshizawa, M.; Ohno, H. *Electrochim. Acta* **2001**, *46*, 1723.

(41) Lee, M.; Choi, U. H.; Colby, R. H.; Gibson, H. W. *Chem. Mater.* **2010**, *22*, 5814.

(42) Chen, H.; Choi, J.-H.; Salas-de la Cruz, D.; Winey, K. I.; Elabd, Y. A. *Macromolecules* **2009**, *42*, 4809.

(43) Ye, Y.; Elabd, Y. A. *Polymer* **2011**, *52*, 1309.

(44) Stancik, C. M.; Lavoie, A. R.; Schütz, J.; Achurra, P. A.; Lindner, P.; Gast, A. P.; Waymouth, R. M. *Langmuir* **2004**, *20*, 596.

(45) Tang, J.; Tang, H.; Sun, W.; Radosz, M.; Shen, Y. *J. Polym. Sci., Part A: Polym. Chem.* **2005**, *43*, 5477.

(46) Hirao, M.; Ito-Akita, K.; Ohno, H. *Polym. Adv. Technol.* **2000**, *11*, 534.

(47) Ye, Y.; Elabd, Y. A. *Polymer* **2011**, *52*, 1309.

(48) Green, M. D.; Salas-de la Cruz, D.; Ye, Y.; Layman, J. M.; Elabd, Y. A.; Winey, K. I.; Long, T. E. *Macromol. Chem. Phys.* **2011**, *212*, 2522.

(49) Armarego, W. L. F.; Chai, C. L. L. *Purification of laboratory chemicals*; 5th ed.; Butterworth-Heinemann: Amsterdam ; Boston, 2003.

(50) Pernak, J.; Feder-Kubis, J.; Cieniecka-Roslonkiewicz, A.; Fischmeister, C.; Griffin, S. T.; Rogers, R. D. *New J. Chem.* **2007**, *31*, 879.

(51) Benoit, D.; Chaplinski, V.; Braslau, R.; Hawker, C. J. *J. Am. Chem. Soc.* **1999**, *121*, 3904.

(52) Aitken, B. S.; Lee, M.; Hunley, M. T.; Gibson, H. W.; Wagener, K. B. *Macromolecules* **2010**, *43*, 1699.

(53) Bara, J. E.; Lessmann, S.; Gabriel, C. J.; Hatakeyama, E. S.; Noble, R. D.; Gin, D. L. *Ind. Eng. Chem. Res.* **2007**, *46*, 5397.

(54) Li, P.; Zhao, Q.; Anderson, J. L.; Varanasi, S.; Coleman, M. R. *J. Polym. Sci., Part A: Polym. Chem.* **2010**, *48*, 4036.

(55) Jovanovski, V.; Marcilla, R.; Mecerreyes, D. *Macromol. Rapid Commun.* **2010**, *31*, 1646.

(56) Mori, H.; Yahagi, M.; Endo, T. *Macromolecules* **2009**, *42*, 8082.

(57) Tang, H.; Tang, J.; Ding, S.; Radosz, M.; Shen, Y. *J. Polym. Sci., Part A: Polym. Chem.* **2005**, *43*, 1432.

(58) Liu, Y.; Cavicchi, K. A.; Mausar, J.; Decker, B. *PMSE Prepr.* **2009**, *100*, 448.

(59) Kazmaier, P. M.; Daimon, K.; Georges, M. K.; Hamer, G. K.; Veregin, R. P. N. *Macromolecules* **1997**, *30*, 2228.

(60) Lacroix-Desmazes, P.; Delair, T.; Pichot, C.; Boutevin, B. *J. Polym. Sci., Part A: Polym. Chem.* **2000**, *38*, 3845.

(61) Bultz, E.; Bender, T. P. *Macromolecules* **2011**, DOI: 10.1021/ma200058f.

(62) Tsai, T.-H.; Maes, A. M.; Vandiver, M. A.; Versek, C.; Seifert, S.; Tuominen, M.; Liberatore, M. W.; Herring, A. M.; Coughlin, E. B. *J. Polym. Sci., Part B: Polym. Phys.* **2012**, 10.1002/polb.23170.

(63) Ye, Y.; Elabd, Y. A. *Macromolecules* **2011**, *44*, 8494.

(64) Fredlake, C. P.; Crosthwaite, J. M.; Hert, D. G.; Aki, S. N. V. K.; Brennecke, J. F. *J. Chem. Eng. Data* **2004**, *49*, 954.

(65) Ohtani, H.; Ishimura, S.; Kumai, M. *Anal. Sci.* **2008**, *24*, 1335.

(66) Chowdhury, A.; Thynell, S. T. *Thermochim. Acta* **2006**, *443*, 159.

(67) Kroon, M. C.; Buijs, W.; Peters, C. J.; Witkamp, G.-J. *Thermochim. Acta* **2007**, *465*, 40.

(68) Brandrup, J.; Immergut, E. H.; Grulke, E. A. *Polymer Handbook*; 4th ed.; Wiley: New York, 1999.

(69) Vogel, H. *Phys. Z.* **1921**, *22*, 645.

(70) Fulcher, G. S. *J. Am. Ceram. Soc.* **1925**, *8*, 339.

(71) Tamman, G.; Hesse, W. *Z. Anorg. Allg. Chem.* **1926**, *156*.

(72) Fetters, L. J.; Lohse, D. J.; Richter, D.; Witten, T. A.; Zirkel, A. *Macromolecules* **1994**, *27*, 4639.

(73) Ratner, M. A.; Shriver, D. F. *Chem. Rev.* **1988**, *88*, 109.

(74) Mauritz, K. A.; Moore, R. B. *Chem. Rev.* **2004**, *104*, 4535.

(75) Huddleston, J. G.; Visser, A. E.; Reichert, W. M.; Willauer, H. D.; Broker, G. A.; Rogers, R. D. *Green Chemistry* **2001**, *3*, 156.

(76) Erdmenger, T.; Vitz, J.; Wiesbrock, F.; Schubert, U. S. *J. Mater. Chem.* **2008**, *18*, 5267.

(77) Canongia Lopes, J. N. A.; Pádua, A. A. H. *J. Phys. Chem. B* **2006**, *110*, 3330.

(78) Triolo, A.; Russina, O.; Bleif, H. J.; Di Cola, E. *J. Phys. Chem. B* **2007**, *111*, 4641.

(79) Wang, Y. T.; Voth, G. A. *J. Am. Chem. Soc.* **2005**, *127*, 12192.

(80) Lee, C. H.; Park, H. B.; Lee, Y. M.; Lee, R. D. *Ind. Eng. Chem. Res.* **2005**, *44*, 7617.

CHAPTER 3

EFFECT OF NANOSCALE MORPHOLOGY ON THE CONDUCTIVITY OF POLYMERIZED IONIC LIQUID BLOCK COPOLYMERS

3.1 Introduction

As a consequence of their unique chemical and physical properties, polymerized ionic liquids (POILs) are emerging as a new class of materials with potential applications ranging from uses in catalysis,[1,2] nanomaterials synthesis,[3] gas separations media,[4-7] and as polymer electrolytes for battery and fuel cell applications.[8,9] A number of strategies have emerged for the application of ionic liquids in advanced materials applications, including the development of "ion gels" comprised of a polymer network swollen with an ionic liquid solvent.[10-12] A common problem encountered with both liquid electrolytes and ion gels is the propensity for electrolyte leakage from these systems. Polymerized ionic liquids enjoy many of the same favorable qualities as small molecule ionic liquids such as low flammability, chemical and thermal stability, and widely tunable physical properties, while mitigating concerns related to electrolyte leakage by virtue of their polymeric structures.[8] POIL "single-ion conductors" may thus serve as ideal polymer electrolytes for advanced electrical energy storage and conversion devices (*e.g.*, fuel cells and batteries).

Recent studies of the ionic conductivity of polymerized ionic liquids have demonstrated that materials having low glass transition temperatures (T_g) are required to obtain high levels of ionic conductivity.[13-15] As a consequence of their low T_gs, these conductive materials are of limited use at ambient temperature in many electrochemical devices due to a lack of mechanical

strength. While chemical crosslinking has been employed as a means to endow polymerized ionic liquids with greater mechanical strength,[16-21] block copolymers that self-assemble to form physically crosslinked, mechanically tough, nanostructured polymer electrolytes have attracted increased attention in the design of polymer electrolytes for electrochemical devices.[22] Microphase separated POIL-containing block copolymers provide an enticing opportunity to develop mechanically robust nanostructured materials, in which the ionic POIL domains form contiguous paths for ion conduction through a non-conducting matrix phase.

Despite numerous reports of microphase separated ion conducting membranes, fundamental studies of the effect of nanoscale morphology on ionic conductivity are relatively scarce in anhydrous systems.[22,23] Balsara and coworkers studied lithium ion conduction in poly(styrene-*b*-ethylene oxide) block copolymers exogenously doped with LiTFSI (TFSI = bis(trifluoromethanesulfonyl)imide) in the vicinity of order-order and order-disorder transitions.[24] The absence of discontinuities in conductivity across phase boundaries prompted them to conclude that morphology had little or no effect on conductivity, in the case when ion conducting blocks comprised the majority phase in the self-assembled morphology ($\phi_{ionic} \geq 0.50$). However, this same group published a subsequent study of a similar system employing simultaneous synchrotron SAXS and electrochemical impedance spectroscopy that revealed a discontinuity in lithium ion conduction across an order-to-disorder transition.[25] Simone and Lodge studied poly(styrene-*b*-ethylene oxide) diblock copolymers swollen with ionic liquid and found that conductivity increased with increasing ionic liquid content and determined that morphologies having continuous ionic domains were significantly more conductive than those in which grain boundaries inhibit ion mobility.[26] Similarly, Elabd and coworkers investigated ionic

conductivities of poly(styrene-*b*-methyl methacrylate) block copolymers containing up to 50 wt% ionic liquid and found higher values of conductivity with increasing connectivity among conducting domains.[27] While these studies provide important insights into the conductivity behavior of microphase separated ion conducting membranes, they all involve exogenous electrolytes doped into non-ionic block copolymers. Recently, several fundamental studies of the effect of morphology on ionic conductivity for anhydrous microphase separated POIL block copolymers have appeared in the literature. The first such study was reported by our group and is the subject of the present chapter.[28] Elabd and coworkers compared the morphologies and ionic conductivities of a series of microphase separated POIL block copolymers with analogous POIL random copolymers, finding that the microphase separated block copolymers exhibited conductivities that were two orders of magnitude higher than the corresponding random copolymers.[29] Such studies will be beneficial to the design of future polymeric single-ion conductors for energy storage and conversion devices.

Recent studies have demonstrated that the ionic conductivity characteristics of POIL homopolymers vary widely as a function of polymer structure and counterion and may be tailored for potential applications as fuel cell and battery polymer electrolytes. An underlying theme that emerges from the works reported by the groups of Colby,[30] Ohno,[13,31] and Elabd[14,15] is that the ionic conductivity of these polymers depends primarily on the glass transition temperatures (T_g) of these materials, reflecting the coupling of ion motion to polymer segmental dynamics. Recently, we described the modular synthesis and physical characterization of a new series of styrenic imidazolium-based polymerized ionic liquid homopolymers prepared by exhaustive functionalization of relatively narrow dispersity poly(4-vinylbenzyl chloride) with

homologous *N*-alkylimidazoles.[32] In this study, we investigated the thermal properties and ionic conductivity of POILs having varied counterions and imidazolium moieties at constant polymer chain length, finding that POILs bearing *N*-hexylidimidazolium groups and bis(trifluoromethansulfonyl)imide ($TFSI^-$) counterions exhibited the highest non-humidified ion conductivity (0.35 mS cm^{-1} at 150 °C).

In the present study, we prepared a series of poly(styrene-*b*-4-vinylbenzyl alkylimidazolium bis(trifluoromethanesulfonyl)imide) (PS-*b*-PVBn(alkyl)ImTFSI) block copolymers derived from post-synthetic modification of relatively narrow dispersity poly(styrene-*b*-4-vinylbenzyl chloride) produced by nitroxide-mediated polymerization (NMP). Films of the POIL diblock copolymers containing a rigid polystyrene block and a low-T_g POIL block were prepared via solvent-casting and melt-pressing with subsequent evaluation of their nanoscale morphology by temperature-dependent synchrotron small angle X-ray scattering (SAXS) and transmission electron microscopy (TEM). Effects of morphology on the ionic conductivity of these single-ion conductors were investigated using electrochemical impedance spectroscopy (EIS). These effects were exemplified by an increase in ionic conductivity of more than an order of magnitude between a lamellar + cylindrical coexistence phase sample (8.6 mol% POIL) and a lamellar sample (17.0 mol% POIL), indicating the importance of connectivity among conductive domains. Additionally, a single sample exhibiting lamellar + cylindrical coexistence morphology (8.6 mol% POIL) showed a large disparity in conductivity depending on the degree of long-range order (solvent-cast *vs* melt-pressed samples).

3.2 Experimental

Materials. All chemicals were purchased from Sigma-Aldrich Chemical Company (Milwaukee, WI, USA) and were used as received unless otherwise noted. Copper(I) bromide was purified according to the literature.[33] Styrene was stirred over CaH_2 to remove inhibitors and then distilled under reduced pressure. 4-Vinylbenzyl chloride was purified by passage through silica gel using hexanes as an eluent followed by removal of hexanes *in vacuo*. *N*-methylimidazole, *N*-butylimidazole, and *N,N,N',N'',N''*-pentamethyldiethylenetriamine were distilled under reduced pressure. *N*-Hexylimidazole was synthesized by a slight modification of a literature procedure in which ethanol was used as a solvent instead of 1-propanol.[34] 2,2,5-Trimethyl-4-phenyl-3-azahexane 3-nitroxide (TIPNO) was prepared according to a previously reported literature procedure.[35]

NMR Spectroscopy. ^{1}H NMR spectra were recorded on Varian Unity Inova 500, Varian Mercury Plus, or Bruker AC+ 300 spectrometers and were referenced relative to tetramethylsilane (in acetone-d_6 and $CDCl_3$) or the residual protiated solvent peak (in DMSO-d_6) in the samples. Block copolymer compositions were calculated using quantitative ^{1}H NMR spectroscopy, and M_n values for these samples were calculated using the M_n of the initial poly(styrene) macroinitiator determined from size exclusion chromatography.

Size Exclusion Chromatography (SEC). Molecular weights of the poly(styrene) macroinitiator and all molecular weight distributions were determined by SEC using a Visctoek GPCMax system using refractive index (RI) detection. Separations employed two Polymer Laboratories (Amherst, MA) Resipore columns (250 mm x 4.6 mm) using a THF eluent at a flow rate of 1.0 mL min^{-1}. The molecular weight of the poly(styrene) macroinitiator, as well as all

reported polydispersity indices (M_w/M_n) are derived from a conventional poly(styrene) calibration curve constructed using 10 narrow molecular weight distribution standards having M_n = 580-377400 g mol^{-1} (Polymer Laboratories, Amherst, MA).

Differential Scanning Calorimetry (DSC). Glass transition temperatures (T_gs) were measured using a TA Instruments Q100 modulated differential scanning calorimeter under N_2 environment. The thermal history of samples hermetically sealed in aluminum pans was erased by heating to 150 °C for three minutes and cooling to -50 °C. Second heating curves recorded over a temperature range of -50 °C to 150 °C using a heating ramp rate of 5 °C min^{-1} were used to determine T_g by the midpoint method.

Small Angle X-Ray Scattering (SAXS). Synchrotron small-angle X-ray scattering (SAXS) measurements were performed at the 5-ID-D beamline of the DuPont-Northwestern-Dow Collaborative Access Team Synchrotron Research Center at the Advanced Photon Source (Argonne, IL). Experiments employed a beam energy of 16 keV (λ=0.7293 Å) and a 3.068 m sample-to-detector distance. Two-dimensional SAXS patterns were recorded on a MAR-CCD detector (133 mm diameter active circular area) with 1024 x 1024 pixel resolution. Film samples were sandwiched between Kapton tape and placed in an array stage. Other samples were heated to the desired temperature in a Linkam DSC and allowed to equilibrate for 5 min before data collection (typical exposure times 0.1 - 1 s). 2D patterns were azimuthally integrated to obtain intensity *vs q* plots using DataSqueeze software package. In anisotropic 2D patterns, azimuthal integrations were performed along the long axis of the profiles to optimize the appearance of scattering reflections for definitive morphological assignment.

Transmission Electron Microscopy (TEM). Samples were sectioned using a RMC MT-7000 ultramicrotome at room temperature using a diamond knife to produce section samples at 75-90 nm thickness. Specimens were placed on 400-mesh Cu grids and exposed to the vapor above a 5 wt % aqueous RuO_4 solution for 1.5 h to preferentially stain the poly(styrene) block. PS-*b*-PVBnHexImTFSI-7.1 was imaged without staining due to the natural contrast stemming from the higher Z = 32 sulfur atoms in the TFSI counterion. TEM micrographs were taken on an LEO EM 912 TEM operating at 120 kV.

Electrochemical Impedance Spectroscopy (EIS). The ionic conductivity of the polymerized ionic liquid (POIL) diblock copolymers was measured using electrochemical impedance spectroscopy (EIS) (Solartron, 1260 impedance analyzer, 1287 electrochemical interface, Zplot software) over a frequency range of 1 Hz to 10^6 Hz at 200 mV. The in-plane ionic conductivity was measured with a four-electrode method using a custom-made Teflon-coated stainless steel cell at controlled temperatures and a dry condition (10% relative humidity) in an environmental chamber (Tenney, BTRS model). An alternating current was applied to the outer electrodes and the real impedance or resistance, R, was measured between the two inner reference electrodes. The resistance was determined from a semi-circle regression of the Nyquist data (imaginary *vs* real impedance), where the real impedance was taken as the x-intercept of this regression. Conductivity was calculated by using the following equation: $\sigma = L/AR$, where L and A are the distance between two inner electrodes and the cross-sectional area of the polymer film ($A = Wl$; W is the film width and l is the film thickness), respectively. The thicknesses of the polymer films were measured with a Mitutoyo digital micrometer (± 0.001 mm). Samples were allowed to equilibrate for 2 h at each measurement condition followed by at least 6

measurements at that condition; the reported value is an average of these steady-state measurements.

Synthesis of 2,2,5-Trimethyl-3-(2-oxyethyl isobutryl)-4-phenyl-3-azahexane (1). Copper(I) bromide (0.12 g, 0.85 mmol) and copper(0) powder (3.24 g, 51.1 mmol) were placed in a 100 mL Schlenk flask under nitrogen. Ethyl α-bromoisobutyrate (3.37 g, 17.0 mmol), TIPNO (2.50 g, 11.3 mmol), *N*,*N*,*N*',*N*'',*N*''-pentamethyldiethylenetriamine (0.14 g, 0.85 mmol), and *N,N*-dimethylformamide (40 mL) were combined in a second dry 100 mL Schlenk tube and freeze-thaw degassed four times. Under a flush of nitrogen, the latter solution was cannula transferred onto the copper mixture to yield a dark green solution. This reaction mixture was vigorously stirred at 40 °C for 60 minutes, during which time it turned dark blue, and then it was stirred overnight at 22 °C. The solution was subsequently filtered through a plug of neutral alumina, which was washed with ethyl acetate (250 mL). The combined organic eluents were concentrated on a rotary evaporator at 40 °C. The resulting crude product was purified by silica gel column chromatography (10 cm x 5 cm diameter) using hexanes/ethyl acetate (30:1 v/v) to furnish the alkoxyamine **1** as a yellow/orange viscous liquid. Yield: 3.41 g (90% yield). ^{1}H NMR (300 MHz, $CDCl_3$, 22°C): δ (ppm) 7.63–7.16 (m, 5 H, -Ar-*H*, both diastereomers), 4.28 – 4.06 (m, 2H, O-C*H*$_2$-CH_3, both diastereomers), 3.70 (d, $J_{H\text{-}H}^3$ = 10.8 Hz, 1H, N-C*H*, minor diastereomer), 3.42 (d, $J_{H\text{-}H}^3$ = 10.8 Hz, 1H, N-C*H*, major diastereomer), 2.48–2.34 (m, 1H, C*H*$(CH_3)_2$, minor diastereomer), 1.90–1.76 (m, 1H, C*H*$(CH_3)_2$, major diastereomer), 1.62 (s, 3H, C(C*H*$_3)_2$, major diastereomer, rotamer A), 1.59 (s, 3H, C(C*H*$_3)_2$, minor diastereomer, rotamer A), 1.55 (s, 3H, C(C*H*$_3)_2$, major diastereomer, rotamer B), 1.48 (s, 3H, C(C*H*$_3)_2$, minor diastereomer, rotamer B), 1.31 (t, $J_{H\text{-}H}^3$ = 7.2 Hz, 3H, O-CH_2-C*H*$_3$, minor diastereomer), 1.28 (t, $J_{H\text{-}H}^3$ = 7.2 Hz,

3H, O-CH_2-CH_3, major diastereomer), 1.24 (d, $J_{H\text{-}H}^3$ = 6.2 Hz, 3H, CH(CH_3)$_2$, minor diastereomer, rotamer A), 1.16 (d, $J_{H\text{-}H}^3$ = 6.2 Hz, 3H, CH(CH_3)$_2$, major diastereomer, rotamer A), 0.93 (s, 9H, C(CH_3)$_3$, major diastereomer), 0.81 (s, 9H, C(CH_3)$_3$, minor diastereomer), 0.72 (d, $J_{H\text{-}H}^3$ = 6.8 Hz, 3H, CH(CH_3)$_2$, minor diastereomer, rotamer B), 0.39 (d, $J_{H\text{-}H}^3$ = 6.8 Hz, 3H, CH(CH_3)$_2$, major diastereomer, rotamer B). ^{13}C NMR (75 MHz, $CDCl_3$, 22°C): δ (ppm, all stereoisomers and rotamers) 175.26, 175.03, 142.04, 140.62, 131.01, 130.26, 127.35, 127.11, 126.50, 126.10, 81.86, 79.57, 73.74, 72.42, 60.57, 60.32, 30.75, 30.18, 28.23, 27.29, 25.97, 25.23, 24.59, 22.83, 22.66, 22.55, 22.06, 21.88, 20.97, 13.94. ESI-MS: calcd. for $C_{20}H_{33}NO_3$ $[M+Na]^+$ 358.2, found 358.3.

Synthesis of Polystyrene Macroinitiator (PS-TIPNO). Freshly purified styrene (34.9 g, 336 mmol) and alkoxyamine **1** (0.322 g, 0.96 mmol) were sealed in a 100 mL Schlenk flask and subjected to four freeze-thaw degassing cycles, after which the flask contents were placed under N_2(g). The flask was placed in an oil bath thermostatted at 125 °C and stirred for 6 hrs 10 min, after which it was chilled in dry ice/isopropanol for 10 minutes before exposure to air. The polymerization reaction was diluted with dichloromethane (60 mL) and twice precipitated into methanol (2 L). Yield: 20.3 g of white powder (58 % conversion). ^{1}H NMR (300 MHz, $CDCl_3$, 22°C): δ (ppm) 7.30 – 6.86 (m, 3 H, Ar-*H meta + para*), 6.85 – 6.27 (m, 2 H, Ar-*H ortho*), 2.30 – 1.66 (m, 1 H, CH_2C*H*), 1.66 – 1.07 (m, 2 H, CH_2CH). SEC (THF, 40 °C): M_n = 19.1 kg mol^{-1}, M_w/M_n = 1.14 (against PS standards).

Representative Synthesis of Poly(styrene-*b*-4-vinylbenzyl chloride) (PS-*b*-PVBCl). Freshly purified 4-(vinylbenzyl choride) (2.39 g, 15.7 mmol), PS-TIPNO (3.0 g, 0.157 mmol), and xylenes (9.05 mL) were freeze-thaw degassed (4x) in a 50 mL Schlenk tube, after which the

flask contents were left under vacuum. The flask was placed in an oil bath thermostatted at 110 °C and stirred for a designated amount of time, after which it was chilled in dry ice/isopropanol for 10 minutes before exposure to air. The polymerization reaction was diluted with dichloromethane (10 mL) and twice precipitated into methanol (500 mL). Yield: 3.71 g of white powder (30 % conversion). $M_{n,NMR}$ = 25.1 kg mol^{-1} (17.6 mol% VBC composition from quantitative ^{1}H NMR) M_w/M_n = 1.26 (against PS standards). ^{1}H NMR (300 MHz, $CDCl_3$, 22°C): δ (ppm) 7.43 – 6.85 (m, 16.0 H, Ar-*H meta* + *para*), 6.85 – 6.13 (m, 11.4 H, Ar-*H ortho*), 4.64 – 4.30 (2.0 H, C*H*$_2$Cl), 2.42 – 1.06 (m, 17.5 H, C*H*$_2$C*H*).

Representative synthesis of PS-*b*-PVBnHexImCl. Poly(styrene-*b*-4-vinylbenzyl chloride) (3.0 g, 0.134 mmol, D.P.$_{VBC}$ = 21.6) and *N*-hexylimidazole (3.2 g, 21.3 mmol) were dissolved in $CHCl_3$ (10.2 mL) and heated to 55 °C for 24 hours. The reaction mixture was then diluted with $CHCl_3$ (10 mL), and the polymer was twice precipitated into rapidly stirred hexanes (500 mL) before vacuum drying. ^{1}H NMR analysis still showed traces of *N*-hexylimidazole, however, this material was pure enough for subsequent reactions. Yield: 3.21 g of white powder (93 % yield). ^{1}H NMR (300 MHz, DMSO-d_6, 22°C): δ (ppm) 10.63 – 9.88 (1.0 H, N=C*H*N), 8.43 – 5.09 (m, 32.1 H, NC*H*=C*H*N, Ar-*H* and ArC*H*$_2$N), 4.17 (s, 2.0 H, NC*H*$_2$C$_5$H$_{11}$), 2.23 – 0.49 (m, 26.6 H, C*H*$_2$C*H* and CH$_2$C$_5$*H*$_{11}$).

Synthesis of PS-*b*-PVBnMeImCl. Poly(styrene-*b*-4-vinylbenzyl chloride) (0.75 g, 0.030 mmol, D.P.$_{VBC}$ = 39.5) and *N*-methylimidazole (1.18 g, 14.4 mmol) were dissolved in *N,N*-dimethylformamide (DMF) (4.0 mL) and heated to 80 °C for 16 h, during which time the solution became cloudy and yellow in color. DMF was removed under vacuum at 50 °C and the residue was triturated with deionized water (15 mL) for 2 h before isolation by centrifugation,

decanting the cloudy supernatant liquid, and vacuum drying at 50 °C. ^{1}H NMR analysis still showed traces of *N*-methylimidazole, however, this material was pure enough for subsequent reactions. Yield: 0.76 g of off-white powder (90 % yield). ^{1}H NMR (300 MHz, DMSO-d_6, 22°C): δ (ppm) 10.31 – 9.73 (m, 1.0 H, N=C*H*N), 8.28 – 5.12 (m, 19.7 H, NC*H*=C*H*N, Ar-*H* and ArCH_2N), 3.87 (s, 3.0 H, NCH_3), 2.24 – 0.74 (6.7 H, CH_2C*H*).

Synthesis of PS-*b*-PVBnBuImCl. The synthesis of PS-*b*-PVBnBuImCl follows that of PS-*b*-PVBnMeImCl. Yield: 0.87 g of off-white powder (96 % yield). ^{1}H NMR (300 MHz, DMSO-d_6, 22°C): δ (ppm) 10.72 – 9.97 (m, 1.0 H, N=C*H*N), 8.73 – 5.08 (m, 23.8 H, NC*H*=C*H*N, Ar-*H* and ArCH_2N), 4.20 (s, 2.0 H, NCH_2C$_3$H$_7$), 2.24 – 0.22 (m, 17.7 H, CH_2C*H* and CH$_2$C$_3$*H*$_7$).

Representative Synthesis of PS-*b*-PVBnHexImTFSI. PS-*b*-PVBnHexImCl (0.64 g, 0.021 mmol, $DP_{VBnHexImCl}$ = 39.2), lithium bis(trifluoromethanesulfonyl)imide (0.72 g, 2.5 mmol), and tetrahydrofuran (THF) (4 mL) were stirred at 55 °C for 24 h, then at 22 °C for 24 h. The reaction mixture was concentrated to a viscous solution and precipitated by adding methanol/water (1:1 v/v) dropwise to the polymer solution. After stirring several minutes, the slurry was centrifuged and the supernatant liquid was decanted before vacuum drying at 50 °C. The polymer was redissolved in a minimum amount of THF and then precipitated twice more by the same procedure until combustion of a small polymer sample no longer resulted in the observation of a red colored flame indicative of the presence of lithium.[36] Finally, the polymer was triturated with pentanes (10 mL) for several hours before vacuum drying at 60 °C. Yield: 0.78 g of white powder (93 % yield). ^{1}H NMR (500 MHz, Acetone-d_6, 22°C): δ (ppm) 9.04 (s, 1.0 H, N=C*H*N), 7.90 – 6.90 (m, 20.4 H, NC*H*=C*H*N and Ar-*H meta* + *para*), 6.88 – 6.33 (m,

11.8 H, Ar-*H ortho*), 5.63 – 5.18 (m, 2.0 H, ArCH_2N), 4.32 (s, 2.0 H, NC$H_2C_5H_{11}$), 2.51 – 1.19 (m, 26.5 H, CH_2C*H* and CH_2-C_4H_8-CH_3), 0.85 (s, 3.0 H, CH_3). *Anal*. Calc.: C, 67.04; H, 6.10; N, 3.97; F, 10.77; Cl, 0.00. Found: C, 65.80; H, 5.93; N, 4.16; F, 10.90; Cl, 0.0.

Synthesis of PS-*b*-PVBnMeImTFSI. The synthesis of PS-*b*-PVBnMeImTFSI follows that of PS-*b*-PVBnHexImTFSI, except that *N,N*-dimethylformamide was used as the reaction solvent. Yield: 0.81 g of white powder (80 % yield). ^{1}H NMR (500 MHz, Acetone-d_6, 22°C): δ (ppm) 8.93 (s, 1H, N=C*H*N), 7.78 – 6.90 (m, 21.8 H, NC*H*=C*H*N and Ar-*H meta* + *para*), 6.88 – 6.33 (m, 12.8 H, Ar-*H ortho*), 5.57 – 5.25 (m, 2.0 H, ArCH_2N), 3.99 (s, 2.0 H, NCH_3), 2.52 – 1.20 (m, 19.8 H, CH_2C*H*). *Anal*. Calc.: C, 67.12; H, 5.63; N, 4.03; F, 10.93; Cl, 0.00. Found: C, 66.86; H, 5.56; N, 3.88; F, 10.65; Cl, <0.25.

Synthesis of PS-*b*-PVBnBuImTFSI. The synthesis of PS-*b*-PVBnBuImTFSI follows that of PS-*b*-PVBnHexImTFSI, except that *N,N*-dimethylformamide was used as the reaction solvent. Yield: 1.03 g of white powder (87 % yield). ^{1}H NMR (500 MHz, Acetone-d_6, 22°C): δ (ppm) 9.02 (s, 1.0 H, N=C*H*N), 7.86 – 6.90 (m, 20.0 H, NC*H*=C*H*N and Ar-*H meta* + *para*), 6.88 – 6.30 (m, 12.0 H, Ar-*H ortho*), 5.59 – 5.23 (m, 2.0 H, ArCH_2N), 4.31 (s, 2.0 H, NC$H_2C_3H_7$), 2.51 – 1.19 (m, 21.5 H, CH_2C*H* and CH_2-C_2H_4-CH_3), 0.91 (s, 3.0 H, CH_3). *Anal*. Calc.: C, 66.81; H, 5.90; N, 4.04; F, 10.95; Cl, 0.00. Found: C, 66.76; H, 5.82; N, 3.95; F, 10.79; Cl, 0.0.

Solvent-Casting PS-*b*-PVBn(alkyl)ImTFSI Block Copolymers. Polymer solutions (7% w/w) in dry THF were prepared in vials. Glass substrates (approximately 4 mm x 45 mm) were cut from microscope slides and cleaned with acetone. Substrates were placed in the bottom of a Petri dish and then polymer solutions were cast on top of the substrates via pipette. The cover

was placed on top of the Petri dish and the solvent was allowed to evaporate for 1-2 hours before another layer of polymer solution was cast on top of the films. This process was repeated one more time for especially brittle samples. The films were allowed to air dry inside the Petri dish overnight at ambient temperature. Polymer films were vacuum annealed at 150 °C for 3 h before slowly cooling to ambient temperature under vacuum.

Melt-Pressing PS-*b*-PVBnHexImTFSI Block Copolymers. As a comparison to solvent-cast films, polymer films were also prepared by melt pressing. The polymer in powder form was melt-pressed (Carver, Model 3851-0) at 150°C, 3500 psi for 10 min into a film of 190 μm in thickness. The melt-pressed films were then annealed at 150°C under vacuum for three days and then stored in a desiccator until further use.

3.3 Results and Discussion

3.3.1 Block Copolymer Synthesis.

We synthesized a series of POIL block copolymers by exhaustive functionalization of poly(styrene-*b*-4-vinylbenzyl chloride) (PS-*b*-PVBCl) diblock copolymers synthesized by nitroxide mediated polymerization (NMP) as previously reported by Stancik *et al*.[37] A single batch of relatively narrow dispersity polystyrene macroinitiator (PS-TIPNO) with M_n = 19.1 kg mol^{-1} was synthesized using alkoxyamine **1** with a high level of control (M_w/M_n = 1.14). We subsequently produced a series of poly(styrene-*b*-4-vinylbenzyl chloride) (PS-*b*-PVBCl) diblock copolymers via chain extension of the polystyrene macroinitiator. (Scheme 3.1) Initial attempts to grow diblock copolymers at 125 °C resulted in broad and bimodal molecular weight distributions due to the fast rate of propagation of the VBCl monomer relative to the initiation of

the polystyryl chain ends. Efforts to slow propagation by addition of excess TIPNO free radical (50-100 mol% with respect to macroinitiator) resulted in bimodal distributions. Thus, we were able to dramatically decrease the rate of polymerization and increase the overall degree of control by lowering the apparent polymerization temperature from 125 °C to 110 °C and by running the polymerizations under static vacuum. We obtained four PS-*b*-PVBCl diblock copolymers with unimodal molecular weight distributions ranging from M_w/M_n = 1.20-1.26 depending on the VBCl incorporation as outlined in Table 3.1. Representative size exclusion chromatography (SEC) traces of the polystyrene macroinitiator and PS-*b*-PVBCl-17.6 block copolymer are shown in Figure 3.1.

Scheme 3.1. Synthesis of poly(styrene-*b*-4-vinylbenzyl chloride) (PS-*b*-PVBCl) block copolymers.

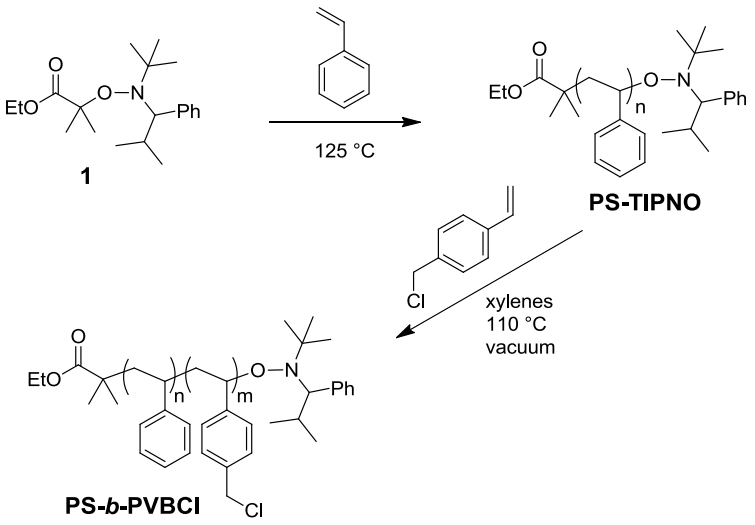

Table 3.1. Molecular parameters of PS-*b*-PVBCl diblock copolymer precursors to POIL-containing block copolymers.

Polymer	VBCl mol%[a]	$M_{n(tot)}$ (kg mol^{-1})[a]	M_w/M_n[b]
PS-*b*-PVBCl-4.8	4.8	20.5	1.20
PS-*b*-PVBCl-8.3	8.3	21.7	1.21
PS-*b*-PVBCl-10.5	10.5	22.4	1.23
PS-*b*-PVBCl-17.6	17.6	25.1	1.26

[a]Determined by quantitative ^{1}H NMR and the M_n = 19.1 kg mol^{-1} for the initial PS-TIPNO macroinitiator. [b]Determined by SEC using conventional calibration with PS standards.

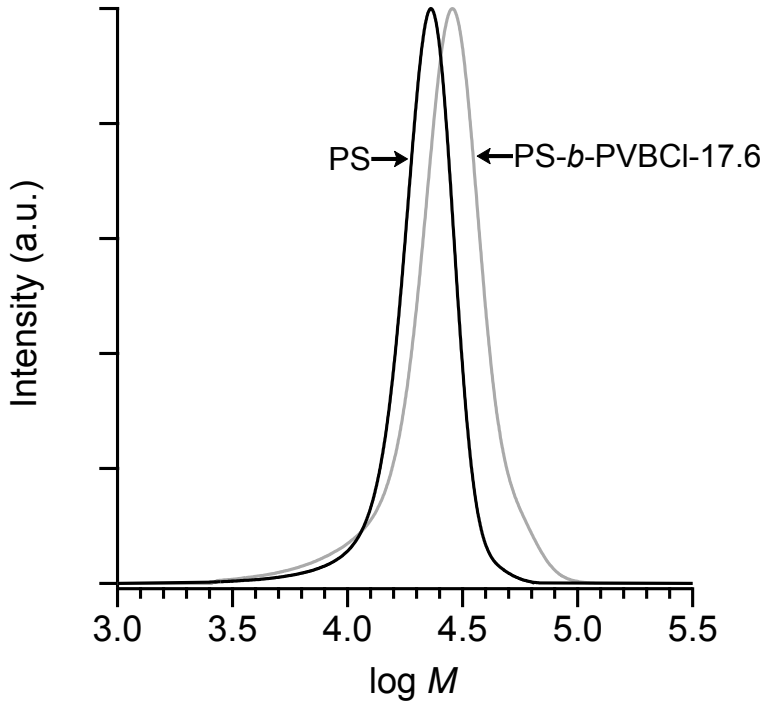

Figure 3.1. Representative SEC refractive index traces of polystyrene macroinitiator and PS-*b*-PVBCl-17.6 diblock copolymer.

Exhaustive functionalization of the PS-*b*-PVBCl block copolymers with excess *N*-alkylimidazole in either $CHCl_3$ at 55 °C or DMF at 80 °C over 24 h quantitatively yielded PS-*b*-PVBn(alkyl)ImCl diblock copolymers (alkyl = CH_3 (Me), *n*-C_4H_9 (Bu), or *n*-C_6H_{13} (Hex)) (Scheme 3.2). In order to accurately probe the effects of nanoscale morphology on ionic conductivity, we sought to study a POIL system with a relatively high intrinsic conductivity that does not sensitively depend on external variables such as humidification. Following recent reports indicating that hydrophobic methacrylate-based and styrenic-based POILs bearing bis(trifluoromethanesulfonyl)imide (TFSI) counterions exhibit high ionic conductivities due to their low glass transition temperatures, we exchanged all counterions in our diblock copolymers for TFSI.[14,32] Therefore, exhaustive salt methatheses of the PS-*b*-PVBn(alkyl)ImCl having varying POIL contents with LiTFSI furnished a series of PS-*b*-PVBn(alkyl)ImTFSI diblock copolymers. Differential scanning calorimetry (DSC) showed that all of the polymers exhibited low glass transition temperatures $T_g \sim 9$ °C for the POIL blocks regardless of alkyl substituent. High field ^{1}H NMR of the resulting block copolymers in acetone-d_6 revealed that the polymer compositions deviated slightly from those of their PS-*b*-PVBCl precursors, likely due to fractionation during polymer isolation. Figure 3.2 shows representative ^{1}H NMR spectra of PS-*b*-PVBnHexImTFSI and its PS-*b*-PVBCl precursor. In each case, polymer compositions were determined by relative integrations of the indicated ^{1}H resonances.

Scheme 3.2. Synthesis of poly(styrene-*b*-4-vinylbenzyl alkylimidazolium TFSI) block copolymers.

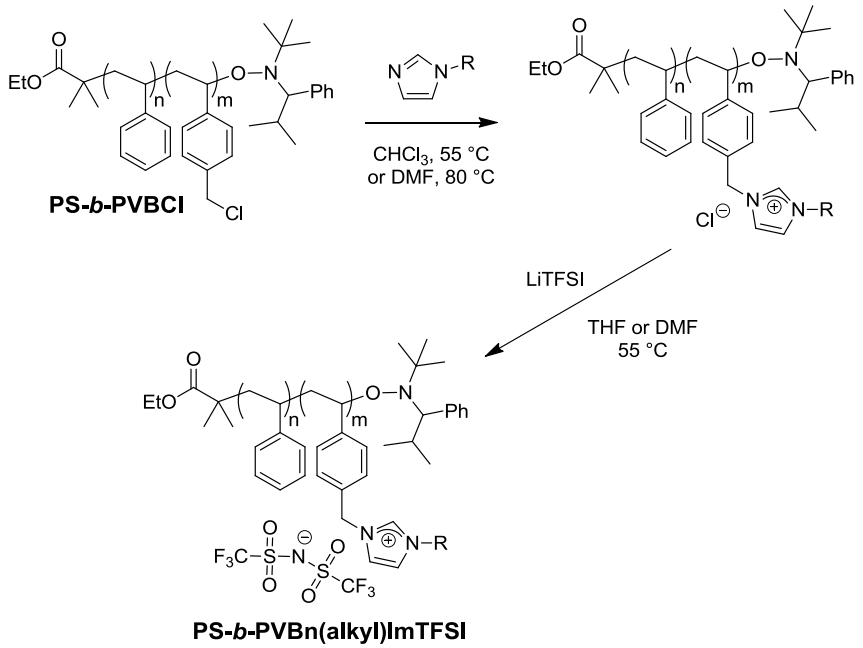

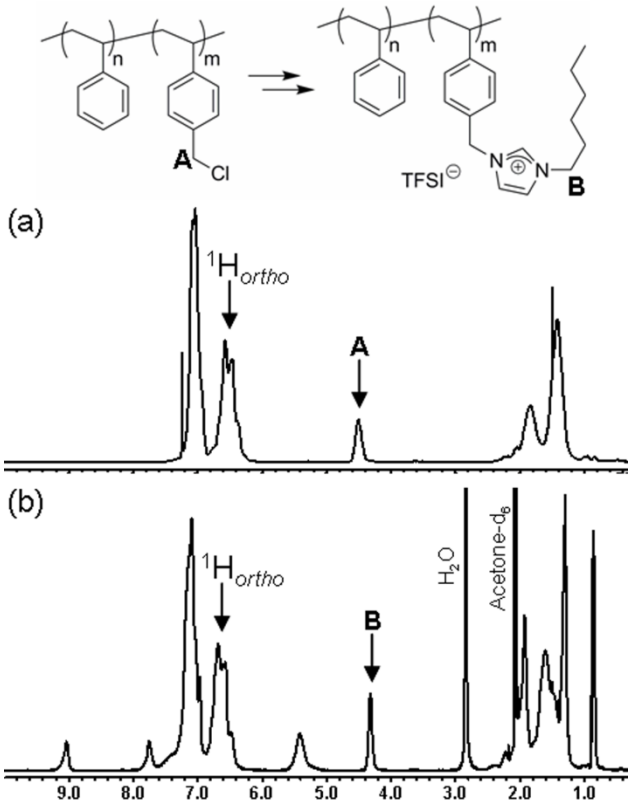

Figure 3.2. ^{1}H NMR spectra of (a) PS-*b*-PVBCl-17.6 in CDCl3 and (b) PS-*b*-PVBnHexImTFSI-17.0 in acetone-d_6. Diblock compositions are calculated from relative integrations of resonances A or B versus the sum of all styrenic *ortho* proton resonances.

3.3.2 Morphological Characterization.

The self-assembly behavior of PS-*b*-POIL block copolymers was investigated using synchrotron small angle X-ray scattering (SAXS) at room temperature. Initial SAXS studies of powder and melt-pressed samples demonstrated a low degree of long-range order in POIL block copolymers evidenced by broad and poorly defined higher order scattering maxima, likely a result of the strong segregation between the ionic and hydrophobic blocks that frustrates

ordering. In an effort to effect higher degrees of long-range nanoscale order in these samples, we solvent-cast films from THF onto glass substrates and vacuum annealed them for 3 h at 150 °C. In order to assess bulk morphologies of these samples using variable temperature SAXS, sacrificial samples of these solvent-cast films were ground into powders. Solvent-cast films used for conductivity studies (*vide infra*) were carefully removed from the glass substrates using Kapton tape and subjected to SAXS analysis with the incident X-ray beam oriented normal to the film plane to assess morphology, level of order, and any possible preferential domain orientation (anisotropy). Samples that proved too brittle for effective solvent casting were melt-pressed into thin films. Due to the sensitivity of electrochemical impedance measurements of ionic conductivity to the alignment of microphase separated domains,[27,38] we analyzed the 2D scattering images of each film for any significant anisotropy (Figure A2.1). For solvent-cast samples, 2D scattering analysis shows little to no anisotropy in the alignment of domains, whereas for melt-pressed samples, a slight degree of anisotropy is observed due to flow experienced during the melt-pressing process. In such samples, we have disregarded this low level of anisotropy in our analyses of the conductivity data.

Table 3.2. Molecular Properties and Morphologies of POIL Diblock Copolymers.

Diblock Copolymer	M_n (kg/mol)[a]	POIL mol%[b]	ϕ_{POIL}[c]	Morphology[d]	Domain Spacing (nm)[f]	POIL T_g (°C)[g]
PS-*b*-PVBnMeImTFSI-15.6	38.0	15.6	-	LAM	39	9
PS-*b*-PVBnBuImTFSI-16.7	39.6	16.7	-	LAM	38	9
PS-*b*-PVBnHexImTFSI-17.0	40.7	17.0	0.50	LAM	35	9
PS-*b*-PVBnHexImTFSI-8.6	31.0	8.6	0.34	LAM+CYL (SC)[e] LAM+CYL (MP)[e]	35 / 37 34	9
PS-*b*-PVBnHexImTFSI-7.1	28.3	7.1	0.29	CYL	42	9
PS-*b*-PVBnHexImTFSI-2.7	24.2	2.7	0.19	CYL	42	9
PVBnHexImTFSI	57.5	100	1.00	-	n/a	9

[a]Calculated from PS-*b*-PVBCl M_n. [b]Determined by quantitative ^{1}H NMR of PS-*b*-POILs. [c]Volume fraction of POIL block determined using ρ(PS) = 0.969 g cm^{-3} and ρ(PVBnHexImTFSI) = 1.096 g cm^{-3} at 150 °C (see Appendix 2 for details). [d]Determined by SAXS and TEM. [e]SC = solvent-cast; MP = melt-pressed. [f]Determined by SAXS using the position of the principle reflection. [g]Determined by DSC.

The morphologies of POIL block copolymer films were determined by indexing azimuthally integrated synchrotron SAXS profiles (Figure 3.3). Solvent-cast PS-*b*-PVBn(alkyl)ImTFSI block copolymers having 15-17% molar composition of the ionic polymer microphase separate into lamellae with a high degree of long range order, regardless of the alkyl substituent (alkyl = CH_3, C_4H_9, or C_6H_{13}). For PS-*b*-PVBnMeImTFSI-15.6 and PS-*b*-PVBnBuImTFSI-16.7, the appearance of up to seven reflections at q*, 2q*, 3q*, 4q*, 5q*, 6q*, and 7q* clearly indicates a lamellar morphology. The profile of PS-*b*-PVBnHexImTFSI-17.0 exhibits reflections at q*, 3q*, and 5q*, with structure factor extinctions of 2q* and 4q*,

indicative of a lamellar morphology with apparent symmetric volume fractions of each block.[39] Domain spacings for these lamellar samples range from 35-39 nm. POIL block copolymers were also subjected to variable-temperature SAXS to identify any order-order transitions or order-disorder transitions in the range 25-150 °C (Figure A2.2). In all cases, we observed no order-order transitions or order-disorder transitions in this temperature range and only minor deviations in domain spacing.

Two complementary films of PS-*b*-PVBnHexImTFSI-8.6 prepared via solvent-casting and melt-pressing exemplify differences between these preparation techniques. The solvent-cast film exhibits coexistence between lamellar and hexagonally packed cylindrical morphologies sharing a single, slightly broadened primary scattering peak. Simone and Lodge saw similar coexistence phases in PS-*b*-PEO diblock copolymers preferentially swelled with ionic liquid where cylinders/lamellae coexistence was observed in place of gyroid morphology due to high segregation strength.[26] The lamellar morphology is evidenced by higher order reflections at 2q*, 4q*, and 5q* with structure factor extinctions of 3q* and 6q* suggesting an apparent 33% volume composition of the ionic block.[39] The higher order reflections indicative of hexagonally packed cylindrical morphology are also seen at q*√3, 2q*, q*√7, and 3q*. Domain spacings of the cylinders and lamellae are 37 nm and 35 nm, respectively, which is roughly consistent with the expected epitaxial relationship between these two phases. An expansion of the azimuthally integrated SAXS pattern for this film is provided in the Appendix 2 (Figure A2.3). Confirmation of phase coexistence is provided by transmission electron microscopy (TEM), in which both hexagonally-packed cylinders and lamellar grains are observed (Figure 3.4.a). In contrast, the SAXS profile of PS-*b*-PVBnHexImTFSI-8.6 prepared by melt-pressing exhibits broad features

consistent with poorly-ordered hexagonally packed cylinders morphology, although coexistence with lamellae cannot be ruled out due to the broad SAXS scattering maxima. A broad primary scattering peak is accompanied by a peak spanning q*√3 and 2q* and another shoulder spanning q*√7 and 3q*. Similar to the solvent-cast sample, TEM studies show that this sample exhibits a coexistence of lamellar and cylindrical morphologies with a low degree of long-range order (Figure 3.4.b). A difference in domain spacing (34 nm) relative to that seen for the solvent-cast sample (37 nm) is likely due to sample anisotropy induced by the melt-pressing process (Figure A2.1).

Moving to lower POIL compositions, the SAXS profiles of melt-pressed PS-*b*-PVBnHexImTFSI-7.1 and PS-*b*-PVBnHexImTFSI-2.7 exhibit fewer features, making assignment of morphology more difficult. The similar profiles of these two films suggest poorly ordered hexagonally packed cylinders morphology as evidenced by broad primary scattering peaks with broad higher order peaks spanning q*√7 and 3q*. The assignment of a hexagonally packed cylindrical morphology was confirmed with TEM (Figure 3.4.c). A striking feature of these SAXS profiles is that the primary scattering peaks are significantly shifted to lower *q*, corresponding to an increased domain spacing (cylinder center-to-center distance) of 42 nm. We propose that this shift is due to swelling of the polystyrene domains by chains having little or no POIL incorporation, as a consequence of the synthetic route used to produce these materials. In the synthesis of the PS-*b*-PVBCl from which we derive our PS-POIL block copolymers, we polymerized the VBCl to relatively low monomer conversions. At such low monomer conversions, controlled living radical polymerizations initially yield materials with high polydispersities that only narrow as the polymerization progresses.[35] Thus the high

polydispersities of the PVBCl blocks of the PS-POIL precursors imply that there are a substantial number of chains that have few (if any) VBCl units, which translates into a substantial number of PS-POIL chains containing one or fewer POIL monomer units.[40] These POIL-deficient chains act as PS homopolymers that swell the polystyrene domains, thus giving rise to the observed increase in domain spacing for these samples.

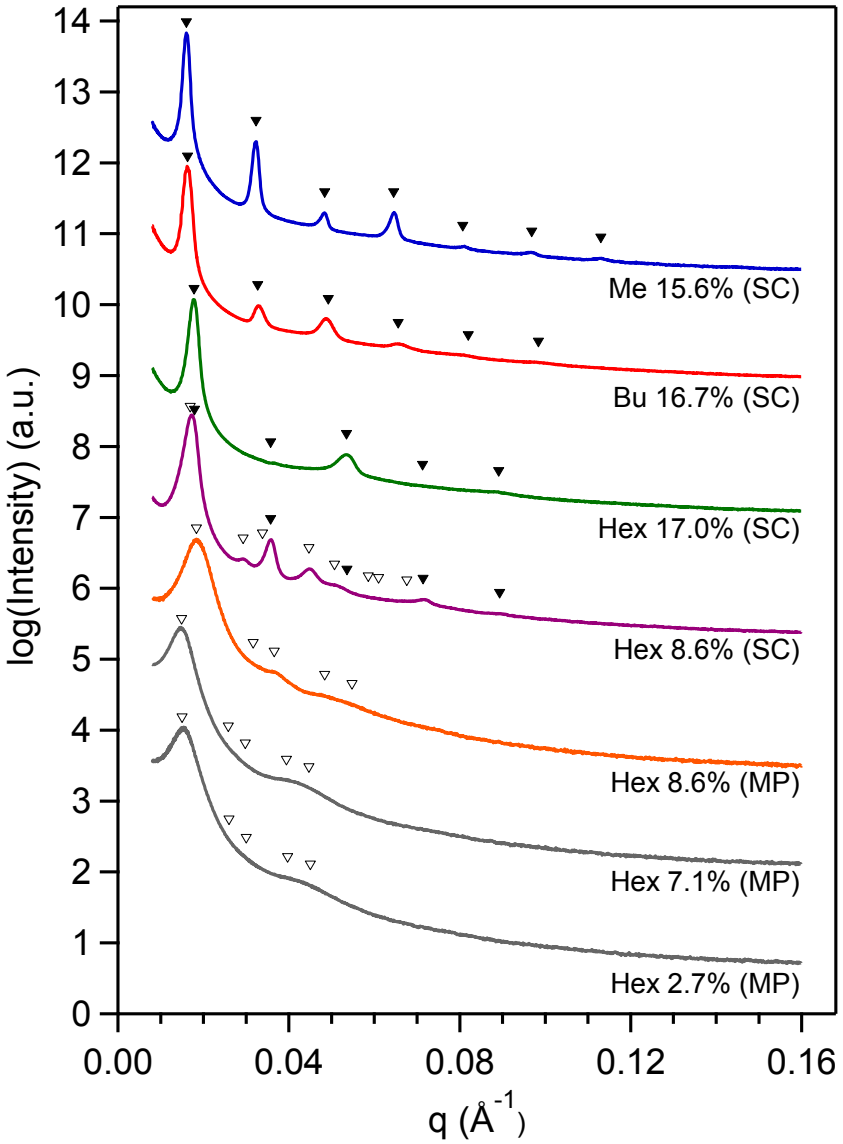

Figure 3.3. Azimuthally-integrated SAXS profiles of PS-*b*-PVBn(alkyl)ImTFSI block copolymer films at 25 °C; each trace is labeled by the imidazolium alkyl substituent, POIL mole fraction, and processing method (SC = solvent cast; MP = melt-pressed). Solid and open arrows indicate reflections associated with lamellar (▼-LAM) and hexagonally-packed cylinders (▽-CYL) morphologies, respectively.

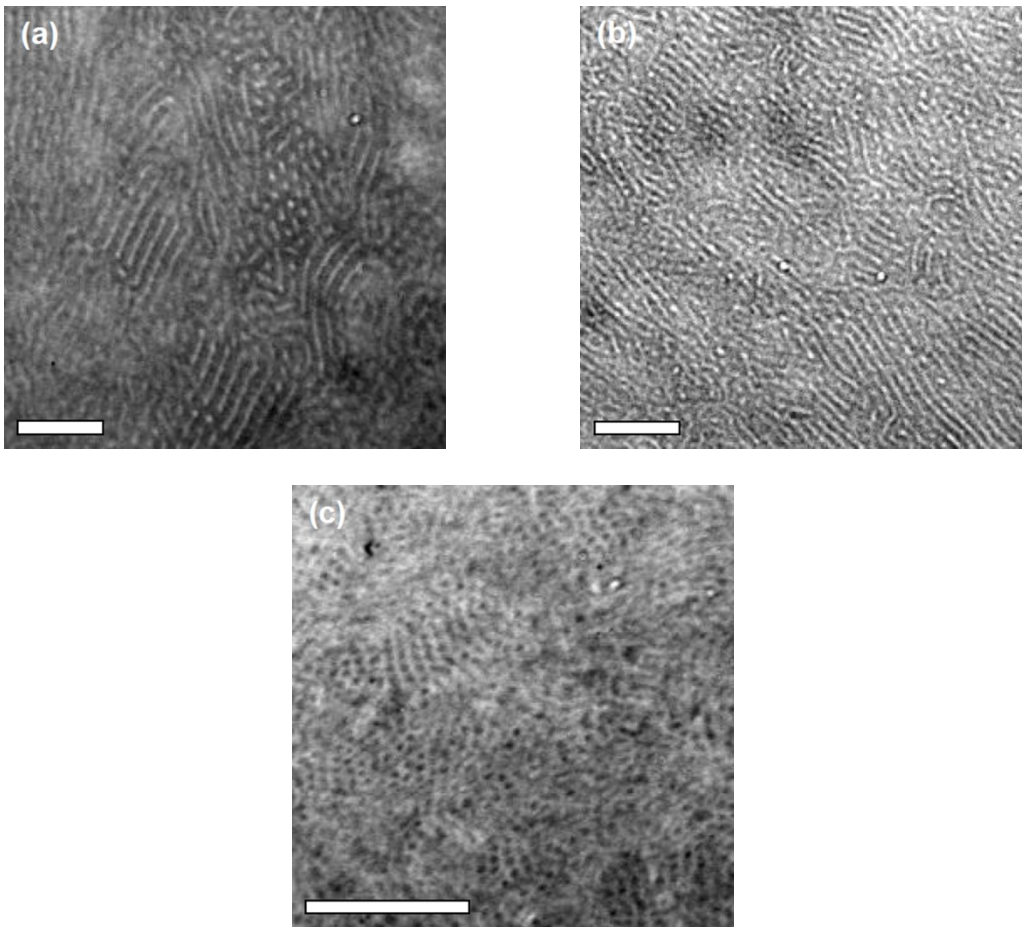

Figure 3.4. TEM images of (a) cylinders/lamellae phase coexistence exhibited by solvent-cast PS-*b*-PVBnHexImTFSI-8.6 in which the PS domains stained with RuO_4 appear dark, scale bar is 200 nm; (b) the cylinders/lamellae phase coexistence exhibited by melt-pressed PS-*b*-PVBnHexImTFSI-8.6 in which the PS domains stained with RuO_4 appear dark, scale bar is 200 nm; and (c) the hexagonally packed cylindrical morphology in melt-pressed PS-*b*-PVBnHexImTFSI-7.1 wherein the PVBnHexImTFSI domains appear dark due to the natural electron density contrast, scale bar is 500 nm.

The domain spacings for microphase separated POIL block copolymers (Table 3.2) suggest that a high degree of conformational asymmetry exists in the block copolymer melts consistent with a strongly segregated system in which the POIL segments exhibit high degrees of chain-stretching. The block copolymers exhibit domain spacings in the range of 34-42 nm, which is comparable to the calculated contour length of a fully extended chain (47-55 nm), suggesting that chains are highly stretched. Stancik *et al.* also observed high levels of chain stretching in PS-POIL block copolymers in neutron scattering studies of PS-*b*-PVBnMeImX (X = Cl, BF_4) that form elongated micelles.[37]

3.3.3 Ionic Conductivity.

Effect of Alkyl Chain Length. Figure 3.5 shows the effect of alkylimidazolium chain length (alkyl = CH_3 (Me), *n*-C_4H_9 (Bu), or *n*-C_6H_{13} (Hex)) on the temperature-dependent in-plane ionic conductivity of the POIL diblock copolymer. All three polymers shown in Figure 3.5 have a similar morphology (lamellar), glass transition temperature of the POIL block (9 ºC), POIL composition (15.6-17.0 mol%), and molecular weight (38.0-40.7 kg mol^{-1}) (Table 3.2). From these data it is clear that when all of these parameters are the same, the resulting ionic conductivities are similar.

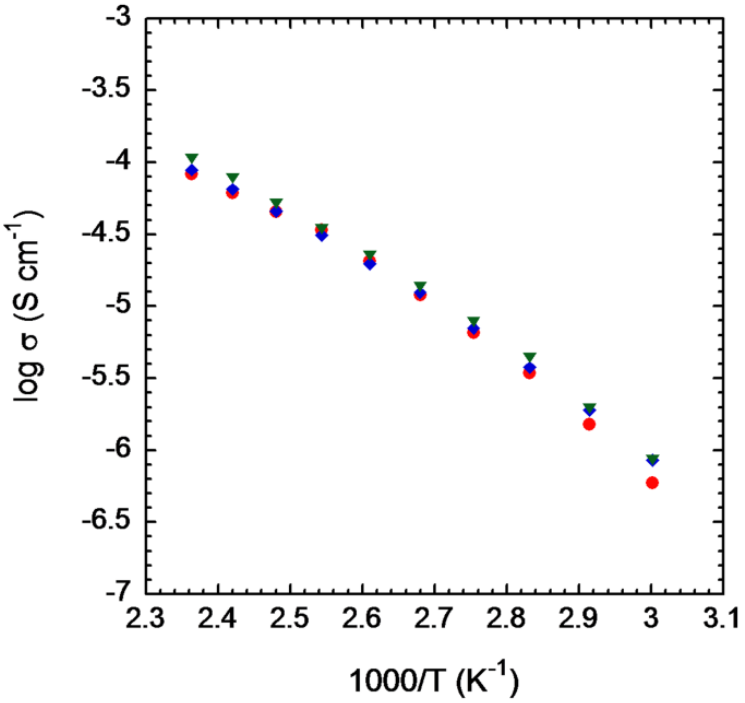

Figure 3.5. Effect of alkyl chain length on the temperature-dependent ionic conductivity of POIL diblock copolymers: PS-*b*-PVBnMeImTFSI-15.6 (●), PS-*b*-PVBnBuImTFSI-16.7 (◆), PS-*b*-PVBnHexImTFSI-17.0 (▼).

Effect of Composition and Morphology. Figure 3.6 shows the temperature-dependent ionic conductivity of PS-*b*-PVBnHexImTFSI as a function of copolymer composition ranging from 8.6 to 100 mol% POIL. Lower POIL block compositions (7.1 mol% and 2.7 mol%) were too resistive to report accurate conductivity values. Since these samples exhibiting hexagonally packed cylindrical morphology have a low degree of long-range order, their poor in-plane ionic conductivity likely stems from numerous morphological defects and large numbers of grain boundaries that serve as "dead ends" for conductive channels (i.e., poor long-range ionic domain connectivity throughout the film). It is clear that the ionic conductivity increases significantly with increasing POIL block composition; however, it does so in a nonlinear fashion. Specifically,

the in-plane conductivity increases by more than an order of magnitude when the POIL block composition is changed only two-fold from 8.6 mol% POIL to 17.0 mol% POIL and increases approximately five-fold when the POIL block composition is changed from 17.0 mol% POIL to 100 mol% POIL homopolymer. Since the nanoscale morphologies of the 8.6 mol% POIL and the 17.0 mol% POIL block copolymers are a coexistence of cylinders and lamellae (where the POIL block is the minor component) and pure lamellae, respectively, we speculate that the nonlinear relationship between ionic conductivity and POIL block composition must be due to morphological effects.

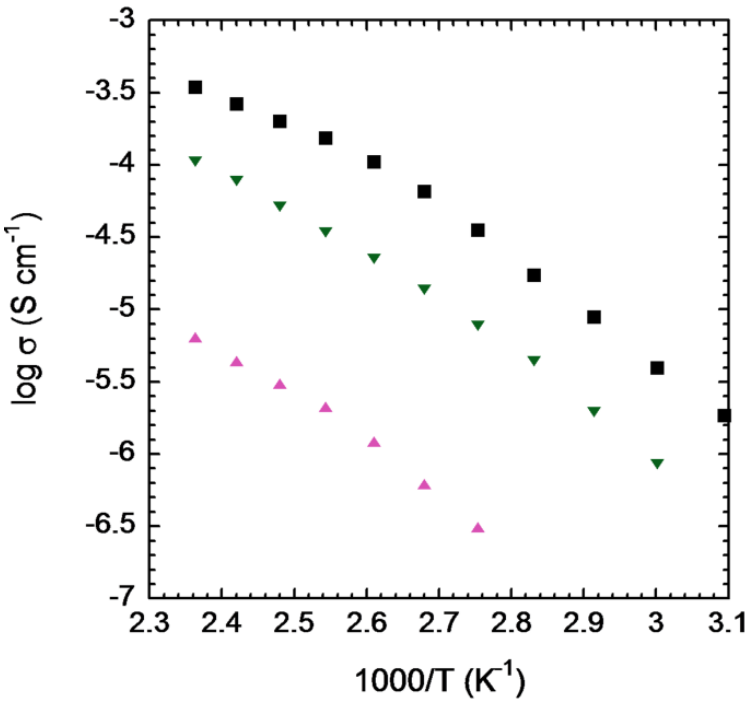

Figure 3.6. Effect of composition on the temperature-dependent ionic conductivity of POIL diblock copolymers: PVBnHexImTFSI (■), PS-*b*-PVBnHexImTFSI-17.0 (▼), PS-*b*-PVBnHexImTFSI-8.6 (▲).

To account for the effects of morphology on ionic conductivity for a diblock copolymer that consists of one conducting component and one non-conducting component, Balsara and co-workers proposed a normalized ionic conductivity or a morphology factor, f:[24]

$$f = \frac{\sigma}{\phi_c \sigma_c} \tag{3.1}$$

where σ is the measured conductivity and ϕ_c and σ_c are the volume fraction and intrinsic conductivity of the conducting phase, respectively. Here, the ionic conductivity of homopolymer (PVBnHexImTFSI) was used as σ_c. Figure 3.7 compares the normalized conductivity for the block copolymer samples with a lamellar (17.0 mol%) and lamellar + cylindrical (8.6 mol%) morphology, corresponding to ϕ_c = 0.50 and 0.34, respectively (see Appendix 2 for detailed volume fraction calculations). For the 17.0 mol% sample, the normalized in-plane conductivity ranges from 0.41 to 0.61, which is smaller than the predicted morphology factor, f = 2/3, for randomly oriented lamellae,[24,41] suggesting that this sample has additional resistances that contribute to slightly less than ideal conductivities (e.g., grain boundaries). Figure 3.7 also shows that in the temperature range below 100 ºC, the normalized conductivity is ~0.42. However, above 100°C, the normalized conductivity increases from ~0.42 to ~0.61. Interestingly, 100ºC corresponds to the glass transition temperature of the styrene block, suggesting that the glass-liquid transition of the non-conducting microphase can impact ionic conductivity. A similar phenomenon was observed in previous work in ionic liquid-doped block copolymers.[27] For the 8.6 mol% sample, the normalized conductivity ranges from 0.03 to 0.05, which is an order of magnitude smaller than the predicted morphology factor, f = 1/3, for randomly oriented conducting cylinders.[24,41] Since this sample exhibits coexistence between lamellae and cylinders,

one would predict *f* to be an intermediate value between that expected for cylinders and lamellae ($1/3 < f < 2/3$). This probably results from a lack of macroscopic connectivity of cylindrical micro-domains across the film or other morphological defects that significantly limit ion conduction.

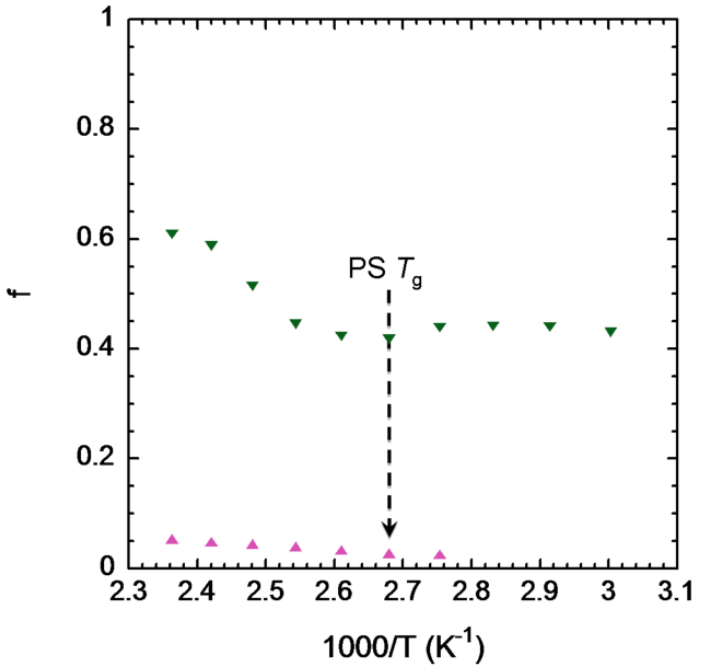

Figure 3.7. Plot of the normalized ionic conductivity or morphology factor *f* as a function of temperature for PS-b-PVBnHexImTFSI-17.0 (▼) and PS-b-PVBnHexImTFSI-8.6 (▲) that emphasizes the effects of morphology and defects on block copolymer conductivity and highlights an increase in the conductivity of PS-*b*-PVBnHexImTFSI-17.0 near the glass transition temperature of poly(styrene).

For the ionic conductivity data presented thus far, all of the polymer films were prepared by solvent casting. To examine the sole effect of morphology on ionic conductivity, the

conductivity of the POIL diblock copolymer at a single POIL composition (8.6 mol%) was measured using two different film preparation techniques: solvent casting and melt pressing. Figure 3.8 shows the results, where the solvent-cast film, which exhibits good long-range order, has a conductivity approximately one order of magnitude higher than the more poorly ordered melt-pressed film. This result again exemplifies the importance of high degrees of connectivity among conducting domains, as morphological defects and grain boundaries serve as effective "dead ends" for ion conduction.

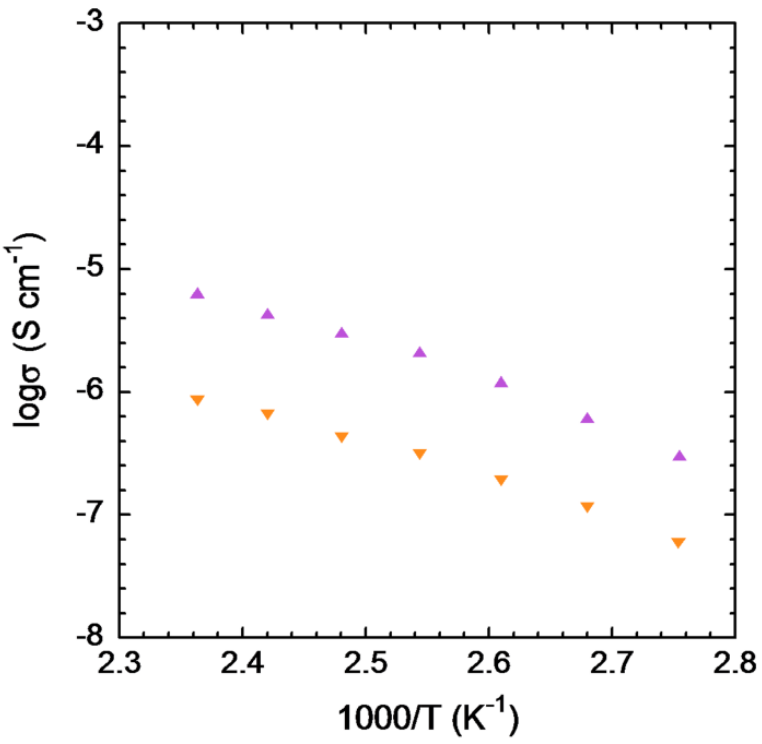

Figure 3.8. Temperature-dependent ionic conductivity for PS-*b*-PVBnHexImTFSI-8.6 films prepared by solvent-casting (▲) and melt-pressing (▼).

3.4 Conclusion

We synthesized a series of PS-*b*-PVBn(alkyl)ImTFSI diblock copolymers with varying compositions by post-polymerization functionalization of PS-*b*-PVBCl with homologous *N*-alkylimidazoles (alkyl = CH_3, *n*-C_4H_9, and *n*-C_6H_{13}). The block copolymers microphase separate into cylinders, lamellae, or coexistence of cylinders + lamellae with varying degrees of long-range order depending on their composition and film-preparation technique (solvent-casting *vs* melt-pressing). Lamellar samples with similar compositions exhibited comparable values of conductivity (~0.1 mS cm^{-1} at 150°C) regardless of imidazolium alkyl substituent. For a compositionally varied series of PS-*b*-PVBnHexImTFSI diblocks, conductivity was dependent on POIL composition, morphology, and degree of long range order. For a lamellar sample (17.0 mol% POIL), conductivity was approximately 5-fold less than for the corresponding homopolymer. Moreover, in comparing a lamellar sample (17.0 mol%) to a lamellar + cylindrical coexistence sample (8.6 mol%), conductivity dropped off by more than an order of magnitude, indicating the potential for cylindrical domains to suffer from morphological defects and grain boundaries that decrease macroscopic connectivity and impede conductivity. Two films of a single sample (8.6 mol%) prepared by different techniques exemplified the importance of long range order to achieve high conductivity, as the well-ordered solvent-cast film exhibited conductivities one order of magnitude greater than the poorly ordered melt-pressed film. Low POIL composition samples (2.7 and 7.1 mol% POIL) having poorly-ordered cylindrical morphology exhibited low conductivities below the measurement detection limit due to a large number of morphological defects (e.g., grain boundaries and “dead ends”). It is evident from this work that the conductivity of microphase separated ion conducting membranes are dependent on

nanoscale morphology, specifically, the degree of connectivity of ionic domains. In particular, samples exhibiting hexagonally packed cylindrical morphology with a minority conducting phase ($\phi_{POIL} < 0.5$) suffer from poor ionic conductivity due to their propensity for morphological defects and grain boundaries.

3.5 References

(1) Kim, J.-H.; Kim, J.-W.; Shokouhimehr, M.; Lee, Y.-S. *J. Org. Chem.* **2005**, *70*, 6714.

(2) Yang, X.; Fei, Z.; Zhao, D.; Ang, W. H.; Li, Y.; Dyson, P. J. *Inorg. Chem.* **2008**, *47*, 3292.

(3) Yuan, J. Y.; Giordano, C.; Antonietti, M. *Chem. Mater.* **2010**, *22*, 5003.

(4) Bara, J. E.; Camper, D. E.; Gin, D. L.; Noble, R. D. *Acc. Chem. Res.* **2010**, *43*, 152.

(5) Bara, J. E.; Noble, R. D.; Gin, D. L. *Ind. Eng. Chem. Res.* **2009**, *48*, 4607.

(6) Tang, J. B.; Shen, Y. Q.; Radosz, M.; Sun, W. L. *Ind. Eng. Chem. Res.* **2009**, *48*, 9113.

(7) Tang, J.; Tang, H.; Sun, W.; Plancher, H.; Radosz, M.; Shen, Y. *Chem. Commun.* **2005**, 3325.

(8) Green, O.; Grubjesic, S.; Lee, S.; Firestone, M. *Polym. Rev.* **2009**, *49*, 339.

(9) Armand, M.; Endres, F.; MacFarlane, D. R.; Ohno, H.; Scrosati, B. *Nat. Mater.* **2009**, *8*, 621.

(10) Lodge, T. P. *Science* **2008**, *321*, 50.

(11) Gu, Y.; Lodge, T. P. *Macromolecules* **2011**, *44*, 1732.

(12) Zhang, S.; Lee, K. H.; Frisbie, C. D.; Lodge, T. P. *Macromolecules* **2011**, *44*, 940.

(13) Yoshizawa, M.; Ohno, H. *Electrochim. Acta* **2001**, *46*, 1723.

(14) Chen, H.; Choi, J.-H.; Salas-de la Cruz, D.; Winey, K. I.; Elabd, Y. A. *Macromolecules* **2009**, *42*, 4809.

(15) Ye, Y.; Elabd, Y. A. *Polymer* **2011**, *52*, 1309.

(16) Clark, T. J.; Robertson, N. J.; Kostalik IV, H. A.; Lobkovsky, E. B.; Mutolo, P. F.; Abruña, H. D.; Coates, G. W. *J. Am. Chem. Soc.* **2009**, *131*, 12888.

(17) Robertson, N. J.; Kostalik IV, H. A.; Clark, T. J.; Mutolo, P. F.; Abruña, H. D.; Coates, G. W. *J. Am. Chem. Soc.* **2010**, *132*, 3400.

(18) Varcoe, J. R.; Slade, R. C. T.; Lam How Yee, E. *Chem. Commun.* **2006**, 1428.

(19) Sun, X. G.; Kerr, J. B. *Macromolecules* **2006**, *39*, 362.

(20) Matsumoto, K.; Endo, T. *Macromolecules* **2009**, *42*, 4580.

(21) Matsumoto, K.; Endo, T. *J. Polym. Sci., Part A: Polym. Chem.* **2010**, *48*, 3113.

(22) Elabd, Y. A.; Hickner, M. A. *Macromolecules* **2011**, *44*, 1.

(23) Wang, X.; Goswami, M.; Kumar, R.; G. Sumpter, B.; Mays, J. *Soft Matter* **2012**, *8*, 3036.

(24) Wanakule, N. S.; Panday, A.; Mullin, S. A.; Gann, E.; Hexemer, A.; Balsara, N. P. *Macromolecules* **2009**, *42*, 5642.

(25) Teran, A. A.; Mullin, S. A.; Hallinan, D. T.; Balsara, N. P. *ACS Macro Letters* **2012**, *1*, 305.

(26) Simone, P. M.; Lodge, T. P. *ACS Appl. Mater. Interfaces* **2009**, *1*, 2812.

(27) Gwee, L.; Choi, J.-H.; Winey, K. I.; Elabd, Y. A. *Polymer* **2010**, *51*, 5516.

(28) Weber, R. L.; Ye, Y. S.; Schmitt, A. L.; Banik, S. M.; Elabd, Y. A.; Mahanthappa, M. K. *Macromolecules* **2011**, *44*, 5727.

(29) Ye, Y.; Choi, J.-H.; Winey, K. I.; Elabd, Y. A. *Macromolecules* **2012**, *45*, 7027.

(30) Lee, M.; Choi, U. H.; Colby, R. H.; Gibson, H. W. *Chem. Mater.* **2010**, *22*, 5814.

(31) Hoshino, K.; Yoshio, M.; Mukai, T.; Kishimoto, K.; Ohno, H.; Kato, T. *J. Polym. Sci., Part A: Polym. Chem.* **2003**, *41*, 3486.

(32) Weber, R. L.; Ye, Y. S.; Banik, S. M.; Elabd, Y. A.; Hickner, M. A.; Mahanthappa, M. K. *J. Polym. Sci., Part B: Polym. Phys.* **2011**, *49*, 1287.

(33) Armarego, W. L. F.; Chai, C. L. L. *Purification of laboratory chemicals*; 5th ed.; Butterworth-Heinemann: Amsterdam ; Boston, 2003.

(34) Pernak, J.; Feder-Kubis, J.; Cieniecka-Roslonkiewicz, A.; Fischmeister, C.; Griffin, S. T.; Rogers, R. D. *New J. Chem.* **2007**, *31*, 879.

(35) Benoit, D.; Chaplinski, V.; Braslau, R.; Hawker, C. J. *J. Am. Chem. Soc.* **1999**, *121*, 3904.

(36) Alyea, H. N. *J. Chem. Educ.* **1971**, *48*, 389.

(37) Stancik, C. M.; Lavoie, A. R.; Schütz, J.; Achurra, P. A.; Lindner, P.; Gast, A. P.; Waymouth, R. M. *Langmuir* **2004**, *20*, 596.

(38) Park, M. J.; Balsara, N. P. *Macromolecules* **2010**, *43*, 292.

(39) Roe, R. J. *Methods of X-ray and neutron scattering in polymer science*; Oxford University Press: New York, 2000.

(40) Lynd, N. A.; Hillmyer, M. A. *Macromolecules* **2005**, *38*, 8803.

(41) Sax, J.; Ottino, J. M. *Polym. Eng. Sci.* **1983**, *23*, 165.

CHAPTER 4

POLYMERIC LITHIUM SINGLE-ION CONDUCTORS FOR USE AS NEW LITHIUM ION BATTERY ELECTROLYTES

4.1 Introduction

Lithium ion batteries are a cornerstone of modern energy storage technology, with applications ranging from hand-held electronics to electric vehicles.[1,2] Essential to all lithium ion batteries is an electrolyte that shuttles lithium ions between the two electrodes. Most commercial battery electrolytes are comprised of lithium salts dissolved in alkyl carbonates and other organic solvents. However, solid polymer and polymer gel electrolytes represent enticing alternatives due to their reduced flammability and increased mechanical strength that may potentially mitigate electromechanical stresses and dendrite formation.[3] Much of the current research on polymeric electrolyte materials focuses on lithium salts dissolved in poly(ethylene oxide) (PEO) homopolymers and block copolymers.[4,5] These materials exhibit two major drawbacks: (1) their electrochemical window is limited (< 4 V *vs.* Li/Li^+), which prevents their use with advanced cathode and anode materials for high voltage and high capacity batteries, and (2) lithium ion mobility is limited relative to the counter-anions due to strong chelation of lithium by the polyether chains.[6,7] This chelation leads to a substantial decrease in the fraction of the total current in the cell carried by Li^+ cations, known as the transference number (t_{Li+}). The transference number is defined as the fraction of current carried by lithium ions in relation to the current carried by all ions through the electrolyte. The transference number is typically in the range of 0.2-0.4 in PEO-based electrolytes, resulting in substantial potential losses in the cell.[8,9]

Polymers with non-coordinating anionic moieties tethered along the chain with lithium counterions, known as lithium single-ion conductors, are expected to have transference numbers, $t_{Li+} \approx 1.0$ by virtue of effective immobilization of anionic groups. Previously reported polymeric lithium salts with carboxylate,[10,11] sulfonate,[12-15] sulfonylimide,[16-19] and alkoxyborate[20-24] counterions suffer from narrow electrochemical windows, poor ionic conductivities, and tedious syntheses. Lithium bis(oxalate)borate (LiBOB) and lithium bis(malonato)borate (LiBMB) (Figure 4.1) are two attractive candidates for the development of oxidatively stable polymeric single-ion conductors, due to their high degree of dissociation in alkyl carbonate solvents and their wide electrochemical stability windows (stable to 4.5 V vs. Li/Li^+).[25]

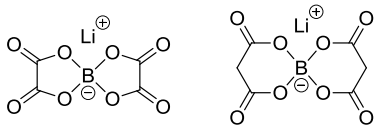

Figure 4.1. Chemical structures of lithium bis(oxolato)borate (LiBOB) and lithium bis(malonato)borate (LIBMB).

Kerr and coworkers have relatively recently studied the incorporation of lithium bis(malonato)borate (LiBMB) groups into crosslinked PEO networks.[26,27] Electrode polarization studies demonstrated the lithium single-ion conducting nature of these new materials. However, these materials suffer from low conductivities, likely due to the low lithium ion concentrations in the polymers coupled with cation chelation by the polyether matrix. While these materials demonstrate some promise, few attempts to develop and to optimize related systems have been reported.[28,29]

Herein we describe the synthesis, molecular characterization, and initial electrochemical characterization of a new polymeric lithium single-ion conductor in which bis(malonato)borate groups are embedded into a linear hydrocarbon backbone. When dissolved in propylene carbonate ([Li^+] = 0.2 M), the polymeric lithium salt exhibits high Li^+ ion conductivity of $\sigma = 2.4 \times 10^{-5}$ S cm^{-1} at 22 °C and the formation of a stable solid electrolyte interphase upon electrochemical cycling to confer a wide electrochemical window of at least 0.05 to 8.0 V *vs.* Li/Li^+. We also describe efforts to internally plasticize these bis(malonato)borate-containing polymers through the incorporation of more flexible linkers between the anionic moieties using thiol-ene polymerization reactions. These efforts yielded candidate materials that exhibit lower glass transition temperatures, T_g, which could lead to optimized materials including solvent-free lithium single-ion conductors.

4.2 Experimental

Materials. All chemicals were purchased from Sigma-Aldrich Chemical Company (Milwaukee, WI) and were used as received unless otherwise noted. $LiBF_4$ was purchased from Strem Chemicals, Inc. (Newburyport, MA) and was dried under vacuum at 85 °C overnight and subsequently stored under nitrogen. Diisopropylamine, hexamethylphosphoramide (HMPA), acetonitrile, and propylene carbonate were distilled from CaH_2, degassed by three freeze-thaw cycles, and stored under nitrogen. Acetone was distilled from $CaSO_4$, degassed by three freeze-thaw cycles, and stored under nitrogen. 1,6-Hexanedithiol was distilled under reduced pressure, degassed by three freeze-thaw cycles, and stored under nitrogen. 2.5 M *n*-Butyllithium in hexanes was titrated against diphenylacetic acid in THF.[30] Dry pentane was obtained by stirring

over anhydrous $MgSO_4(s)$ followed by filtering. 2,2′-(Ethylenedioxy)diethanethiol (triethyleneglycol-1,8-dithiol) was purified by passage through a plug of activated silica under inert atmosphere. Anhydrous and anaerobic THF and toluene were obtained by sparging analytical grade solvent with nitrogen for 30 minutes, followed by cycling through a column of activated alumina in a Vacuum Atmospheres Solvent purification system.

NMR Spectroscopy. ^{1}H and ^{13}C NMR spectra were recorded on Varian Inova 500, Varian Mercury Plus 300, or Bruker AC+ 300, or Bruker Avance 400 spectrometers and were referenced relative to the residual protiated solvent peak.

Mass Spectrometry. Mass Spectrometry was performed using a Waters (Micromass) LCT® electrospray ionization time-of-flight mass spectrometer operating in either negative or positive ion detection mode. Samples dissolved in methanol were electrosprayed with a sample cone voltage of 20 V.

Size Exclusion Chromatography (SEC). The molecular weight and molecular weight distribution of poly(lithium bis(non-8-enyl-malonato) borate) was determined by SEC using a Waters system comprised of a Waters 515 HPLC pump with a Rheodyne 7725i manual injector, a Waters temperature control module, and a Waters 2410 refractive index (RI) detector. Separations employed two Viscotek (Houston, TX) ViscoGEL I-Series columns (I-MBLMW-3078 & I-MBHMW-3078) (30 cm x 7.8 mm) using a *N*,*N*-dimethylformamide / 0.1 M LiBr eluent at a flow rate of 1.0 mL min^{-1} at 70 °C. The reported number average molecular weight (M_n) and molecular weight distribution ($Đ = M_w/M_n$) were measured using a conventional poly(ethylene oxide) calibration curve that was constructed using twelve narrow molecular weight distribution standards having M_n = 106-1,258,000 g mol^{-1} (Agilent Technologies).

SEC analyses of the remaining linear polymers were conducted on a home-built system with a Waters 410 Differential Refractometer. Separations employed two Polymer Labs PolyPore columns (30 cm x 7.5 mm) using a *N*,*N*-dimethylformamide / 0.1 M LiBr eluent at a flow rate of 0.8 mL min^{-1}, with the columns and detector thermostatted at 70°C and 50°C respectively. The number average molecular weight (M_n) and molecular weight distributions (M_w/M_n) are reported against a conventional poly(styrene) calibration curve constructed using ten narrow molecular weight PS standards (M_n = 580 – 377,400 g mol^{-1}, Polymer Laboratories). Data was acquired using a NI USB-6008 DAQ and a custom LabView (National Instruments) interface written by Adam Schmitt. Data reduction employed custom procedures written in Igor Pro written by Adam Schmitt.

Elemental Analysis. Elemental analyses were conducted at Columbia Analytical Services (Tucson, AZ, USA) using standard combustion analysis with infrared and thermal conductivity detection for carbon and hydrogen content. Inductively coupled plasma-optical emission spectrometry (ICP-OES) was used to quantify the lithium content where reported.

Thermogravimetric Analysis (TGA). The thermal stability of poly(lithium bis(non-8-enyl-malonato) borate) was measured on a TA Instruments Q500 Thermogravimetric Analyzer using a ramp rate of 2 °C min^{-1} with under an $N_2(g)$ purge (50 mL min^{-1}) over a temperature range 25-550 °C.

Differential Scanning Calorimetry (DSC). Thermal transition temperatures were measured using a TA Instruments Q100 modulated differential scanning calorimeter under nitrogen atmosphere. The thermal history of samples hermetically sealed in aluminum pans was erased by heating to 180 °C for three minutes and cooling to -40 °C at a ramp rate of 10 °C

min^{-1}. Reported data are derived from the second heating curves, which were recorded over a temperature range of -40 °C to 180 °C with a heating ramp rate of 5 °C min^{-1}.

Electrochemical Impedance Spectroscopy. The ionic conductivities of poly(LiBNMB) and LiTFSI in anhydrous and anaerobic propylene carbonate were measured by electrochemical impedance spectroscopy using a Solartron 1287 Electrochemical Interface and 1260 Impedance Analyzer equipped with the Zplot software. All measurements employed a frequency range $\omega = 0.1 – 10^5$ Hz, with an AC amplitude of 10 mV and a DC offset of 0 mV *vs.* open circuit potential. Electrolyte solutions were prepared under argon in a glovebox by dissolving an appropriate amount of the desired Li-salt in propylene carbonate solution to obtain a final electrolyte composition with a concentration $[Li^+] = 0.2$ mol L^{-1}. The solutions were loaded into a custom-made, hermetically sealed, Teflon cell with symmetric lithium foil electrodes. (Appendix 3, Figure A3.1) The surface area of each electrode was 0.025 cm^2 with a 0.487 cm distance between electrodes. The high frequency non-capacitive plateau of the Bode plot (total impedance, $|Z|$ *vs.* frequency, ω, where $|Z|$ is the sum of the absolute values of the real impedance, Z', plus the imaginary impedance, Z'') was taken as the electrolyte solution resistance, while the total resistance was determined by the low frequency non-capacitive plateau of the same plot. From these resistances, the conductivity was calculated as $\sigma = L / AR$, where L is the distance between electrodes and A is the cross-sectional area of the electrodes.

Cyclic Voltammetry (CV). The electrochemical stabilities of poly(LiBNMB) and LiTFSI were measured by cyclic voltammetry using a Gamry PCI4/300 Potentiostat/Galvanostat/Zero Resistance Ammeter, with data reduction in the Gamry Framework & Echem Analyst software. CV measurements were conducted in the potential range

0.05–8.0 V *vs.* Li/Li^+, using a platinum working microelectrode and a lithium foil counter electrode submerged in the electrolyte. Electrolyte solutions were prepared under argon in a glovebox by dissolving an appropriate amount of either poly(LiBNMB) or LiTFSI in propylene carbonate solution to obtain a final electrolyte composition with a concentration $[Li^+] = 0.2$ mol L^{-1}. Starting at open circuit potential (~ 3 V *vs.* Li/Li^+), anodic sweeps scanned between 7 V and 2 V at 10 mV sec^{-1}. Cathodic sweeps started at open circuit potential and scanned between 0.05 V and 3 V at 10 mV sec^{-1}. Full sweeps started at open circuit potential and scanned between 8 V and 0.2 V at 1 V sec^{-1}.

Synthesis of non-8-enyl-malonic acid (1). An oven-dried 500 mL 2-neck flask equipped with magnetic stirbar and addition funnel was charged with diisopropylamine (12.8 mL, 91.1 mmol) and THF (180 mL) under nitrogen. After chilling the solution to -25 °C in a dry ice water/ethanol (1:1 v/v) bath, *n*-butyllithium (34 mL of a 2.65 M solution in hexanes, 89.0 mmol) was added dropwise via addition funnel. The solution was stirred for 30 min, after which a degassed solution of undecenoic acid (8.0 g, 43.4 mmol) in THF (44 mL) was added dropwise via addition funnel, causing the solution to become turbid. Upon addition of HMPA (8 mL, 43.4 mmol) via addition funnel, the cooling bath was removed, and the reaction was warmed to room temperature over 30 min to yield a clear, yellow enolate solution. The solution was then cooled again to -25 °C. A second 500 mL 2-neck flask under $N_2(g)$ purge was charged with $CO_2(s)$ (200 g, 4.5 mol) and chilled to -25 °C. The enolate solution was cannula transferred onto the $CO_2(s)$ under $N_2(g)$ purge to yield a clear solution. After stirring at -25 °C for 30 minutes, the cooling bath was removed and the reaction was stirred at 22 °C overnight, during which time the reaction gelled. The reaction was quenched by the addition of 10% HCl(*aq*) (100 mL), causing two layers

to form, then transferred to a separatory funnel. The organic layer was collected and the aqueous layer was extracted with ether (3x75 mL). The organic layers were combined and then washed successively with 2M HCl(*aq*) (3x50 mL), water (75 mL), saturated NaCl(*aq*) (75 mL), and then dried over anhydrous $MgSO_4(s)$. The solvent was removed on a rotary evaporator to yield 9.5 g of white solid. The crude product was recrystallized from heptane to yield white crystals. Yield: 9.07 g (92% yield). ^{1}H NMR (300 MHz, DMSO-d_6, 22 °C): δ (ppm) 12.62 (s, 2H, CH(COO*H*)$_2$), 5.78 (ddt, $J_{H\text{-}H}^3$ = 17.0, 10.3, 6.8 Hz, 1H, CH_2=C*H*CH_2), 4.98 (ddt, $J_{H\text{-}H}^3$ = 17.2, 1.6 Hz, $J_{H\text{-}H}^2$ = 2.2 Hz, 1H, C*H*$_2$=$CHCH_2$), 4.93 (ddt, $J_{H\text{-}H}^3$ = 10.2, 1.2 Hz, $J_{H\text{-}H}^2$ = 2.3 Hz, 1H, C*H*$_2$=$CHCH_2$), 3.17 (t, $J_{H\text{-}H}^3$ = 7.5 Hz, 1H, C*H*$(COOH)_2$), 2.00 (dt, $J_{H\text{-}H}^3$ = 7.0, 6.8 Hz, 2H, CH_2=CHC*H*$_2$), 1.73–1.63 (m, 2H, C*H*$_2$CH$(COOH)_2$), 1.40–1.16 (m, 10H, CH_2=$CHCH_2$(C*H*$_2$)$_5CH_2$CH$(COOH)_2$). ^{13}C NMR (75 MHz, DMSO-d_6, 22 °C): δ (ppm) 170.90, 138.82, 114.64, 51.60, 33.18, 28.69, 28.64, 28.41, 28.24, 26.79. ESI-MS: calcd. for $C_{12}H_{20}O_4Na$ $[M+Na]^+$ 251.1, found 251.1.

Synthesis of non-8-enyl-malonic acid trimethylsilyl ester (2). An oven-dried 200 mL Schlenk flask was charged with a magnetic stirbar, imidazole (5.04 g, 73.58 mmol), and THF (70 mL) under nitrogen. Trimethylsilyl chloride (11.5 mL, 87.60 mmol) was added via syringe to form a white precipitate. A degassed solution of non-8-enyl-malonic acid (8.0 g, 35.04 mmol) in THF (30 mL) was cannula transferred into the reaction flask over 10 minutes, followed by additional THF (20 mL) to ensure complete transfer of the diacid. The solution was stirred vigorously overnight at 22 °C. Volatiles were removed under vacuum to yield a white paste, which was extracted with dry pentane (60 mL). The resulting suspension was stirred vigorously for 1 h and allowed to settle. This pentane extract was cannula filtered, and the remaining white solid was washed with pentane (2 x 35 mL). The combined pentane washes were concentrated

under vacuum to yield a clear, slightly yellow liquid. (Alternatively, pentane extraction of the desired product was achieved by Schlenk filtration through a medium frit.) Yield: 12.2 g (93 % yield). This water-sensitive intermediate was used without further purification. ^{1}H NMR (300 MHz, DMSO-d_6, 22 °C): δ (ppm) 5.78 (ddt, $J_{H\text{-}H}^{3}$ = 17.2, 10.2, 6.7 Hz, 1H, CH_2=C*H*CH_2), 4.98 (ddt, $J_{H\text{-}H}^{3}$ = 17.2, 1.6 Hz, $J_{H\text{-}H}^{2}$ = 2.2 Hz, 1H, C*H*$_2$=CHCH_2), 4.93 (ddt, $J_{H\text{-}H}^{3}$ = 10.2, 1.2 Hz, $J_{H\text{-}H}^{2}$ = 2.3 Hz, 1H, C*H*$_2$=CHCH_2), 3.35 (t, $J_{H\text{-}H}^{3}$ = 7.5 Hz, 1H, C*H*(COOSi(CH$_3$)$_3$)$_2$), 2.00 (dt, $J_{H\text{-}H}^{3}$ = 7.2, 6.8 Hz, 2H, CH_2=CHC*H*$_2$), 1.74–1.64 (m, 2H, C*H*$_2$CH(COOSi(CH$_3$)$_3$)$_2$), 1.40–1.15 (m, 10H, CH_2=CHCH_2(C*H*$_2$)$_5$$CH_2$CH(COOSi(CH$_3$)$_3$)$_2$), 0.24 (s, 18 H, CH(COOSi(C*H*$_3$)$_3$)$_2$). ^{13}C NMR (75 MHz, DMSO-d_6, 22 °C): δ (ppm) 169.26, 138.72, 114.56, 53.96, 33.15, 28.50, 28.27, 28.16, 28.06, 26.39, -0.60.

Synthesis of lithium bis(non-8-enyl-malonato) borate (LiBNMB). $LiBF_4$ (1.49 g, 15.89 mmol) was slurried in a 100 mL Schlenk flask under nitrogen equipped with a rubber septum. A degassed solution of non-8-enyl-malonic acid trimethylsilyl ester (11.84 g, 31.77 mmol) in acetonitrile (25 mL) was then added via cannula, along with more acetonitrile (15 mL) to ensure complete transfer. This reaction mixture was stirred under nitrogen at 45-55 °C, which caused the solution to become turbid. The flask was periodically vented using a needle to purge trimethylsilyl fluoride from the headspace of the reaction flask. After 8 d, volatiles were removed from the reaction mixture under vacuum to yield 6.75 g of crude white solid (90 % yield). A portion of the crude product (3.25 g) was dissolved in diethyl ether (300 mL) and then washed successively with saturated Li_2CO_3(*aq*) (4 x 25 mL), water (50 mL), saturated Li_2CO_3(*aq*) (50 mL), ~10 M LiCl(*aq*) (2 x 25 mL), and water (2 x 25 mL). More diethyl ether (~ 200 mL) was added during the repeated washings and reaction work up. The ethereal solvent was then

removed by rotary evaporation. The resulting solid was dried by co-evaporation with toluene (2 x 50 mL), followed by freeze-drying twice from C_6H_6 (12 mL). The dry, white powder was stored under nitrogen. Yield: 2.59 g (80 % recovery). Alternatively, LiBNMB may be purified by trituration with hot heptane as described in Appendix 3. ^{1}H NMR (300 MHz, DMSO-d_6, 22 °C): δ (ppm) 5.79 (ddt, $J_{H\text{-}H}^3$ = 17.1, 10.3, 6.7 Hz, 2H, CH_2=C*H*CH_2), 4.99 (ddt, $J_{H\text{-}H}^3$ = 17.2, 1.7 Hz, $J_{H\text{-}H}^2$ = 2.1 Hz, 2H, C*H*$_2$=$CHCH_2$), 4.93 (ddt, $J_{H\text{-}H}^3$ = 10.2, 1.1 Hz, $J_{H\text{-}H}^2$ = 2.2 Hz, 2H, C*H*$_2$=$CHCH_2$), 3.35 (t, $J_{H\text{-}H}^3$ = 5.5 Hz, 2H, C*H*$(COO)_2B$), 2.00 (dt, $J_{H\text{-}H}^3$ = 7.2, 6.9 Hz, 4H, CH_2=CHC*H*$_2$), 1.84–1.72 (m, 4H, C*H*$_2$$CH(COO)_2B$), 1.40–1.18 (m, 20H, CH_2=$CHCH_2$(C*H*$_2$)$_5$$CH_2CH(COO)_2B$). ^{13}C NMR (75 MHz, DMSO-d_6, 22 °C): δ (ppm) 168.21, 138.84, 114.62, 47.66, 33.17, 29.01, 28.64, 28.42, 28.24, 27.00, 26.23. ESI-MS: calcd. for $C_{24}H_{36}BO_8$ $[M]^-$ 463.3, found 463.2. The ^{1}H NMR spectrum is provided in Figure 4.2.

Acyclic diene metathesis (ADMET) polymerization of lithium bis(non-8-enyl-malonato) borate to obtain poly(LiBNMB). Under a nitrogen atmosphere, an oven-dried 50 mL Schlenk tube was charged with a magnetic stirbar, lithium bis(non-8-enyl-malonato) borate (3.008 g, 6.38 mmol), Grubbs 2nd generation catalyst (33.8 mg, 42.5 μmol), and anhydrous propylene carbonate (12.0 mL). The flask was heated to 45 °C in an oil bath and placed under to dynamic vacuum. After stirring for 48 h, the flask was back-filled with nitrogen and the glass stopper swapped for a septum under a flush of nitrogen. Propylene carbonate (4 mL) was added to the solution, and then the solution was added dropwise to vigorously stirring toluene (150 mL) under nitrogen atmosphere to precipitate the polymer. After stirring overnight, the supernatant solution was removed via cannula and then fresh toluene (50 mL) was added, stirred for 30 minutes, and removed via cannula. Volatiles were removed under vacuum at 65 °C. The polymer

was redissolved in propylene carbonate (25 mL) and then precipitated again into vigorously stirring toluene (150 mL). Volatiles were again removed under vacuum at 65 °C. In order to remove as much propylene carbonate as possible, the polymer was cut into small pieces (~ 3–5 mm) in a glovebox and placed in a 25 mL Schlenk tube. The tube was heated to 120 °C under vacuum on a Schlenk line for 12 h. Quantitative ^{1}H NMR analyses reveal that the polymer sample contained ~7.8 wt% propylene carbonate; however, no further attempts to remove the remaining solvent were made, given that electrochemical measurements were subsequently made in propylene carbonate. Polymer samples for thermal analyses were instead precipitated from acetone into toluene, followed by vigorous drying in order to minimize trapped solvent. These samples were not used in any electrochemical tests, given that acetone diminishes the observed electrochemical stability. Yield: 2.36 g (79 % yield). ^{1}H NMR (500 MHz, DMSO-d_6, 22 °C): δ (ppm) 5.43–5.29 (m, 2H, CH_2CH=C$H$$CH_2$), 3.38–3.30 (m, 2H, C$H$$(COO)_2B$), 2.06–1.87 (m, 4H, C$H_2$CH=CHC$H_2$), 1.84–1.72 (m, 4H, C$H_2$$CH(COO)_2B$), 1.40–1.16 (m, 20H, CH=$CHCH_2(CH_2)_5CH_2CH(COO)_2B$). ^{13}C NMR (125 MHz, DMSO-d_6, 22 °C): δ (ppm) 168.21, 168.18, 130.13, 130.05, 129.98, 129.64, 47.70, 32.04, 29.12, 29.05, 28.97, 28.90, 28.74, 28.60, 28.44, 26.99, 26.69, 26.31, 26.12, 26.00. *Anal*. Calcd (w/PC): C, 58.77; H, 7.19; Li, 1.45. Found: C, 58.13; H, 6.90; Li, 1.46. *Anal.* Calcd (neat): C, 59.75; H, 7.29; Li, 1.57. Found: C, 59.05; H, 7.16; Li, 1.49. SEC (DMF + 0.1 M LiBr, 70 °C): M_n = 34.3 kg mol^{-1}, M_w/M_n = 2.04 (against PEO standards). The ^{1}H NMR spectrum is provided in Figure 4.3 and the SEC trace is provided in Figure 4.4.

Thiol-ene copolymerization of LiBNMB with 1,6-hexanedithiol to obtain poly(LiBNMB-*co*-HDT). Lithium bis(non-8-enylmalonato)borate (0.257 g, 0.532 mmol), 1,6-

hexanedithiol (88 mg, 0.532 mmol), azobisisobutyronitrile (AIBN) (10.2 mg, 0.061 mmol) and *N,N*-dimethylformamide (1.07 mL) were sealed in a 25 mL pear-shaped flask and subjected to three freeze-thaw degassing cycles. After heating this reaction mixture to 60°C with stirring for 40 h, it was chilled under running water and exposed to air to terminate the reaction. The resulting polymer was dissolved in acetone and then precipitated four times into stirring diethyl ether/pentane (3:1, 15 mL) to yield a white solid after centrifugation and drying under vacuum at 75 °C. ^{1}H NMR (400 MHz, DMSO-d_6, 22 °C): δ (ppm) 3.38–3.29 (m, 2H, C*H*$(COO)_2$B), 2.48–2.42 (m, 8H, SCH_2), 1.83–1.73 (m, 4H, CH_2CH$(COO)_2$B), 1.54–1.44 (m, 8H, SCH_2CH_2), 1.39–1.12 (m, 28H, $S(CH_2)_2CH_2$ + $(CH_2)_6CH_2CH(COO)_2$B) ^{13}C NMR (100 MHz, DMSO-d_6, 22 °C): δ (ppm) 168.19, 168.15, 47.69, 31.13, 31.06, 29.18, 29.07, 28.89, 28.80, 28.62, 28.26, 27.82, 26.99, 26.26. SEC (DMF + 0.1 M LiBr, 70 °C): M_n = 21.2 kg mol^{-1}, M_w/M_n = 2.37 (against PS standards). The ^{1}H NMR spectrum and SEC trace are provided in Appendix 3 (Figure A3.2 and Figure A3.3).

Thiol-ene copolymerization of LiBNMB with 2,2′-(ethylenedioxy)diethanethiol (triethyleneglycol-1,8-dithiol) to obtain poly(LiBNMB-*co*-TEGDT). Lithium bis(non-8-enylmalonato)borate (0.50 g, 1.06 mmol), 2,2′-(ethylenedioxy)diethanethiol (triethyleneglycol-1,8-dithiol) (0.194 g, 1.06 mmol), azobisisobutyronitrile (AIBN) (12.1 mg, 0.074 mmol) and *N,N*-dimethylformamide (1.6 mL) were sealed in a 25 mL pear-shaped flask and subjected to three freeze-thaw degassing cycles. The flask was placed in an oil bath thermostatted at 60°C and stirred. After 100 h, the reaction flask was chilled under running water and exposed to air to stop the reaction. The polymer was dissolved in acetone and then precipitated three times into stirring diethyl ether/pentane (3:1, 15 mL) to yield a white solid after centrifugation and drying under

vacuum at 70 °C. ^{1}H NMR (400 MHz, DMSO-d_6, 22 °C): δ (ppm) 3.57–3.47 (m, 8H, CH_2O), 3.37–3.30 (m, 2H, CH(COO)$_2$B), 2.65–2.58 (m, 4H, SCH_2CH$_2$O), 2.54–2.47 (m, 4H, SCH_2CH$_2$CH$_2$), 1.82–1.72 (m, 4H, CH_2CH(COO)$_2$B), 1.54–1.44 (m, 4H, SCH$_2$CH_2CH$_2$), 1.37–1.12 (m, 24H, (CH_2)$_6$CH$_2$CH(COO)$_2$B). ^{13}C NMR (100 MHz, DMSO-d_6, 22 °C): δ (ppm) 168.19, 168.15, 70.30, 69.53, 47.68, 31.52, 30.66, 29.30, 29.07, 28.91, 28.80, 28.62, 28.24, 26.97, 26.27. SEC (DMF + 0.1 M LiBr, 70 °C): M_n = 46.3 kg mol^{-1}, M_w/M_n = 2.26 (against PS standards). The ^{1}H NMR spectrum is provided in Figure 4.7 and the SEC trance is provided in Appendix 3 (Figure A3.4).

4.3 Results and Discussion

4.3.1 LiBNMB Monomer Synthesis and ADMET Polymerization

We synthesized a α,ω-diene monomer based on a LiBMB core amenable to polymerization by acyclic diene metathesis (ADMET) polymerization in three steps starting from a biorenewable[31] carboxylic acid (Scheme 4.1). α-Carboxylation of 10-undecenoic acid via enolate formation with lithium diisopropylamide and subsequent trapping by CO_2(*s*) yielded non-8-enylmalonic acid **1** in high yield. Reaction of non-8-enylmalonic acid with trimethylsilyl chloride in the presence of imidazole cleanly afforded bis(trimethylsilyl) ester **2**. The bis(malonato)borate chelate core was formed by reaction of **2** with commercially available $LiBF_4$ with concomitant $(CH_3)_3SiF$ elimination in a method similar to that employed by Gores to make non-symmetric or "mixed" borate salts.[32] This convenient synthesis circumvents the need for $LiB(OMe)_4$, which is not commercially available.[25,33] This route led to the desired lithium

bis(non-8-enylmalonato)borate (**LiBNMB**) α,ω-diene monomer in high yield and purity, as seen by ^{1}H NMR spectroscopy (Figure 4.2).

Scheme 4.1. Synthesis of lithium bis(non-8-enylmalonato) borate (LiBNMB) monomer.

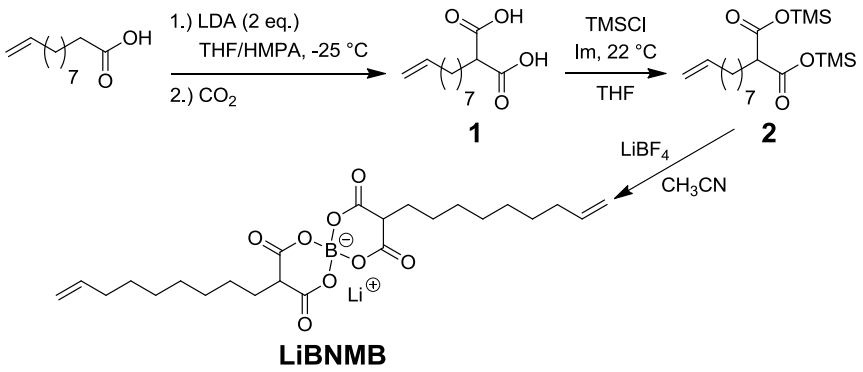

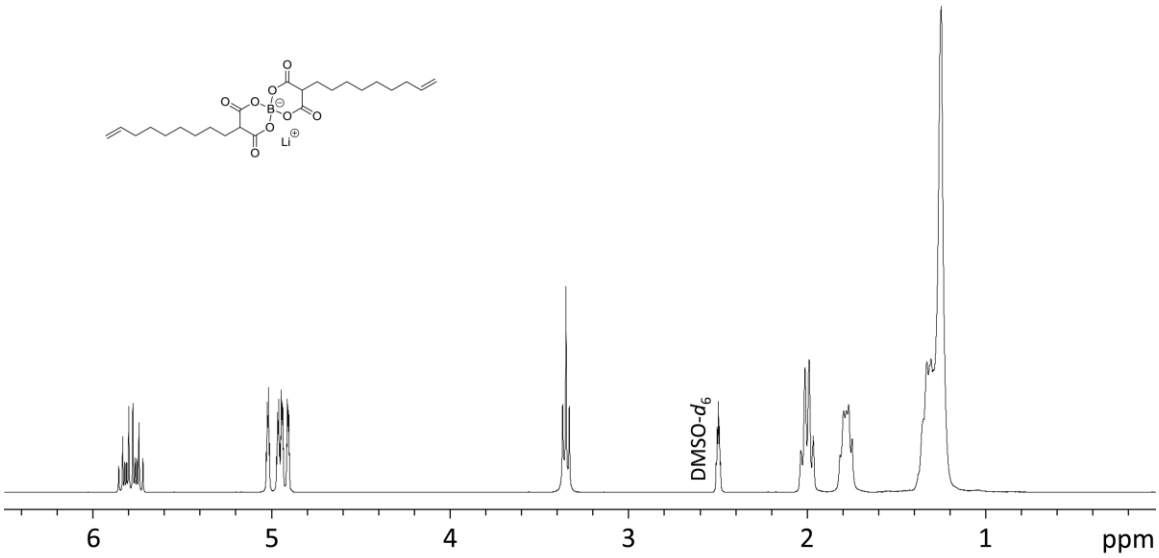

Figure 4.2. ^{1}H NMR spectrum (300 MHz, DMSO-d_6, 22°C) of lithium bis(non-8-enyl-malonato) borate (LiBNMB) monomer.

To maintain a purely hydrocarbon polymer backbone and avoid the incorporation of Lewis-basic moieties that would potentially reduce Li^+ mobility (as in the case of PEO-based systems),[4,5] we investigated the acyclic diene metathesis (ADMET) polymerization of LiBNMB. As a step-growth polymerization based on olefin metathesis catalysis, ADMET is a versatile and functional group tolerant polymerization technique that enables the synthesis of polymer scaffolds with precisely positioned chemical functionalities.[34,35] ADMET polymerization of LiBNMB was conducted in anhydrous propylene carbonate using Grubbs' second generation olefin metathesis catalyst (Scheme 4.2), under dynamic vacuum to remove the ethylene generated by the reaction to achieve high monomer conversions. After 48 h, the polymer was diluted with propylene carbonate and precipitated twice into dry toluene. High field ^{1}H NMR of the resulting polymer revealed the apparent absence of end-groups, suggesting a high degree of polymerization (Figure 4.3). Size exclusion chromatography in *N*,*N*-dimethylformamide with 0.1 M LiBr confirmed the formation of a polymer with M_n = 34.3 kg mol^{-1} and M_w/M_n = 2.04 (against PEO standards) (Figure 4.4). Since ADMET is a step growth polymerization that does not typically proceed to high molecular weight,[36] we are currently investigating the reason why a high degree of polymerization was obtained.

Scheme 4.2. Acyclic diene metathesis (ADMET) polymerization of LiBNMB.

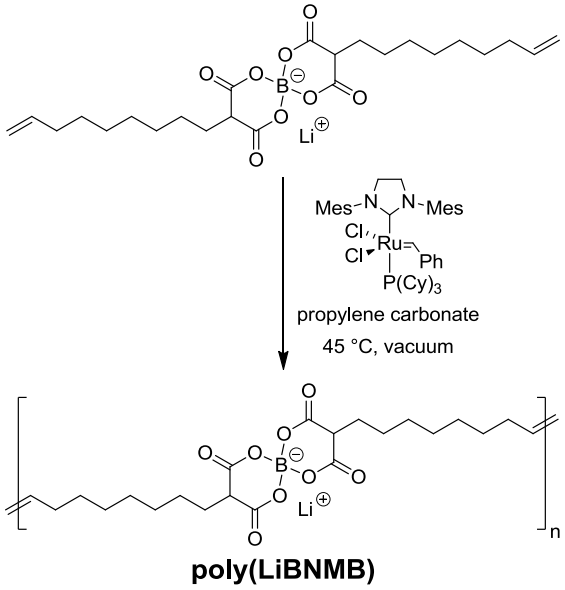

poly(LiBNMB)

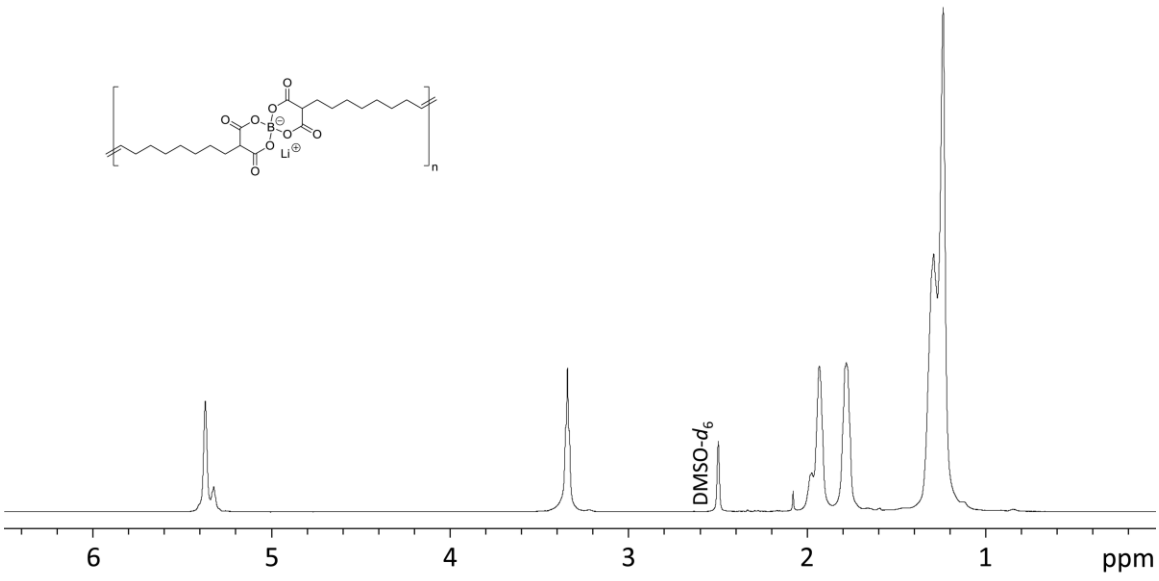

Figure 4.3. ^{1}H NMR spectrum (500 MHz, DMSO-d_6, 22°C) of poly(lithium bis(non-8-enyl-malonato) borate) (poly(LiBNMB)).

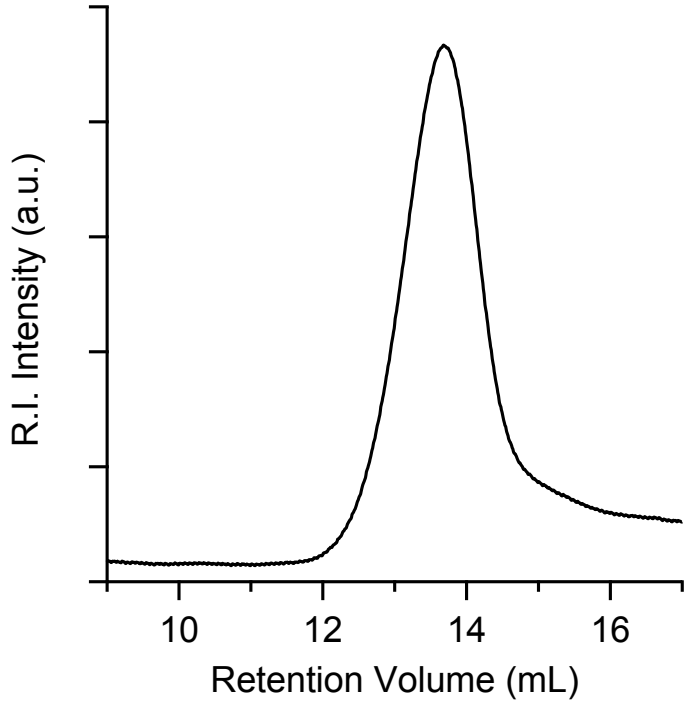

Figure 4.4. Size exclusion chromatography (SEC) refractive index trace of poly(LiBNMB) in DMF with 0.1 M LiBr.

We investigated the thermal properties of poly(LiBNMB) using thermogravimetric analysis (TGA) and differential scanning calorimetry (DSC). TGA of poly(LiBNMB) demonstrates its exceptional thermal stability up to ~190 °C with decomposition waves occurring near 195 – 250 °C and 340 – 450 °C (Figure 4.5). This decomposition onset temperature is lower than that reported for the parent salt lithium bis(malonato)borate (245 °C), possibly due to the presence of alkyl and alkenyl substituents on the bis(malonato)borate anion.[25] The DSC profile of poly(LiBNMB) exhibits no discernible features in the second heating curve in the range -30 – 180 °C (Figure 4.6).

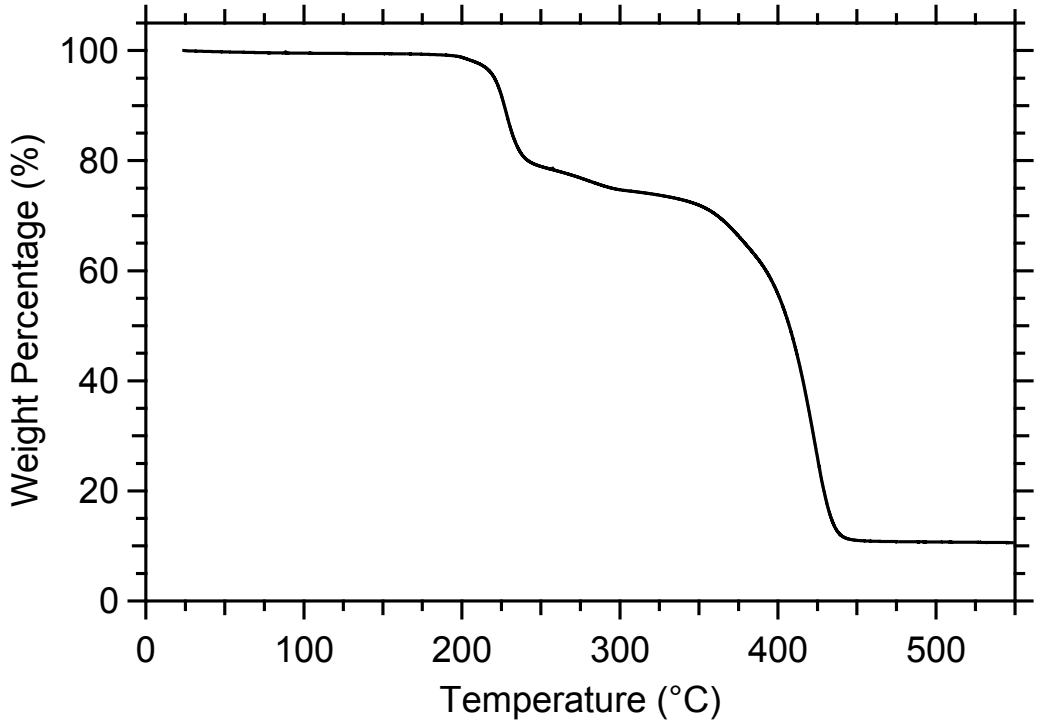

Figure 4.5. Thermogravimetric analysis (TGA) illustrates the thermal stability of poly(LiBNMB) up to 190 °C.

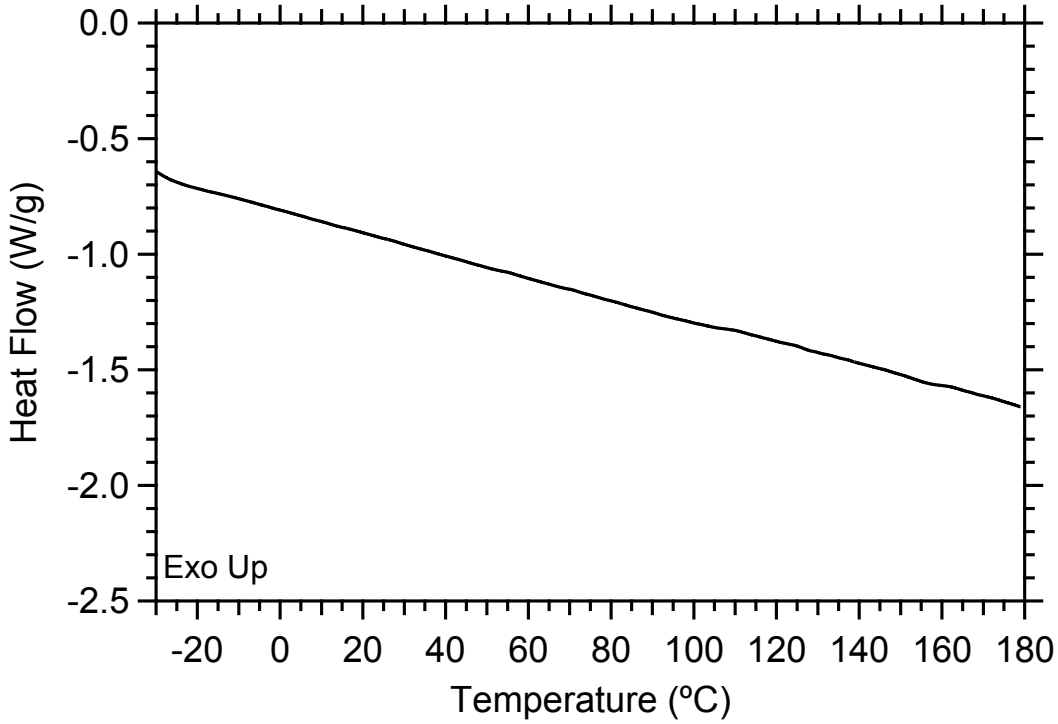

Figure 4.6. Differential scanning calorimetry (DSC) second heating curve for poly(LiBNMB) displaying no discernible features in the range -30 – 180 °C.

4.3.2 Copolymerization with Other Monomers

In an attempt to obtain structurally analogous variations of poly(LiBNMB) with different thermal properties and thermal decomposition profiles, we examined other methods for enchaining LiBNMB into linear polymers with more flexible backbones. The thiol-ene reaction has been established as a powerful tool in step-growth polymer synthesis, with numerous advances in the synthesis of polymers by thiol-ene chemistry reported by the groups of Bowman, Hoyle, and others.[37,38] Since thiol-ene polymerization necessarily introduces thioether linkages in the polymer backbone, we sought to determine whether or not these thioethers would introduce

sufficient backbone flexibility that would manifest in lower (and accessible) polymer glass transition temperatures below the onset of decomposition at 195 °C.

We first polymerized LiBNMB with 1,6-hexanedithiol with stoichiometric balance of the thiol and olefin functional groups in DMF using AIBN as initiator at 60 °C. (Scheme 4.3) After 40 h, the polymer, poly(lithium bis(non-8-enylmalonato)borate-*co*-hexanedithiol) (poly(LiBNMB-*co*-HDT)) was precipitated from ether/pentane. We encountered difficulties in removing residual DMF from the polymer, presumably due to its high affinity for the Lewis acidic Li^+ ions. Consequently, we precipitated the polymer several times from acetone into ether/pentane followed by drying at high temperature to reduce the residual DMF to < 0.35 wt%. The ^{1}H NMR spectrum of poly(LiBNMB-*co*-HDT) matched well with the resonances anticipated for the polymer and confirmed the apparent consumption of olefins and thiols present in the monomers. (Appendix 3, Figure A3.2). SEC analyses demonstrated the formation of a modest molecular weight polymer with M_n = 21.2 kg mol^{-1} and a broad dispersity M_w/M_n = 2.37, as expected for a step-growth mechanism (Appendix 3, Figure A3.3).

Scheme 4.3. Thiol-ene copolymerization of LiBNMB with α,ω-dithiols.

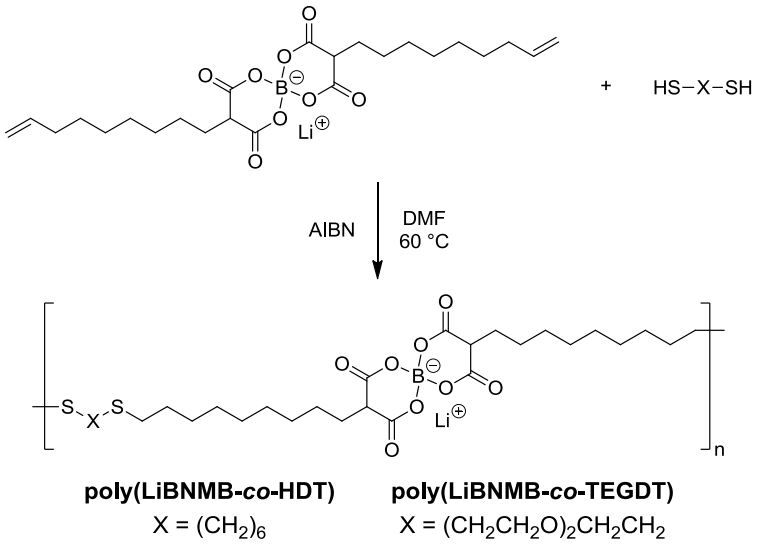

We also synthesized a step-growth polymer of LiBNMB with triethyleneglycol-1,8-dithiol under similar thiol-ene polymerization conditions to furnish poly(lithium bis(non-8-enylmalonato)borate-*co*-triethyleneglycol-1,8-dithiol) (poly(LiBNMB-*co*-TEGDT)). (Scheme 4.3) In addition to the thioether linkages introduced into the backbone, we hypothesized that the ether linkages would further increase polymer backbone flexibility and potentially act as an internal plasticizer, thereby increasing lithium ion dissociation and eliminating the need for an exogenous solvent. We noted that the removal of residual DMF from the polymer was more easily accomplished than with the 1,6-hexanedithiol polymer, presumably due to the chelation of Li^+ ions by the ether linkages in the polymer chain that reduced competitive coordination by DMF. Quantitative ^{1}H NMR spectroscopy again showed the apparent consumption of olefins and thiols from monomer units and confirmed the structure of the resulting polymer (Figure 4.7). Size exclusion chromatography again showed the formation of a moderate molecular weight

polymer with M_n = 46.3 kg mol^{-1} and M_w/M_n = 2.26, as expected for a step-growth polymerization. (Appendix 3, Figure A3.4).

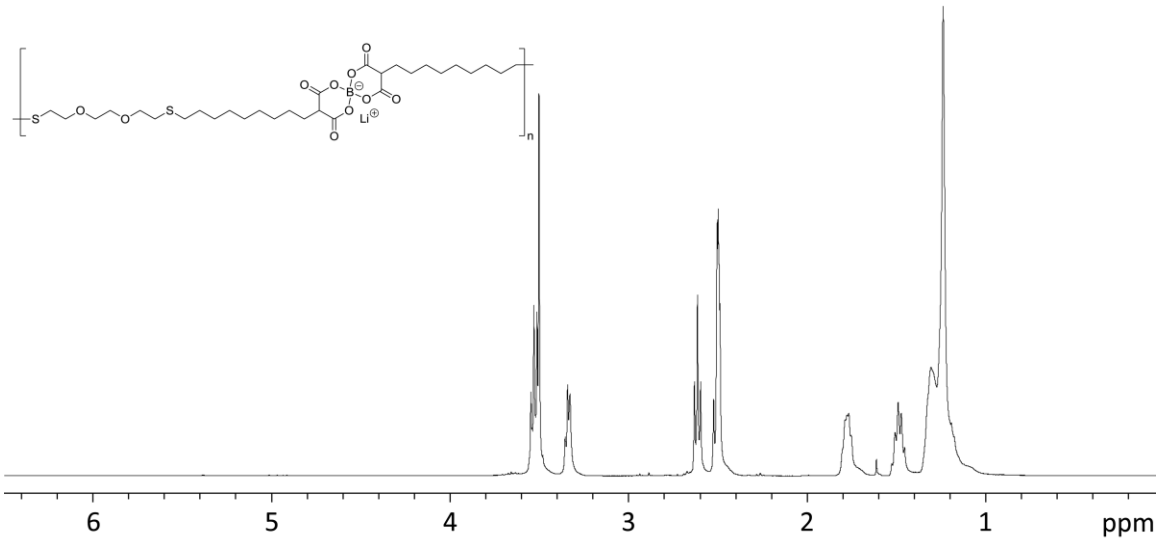

Figure 4.7. ^{1}H NMR spectrum (400 MHz, DMSO-d_6, 22°C) of poly(lithium bis(non-8-enyl-malonato)borate-*co*-triethyleneglycol-dithiol) (poly(LiBNMB-*co*-TEGDT)).

The thermal stabilities of poly (LiBNMB-*co*-HDT) and poly(LiBNMB-*co*-TEGDT) were studied using TGA (Figure 4.8). The thermal decomposition profile of poly(LiBNMB-*co*-HDT) was very similar to that of poly(LiBNMB), with a decomposition onset temperature of ~ 195 °C. TGA analysis of this polymer was ceased just above 400 °C due the sulfurous odor indicative of oxidative decomposition of the thioether linkages. The introduction of the ether linkages apparently decreases the thermal stability of poly(LiBNMB-*co*-TEGDT), which exhibits a decomposition onset temperature of 175 °C. Since the weight loss associated with the first decomposition wave is similar for both thiol-ene polymers (~ 15 wt%) and is also similar to the weight loss for the first decomposition wave of poly(LiBNMB) (~ 20 wt%), we speculate that

this initial decomposition event must involve breakdown of the bis(malonato)borate (BMB) moiety common to these three polymer samples. Since the BMB group constitutes a slightly larger percentage of the mass for poly(LiBNMB) than for the thiol-ene polymers, this analysis is qualitatively consistent with the observed weight losses.

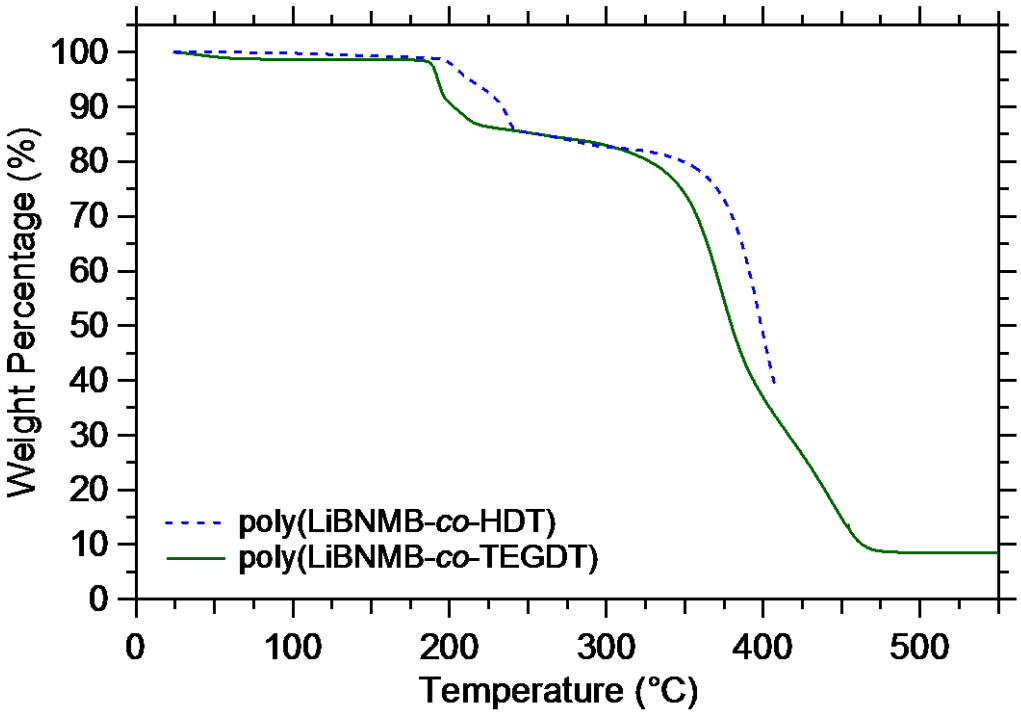

Figure 4.8. Thermogravimetric analysis (TGA) of poly(LiBNMB-*co*-HDT) and poly(LiBNMB-*co*-TEGDT).

To determine the effectiveness of introducing different thioether linkages into the LiBNMB polymers on rendering the thermal transitions accessible by dropping them below the decomposition onset temperature, we studied poly(LiBNMB-*co*-HDT) and poly(LiBNMB-*co*-TEGDT) by differential scanning calorimetry (DSC) (Figure 4.9). Similar to poly(LiBNMB), the second heating curve of poly(LiBNMB-*co*-HDT) shows no thermal transitions below the

decomposition temperature of the polymer in the range -40 – 150 °C. From this data, we conclude that the addition of alkyl thioethers to the polymer chain do little to increase its flexibility and lower the observed glass transition temperature, T_g. In contrast to poly(LiBNMB) and poly(LiBNMB-*co*-HDT), the second heating curve in the DSC of poly(LiBNMB-*co*-TEGDT) shows a distinct T_g = 71 °C, which is well within the range of thermal stability for this polymer. The drastic decrease in T_g compared to the other polymers studied suggests that the ethylene glycol units in the polymer backbone strongly affect polymer segmental dynamics. Not only do the ethylene glycol units provide flexibility in the polymer backbone to lower T_g, they also probably act as an internal solvent that increases the extent of ion dissociation in the polymeric lithium salt.

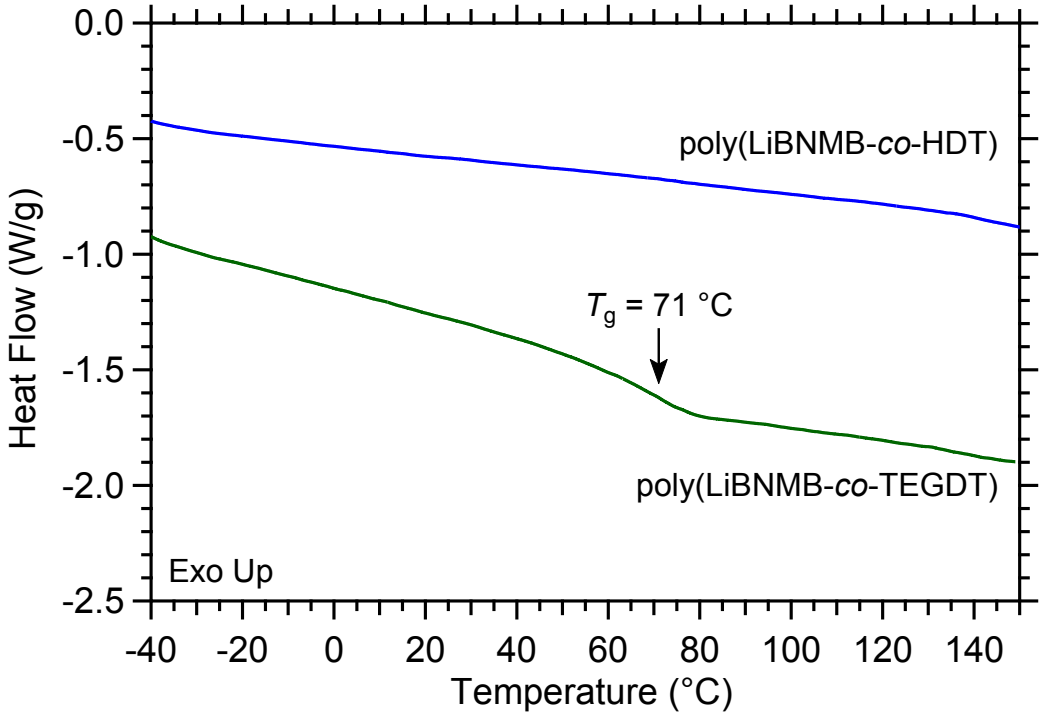

Figure 4.9. Differential scanning calorimetry of poly(LiBNMB-*co*-HDT) and poly(LiBNMB-*co*-TEGDT).

4.3.3 Ionic Conductivity of poly(LiBNMB)

To determine the utility of these new lithium single-ion conductors as potential lithium ion battery electrolytes, we studied the electrochemical behavior of poly(LiBNMB) synthesized by ADMET polymerization. Although we were able to lower the T_g of the LiBNMB polymers by introducing ethylene glycol units into the polymer backbone, we were concerned about the ability of these moieties to chelate lithium ions and impede their motion. Therefore, we chose to study poly(LiBNMB) because it has an entirely hydrocarbon backbone.

As a consequence of the inaccessibly high T_g of poly(LiBNMB), we studied its ionic conductivity in propylene carbonate solutions using electrochemical impedance spectroscopy. As

a control, we also studied the ionic conductivity of a propylene carbonate solution of lithium bis(trifluoromethanesulfonyl)imide (LiTFSI) at the same Li^+ ion concentration and temperature. Overlaid Bode plots of the total impedance, |Z|, *vs.* frequency, ω, at 22 °C for poly(LiBNMB) and LiTFSI at a concentration of $[Li^+] = 0.2$ M in propylene carbonate are given in Figure 4.10. The high frequency plateau in the Bode plot represents the solution resistance, which is due to bulk ion motion in solution far from the electrode interface. Using this value to calculate ionic conductivity of the solution, we find that poly(LiBNMB) has a room temperature solution conductivity of 4.4×10^{-4} S cm^{-1}, whereas the solution conductivity of LiTFSI is a factor of ~ 3.5 greater at 1.6×10^{-3} S cm^{-1}. The solution conductivity depends primarily on the concentration of mobile ions in solution, with contributions from both ion pair dissociation and ion solvation. We assume that the measured solution conductivity of poly(LiBNMB) is primarily due to Li^+ ion motion since polymer chain diffusion is expected to be quite slow in the frequency range probed by EIS. The measured solution conductivity of LiTFSI has a significant contribution from anion motion, since LiTFSI has a transference number on the order of 0.2 – 0.4.[39] Accounting for this adjustment and assuming slow polymeric ion diffusion in solution, the solution Li^+ ion conductivity of poly(LiBNMB) is nearly equivalent to that of LiTFSI, indicating that lithium motion in the bulk of the solution is not inhibited by enchainment of the anion.

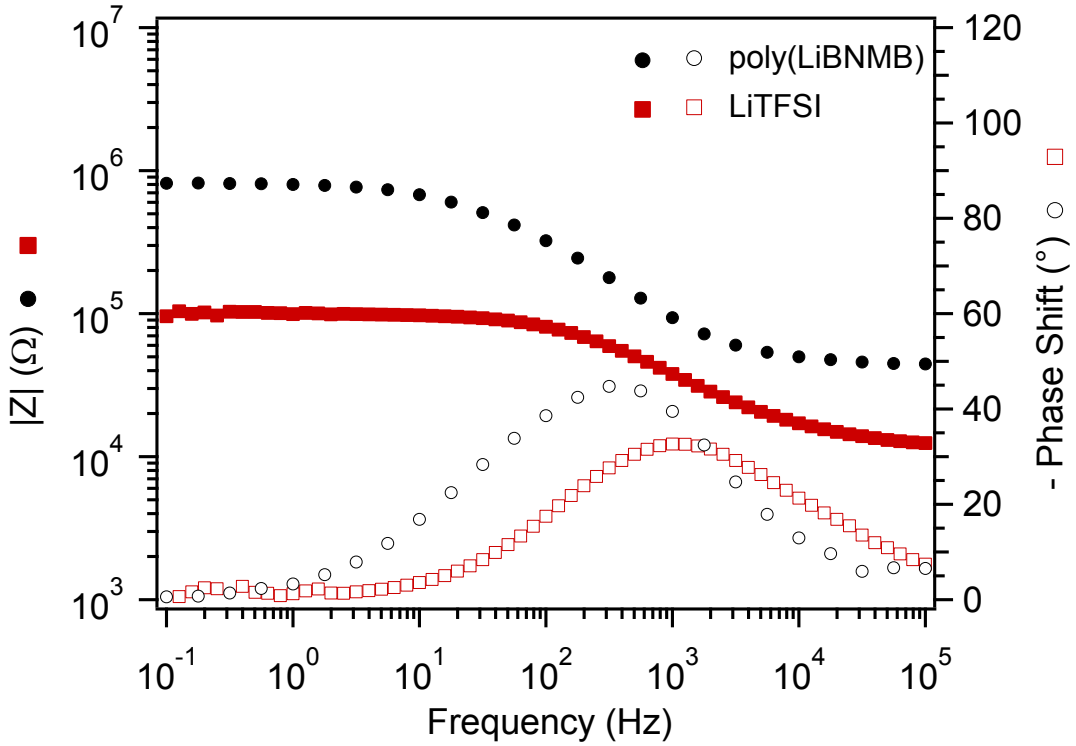

Figure 4.10. Bode plots (total impedance, |Z| *vs.* frequency, ω) of the electrochemical impedance for poly(LiBNMB) and LiTFSI in propylene carbonate ($[Li^+]$ = 0.2 M).

The low frequency plateau in the Bode plot shown in Figure 4.10 represents the total resistance of the solution, which is a sum of the solution resistance and the interfacial resistance at the electrode surface. Whereas the solution resistance represents the motion of ions in the bulk, the interfacial resistance describes the motion of ions through the electrical double layer formed at the electrode interface. The latter resistance depends on both the concentration and diffusion rates of the ions that form the double layer. The total conductivity of poly(LiBNMB) is 2.4 x 10^{-5} S cm^{-1}, which is approximately a factor of eight lower than the total conductivity of LiTFSI (2.0 x 10^{-4} S cm^{-1}). This is a much larger difference than that observed for the solution resistance. While the low transference number of LiTFSI accounts for a significant portion of this

difference, the total lithium conductivity of poly(LiBNMB) still falls below the lithium conductivity of LiTFSI by a factor of ~ 2 - 3. We propose that the slower rate of diffusion of anionic segments of poly(LiBNMB) compared to TFSI anions leads to sluggish rearrangement of the electrical double layer that retards lithium ion motion at the electrode interface.

A major challenge in the development of high power lithium-ion batteries, especially for electric vehicle applications, is the development of electrolytes that are able to withstand the demanding oxidative and reductive potentials at the surfaces of high-voltage cathode and high capacity anode materials.[7] In this connection, we investigated the electrochemical stability of poly(LiBNMB) by cyclic voltammetry (Figure 4.11). In a lithium half-cell test equipped with a Pt working microelectrode and a Li foil counter electrode, we observed no features in a cathodic sweep from open circuit potential (~ 3 V vs. Li/Li^+) to 50 mV with a sweep rate of 10 mV s^{-1}, demonstrating the reductive stability of poly(LiBNMB). In the anodic sweep from open circuit potential to 7.0 V (*vs.* Li/Li^+) an irreversible oxidation wave is observed during the first cycle near ~5 V with only minor features visible on subsequent cycles. Since the feature is irreversible, this oxidative decomposition product must persist in the cell through subsequent cycles. Absence of any current associated with this decomposition in subsequent cycles further suggests that the decomposition product must passivate the electrode to prevent further oxidative decomposition. Therefore, we attribute this oxidation wave to the formation of a solid electrolyte interphase (SEI) layer at the electrode/electrolyte interface. Formation of SEI layers in lithium ion batteries is well-precedented and is typically necessary for sustained function of the cell without incurring capacity losses upon repeated charge/discharge cycles.[40] The stability of this SEI layer endows the polymer electrolyte with excellent oxidative stability up to $\geq$ 7 V *vs.* Li/Li^+. Consistent with

the formation of an SEI layer, we observed that cycling the cell caused increased impedance as assessed by EIS. More explicitly, the conductivity of poly(LiBNMB) decreased by a factor of three to 7.7 x 10^{-6} S cm^{-1} upon SEI layer formation (Figure 4.12).

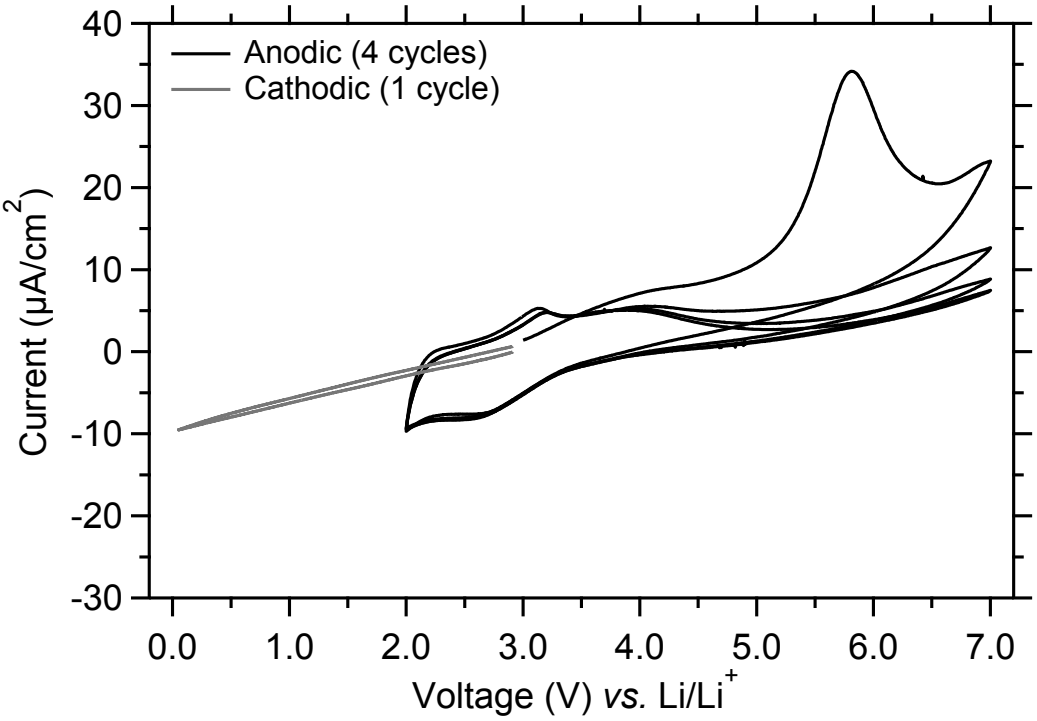

Figure 4.11. Cyclic voltammograms of poly(LiBNMB) in propylene carbonate using a Pt working electrode and a Li reference electrode at a sweep rate of 10 mV s^{-1}. The first cycle exhibits an irreversible electrochemical event at an onset potential of 5 V, yet this electrolyte decomposition is not observed in subsequent cycles.

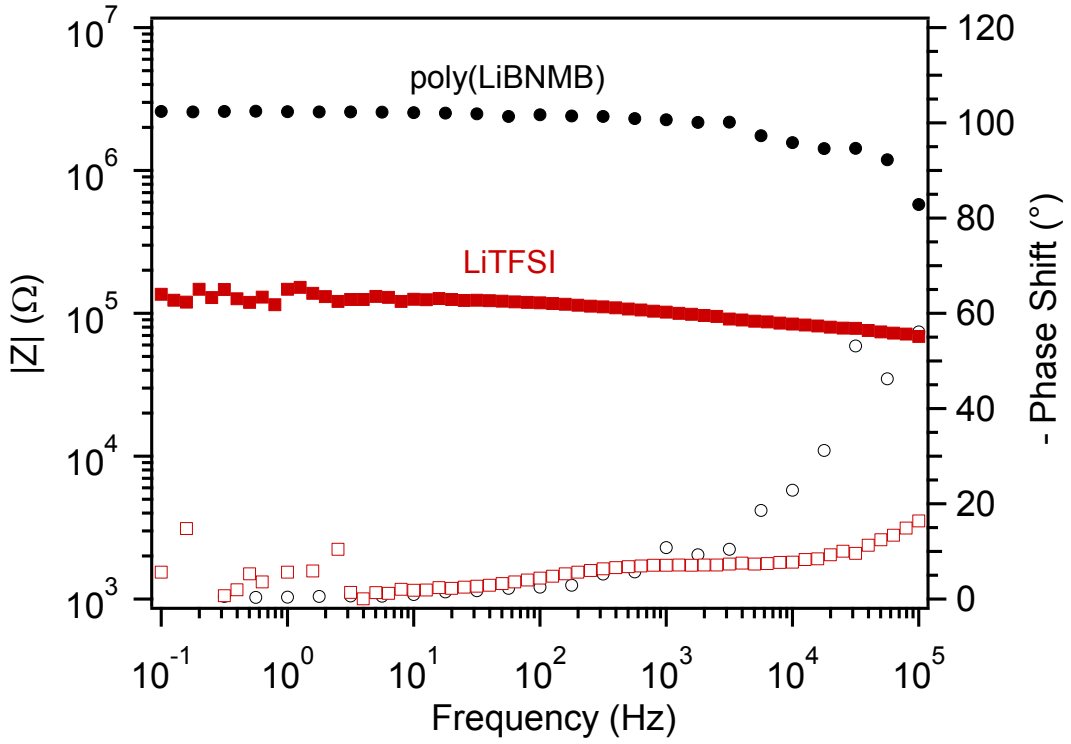

Figure 4.12. Bode plot of the electrochemical impedance spectroscopy of poly(LiBNMB) and LiTFSI in propylene carbonate ([Li^+] = 0.2 M) after cycling to 7 V *vs.* Li/Li^+.

Finally, we compared the electrochemical stability of poly(LiBNMB) with the state-of-the-art lithium electrolyte salt LiTFSI. Figure 4.13 shows a large oxidative current associated with iterative decomposition of LiTFSI above 6 V *vs.* Li/Li^+ across numerous cycles, consistent with literature reports.[3,41] Attendant with this decomposition, we see an increase in the impedance of the LiTFSI solution as assessed by EIS (Figure 4.12). The current generated from the breakdown of LiTFSI is orders of magnitude larger than the current associated with the decomposition of poly(LiBNMB) to form an SEI (Note the difference in y-axis scales between Figure 4.11 and Figure 4.13). In stark contrast to the oxidative decomposition of LiTFSI, after

the initial SEI formation, poly(LiBNMB) may be cycled between 0.2 V and 8 V vs. Li/Li^+ without any visible decomposition (Figure 4.13). The extremely wide electrochemical window of poly(LiBNMB) positions it as a promising candidate for a high-voltage lithium ion battery electrolyte. We speculate that the unusual stability of poly(LiBNMB) arises from polymer decomposition at the electrode interface that yields a surface-bound polymer that adheres through multiple binding points. This polymeric "shield" protects the electrolyte from further decomposition reactions in subsequent electrochemical cycles.

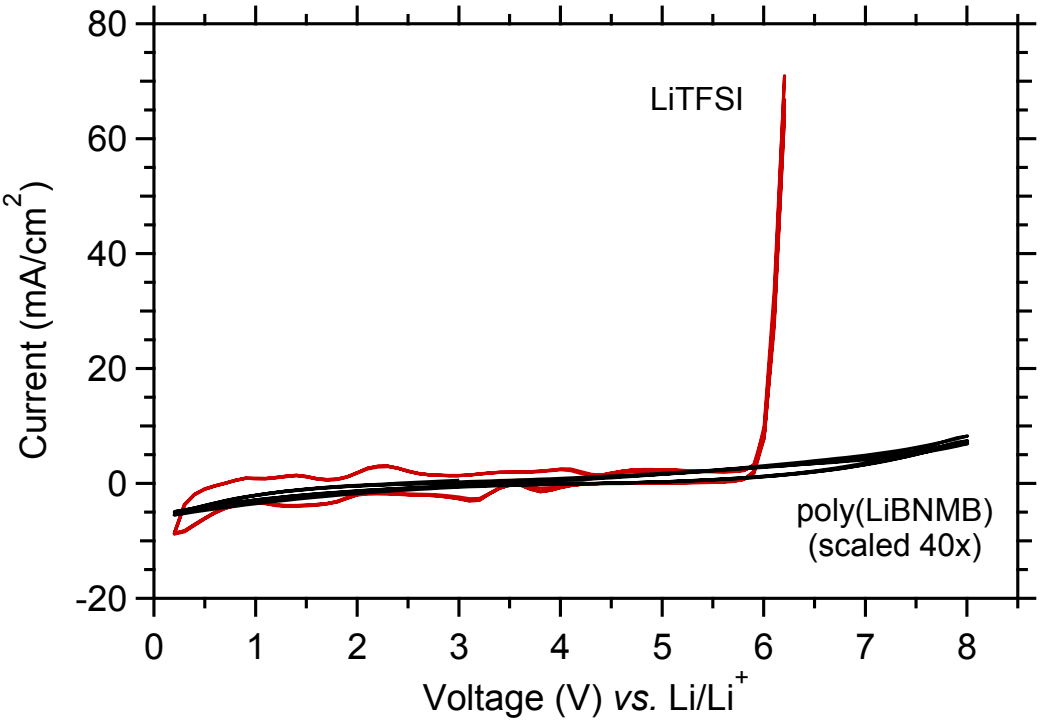

Figure 4.13. Cyclic voltammograms of LiTFSI and poly(LiBNMB) in propylene carbonate using a Pt working electrode and a Li counter electrode at a sweep rate of 1 V s^{-1}. The CV of poly(LiBNMB) is scaled by a factor of 40 relative to the CV of LiTFSI in order to make the shape of the curve visible.

4.4 Conclusions

We have demonstrated the facile synthesis of a new polymeric, lithium single-ion conductor based on lithium bis(malonate)borate by step growth polymerization using ADMET or thiol-ene reactions. Liquid electrolytes comprising the ADMET polymer poly(LiBNMB) dissolved in propylene carbonate exhibit high lithium ion-conductivities similar to solutions of LiTFSI at the same lithium-ion concentration ($[Li^+]$ = 0.2 M). Remarkably, poly(LiBNMB) forms stable solid electrolyte interphase layers at the electrolyte/electrode interface, which are ultimately stable over the electrochemical window 50 mV – 8 V vs. Li/Li^+. We tentatively attribute the stability of this SEI layer to the decomposition of the polymer at the electrode interface to form a multivalent protective layer that prevents further electrolyte decomposition. This line of reasoning suggests that polymeric lithium salt electrolytes could be useful precursors for SEI layer formation for improved lithium-ion battery performance. Future studies include investigating the performance of this lithium single-ion conducting electrolyte in a lithium ion battery full cell test.

Based on our preliminary successes in producing lower T_g polymers derived from LiBNMB through the introduction of ethylene glycol linkers via thiol-ene polymerizations, we suggest continuing studies of various dithiol linkers, including branched dithiols and dithiols incorporating longer ethylene glycol units, toward the development of solvent-free lithium single-ion conducting polymers.

4.5 References

(1) Goodenough, J. B.; Kim, Y. *Chem. Mater.* **2010**, *22*, 587.

(2) Marom, R.; Amalraj, S. F.; Leifer, N.; Jacob, D.; Aurbach, D. *J. Mater. Chem.* **2011**, *21*, 9938.

(3) Xu, K. *Chem. Rev.* **2004**, *104*, 4303.

(4) Wanakule, N. S.; Panday, A.; Mullin, S. A.; Gann, E.; Hexemer, A.; Balsara, N. P. *Macromolecules* **2009**, *42*, 5642.

(5) Young, W. S.; Epps, T. H. *Macromolecules* **2009**, *42*, 2672.

(6) Etacheri, V.; Marom, R.; Elazari, R.; Salitra, G.; Aurbach, D. *Energy Environ. Sci.* **2011**, *4*, 3243.

(7) Manthiram, A. *J. Phys. Chem. Lett.* **2011**, *2*, 176.

(8) Doyle, M.; Fuller, T. F.; Newman, J. *Electrochim. Acta* **1994**, *39*, 2073.

(9) Ghosh, A.; Wang, C.; Kofinas, P. *J. Electrochem. Soc.* **2010**, *157*, A846.

(10) Ryu, S.-W.; Trapa, P. E.; Olugebefola, S. C.; Gonzalez-Leon, J. A.; Sadoway, D. R.; Mayes, A. M. *J. Electrochem. Soc.* **2005**, *152*, A158.

(11) Ioannou, E. F.; Mountrichas, G.; Pispas, S.; Kamitsos, E. I.; Floudas, G. *Macromolecules* **2008**, *41*, 6183.

(12) Tada, Y.; Sato, M.; Takeno, N.; Nakacho, Y.; Shigehara, K. *Chem. Mater.* **1994**, *6*, 27.

(13) Sun, X.; Hou, J.; Kerr, J. *Electrochim. Acta* **2005**, *50*, 1139.

(14) Matsumoto, K.; Endo, T. *J. Polym. Sci., Part A: Polym. Chem.* **2010**, *48*, 3113.

(15) Dou, S. C.; Zhang, S. H.; Klein, R. J.; Runt, J.; Colby, R. H. *Chem. Mater.* **2006**, *18*, 4288.

(16) Ohno, H.; Ito, K. *Chem. Lett.* **1998**, 751.

(17) Matsumoto, K.; Endo, T. *J. Polym. Sci., Part A: Polym. Chem.* **2011**, *49*, 1874.

(18) Siska, D. P.; Shriver, D. F. *Chem. Mater.* **2001**, *13*, 4698.

(19) Bouchet, R.; Maria, S.; Meziane, R.; Aboulaich, A.; Lienafa, L.; Bonnet, J.-P.; Phan, T. N. T.; Bertin, D.; Gigmes, D.; Devaux, D.; Denoyel, R.; Armand, M. *Nat. Mater.* **2013**, *12*, 452.

(20) Xu, W.; Williams, M. D.; Angell, C. A. *Chem. Mater.* **2002**, *14*, 401.

(21) Matsumi, N.; Sugai, K.; Sakamoto, K.; Mizumo, T.; Ohno, H. *Macromolecules* **2005**, *38*, 4951.

(22) Aoki, T.; Konno, A.; Fujinami, T. *Electrochim. Acta* **2004**, *50*, 301.

(23) Nishihara, Y.; Miyazaki, M.; Tomita, Y.; Kadono, Y.; Takagi, K. *J. Polym. Sci., Part A: Polym. Chem.* **2008**, *46*, 7913.

(24) Liang, S. W.; Choi, U. H.; Liu, W. J.; Runt, J.; Colby, R. H. *Chem. Mater.* **2012**, *24*, 2316.

(25) Xu, W.; Angell, C. A. *Electrochem. Solid-State Lett.* **2001**, *4*, E1.

(26) Sun, X. G.; Kerr, J. B.; Reeder, C. L.; Liu, G.; Han, Y. B. *Macromolecules* **2004**, *37*, 5133.

(27) Sun, X. G.; Kerr, J. B. *Macromolecules* **2006**, *39*, 362.

(28) Zhu, Y. S.; Gao, X. W.; Wang, X. J.; Hou, Y. Y.; Liu, L. L.; Wu, Y. P. *Electrochem. Commun.* **2012**, *22*, 29.

(29) Zhu, Y. S.; Wang, X. J.; Hou, Y. Y.; Gao, X. W.; Liu, L. L.; Wu, Y. P.; Shimizu, M. *Electrochim. Acta* **2013**, *87*, 113.

(30) Kofron, W. G.; Baclawski, L. M. *J. Org. Chem.* **1976**, *41*, 1879.

(31) Baumann, H.; Buhler, M.; Fochem, H.; Hirsinger, F.; Zoebelein, H.; Falbe, J. *Angew. Chem. Int. Edit. Engl.* **1988**, *27*, 41.

(32) Schreiner, C.; Amereller, M.; Gores, H. J. *Chem. Eur. J.* **2009**, *15*, 2270.

(33) Sun, X. G.; Reeder, C. L.; Kerr, J. B. *Macromolecules* **2004**, *37*, 2219.

(34) Opper, K. L.; Wagener, K. B. *J. Polym. Sci., Part A: Polym. Chem.* **2011**, *49*, 821.

(35) Atallah, P.; Wagener, K. B.; Schulz, M. D. *Macromolecules* **2013**, DOI: 10.1021/ma400067b.

(36) Hiemenz, P. C.; Lodge, T. *Polymer chemistry*; 2nd ed.; CRC Press: Boca Raton, 2007.

(37) Hoyle, C. E.; Lee, T. Y.; Roper, T. *J. Polym. Sci., Part A: Polym. Chem.* **2004**, *42*, 5301.

(38) Hoyle, C. E.; Bowman, C. N. *Angew. Chem.* **2010**, *49*, 1540.

(39) Hayamizu, K.; Aihara, Y.; Arai, S.; Martinez, C. G. *J. Phys. Chem. B* **1999**, *103*, 519.

(40) Xu, K.; von Cresce, A. *J. Mater. Chem.* **2011**, *21*, 9849.

(41) Ue, M.; Takeda, M.; Takehara, M.; Mori, S. *J. Electrochem. Soc.* **1997**, *144*, 2684.

CHAPTER 5

RHEOLOGICAL AND ION TRANSPORT PROPERTIES OF LITHIUM SINGLE-ION CONDUCTING NETWORK GELS SYNTHESIZED BY THIOL-ENE CHEMISTRY

5.1 Introduction

Rechargeable lithium ion batteries are the dominant technology for electrochemical energy storage in portable electronics due to their high energy density and long cycling lifetime.[1,2] To extend this technology into larger markets such as automotive batteries and electrical energy grid storage, vast improvements in the safety and performance of lithium ion batteries are required.[3] While promising new developments in high voltage cathode and high capacity anode materials are helping to realize batteries with higher power densities, improvements in battery electrolytes must not be overlooked.[4]

Currently, commercial battery electrolytes rely on the combination of a porous separator imbibed with a nonaqueous liquid electrolyte, which comprises an organic solvent and a dissolved lithium salt.[5] The separator in this cell design is typically a porous polyolefin mat (e.g. high density polyethylene) that serves to physically separate the electrodes to prevent short circuiting of the battery, and the liquid electrolyte allows for the exchange of lithium ions between electrodes. This cell construction suffers from significant safety hazards associated with liquid electrolyte leakage and the formation of lithium dendrites, both of which may lead to thermal runaway and catastrophic failure of the battery.[6]

Solid polymer electrolytes and network gel electrolytes offer the advantage of combining the functions of both the separator and the electrolyte into a single material.[7,8] Solid polymer electrolytes comprised of lithium salt solutions in high dielectric polymers such as poly(ethylene oxide) exhibit low ionic conductivities that stem from the dependence of ion motion on polymer segmental dynamics.[9] Alternatively, the covalent crosslinks of a network gel electrolytes offer mechanical robustness and rigidity, while the liquid-like nature of the contained electrolyte solution maintains higher ionic conductivity.

Although numerous network gel electrolytes for lithium ion batteries have been reported in the literature,[10-19] these electrolytes (and *most* commonly used lithium electrolytes) exhibit low lithium ion transference numbers:

$$t_{\mathrm{Li+}} = \frac{I_{Li+}}{I_{total}} = \frac{I_{Li+}}{I_{anion}+I_{Li+}} \qquad (5.1)$$

where $I_{\mathrm{Li+}}$ is the current due to lithium ion motion and I_{total} is the total current due to the motion of both Li^+ and the charge compensating counterion. Thus, $t_{\mathrm{Li+}}$ reflects the total fraction of charge in the cell carried by lithium ions, and $t_{\mathrm{Li+}} \sim 0.2\text{-}0.4$ for common electrolytes such as LiTFSI in propylene carbonate or poly(ethylene oxide).[20] These low transference numbers indicate that the anions are significantly more mobile than the cations, which is due to lithium ion chelation by the Lewis basic atoms in the liquid or polymeric electrolytes. Low $t_{\mathrm{Li+}}$ values lead to losses in current density and the generation of electrolyte concentration gradients that diminish battery performance.[21] Polymeric lithium single-ion conductors, in which negatively charged counterions are immobilized in a polymer matrix with mobile Li^+ cations, mitigate these problems as they exhibit transference numbers $t_{\mathrm{Li+}} \sim 1.0$.

Only a few examples of lithium single-ion conducting network gel electrolytes have been studied in detail. Kerr and coworkers described the synthesis and electrochemical characterization of several lithium single-ion conducting networks derived from comb-shaped polyacrylates[22] or polyethers[23,24] bearing pendant vinyl groups that were covalently crosslinked by hydrosilylation with a bis(silane) based on a lithium bis(malonato)borate salt. The ionic conductivities of the acrylate-based networks were generally lower than those of the polyether networks, as a consequence of the lower glass transition temperature (T_g) of latter systems. Introduction of ethylene carbonate/ethylmethyl carbonate (1:1 *w*/*w*) was found to increase the conductivities of these gels due to increased lithium-ion dissociation in the higher dielectric solvent. Since the network crosslinker is the sole source of lithium salt in these systems, Kerr and co-workers could not deconvolute the relative contributions of lithium ion concentration and crosslink density on ionic conductivity. Endo and coworkers recently developed an epoxy network gel electrolyte that incorporates covalently tethered lithium sulfonates[25] and lithium sulfonylimides[26] in a polymer matrix. The lower degree of dissociation of the lithium sulfonates as compared to the sulfonylimides manifested the significantly lower lithium conductivities of the sulfonated materials. They also found that the lithium conductivity could be modestly increased by increasing the amount of Li^+ salt-bearing monomer up to 25 wt%. These epoxy networks also exhibit substantially greater conductivities upon swelling with propylene carbonate. However, the latter studies maintained stoichiometric balance between epoxy monomer units and aliphatic diamine hardener units, preventing analysis of the effects of crosslink density on ionic conductivity.

The formation of structurally uniform network gels that exhibit high lithium ion conductivities requires the development of highly efficient, step-growth crosslinking polymerizations, as exemplified by the aforementioned materials derived from nucleophilic epoxide ring-opening and Pt-catalyzed hydrosilylation reactions. One powerful, yet under-utilized tool for the synthesis of network gels is the thiol-ene reaction, a highly efficient anti-Markovnikov addition of an alkylthiol S-H bond across an olefin to yield a thioether linkage. Bowman and Hoyle, among others, have recently synthesized numerous network polymers and polymer gels using thiol-ene reactions.[27,28] Reaction of di-olefins with multifunctional thiols having three or more S-H moieties results in the formation of crosslinked polymer networks. The step-growth nature of thiol-ene crosslinking polymerizations drives gelation at high conversions relative to chain growth crosslinking polymerizations, allowing the polymerization to proceed essentially to completion to yield a homogenously crosslinked gel with few defects (loops and free chain ends).[29,30] This situation is quite different from chain-growth crosslinking polymerizations (e.g. acrylates, styrenics) that reach the gel point at low monomer conversions to yield more heterogeneous gels.

To date, only two reports have described the use of thiol-ene crosslinking polymerizations to produce crosslinked gel electrolytes for lithium ion batteries. Tew and coworkers recently described the synthesis of crosslinked, elastomeric networks comprised of poly(ethylene oxide) and poly(dimethylsiloxane) segments end-functionalized with norbornene moieties, which were crosslinked with a simple trithiol. In these systems, the ionic conductivities scale with the concentration of added lithium salt.[31] Even more recently, Johansson and coworkers formed crosslinked, solid polymer electrolytes from the reaction of simple trithiols

with mixtures of telechelic and semi-telechelic methacryloyl poly(ethylene oxide) segments.[32] By varying the relative amounts of the telechelic and semi-telechelic building blocks and the trithiol crosslinker, they varied the crosslink densities within these materials. They observed that increased crosslinking by thiols (as opposed to chain propagation of dimethacrylates) both lowers and narrows the breadth of the T_g of the material, leading to increases in ionic conductivity. They also demonstrated that these thioether-containing networks exhibited an electrochemical window between 2.0-6.0 V (*vs.* Li/Li^+). Therefore, these studies demonstrate the utility of thiol-ene chemistry in the synthesis of polymeric electrolytes.

In this chapter, we explore the thiol-ene crosslinking polymerization chemistry of lithium bis(non-8-enyl-malonato) (LiBNMB) to generate mechanically robust lithium single-ion conducting network gel electrolytes toward the development of robust electrolyte/separator hybrids for lithium ion batteries. This work builds on our results in Chapter 4, where we described the synthesis of LiBNMB and its subsequent polymerization by acyclic diene metathesis (ADMET) and by thiol-ene polymerizations to yield well-defined linear polymers with high conductivities and unusually wide electrochemical stability windows in propylene carbonate solution. By conducting thiol-ene copolymerizations of LiBNMB with mixtures of dithiols and trithiols under stoichiometric balance of olefins to thiols in propylene carbonate, we produce a series of network gel electrolytes with varying crosslink densities and thus varied gel moduli. Within this series of gels, we demonstrate qualitatively that more tightly crosslinked gels exhibit larger elastic storage moduli, which are inversely correlated with the total ionic conductivities of the gels. Variable temperature conductivity studies also demonstrate that ion conduction exhibits Arrhenius behavior, which suggests a solvent-mediated lithium ion transport

mechanism. Finally, we directly demonstrate the lithium single-ion conducting nature of these networks by subjecting them to charge-discharge cycles in a symmetrical Li/Li cell.

5.2 Experimental

Materials. Lithium bis(non-8-enyl-malonato) borate (LiBNMB) was synthesized as described in Chapter 4. All other chemicals were purchased from Sigma-Aldrich Chemical Company (Milwaukee, WI). 1,6-Hexanedithiol was distilled under reduced pressure. Trimethylpropane tris(3-mercaptopropionate) was purified by passing through a plug of activated silica under inert atmosphere. Propylene carbonate was distilled from CaH_2 under reduced pressure.

NMR Spectroscopy. ^{1}H NMR spectra were recorded on a Bruker Avance-400 MHz spectrometer and were referenced relative to the residual protiated solvent peak.

Infrared Spectroscopy. IR spectra were recorded on a Bruker Tensor FT-IR from 4000 – 800 cm^{-1} using a diamond crystal attenuated total reflectance (ATR) stage.

Thermogravimetric Analysis. The thermal stability of gels was measured on a TA Instruments Q500 Thermogravimetric Analyzer using a ramp rate of 10 °C min^{-1} with under either an $N_2(g)$ or $O_2(g)$ purge (50 mL min^{-1}) over a temperature range 25-600 °C.

Synthesis of Gels. Inside of a glovebox under an argon atmosphere, 1,6-hexanedithiol (dithiol), trimethylpropane tris(3-mercaptopropionate) (trithiol), propylene carbonate, lithium bis(non-8-enyl-malonato) borate (LiBNMB), and 2,2′-azobis(isobutyronitrile) (AIBN) were weighed into 20 mL scintillation vials that were capped and sealed with electrical tape. These solutions were prepared with a relatively constant concentration of the lithium salt [Li(BNMB)]

= 0.91 M in propylene carbonate, with varying amounts of dithiol and trithiol with the stoichiometric balance [olefins] = [thiols] to obtain the desired crosslink densities. The AIBN loading was 5 mol% with respect to [olefin]. The experimental molar ratios of [dithiol]/[trithiol] = 0.0, 0.45, 1.06, 2.84. The vials were taken out of the glovebox and mixed using a vortex mixer for 2 min, followed by sonication for 2 min, followed by centrifugation for 10 min before returning them to the glovebox. The solutions were cured in a custom-made stainless steel mold, consisting of a solid bottom plate and a top plate with five 25 mm diameter holes secured by eight bolts. The walls of the wells were covered with Teflon tape to mitigate wetting of the walls by the gels, which would cause the gels to adopt non-uniform thicknesses. The mold was placed on a hot plate that was heated to 60 °C. Upon reaching 60 °C, the mold was agitated to ensure the solutions uniformly covered the bottom of each well. To mitigate the loss of solvent while enabling escape of N_2(g) evolved from AIBN decomposition, the mold was loosely covered with a Teflon sheet to mitigate solvent loss. This assembly was placed inside of a plastic bag, and the gels were allowed to cure at 60 °C for a total of 3 h. Upon slow cooling to 22 °C overnight, the free-standing gels were removed from the mold. Three 8.5 mm disks of each gel were punched out of these films using a hole punch for electrochemical impedance spectroscopy and rheology measurements. The disks were stored under argon.

Dynamic Mechanical Spectroscopy. Rheological measurements employed a TA Instruments ARES strain-controlled rheometer fitted with 8 mm diameter parallel plates. Dynamic strain sweep measurements conducted at 40 °C established that strains between 0.1 and 10.0 % resulted in a linear viscoelastic response. Isothermal dynamic frequency sweeps were performed at 40 °C at 1 % strain in the frequency range $0.1 \leq \omega \leq 10$ Hz. Isochronal dynamic

temperature sweeps were performed using $\omega = 1$ Hz with a 1 % strain between $T = 40 – 130$ °C, using a heating ramp rate of 2 °C min^{-1}.

Electrochemical Impedance Spectroscopy (EIS). The ionic conductivities of gels were measured using electrochemical impedance spectroscopy (Metrohm Autolab, PGSTAT302N & FRA32M, Nova 1.10 software) over a frequency range $0.1 \leq \omega \leq 10^6$ Hz with an amplitude of 50 mV. The gel disks were loaded into a hermetically sealed, custom-built, two-electrode cell equipped with stainless steel blocking electrodes. The distance between electrodes was 0.27 mm. Polymer network gel samples with thicknesses ~0.4 mm and diameters ~8.5 mm of each disk were measured using VWR-brand digital calipers (± 0.01 mm). Gels were loaded into the cell in a glovebox under argon atmosphere to avoid water uptake then brought out of the glovebox for impedance measurements. Ten duplicate measurements were performed on each of three different polymer gel disks for each of four crosslink densities.

The different resistances obtained from EIS were determined by fitting the data to an equivalent $[R_s(R_{if}Q_{dl})(R_{be}Q_{be})]$ circuit (R_i = resistor, Q_i = constant phase element) in the Nova software. The resistance to ion motion in the bulk of the gel, which we hereafter refer to as the "solution" resistance (R_s), may be extracted by extrapolation of the high frequency intercept (near the origin) of the high-frequency semicircle of the Nyquist plot (imaginary impedance, $Z''(\omega)$, *vs.* real impedance, $Z'(\omega)$). The diameter of the high-frequency semicircle in the Nyquist plot represents the interfacial resistance (R_{if}). The sum represents the total resistance of the electrolyte ($R_{total} = R_s + R_{if}$) and corresponds to the lower frequency intercept (farther from the origin) of the high frequency semicircle in the Nyquist plot. In cases where a high-frequency semicircle in the Nyquist plot was not visible or could not be fit by the Nova software, the

closest approach to the real axis or intercept of the real axis was used as the total resistance (R_{total}). Solution conductivity (σ_s) values were then calculated using the equation $\sigma_s = L / AR_s$, where L is the thickness of the gel disk and A is the cross-sectional area of the gel disk. Similarly, total conductivity (σ_{total}) values were calculated using the equation $\sigma_{total} = L / AR_{total}$,

For variable temperature studies, the aforementioned samples cell was loaded with a gel disk, connected to the potentiostat via high-temperature shielded wire, and placed in a Thermo-Scientific vacuum oven. The sample was equilibrated at each temperature for at least ten minutes as determined by stable readings from a digital thermocouple, after which at least three duplicate measurements were obtained in the frequency range of $10 \leq \omega \leq 10^6$ Hz with an applied potential amplitude of 50 mV.

Charge/Discharge Chronopotentiometry of Li/Li Symmetrical Cells. The charge/discharge behavior of a symmetrical Li/Li cell with the crosslinked gel as the separator/electrolyte was measured by chronopotentiometry (Metrohm Autolab, PGSTAT302N). A gel disk was placed between two 1.0 mm thick lithium electrodes in a hermetically-sealed, custom-built, two-electrode cell with stainless steel blocking electrodes. While the cell was subjected to four charge/discharge cycles consisting of 10 min resting (no current), 1 h charge (+ 2.0 μA), 10 min rest, then 1 h discharge (– 2.0 μA), the potential was recorded as a function of time.

5.3 Results and Discussion

5.3.1 Synthesis of Thiol-ene Network Gels.

We prepared a series of lithium single-ion conducting network polymer gels with varied degrees of crosslink density, as potentially new, multifunctional separator/electrolyte materials for lithium ion batteries. Based on our successful linear copolymerizations of lithium bis(non-8-enyl-malonato) borate (LiBNMB) with α,ω-dithiols via thiol-ene chemistry in Chapter 4, we sought to extend this facile chemistry to produce crosslinked polymer network gels. Our synthetic approach relies on the free-radical thiol-ene crosslinking polymerization of the diolefin LiBNMB with varying amounts of 1,6-hexanedithiol as a chain-extending monomer and trimethylpropane tris(3-mercaptopropionate) as a chain-branching (or crosslinking, CL) monomer in propylene carbonate (Scheme 5.1). In order to directly study the effects of crosslink density on the ionic conductivities of these gels, we prepared each sample with a constant lithium ion concentration of $[Li^+]$ = 0.91 M. Since we sought to correlate the crosslink density with the conductivity profiles of these gels, our crosslinking polymerizations were conducted in a manner that maintained the stoichiometric balance between olefin and total number of thiol functional groups within experimental error, while systematically varying the ratio of dithiol to trithiol monomer units. Four crosslinked gels were prepared containing 26, 48, 69, and 100 mol% trithiol relative to the total thiol content in the reaction. Hereafter, the resulting gels will be referred to as 26CL, 48CL, 69CL, and 100CL to reflect the amount crosslinking monomer used to make the gel, whereby 26CL is most lightly crosslinked and 100 CL is most densely crosslinked.

Scheme 5.1. Synthesis of LiBNMB thiol-ene gels.

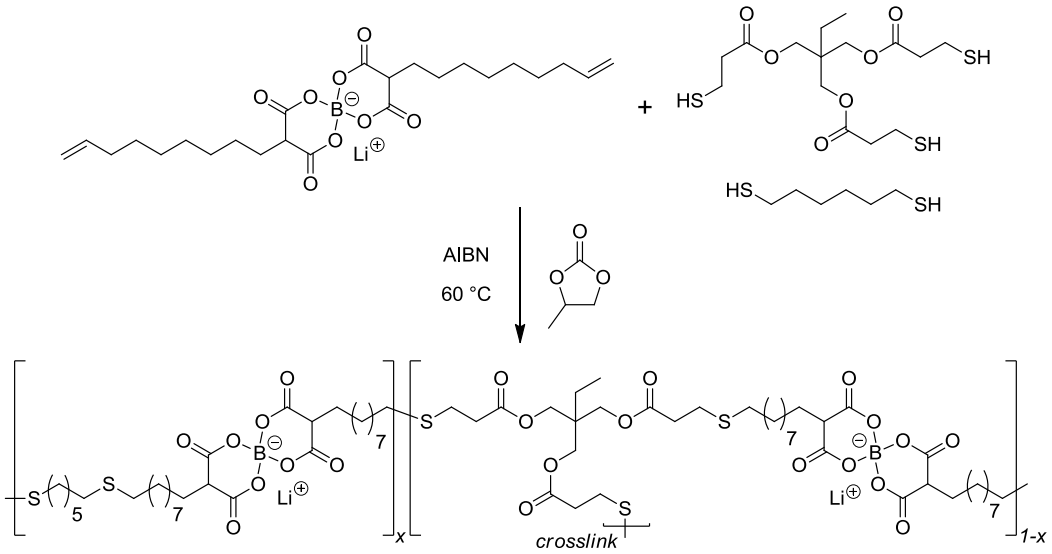

Thiol-ene polymerization may be initiated by a wide variety of free radical sources, which led us to explore several radical initiators for our crosslinking polymerizations. In spite of the ubiquitous use of photoinitiators such as 2,2-dimethoxy-2-phenylacetophenone in thiol-ene polymerizations,[33] the formation of electrochemically unstable aldehyde reaction byproducts prevented our use of these reagents. Thus, we considered acyl peroxide and azo-nitrile initiators that generate more electrochemically benign byproducts that are tolerable in a lithium ion battery.[34] Attempts to use benzoyl peroxide (BPO) at 85 °C (decomposition half-life $t_{1/2}$ = 10 h at 73 °C) resulted in non-cured solutions after 15 hours. Lauroyl peroxide (LPO) at 70 °C ($t_{1/2}$ = 10 h at 64 °C) was marginally more effective, yielding solid gels for samples containing 69 and 100 mol% trithiol. Samples containing lower trithiol crosslinker concentrations furnished only partially cured gels. We ascribe the latter result to the sparing solubility of LPO in the reaction mixture, which greatly reduces the number of active radicals available to initiate polymerization.

Thiol-ene crosslinking polymerizations initiated by the free radical initiator 2,2′-azo-bis(isobutyronitrile) (AIBN) at 60 °C ($t_{1/2}$ = 10 h at 60 °C) led to the formation of robust crosslinked gels after 3 hours. We initially cured these gels as thin films (~ 0.25 mm thick) between glass plates under an inert atmosphere in an oven. However, this sample curing geometry led to the trapping of numerous bubbles in the film, probably as a result of $N_2(g)$ liberation upon AIBN decomposition and possible propylene carbonate volatilization. Attempts to mitigate these effects by reducing the AIBN loading in the polymerization reaction led to poorly formed gels that tended to rip upon separation of the glass plates.

Since the gels with trapped gas bubbles had ill-defined cross-sectional areas that would prevent quantitative analyses of their conductivity and rheology data, we devised a new sample geometry for gel curing. The gels were cured in a stainless steel mold comprising five isolated wells open to an inert atmosphere, with a detachable bottom plate to facilitate the removal of the disks after curing. The mold is pictured in Figure A4.1 in Appendix 4. By heating the crosslinking polymerization formulations in the metal mold heated to 60 °C from the bottom in open wells, the gels were cured from the bottom to the top of the well to obviate trapping of gas bubbles. We note that a small amount of propylene carbonate did volatilize into the headspace above each sample well during the 3 h reaction course; however, this effect was minimal and was systematically observed in each sample well.

The solid gels obtained from these AIBN-initiated thiol-ene polymerizations were subjected to Fourier-transform infrared (FTIR) spectroscopy to assess the extent of functional group conversion and crosslinking. Previous reports have established that the extent of reaction in thiol-ene polymerizations may be monitored by FTIR, by monitoring the disappearance of the

thiol S-H stretching band near 2570 cm^{-1}.[35] While we did not monitor the reaction conversion *in situ*, we confirmed the absence of unreacted thiols by FTIR of each of the gels post-polymerization. The absence of any peaks in the region near 2570 cm^{-1} in Figure 5.1 indicates a high degree of thiol consumption, implying that each of the polymerizations went to high conversion. For comparison, IR spectra of neat trithiol and trithiol in propylene carbonate are provided in Figure A4.2 in Appendix 4.

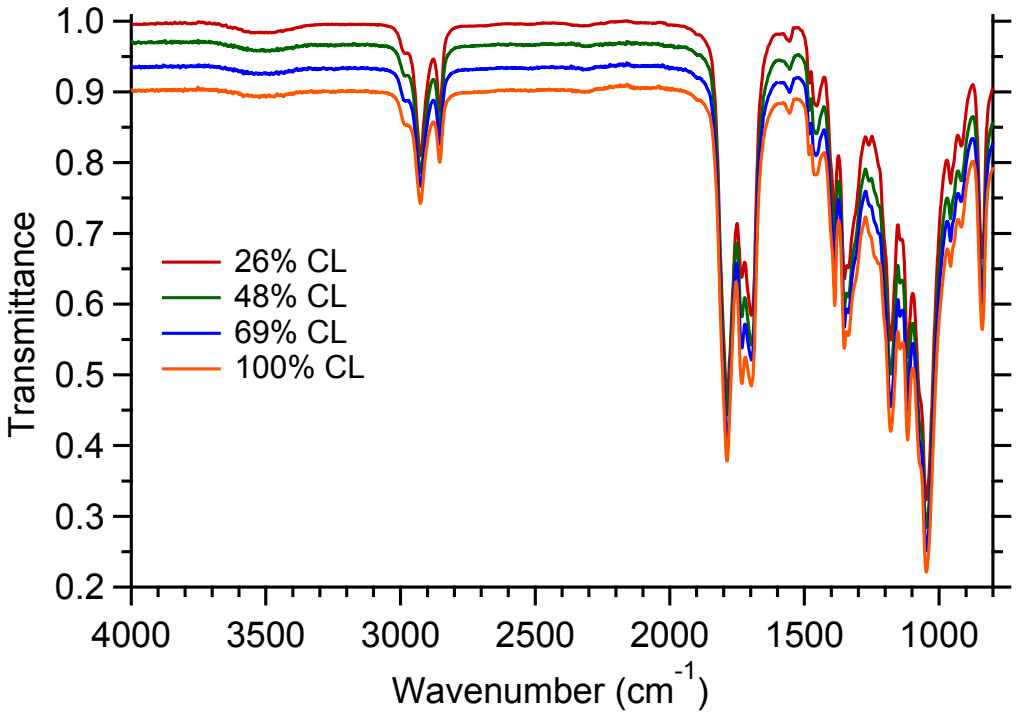

Figure 5.1. FTIR spectra of crosslinked gels do not exhibit any bands near 2570 cm^{-1}, indicating the absence of free thiols, which implies the nearly complete reaction extent in each of these crosslinking polymerization reactions. Spectra are vertically offset for clarity.

We characterized the thermal decomposition profile of 100CL by thermogravimetric analysis (TGA) under nitrogen and under oxygen, in order to assess its thermal stability. The thermal stability of the gel is insensitive to the presence or absence of oxygen, as indicated by the data shown in Figure 5.2. TGA indicates a weight loss of ~ 45 wt% up to 230 °C, which we primarily attribute to volatilization of propylene carbonate (*b.p.* 240 °C). Given that the gels are comprised of only ~ 40 wt% PC, this result also suggests some decomposition of the polymer network. This is consistent with our previous TGA analyses of linear thiol-ene polymers in Chapter 4 (Figure 4.3), where we observed initial weight loss near 200 – 250 °C. Events related to polymer network decomposition begin above ~ 250 °C, with full sample decomposition by ~ 475 – 500 °C.

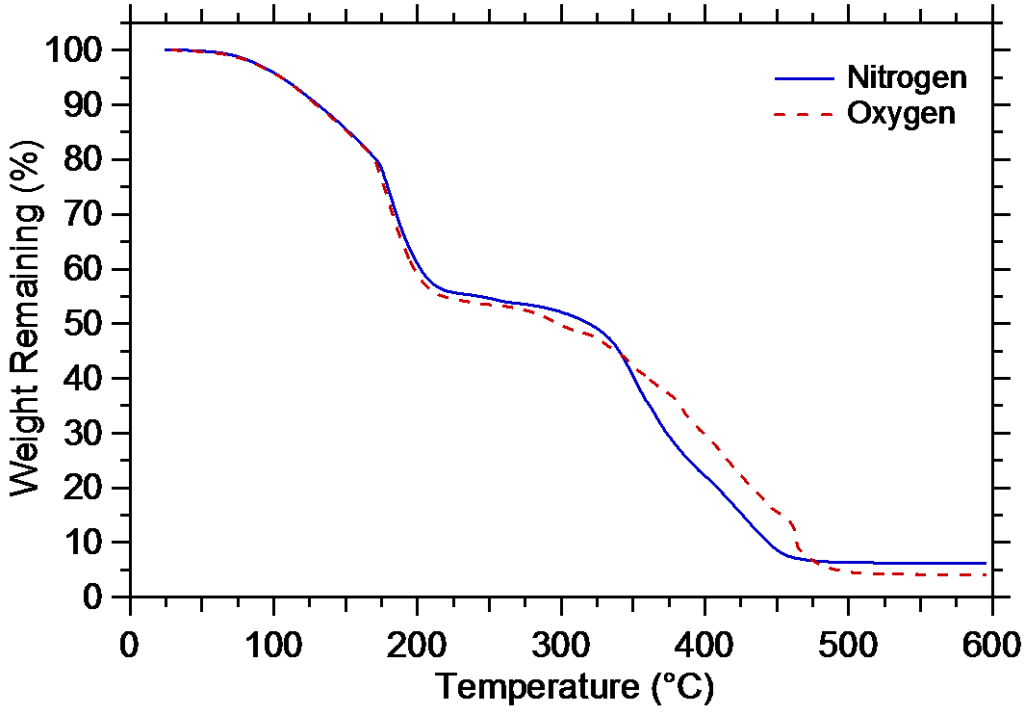

Figure 5.2. Thermogravimetric analysis of 100CL under both $N_2(g)$ and $O_2(g)$, indicating two decomposition events: (1) loss of volatile propylene carbonate up to 250 °C, and (2) polymer network decomposition beginning at ~200-250 °C. The relative insensitivity of this decomposition profile to the presence or absence of oxygen implies that these decomposition events are intrinsic to these crosslinked gels.

5.3.2 Rheological Analyses of Thiol-ene Network Gels.

We performed rheological studies on our network gel electrolytes, as an initial step in assessing the effects of gel modulus on ionic conductivity and to determine their ultimate utility as lithium ion battery separator/electrolyte hybrids. One distinct advantage of network gel electrolytes for lithium ion batteries is their mechanical integrity, which allows them to maintain shape for potential use in flexible batteries.[36] Desirable properties of network gel electrolytes

include sufficient mechanical strength to prevent contact between the electrodes and large elastic moduli to mitigate dendrite formation and consequent catastrophic battery failure.

The frequency-dependent rheological response of our gels as a function of crosslinking loading is depicted in plots of dynamic elastic storage shear modulus $G'(\omega)$ and loss modulus $G''(\omega)$ as a function of the frequency ω in Figure 5.3. The magnitude of $G'(\omega)$ is much larger than $G''(\omega)$ in each gel, confirming that these materials behave as crosslinked networks. The storage modulus of the gels increases with the amount of trithiol crosslinker, indicating increased crosslinker incorporation yields more tightly crosslinked networks. $G'(\omega)$ for the most lightly crosslinked gel, 26CL, exhibits a modest frequency dependence in the range $0.1 \leq \omega \leq 10$ Hz. This observation indicates that this frequency range is at the edge of the rubbery plateau region. The 48 CL gel modulus $G'(\omega)$ is higher, while the frequency dependence is substantially weaker, as anticipated. Surprisingly, 69CL and 100CL have very similar $G'(\omega)$ across the entire measured frequency range. We suspect that this similarity is due to the formation of loop defects in the 100CL network materials. Previous reports indicate that thiol propionate esters react more quickly than simple alkylthiols due to weakening of the thiol S-H bond by intermolecular hydrogen bonding to the Lewis basic ester carbonyl.[27] Thus, we envision that the polymerization rate for 26CL, 48CL, and 69CL is slower due to the differential reactivities of the dithiol chain-extender and the trithiol crosslinker, which enables formation of networks with fewer defects (loops, free chain ends) as compared to 100CL. Since 100CL will cure more quickly, the likelihood of network defects is increased, causing the gel to have a lower storage modulus than predicted.

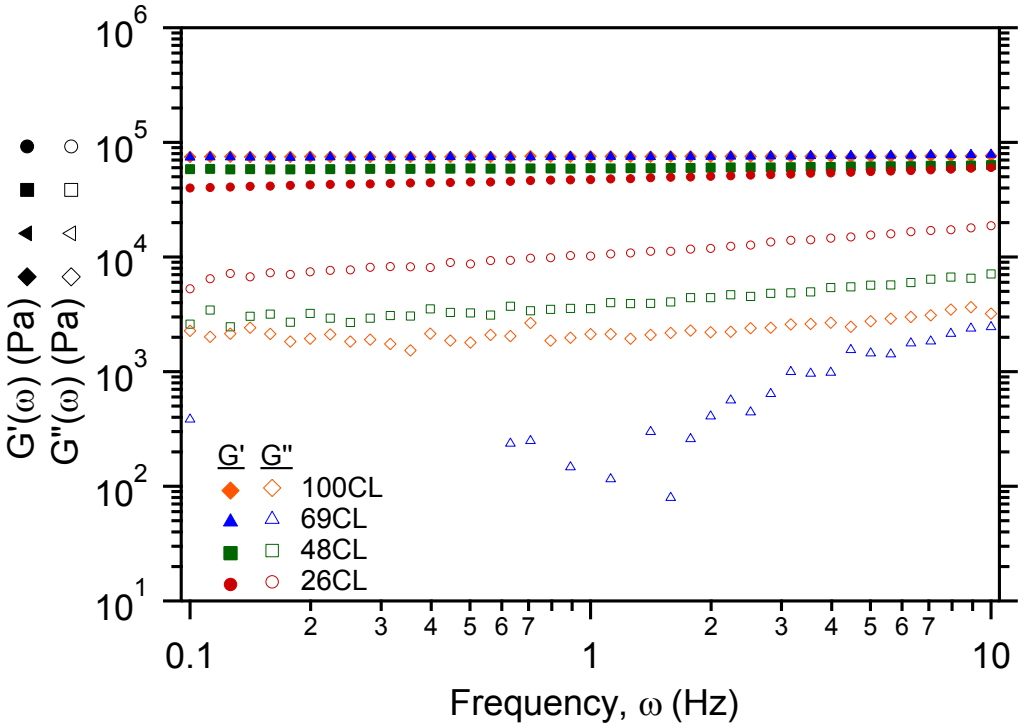

Figure 5.3. Dynamic frequency sweeps of crosslinked gels at 40 °C demonstrate nearly frequency-independent dynamic elastic storage shear moduli G′(ω) for the frequency range $0.1 \leq \omega \leq 10$ Hz (1% applied oscillatory strain) that are much larger than the loss moduli G″(ω), characteristic of a crosslinked gel. The value of G′(ω) increases slightly with increasing crosslink density.

The temperature-dependent dynamic mechanical response of the 100CL gel was investigated between $T = 40 - 130$ °C. These rheological measurements were made using a strain controlled ARES-LS2 rheometer, with which we maintained a constant normal force on the sample during the course of the experiment by adjusting the gap thickness between the parallel-plates of the rheometer. The gap expanded from an initial value of 0.55 mm at 40 °C (20 g normal force) to a value of 0.74 mm at 130 °C (140 g normal force), indicative of substantial

thermal expansion that likely arises from expansion of both the solvent and the gel. The data shown in Figure 5.4 demonstrates that G′(ω) of the gel increases by a factor of 2.6 during the heating ramp. We attribute this storage modulus increase to the evaporation of the propylene carbonate solvent in the forced convection oven used to heat the sample, which results in a stiffer material. We note that the sample thickness upon cooling decreased from 0.55 mm to 0.50 mm, consistent with solvent evaporation. A subsequent dynamic frequency sweep at 40 °C indicates an increase in modulus also consistent with the solvent loss at elevated temperature (Figure 5.5).

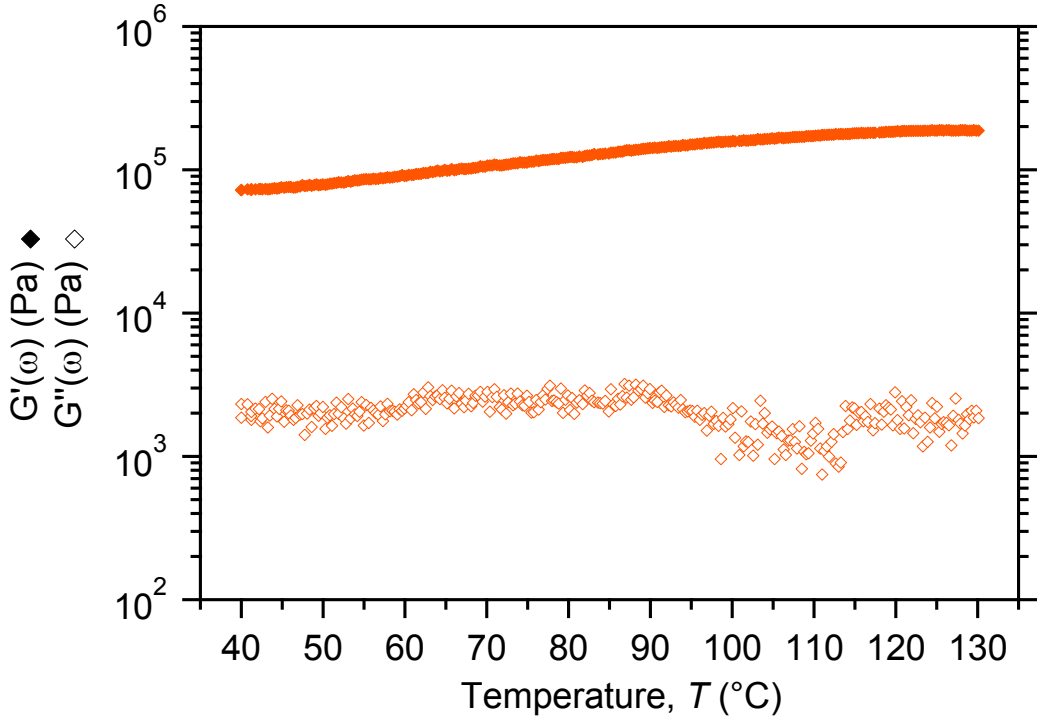

Figure 5.4. Plot of dynamic elastic storage shear modulus G′(ω) and loss modulus G″(ω) versus temperature for 100CL at a frequency ω = 1 Hz with 1% applied oscillatory strain showing an increase in G′(ω) due to evaporation of propylene carbonate.

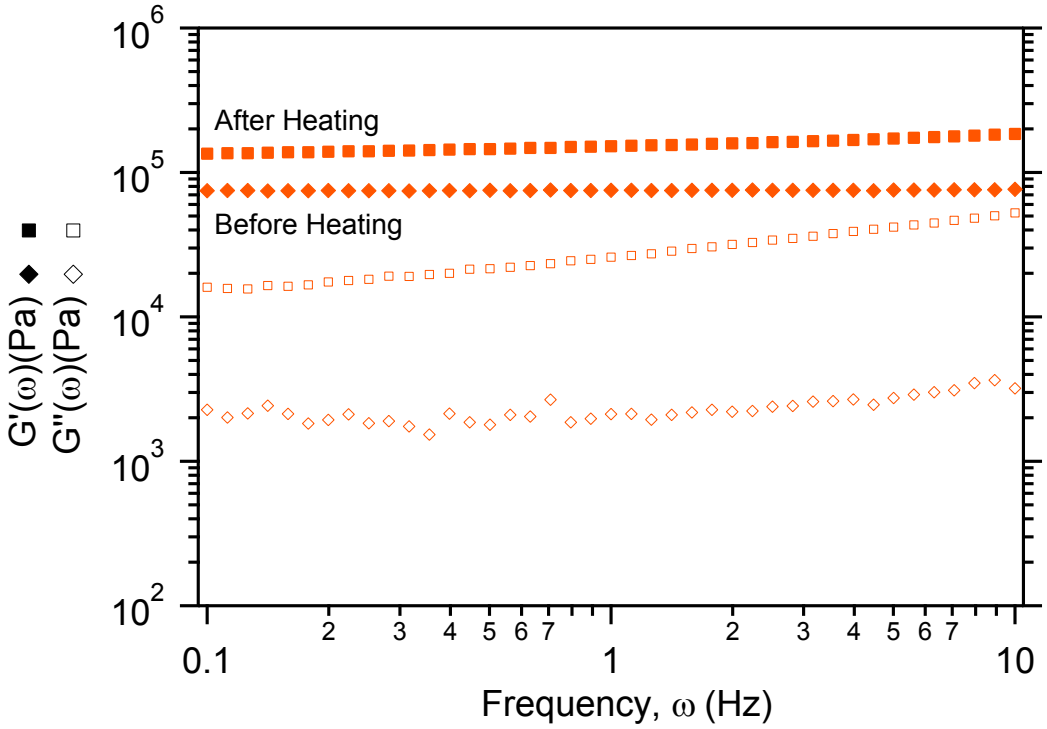

Figure 5.5. Dynamic frequency sweeps of 100CL at 40 °C before and after a temperature sweep up to 130 °C showing an increase in the elastic storage shear modulus G′(ω) for the frequency range $0.1 \leq \omega \leq 10$ Hz (1% applied oscillatory strain) after heating due to evaporation of propylene carbonate.

5.3.3 Ionic Conductivity of Thiol-ene Network Gels.

The lithium ion conductivities of the crosslinked gels were studied by electrochemical impedance spectroscopy (EIS). Gel disks were placed between two stainless steel blocking electrodes in a custom-made, hermetically sealed cell shown in Figure A5.3 of Appendix 5. Initial studies demonstrated no variation of the measured impedance response with varying set potentials (0 to 200 mV) and AC amplitudes (5 to 200 mV). Therefore, we chose a set potential of 0 mV and an AC potential amplitude of 50 mV for our impedance measurements. Over the

frequency range $0.1 \leq \omega \leq 10^6$ Hz, the Nyquist plots of the imaginary impedance $Z''(\omega)$ *vs.* real impedance $Z'(\omega)$ shown in Figure 5.6 exhibit a high frequency semicircle along with a portion of a much larger low frequency semicircle that we approximate by a capacitive slope.

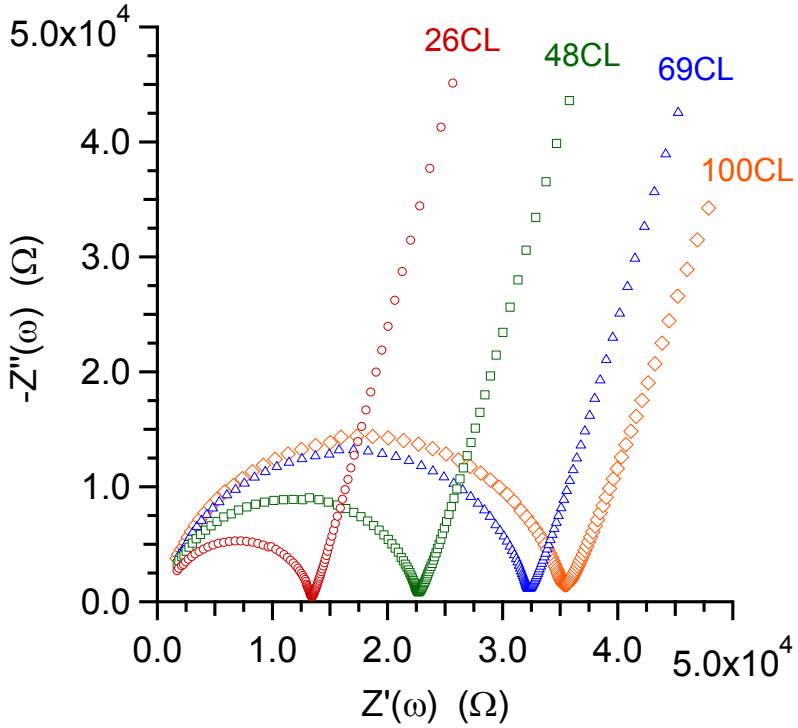

Figure 5.6. Electrochemical impedance spectroscopy Nyquist plots of imaginary impedance, $-Z''(\omega)$, *vs.* real impedance, $Z'(\omega)$, in the high frequency range ($\sim 4 \leq \omega \leq 10^6$ Hz) for crosslinked gels exhibiting a high frequency semicircle followed by a low-frequency capacitive slope.

We interpret these Nyquist plots in terms of the equivalent electrochemical circuit model depicted in Figure 5.7, in which each component physically represents a specific impedance associated with the gel, including its interfaces. Extrapolation of the semicircle to the high frequency (low $Z'(\omega)$) intercept of the real axis provides the resistance to ion motion in the bulk

of the gel, which we hereafter refer to as the solution resistance, R_s. The solution resistance depends primarily on the concentration of mobile ions in solution, with dominant contributions from ion-pair dissociation and ion solvation. The diameter of the semicircle corresponds to an interfacial resistance associated with ion transport through the electrical double layer formed at the electrode interface. Since there is a time constant associated with the formation of the double layer, there is a capacitive element associated with this interfacial impedance that gives rise to the observed semicircle in the Nyquist plot. The interfacial resistance depends on both the concentration and the diffusivity of the ions that form the electrical double layer. The sum of the solution resistance and the interfacial resistance, $R_{total} = R_s + R_{if}$, gives the total ionic resistance of the polymer gel, from which the total ionic conductivity σ_{total} may be calculated. While this sum represents the practical lithium ion conductivity for a potential battery application, the individual values of R_s and R_{if} provide molecular level insights into the physical phenomena governing ion motion in these materials. Finally, the large, low frequency slope arises from the buildup of electrical charge at the stainless steel blocking electrodes, since lithium ions cannot intercalate into or de-intercalate from them. The resistance associated with the blocking electrodes (R_{be}) is effectively infinite, so that the capacitive character dominates this element leading to the observed slope.

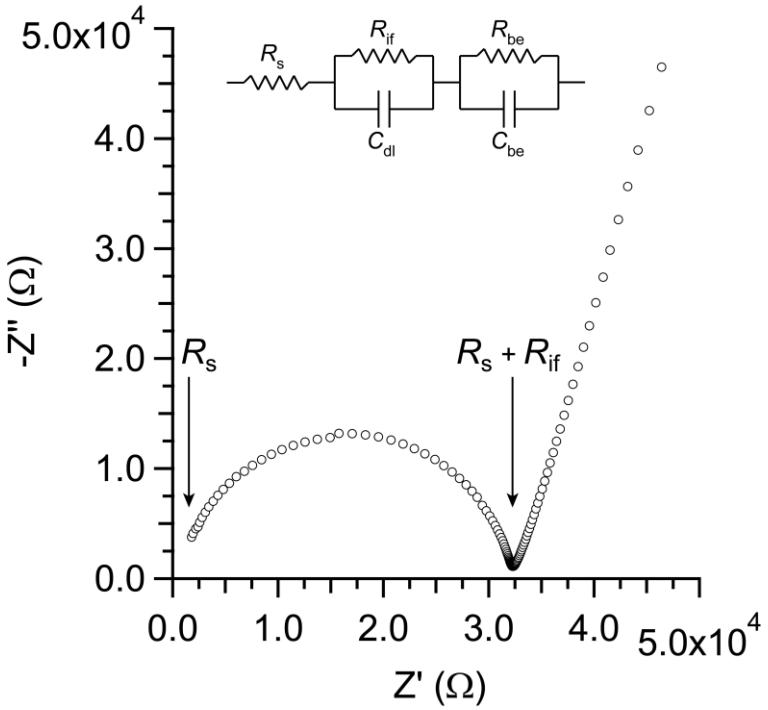

Figure 5.7. Analysis of a representative Nyquist plot from the electrochemical impedance spectroscopy of 69CL at 22 °C using stainless steel blocking electrodes in terms of an equivalent circuit. R_s = solution resistance, R_{if} = interfacial resistance, R_{be} = blocking electrode resistance, C_{dl} = double layer capacitance, C_{be} = blocking electrode capacitance.

We extracted the solution resistance and the interfacial resistance of our crosslinked gel electrolytes, in order to determine the mechanism of ion motion in the bulk gel and to assess their overall lithium conductivity for potential battery applications. From multiple measurements of R_s on each of three different disks of each sample with different crosslink densities, we determined the solution conductivities σ_s. These σ_s values were then averaged across all of the individual samples to obtain average solution conductivities for each crosslink density. These conductivities are plotted as a function of the mole fraction of trithiol crosslinker in Figure 5.8.a. The error bars

represent the experimental error propagated from the standard deviation of at least ten EIS measurements for each disk and the error associated with thickness and cross sectional area measurements of each sample. These conductivities are then averaged for each mole fraction of trithiol to give average solution conductivities, σ_s shown in Figure 5.8.b. Within experimental error, the solution conductivity depends only weakly on the crosslink density. Since lithium ion concentration is constant across all samples and the extent of ion dissociation should be constant due to the identical structure of ion pairs and solvent, this result is not unexpected. Thus, we conclude that propylene carbonate-solvated lithium ions move through the polymer matrix, in which the relatively large mesh size of the network does not impede ion motion.

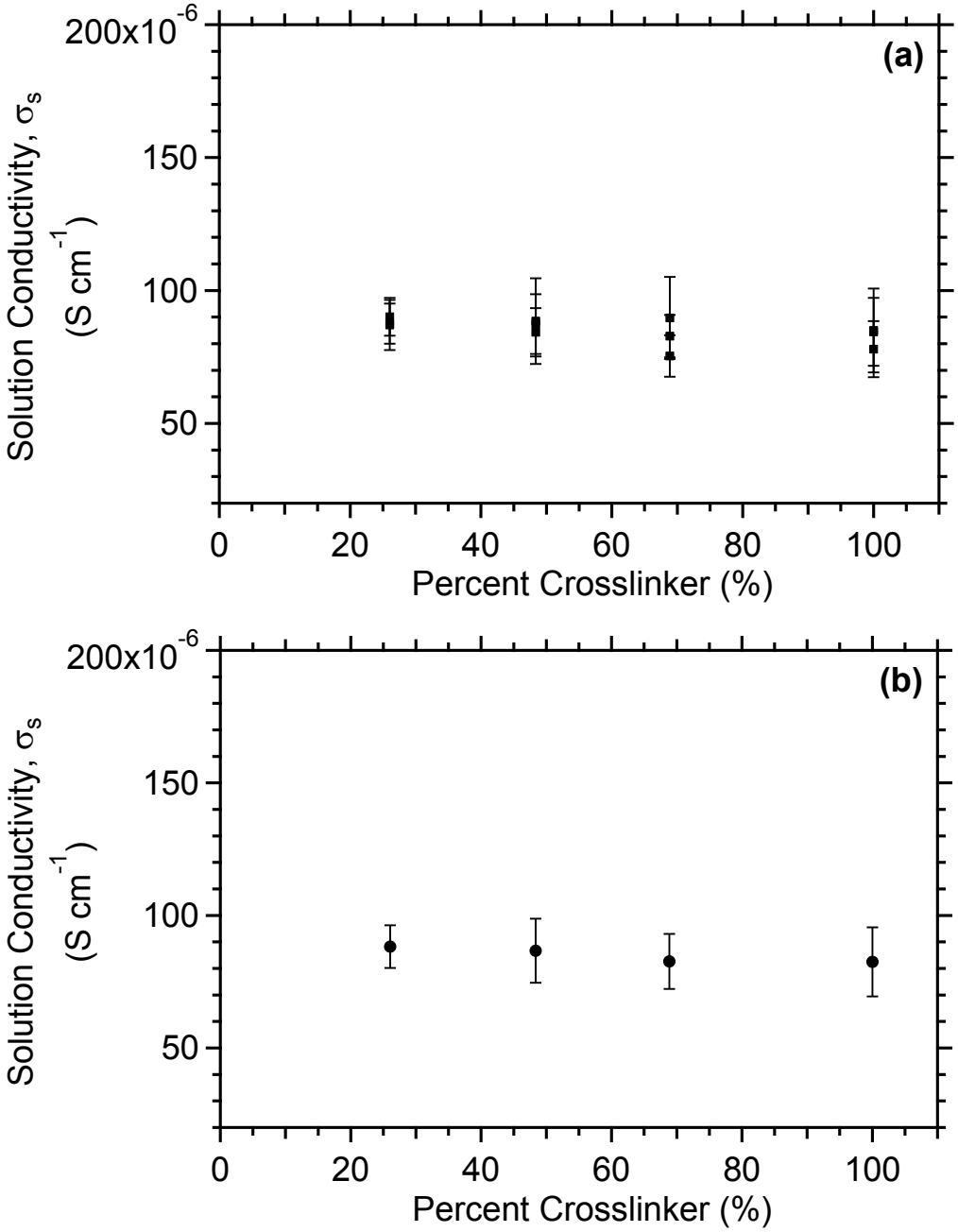

Figure 5.8. Room temperature solution conductivities (σ_s) plotted versus mole fraction of trithiol crosslinker (a) for individual crosslinked gels and (b) averaged over three samples of each crosslinker percentage indicating minimal dependence of solution conductivity on crosslink density of the gel.

Although the solution conductivity σ_s is independent of the crosslink density, the total conductivity σ_{total} calculated from $R_{total} = R_s + R_{if}$ clearly depends on the crosslinker content. Figure 5.9 shows the total conductivity σ_{total} for individual samples at different amounts of added trithiol crosslinker. The measured total conductivities are generally consistent amongst disks having the same crosslinker amount, and they typically lie within experimental error from one another. The only exception is 100CL, for which one of the disks exhibits a slightly lower total conductivity than the others. The reasons for this reproducible, experimental discrepancy are unknown. We observe a three-fold decrease in total ionic conductivity as the amount of thiol crosslinker increases from 26 to 100 mol% in the gels. Johansson and coworkers observed similarly modest changes in conductivity in lightly crosslinked thiol-ene network polymer electrolytes.[32] We note that 69CL and 100CL exhibit very similar total conductivities as well as very similar dynamic elastic storage shear moduli (Section 5.3.2).

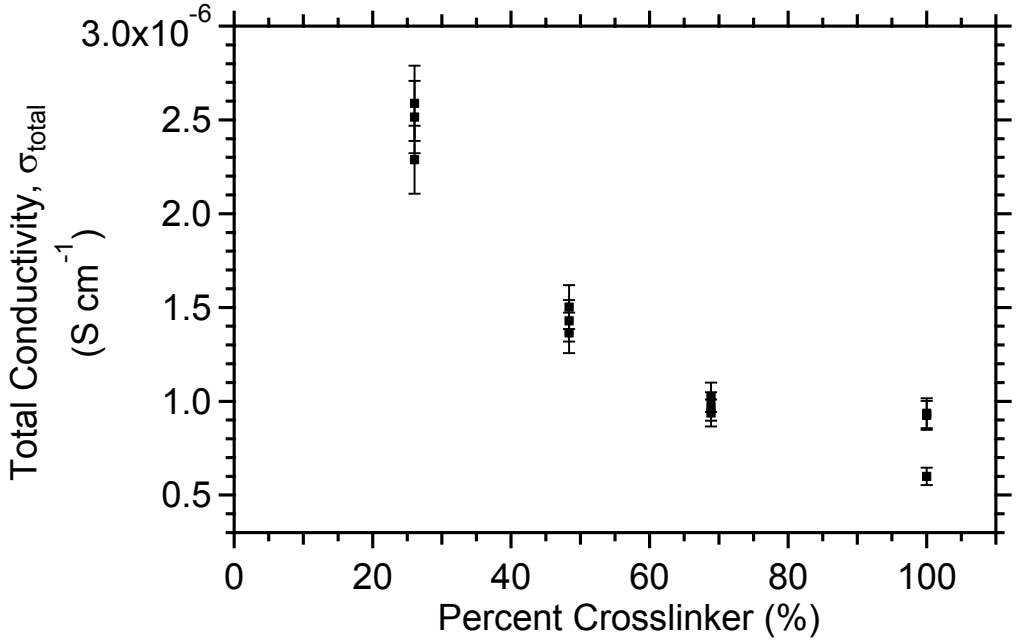

Figure 5.9. Room temperature total conductivities σ_{total} plotted versus mole fraction of trithiol crosslinker for individual crosslinked gels calculated from $R_{total} = R_s + R_{if}$ indicating significant total conductivity dependence on network gel crosslink density.

Figure 5.10 depicts the correlation between the observed gel storage moduli G′(ω) and their total ionic conductivities σ_{total}, by overlaying the experimentally determined parameters that are collected in Table 5.1. The trade-off between storage modulus and total ionic conductivity is clearly apparent: gels with lower G′(ω) values exhibit higher lithium conductivities, while more tightly crosslinked gels have diminished lithium ion conductivities. In spite of the apparent inverse dependence of total lithium ion conductivity on storage modulus, we note that these relatively small variations are within one order of magnitude. More explicitly, the total ionic conductivity σ_{total} only changes by a factor of three between 26 CL and 100 CL and G′(ω) only changes by less than a factor of two. Since we previously concluded that the motion of ions

through the bulk gel is unaffected by the crosslink density of the polymer network, the decrease in total ionic conductivity is entirely due to increases in interfacial resistance R_{if}. The effect of the polymer gel network crosslink density on R_{if} originates from the relative abilities of anionic BNMB-bearing segments in the polymer to diffuse near the electrode to form the interfacial double layer. Since the more tightly crosslinked networks in which the counterions are immobilized exhibit lower segmental mobilities implied by their higher storage moduli, they exhibit larger impedances associated with the ion transport through the electrical double layer at the electrode interface.

Table 5.1 Summary of the rheological and conductivity properties of gels.

% Crosslinker (%)[a]	$G'(\omega)_{40°C}$ (kPa)[b]	$\sigma_{s,22°C} / 10^{-5}$ (S cm^{-1})[c]	$\sigma_{total,22°C} / 10^{-6}$ (S cm^{-1})[d]	E_a (kJ mol^{-1})[e]
26	39.9	8.8 ± 0.8	2.5 ± 0.2	--
48	58.5	8.7 ± 1.2	1.4 ± 0.1	37
69	73.8	8.3 ± 1.0	0.98 ± 0.08	46
100	74.8	8.2 ± 1.3	0.82 ± 0.07	51

[a]Calculated as [trithiol] / ([trithiol] + [dithiol]). [b]Taken as the dynamic elastic storage shear moduli measured at 0.1 Hz in the dynamic frequency sweep at 40 °C. [c]Solution ionic conductivity calculated from R_s. [d]Total ionic conductivity calculated from $R_{total} = R_s + R_{if}$. [e]Calculated from an Arrhenius fit of the temperature-dependent total ionic conductivity, σ_{total}. 26CL was not measured. 69CL and 100 CL ruptured during variable-temperature conductivity measurements.

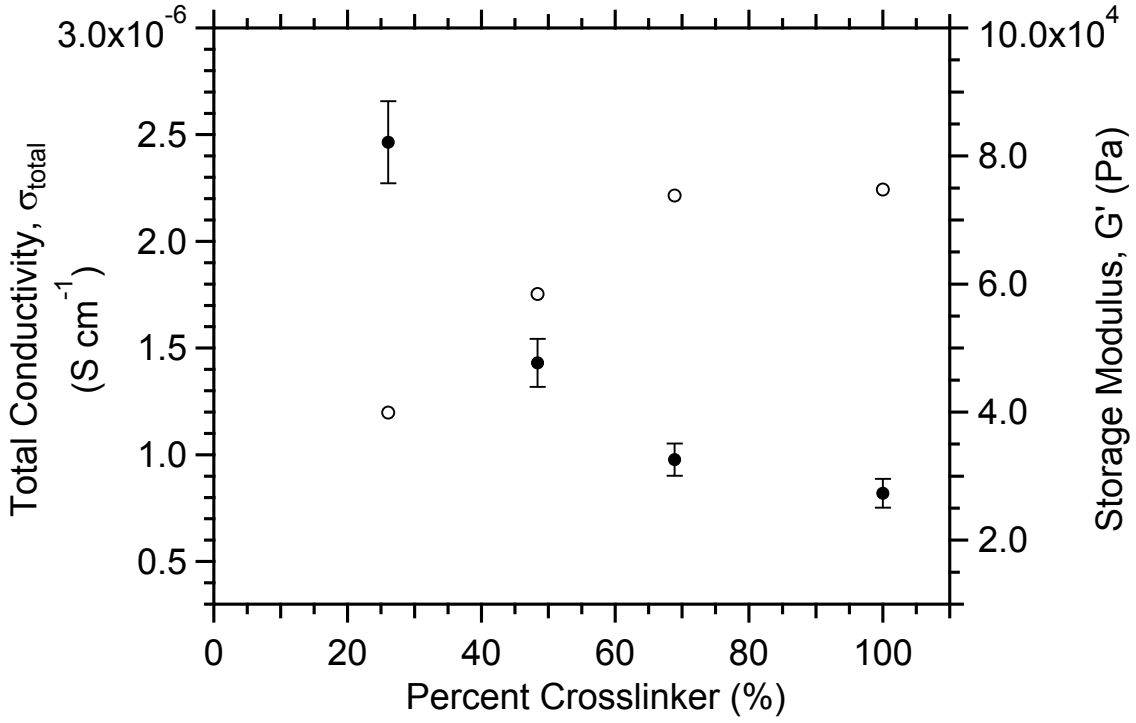

Figure 5.10. Average total ionic conductivity σ_{total} (●, left axis) and elastic storage shear modulus G′(ω) (○, right axis) plotted against mole fraction of trithiol crosslinker indicating an inverse relationship between total ionic conductivity and storage modulus in these crosslinked network gels. The total conductivities σ_{total} were measured at 22 °C and the storage moduli G′(ω) were measured at 0.1 Hz in the dynamic frequency sweep at 40 °C.

The lithium ion conductivities for our materials are somewhat lower than those reported by Kerr[24] and Endo[26] for their network lithium single-ion conductors swollen with solvent. Kerr and coworkers observed room temperature lithium ion conductivities on order of 1.2 x 10^{-5} S cm^{-1} for their lithium bis(malonato)borate-crosslinked polyether comb networks swollen with ethylene carbonate/ethyl methyl carbonate (1:1 v/v), whereas Endo and coworkers observed room temperature conductivities on order of 7.2 x 10^{-5} S cm^{-1} for epoxy networks bearing

immobilized lithium sulfonylimide groups swollen with propylene carbonate. Although our observed total ionic conductivities ranging from $8.2 \times 10^{-7} - 2.5 \times 10^{-6}$ S cm^{-1} fall short of these values, we caution against direct quantitative comparisons of ionic conductivities, as the absolute values depend sensitively on the exact geometry and experimental setup for impedance measurements that govern the contribution of R_{if}.

We used variable temperature EIS measurements to probe the mechanism of ion motion in these lithium single-ion conductors. From our previous studies of hydrophobic and hydrophilic polymerized ionic liquid homopolymers in Chapter 2, we determined that solvated and non-solvated polymers conduct ions by different mechanisms. Whereas solvent-free polymers exhibit Vogel-Fulcher-Tammann (VFT) behavior consistent with ion transport mediated by polymer segmental motion, ion transport in solvated polymer systems exhibits Arrhenius behavior consistent with solvent-mediated transport mechanisms. Thus, variable temperature conductivity measurements provide a ready means for identifying the underlying ion transport mechanism: the linearity of a logarithmic plot of conductivity versus inverse temperature ($\log \sigma$ *vs.* $1/T$) implies Arrhenius-type behavior, while curvature in this plot suggests VFT behavior. As a consequence of the previously noted thermal expansion observed in our temperature-dependent rheology measurements (> 35 %), we modified our conductivity cell with spring-loaded compression screws to accommodate gel expansion. The $\log(\sigma_{total})$ *vs.* $1/T$ plot for 48 CL over the temperature range $T = 20 - 130$ °C is given in Figure 5.11. The apparent linearity of this plot suggests Arrhenius-type behavior, although the relative contributions of R_{if} and R_s could not be deconvoluted due to experimental limitations. Thus the exact mechanism of ion transport is obscured. By extracting the slope of the line of best fit for the data we are able to

determine that the Arrhenius activation energy for ion conduction is 37 kJ mol^{-1}, which is similar to the activation energy we found for hydrated hydrophilic polymerized ionic liquid homopolymers in Chapter 2. After cooling 48CL back to 22 °C, we placed it in the hermetically sealed sample cell in which all of the room temperature EIS measurements had been performed. The total conductivity of 48 CL ($1.7 \pm 0.2 \times 10^{-6}$ S cm^{-1}) closely matched the previously measured value ($1.4 \pm 0.1 \times 10^{-6}$ S cm^{-1}), suggesting that the apparent loss of propylene carbonate solvent observed in the rheological measurements in Section 5.3.2 does not occur in the conductivity cell.

The above conductivity analyses implicitly assume a constant volume for each gel at all temperatures, which is inconsistent with our rheological observations that suggest a large degree of swelling at elevated temperatures. Measurement of the sample dimensions at each temperature would be required to obtain accurate ionic conductivity values; however, this is experimentally impractical. Therefore, we note that there is some additional error inherent in the calculated conductivities from these variable-temperature measurements.

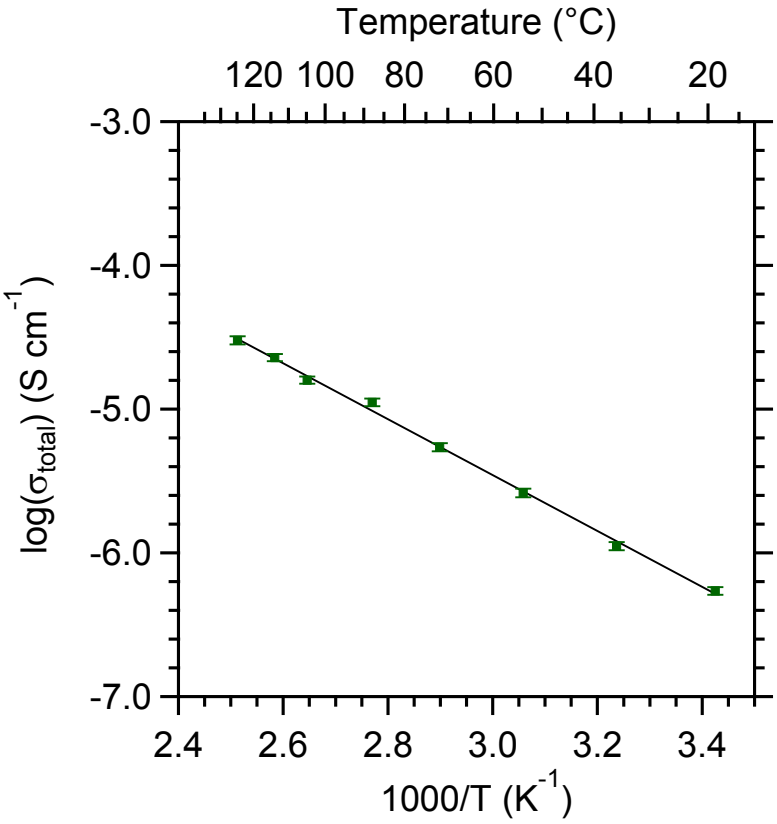

Figure 5.11. Temperature-dependent total ionic conductivity σ_{total} plotted versus inverse temperature for 48CL measured by EIS in a modified conductivity cell allowing for volume expansion during heating. The line represents a line of best fit with the equation $\log(\sigma_{total}) = -1.945 \times (1000/T) + 0.376$ ($R^2 = 0.9955$).

In an effort to control the effects of thermal expansion of the gels, we measured the variable temperature conductivity of 100CL and 69CL constrained inside a hermetically sealed cell. EIS measurements of 100CL employed stainless steel blocking electrodes, whereas Pt blocking electrodes were used in measurements of 69CL. Between T = 20 – 130 °C, the linear $\log(\sigma_{total})$ *vs.* $1/T$ plots for both 69CL and 100CL suggest a solvent-assisted lithium ion transport

mechanism (Figures 5.12 & 5.13). From these plots, we obtain Arrhenius activation energies for ion conduction of 46 kJ mol^{-1} for 69 CL and 51 kJ mol^{-1} for 100CL.

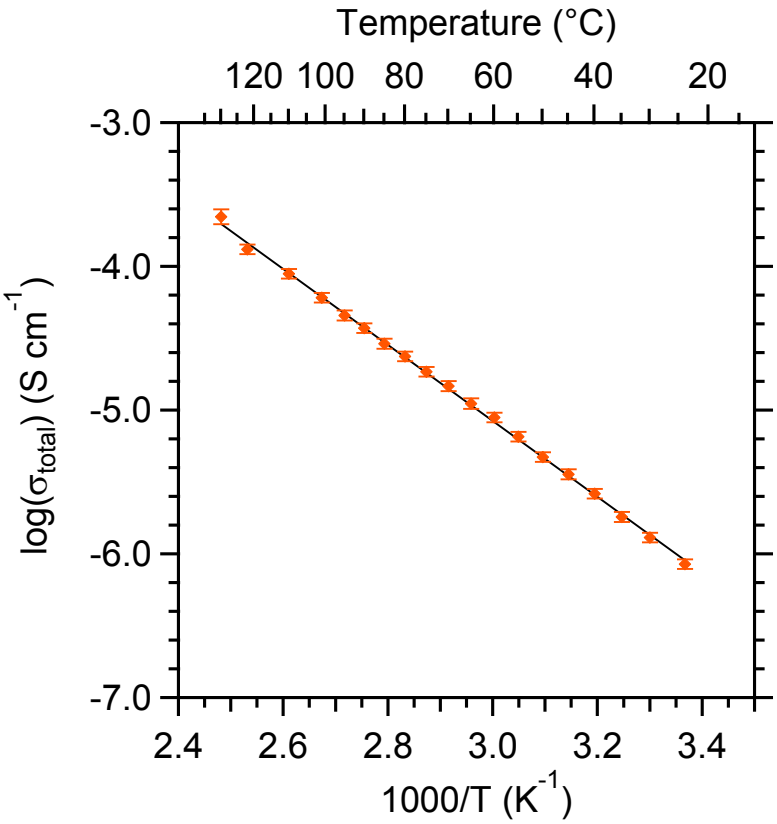

Figure 5.12. Temperature-dependent total ionic conductivity σ_{total} plotted versus inverse temperature for 100CL measured by EIS in a hermetically-sealed conductivity cell with stainless steel electrodes. Note that the gel ruptured during heating. The line represents a line of best fit with the equation $\log(\sigma_{total}) = -2.641 \times (1000/T) + 2.848$ ($R^2 = 0.9906$).

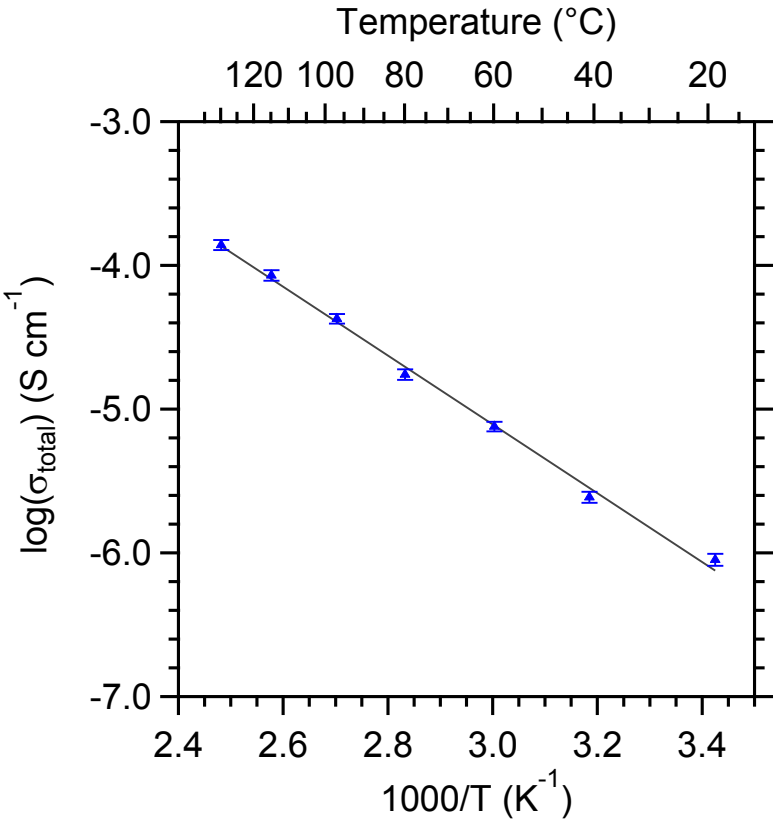

Figure 5.13. Temperature-dependent total ionic conductivity σ_{total} plotted versus inverse temperature for 69CL measured by EIS in a hermetically-sealed conductivity cell with stainless steel electrodes. Note that the gel ruptured during heating. The line represents a line of best fit with the equation $\log(\sigma_{total}) = -2.395 \times (1000/T) + 2.076$ ($R^2 = 0.9933$).

Upon cooling and opening the cells after performing these temperature-dependent measurements, we noticed that the gels had ruptured under the compressive force associated with their thermal expansion. The resulting materials were stringy in texture and no longer retained the original disk shape. Since the gels ruptured between both stainless steel and platinum electrodes, the electrode surface chemistry does not apparently catalyze the decomposition of the

gels. Hence we postulate that the complete failure of these covalent network gels occurs due to the force of the expected thermal expansion (*vide infra*) within the incommensurate confinement of the electrochemical measurement cell. In other words, gel thermal expansion results in stress that breaks the covalent gel network. This hypothesis is supported by the observation that 48CL did not rupture, since it was not confined to the hermetically sealed cell during temperature-dependent conductivity measurements.

We propose that the deviations from linearity for the Arrhenius conductivity plots of 100CL and 69CL are due to the thermal expansion leading to failure of these gels. While these unforeseen complications may alter the data slightly, we do not anticipate substantial deviations. The loss of the network structure upon gel rupture should not significantly affect the observed conductivity since temperature has a much larger effect on conductivity than the network structure and dynamics. Total ionic conductivity changes by more than two orders of magnitude across a temperature window of ~ 100 °C, but only by a factor of three across different crosslink densities. Because of the high degree of linearity in the data obtained from 69CL and 100CL, we propose that the validity of the data is maintained in spite of the failure of the gels at high temperatures.

From the temperature-dependent ionic conductivity data of 48CL, 69CL, and 100CL, we suggest that lithium conduction occurs via a solvent-mediated transport mechanism based on the apparent linearity of the $\log(\sigma_{total})$ vs. $1/T$ plots and the magnitude of the activation barriers for ion transport. Even though the ion conduction *mechanism* within the bulk of the gel is independent of crosslink density, the total conductivity is affected by the network structure. Similar to the trend observed in the room-temperature conductivity measurements, in which the

total conductivity decreases with increasing crosslink density due to limited mobilities of polymeric anions at the interfacial double layer, we note a similar increase in the Arrhenius activation energy with increasing crosslink density. This activation energy must be associated with the rearrangement of anionic polymer segments to form the electrical double layer and the resistance of moving ions through it. Since the more highly crosslinked polymer has less mobile polymer segments, the energy associated with rearranging them at the interface is higher. Although the linearity of the variable temperature data suggests that such a process obeys Arrhenius behavior consistent with solvent-mediated ion transport, we cannot rule out the possibility that the data may fit a Vogel-Fulcher-Tamman model indicating pure polymer segmental dynamics-mediated transport since the temperature range studied was relatively narrow and significantly above T_g. Additionally, the inability to deconvolute the solution resistance R_s from the interfacial resistance R_{if} in these experiments further obfuscates the active ion transport mechanism.

Finally, to prove that the gels are in fact lithium single-ion conductors, we studied the chronopotentiometric response of 26CL in a symmetrical cell in which both electrodes were made of Li foil. This cell was subjected to four charge/discharge cycles with a sequence of 10 min rest (no current), 1 h charge (+ 2.0 μA), 10 min rest, then 1 h discharge (– 2.0 μA). The chronopotentiometry data are summarized in Figure 5.14. As expected for a lithium single-ion conductor, the potential changes in a step-wise fashion upon application or removal of the current, indicating that polarization due to anion motion does not occur. Kerr and coworkers reported similar observations for their lithium bis(malonato)borate-crosslinked polyether comb single-ion conductors.[23] In contrast to lithium single-ion conducting systems, binary salt

mixtures display dramatically different charge/discharge profiles in Li/Li symmetrical cells due to electrode polarization by both cation and anion movement.[37]

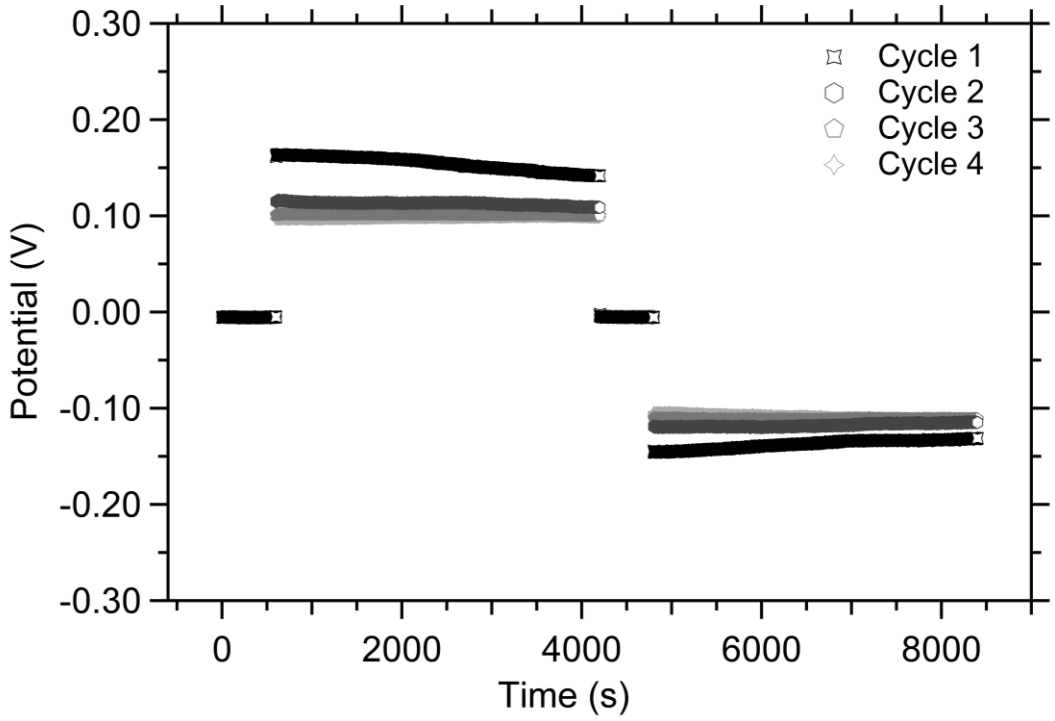

Figure 5.14. Chronopotentiometry of 26 CL in a symmetric Li/Li cell plotting cell potential versus time for four charge/discharge cycles with a sequence of 10 min rest (0.0 μA), 1 h charge (+ 2.0 μA), 10 min rest, then 1 h discharge (– 2.0 μA). The step-wise change in potential upon changing the cell current indicates the lithium single-ion conducting nature of the crosslinked gels with no polarization observed.

5.3.4 Investigation of Ruptured Thiol-ene Network Gels.

To study the mechanism of high temperature failure of our thiol-ene crosslinked polymer network electrolytes , we intentionally ruptured samples of 48CL and 100CL by heating them to

130 °C for 30 minutes in the hermetically sealed conductivity cell. Upon cooling, we extracted the ruptured gels with CD_3CN for 12 h at 22 °C to leach out any soluble byproducts of gel failure for subsequent ^1H NMR analysis. The resulting ^1H NMR spectrum associated with 48CL is shown in Figure 5.15, along with spectra associated with leaching a non-ruptured gel control with CD_3CN and the reagents comprising the gel. The ^1H NMR of the ruptured 48CL shows resonances associated with each of its component reagents (LiBNMB, trimethylpropane tris(3-mercaptopropionate), and 1,6-hexanedithiol), whereas the control sample shows only resonances associated with propylene carbonate extracted from the gel. Thus, the ^1H NMR spectrum of the extracted ruptured gel must arise from the byproducts of network failure. Resonances at δ 3.28, 1.87, and 1.38 – 1.26 ppm derive from the corresponding protons in LiBNMB. Noticeably, the resonances from the olefin protons as well as the protons α to the olefin in LiBNMB monomer are absent, suggesting that gel failure is not due to a thermal reversal of the thiol-ene reaction. Resonances at δ 2.72 and 2.49 ppm are due to protons α to sulfur. Since these resonances are shifted slightly from the corresponding thiol starting materials, we assign these resonances to the protons α to sulfur in thioether linkages as the extent of deshielding changes only minimally from a thiol to a thioether. This observation along with the absence of characteristic triplet resonances due to thiol S-H protons (δ 1.69 ppm (trithiol) and δ 1.56 ppm (dithiol)) implies that the thioether linkages remain intact upon network failure. The absence of the singlet at δ 4.05 ppm corresponding to the ester methylene protons in the trithiol implies that the network failure occurs by scission of the ester linkages. The results of similar studies of 100CL in Figure A4.4 in Appendix 4 conform to a similar chemical interpretation. Although these spectroscopic data do not conclusively discern the mechanism of gel rupture, they do suggest that covalent bond

cleavage plays a role in the degradation, leading to the lower molecular weight byproducts seen in ^{1}H NMR. FTIR analyses of the ruptured 69CL sample indicate no significant changes, indicating that the bonds that break during network failure represent a very small fraction of the bulk sample given their weak FTIR band intensities (Figure 5.16).

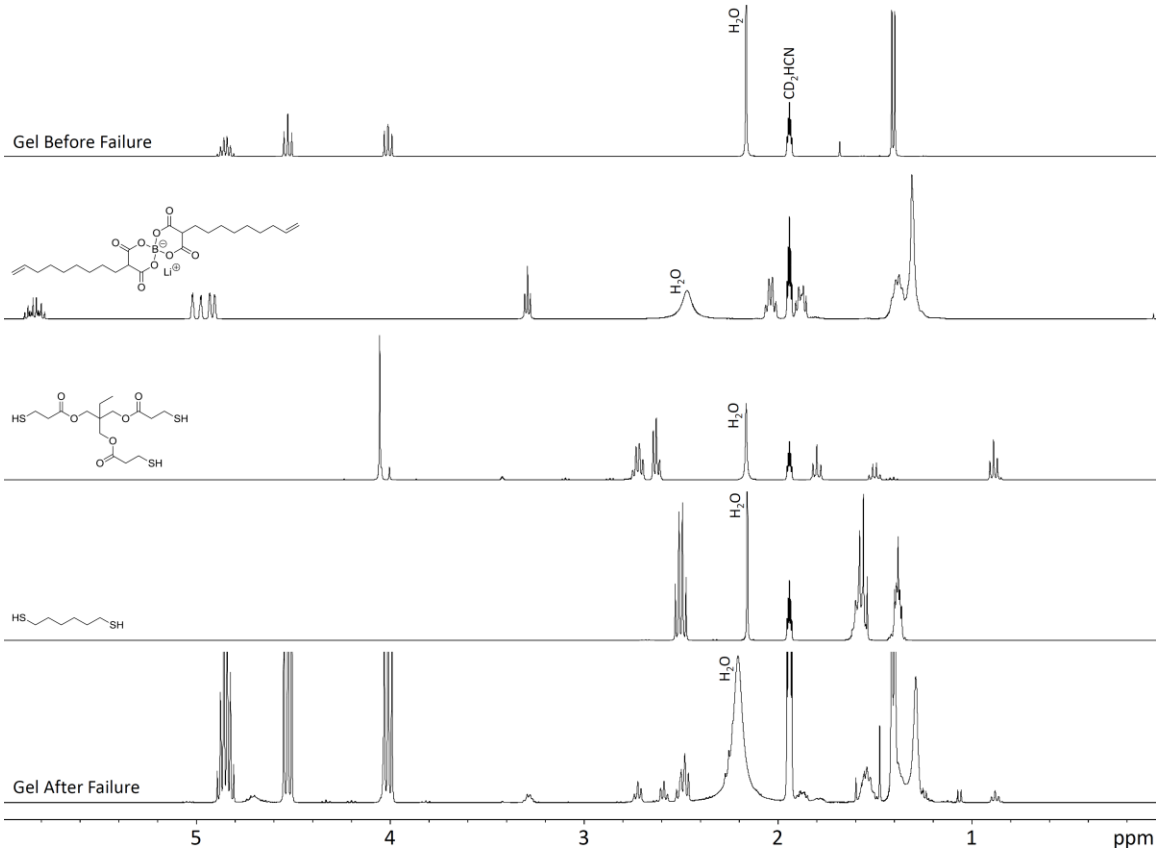

Figure 5.15. ^{1}H NMR spectra (400 MHz, CD_3CN, 22°C) of the soluble fraction of a disk of 48CL before failure (top) and after failure (bottom) along with spectra of reagents (LiBNMB, trimethylpropane tris(3-mercaptopropionate), and 1,6-hexanedithiol) used to make the gel for comparison. The absence of resonances assignable as ester protons in the ruptured gel suggests that network failure occurs by cleavage of the ester linkages.

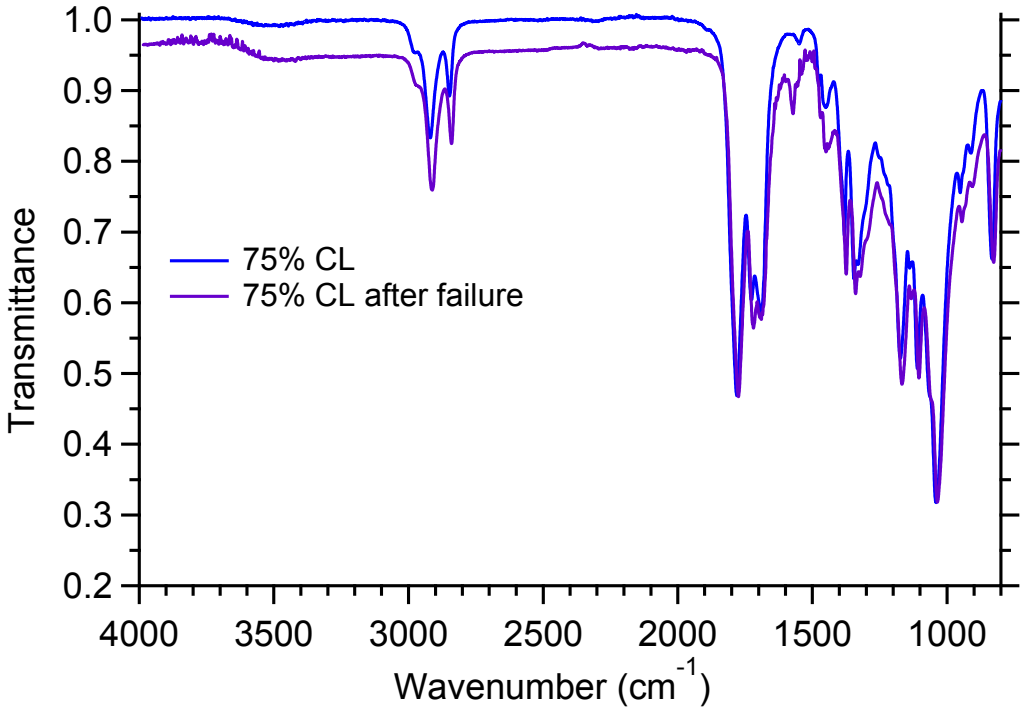

Figure 5.16. FTIR spectra of 69CL before failure (top, blue) and after failure (bottom, purple) showing no discernible differences upon failure, indicating that bonds broken during rupture comprise a very small fraction of the bulk. The spectra have been vertically offset for clarity.

5.4 Conclusions

We have synthesized a series of lithium single-ion conducting network gel electrolytes by a thiol-ene crosslinking polymerization and studied their rheological and lithium conductivity properties. We found that frequency-independent storage moduli $G'(\omega)$ increase slightly with trithiol crosslinker density, while the total lithium-ion conductivities σ_{total} decrease. Since the solution conductivity σ_S remains constant across all crosslinker loadings, we conclude that the decrease in total conductivity σ_{total} is due to differences in diffusion of anionic polymer segments

to form the interfacial double layer at the electrode. Through variable temperature electrochemical impedance spectroscopy, we observe apparent Arrhenius behavior that may indicate a solvent-assisted ion transport mechanism; however, a polymer-mediated transport mechanism cannot be ruled out due to the limited temperature range over which the data was collected far above the T_g of the system.. The Arrhenius activation energy for ion motion apparently increases with increasing crosslink density in these gel networks. The single-ion conducting nature of these gels was demonstrated by a lack of polarization in the charge/discharge cycle for a symmetrical Li/Li cell. We also found that the gels rupture at high temperatures when confined in a hermetically sealed cell due to thermal expansion. *Post mortem* analysis of the gels suggests that the gels may fail by cleavage of the ester bonds in the trithiol crosslinker.

5.5 References

(1) Goodenough, J. B.; Park, K. S. *J. Am. Chem. Soc.* **2013**, *135*, 1167.

(2) Etacheri, V.; Marom, R.; Elazari, R.; Salitra, G.; Aurbach, D. *Energy Environ. Sci.* **2011**, *4*, 3243.

(3) Dunn, B.; Kamath, H.; Tarascon, J. M. *Science* **2011**, *334*, 928.

(4) Manthiram, A. *J. Phys. Chem. Lett.* **2011**, *2*, 176.

(5) Xu, K. *Chem. Rev.* **2004**, *104*, 4303.

(6) Bandhauer, T. M.; Garimella, S.; Fuller, T. F. *J. Electrochem. Soc.* **2011**, *158*, R1.

(7) Scrosati, B.; Vincent, C. A. *MRS Bull.* **2000**, *25*, 28.

(8) Kerr, J. B. In *Lithium Batteries: Science and Technology*; Nazri, G., Pistoia, G., Eds.; Kluwer Academic Publishers: Boston, 2004, p 574.

(9) Andreev, Y. G.; Bruce, P. G. *Electrochim. Acta* **2000**, *45*, 1417.

(10) Kono, M.; Hayashi, E.; Watanabe, M. *J. Electrochem. Soc.* **1998**, *145*, 1521.

(11) Oh, B.; Vissers, D.; Zhang, Z.; West, R.; Tsukamoto, H.; Amine, K. *J. Power Sources* **2003**, *119*, 442.

(12) Tigelaar, D. M.; Meador, M. A. B.; Kinder, J. D.; Bennett, W. R. *Macromolecules* **2006**, *39*, 120.

(13) Lee, K. H.; Kim, K. H.; Lim, H. S. *J. Electrochem. Soc.* **2001**, *148*, A1148.

(14) He, D.; Cho, S. Y.; Kim, D. W.; Lee, C.; Kang, Y. *Macromolecules* **2012**, *45*, 7931.

(15) Krebs, H.; Yang, L.; Shirshova, N.; Steinke, J. H. G. *React. Funct. Polym.* **2012**, *72*, 931.

(16) Matsumoto, K.; Endo, T.; Katsuda, K.; Lee, H.; Yamada, K. *J. Polym. Sci., Part A: Polym. Chem.* **2012**, *50*, 5161.

(17) Matsumoto, K.; Sogabe, S.; Endo, T. *J. Polym. Sci., Part A: Polym. Chem.* **2012**, *50*, 1317.

(18) Ramanjaneyulu, K.; Bar, N.; Arif Sher Shah, M. S.; Manorama, S. V.; Basak, P. *J. Power Sources* **2012**, *217*, 29.

(19) Basrur, V. R.; Guo, J.; Wang, C.; Raghavan, S. R. *ACS Appl. Mater. Interfaces* **2013**, *5*, 262.

(20) Ghosh, A.; Wang, C.; Kofinas, P. *J. Electrochem. Soc.* **2010**, *157*, A846.

(21) Ryu, S.-W.; Trapa, P. E.; Olugebefola, S. C.; Gonzalez-Leon, J. A.; Sadoway, D. R.; Mayes, A. M. *J. Electrochem. Soc.* **2005**, *152*, A158.

(22) Sun, X. G.; Reeder, C. L.; Kerr, J. B. *Macromolecules* **2004**, *37*, 2219.

(23) Sun, X. G.; Kerr, J. B.; Reeder, C. L.; Liu, G.; Han, Y. B. *Macromolecules* **2004**, *37*, 5133.

(24) Sun, X. G.; Kerr, J. B. *Macromolecules* **2006**, *39*, 362.

(25) Matsumoto, K.; Endo, T. *J. Polym. Sci., Part A: Polym. Chem.* **2010**, *48*, 3113.

(26) Matsumoto, K.; Endo, T. *J. Polym. Sci., Part A: Polym. Chem.* **2011**, *49*, 1874.

(27) Hoyle, C. E.; Lee, T. Y.; Roper, T. *J. Polym. Sci., Part A: Polym. Chem.* **2004**, *42*, 5301.

(28) Hoyle, C. E.; Bowman, C. N. *Angew. Chem.* **2010**, *49*, 1540.

(29) Jacobine, A. F.; Glaser, D. M.; Grabek, P. J.; Mancini, D.; Masterson, M.; Nakos, S. T.; Rakas, M. A.; Woods, J. G. *J. Appl. Polym. Sci.* **1992**, *45*, 471.

(30) Chiou, B. S.; English, R. J.; Khan, S. A. *Macromolecules* **1996**, *29*, 5368.

(31) Walker, C. N.; Versek, C.; Touminen, M.; Tew, G. N. *ACS Macro Letters* **2012**, *1*, 737.

(32) Willgert, M.; Kjell, M. H.; Lindbergh, G.; Johansson, M. *Solid State Ionics* **2013**, *236*, 22.

(33) Hoyle, C. E.; Lowe, A. B.; Bowman, C. N. *Chem. Soc. Rev.* **2010**, *39*, 1355.

(34) Echeverri, M.; Kim, N.; Kyu, T. *Macromolecules* **2012**, *45*, 6068.

(35) Xi, W.; Krieger, M.; Kloxin, C. J.; Bowman, C. N. *Chem. Commun.* **2013**, *49*, 4504.

(36) Agrawal, R. C.; Pandey, G. P. *J. Phys. D. Appl. Phys.* **2008**, *41*.

(37) Kerr, J. B.; Sloop, S. E.; Liu, G.; Han, Y. B.; Hou, J.; Wang, S. *J. Power Sources* **2002**, *110*, 389.

CHAPTER 6

CONCLUSIONS

The global energy outlook is changing and the world must look toward renewable energy sources to meet the ever-increasing energy demand in the twenty first century and beyond. Along with the implementation of renewable sources comes the necessity to store this energy for both stationary and portable consumption. Electrochemical devices such as fuel cells and lithium ion batteries will play a large role in these endeavors; however improvements in the materials used in these devices, particularly electrolyte materials, are necessary in order to make them viable on a global scale. One particular class of high-performance electrolytes that has garnered much attention is that of single-ion conductors, in which one of the ions in the ion pair is immobilized on a polymeric scaffold. In this thesis we described our efforts to develop next generation single-ion conducting electrolytes as well as to understand the fundamental structure-property relationships that govern ion motion in this medium.

In Chapter 1, we reviewed the classes of polymeric single-ion conducting polymers including hydroxide-conducting polymers, polymerized ionic liquids, and polymeric lithium single-ion conductors, with a focus on their potential applications as electrolytes for alkaline fuel cells and lithium ion batteries. We summarized recent research efforts to develop chemically stable hydroxide conducting polymers through design of different tethered cationic groups and polymer backbones. We described numerous structure-property relationships in polymerized ionic liquids in an effort to establish design criteria for obtaining highly conductive polymeric single-ion conductors. Finally, we reviewed the effects of tethered anion structure and polymer

architecture on the lithium ion conductivity and electrochemical stability of polymeric lithium single-ion conductors.

In Chapter 2 we described the modular synthesis and attendant characterization of two series of polymerized ionic liquids. A series of hydrophobic polymerized ionic liquids with fluorinated counterions exemplified the effect of counterion structure on the glass transition temperature of the polymer, particularly that bulky, non-coordinating anions act to plasticize the polymer and depress T_g. Furthermore, measurements of ionic conductivity indicate that ion motion in these systems is intimately coupled to polymer segmental dynamics with low T_g polymers exhibiting higher conductivities. While conductivity in these solvent-free systems depends primarily on polymer chain dynamics, effects of counterion size, symmetry, and concentration contribute to ion motion as well. In contrast, measurements of a series of hydrophilic polymerized ionic liquids indicate that ionic conductivity depends primarily on the degree of hydration of the polymer such that ion motion in these systems is decoupled from the polymer segmental dynamics. From these studies, we can comment on general design criteria for developing highly conductive polymeric single-ion conductors. In solvent-free systems, polymers should have a low T_g since ion motion depends primarily on chain dynamics. This may be accomplished by the use of flexible-polymer backbones, by introducing internal plasticizers such as branches, or by modulating the structure of the mobile ion, if possible. Additionally, these modifications should not compromise the overall concentration of ions in the material. In solvated systems, the polymer should be designed such that the ions are as highly solvated as possible, primarily through modification of the tethered ion and proximal substituents.

In Chapter 3 we investigated fundamental morphology-conductivity relationships in polymeric single-ion conductors by synthesizing and characterizing a series of poly(styrene)-poly(ionic liquid) diblock copolymers. We correlated the ionic conductivity of these materials with their melt-phase nanostructured morphologies, as determined by x-ray scattering and transmission electron microscopy. We determined that morphologies comprised of cylindrical ionic domains in a non-conducting matrix exhibited diminished ionic conductivities that we attribute to their propensity to form "dead ends" due to morphological defects and grain boundaries. These studies indicate that the design of a highly conductive single-ion conducting block copolymer should focus on morphologies in which the ionic block comprises the majority phase such that continuous ionic pathways are available for ion motion. In such a system, ions may move more freely through the material without being inhibited by "dead ends."

Chapter 4 described the synthesis of a polymeric lithium single-ion conductor for potential use as an electrolyte in next-generation lithium ion batteries. By tethering anions into the backbone of a polymer chain, we minimized the motion of the polymeric anions thereby enhancing the lithium ion transference number. We synthesized a polymer incorporating electrochemically stable bis(malonato)borate anions into the polymer backbone via acyclic diene metathesis and demonstrated its high lithium ion conductivity in propylene carbonate solution. Upon electrochemical cycling, this polymer formed a highly robust solid-electrolyte interphase at oxidizing potentials that imparted a surprisingly wide electrochemical window on the electrolyte system. We also investigated an alternative thiol-ene method of polymerization to incorporate the bis(malonato)borate anion into a low T_g polymer for potential use as a solvent-free polymeric lithium single-ion conductor.

In Chapter 5 we described the rheological and ion conducting properties of a series of crosslinked lithium single-ion conducting polymer network gels synthesized by thiol-ene gelation polymerization. Through a combination of rheology and electrochemical impedance spectroscopy, we demonstrated that the solution lithium conductivity in these gels was independent of crosslink density, but that higher interfacial resistances in the more tightly crosslinked networks decreased overall lithium conductivity, although this effect was relatively small. Variable-temperature conductivity measurements indicated a solvent-assisted ion transport mechanism as would be expected for a solvent-swollen gel. Polarization studies in a symmetric Li/Li cell indicated the lithium single-ion conducting nature of the crosslinked gel.

Electrochemical applications such as grid storage, automotive propulsion, and more powerful portable electronics demand higher performance and safety from lithium ion batteries. Although new high voltage cathode materials and high capacity anode materials are driving the development of next-generation of lithium ion batteries, they must be accompanied by new electrolyte materials in order to realize the necessary gains in performance and safety. The enhanced safety of polymeric electrolytes coupled with the performance benefits of lithium single-ion conductors position polymeric lithium single-ion conductors among the forefront of promising electrolyte materials for use in future battery electrolytes. Such materials have received only modest attention and further study is warranted to maximize their impact as potential electrolyte materials.

The successful implementation of a polymeric lithium single-ion conductor into a viable lithium ion battery has not been accomplished to date. Major limitations must be overcome to enable these materials as electrolytes in commercial applications. Criteria for successful

implementation of a lithium single-ion conducing electrolyte include (1) high lithium ion conductivity and (2) anodic and cathodic electrochemical stability. Ideally, these criteria should be met utilizing materials derived from cheap and renewable chemical feedstocks.

The structure-property relationships developed for polymerized ionic liquids may be directly applied to maximize the lithium ion conductivity of polymeric lithium single-ion conductors. In order to obtain high lithium ion conductivity materials must either have a low T_g or be plasticized with an electrolyte solvent. The former case may be accomplished by the incorporation of flexible segments, branches, or other internally plasticizing moieties into the polymer structure, whereas the latter case necessitates crosslinking of the polymer in order to retain true single-ion conducting behavior. Solvated ion transport tends to be more facile than polymer dynamics-mediated transport, so the development of solvated crosslinked polymer architectures likely holds more promise as potential electrolytes. Ideally, these networks should utilize non-flammable solvents, which represent an entirely separate area of research.

Electrochemical stability in a polymeric lithium single-ion conductor may be accomplished by careful design of tethered anionic species and ancillary structures that comprise the polymeric matrix. Particularly, electrochemically labile linkages such as esters should be avoided in the polymer backbone, as cleavage of these linkages will degrade polymer mechanical properties. By coupling suitable polymeric backbones available from a range of polymerization techniques with an array of electrochemically stable anionic moieties, numerous electrochemically stable combinations may be found.

Still much progress is needed to expand lithium single-ion conductors from an academic curiosity into commercially viable electrolytes for high-performance batteries. Achieving high

lithium ion conductivity and wide electrochemical stability with cheaply derived materials are necessary to making this goal a reality. Surely this may be accomplished by judicious design of chemical structures and macromolecular architectures, limited only by the imagination.

APPENDIX 1

SUPPORTING INFORMATION FOR CHAPTER 2: THERMAL AND ION TRANSPORT PROPERTIES OF HYDROPHILIC AND HYDROPHOBIC POLYMERIZED STYRENIC IMIDAZOLIUM IONIC LIQUIDS

Table A1.1. Key of Experimental Sample Names to Chapter 2 Sample Names

Chapter 3 Sample Name	**Experimental Sample Name**
Alkoxyamine 1	RLW-III-188
PVBCl	RLW-IV-013
PVBnMeImCl	RLW-IV-038-A
PVBnBuImCl	RLW-IV-038-B
PVBnHexImCl	RLW-IV-019 / RLW-IV-053
PVBnHexImPF_6	RLW-IV-030-B
PVBnHexImBF_4	RLW-IV-030-A
PVBnHexImTFSI	RLW-IV-030-C

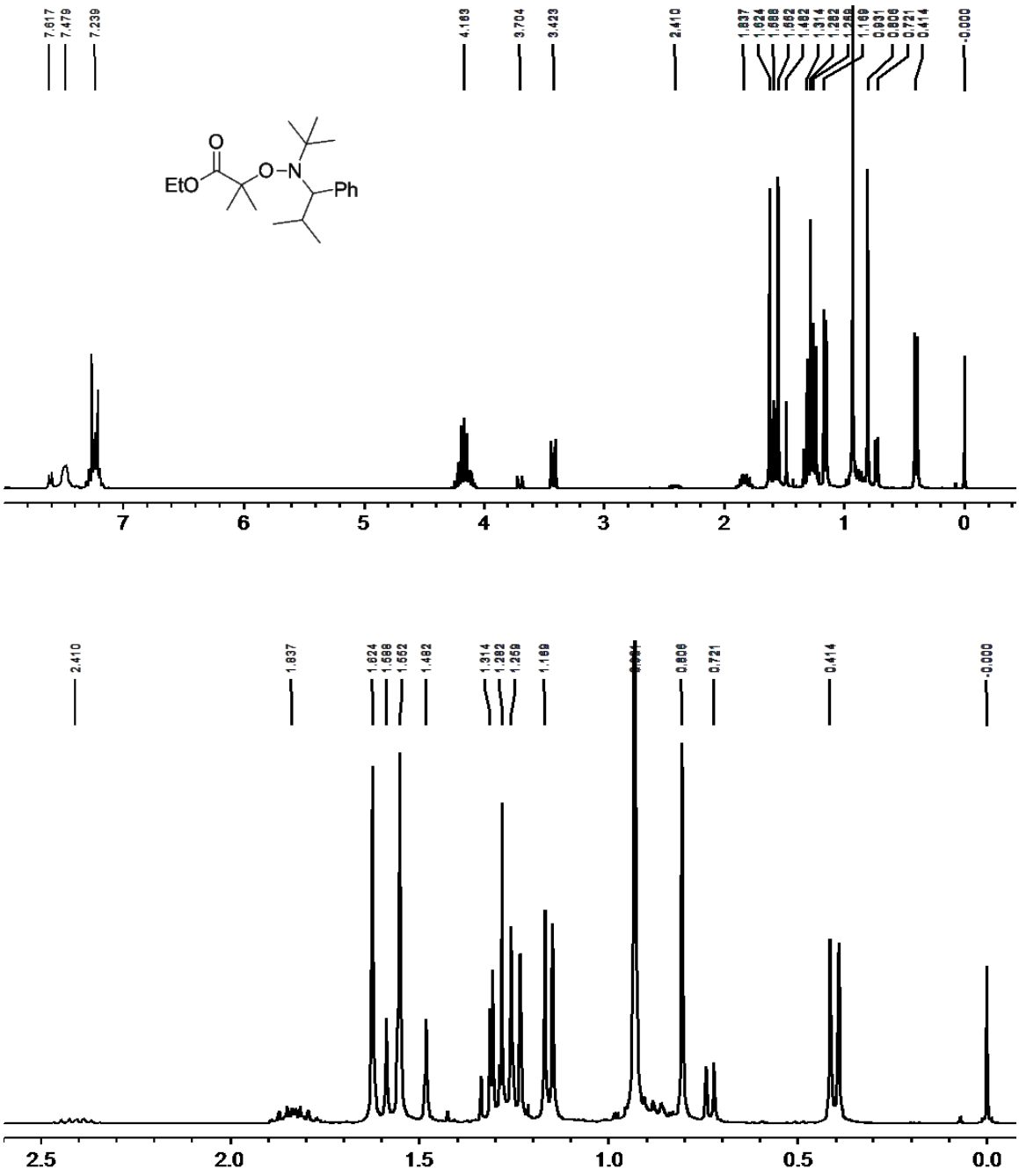

Figure A1.1. ^{1}H NMR spectrum of alkoxyamine 1. The lower spectrum is an enlargement of the up field region of the spectrum (300 MHz, $CDCl_3$, 22°C).

a) PVBCl (300 MHz, $CDCl_3$, 22°C)

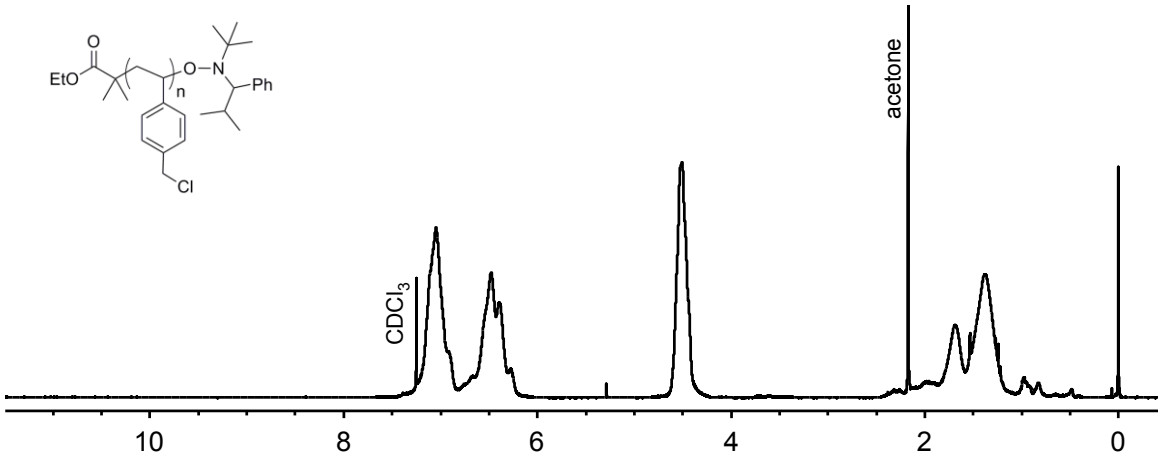

b) PVBnMeImCl (300 MHz, DMSO-d_6, 22°C)

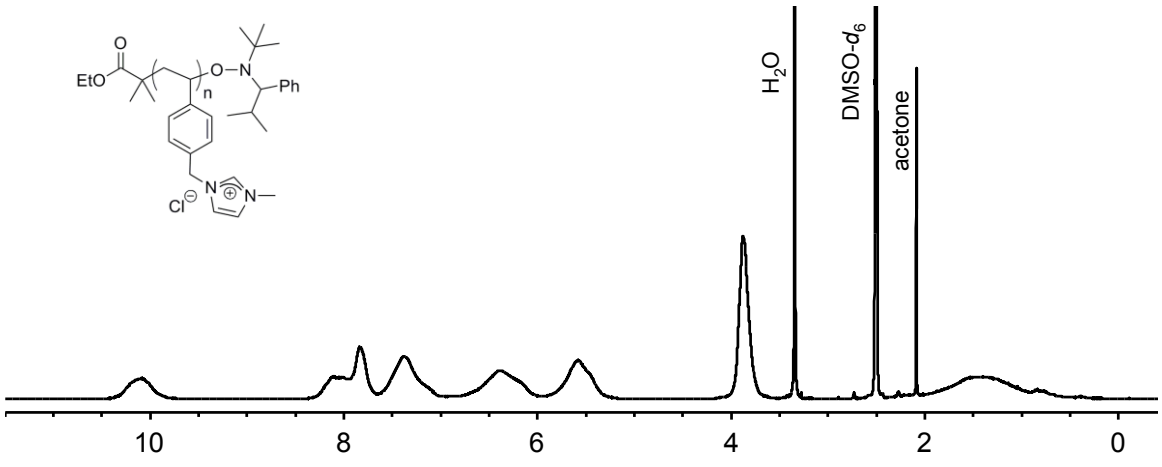

Figure A1.2. ^{1}H NMR spectra of (*a*) PVBCl, (*b*) PVBnMeImCl, (*c*) PVBnBuImCl, (*d*) PVBnHexImCl, (*e*) PVBnHexImPF_6, (*f*) PVBnHexImBF_4, and (*g*) PVBnHexImTFSI.

c) PVBnBuImCl (300 MHz, DMSO-d_6, 22°C)

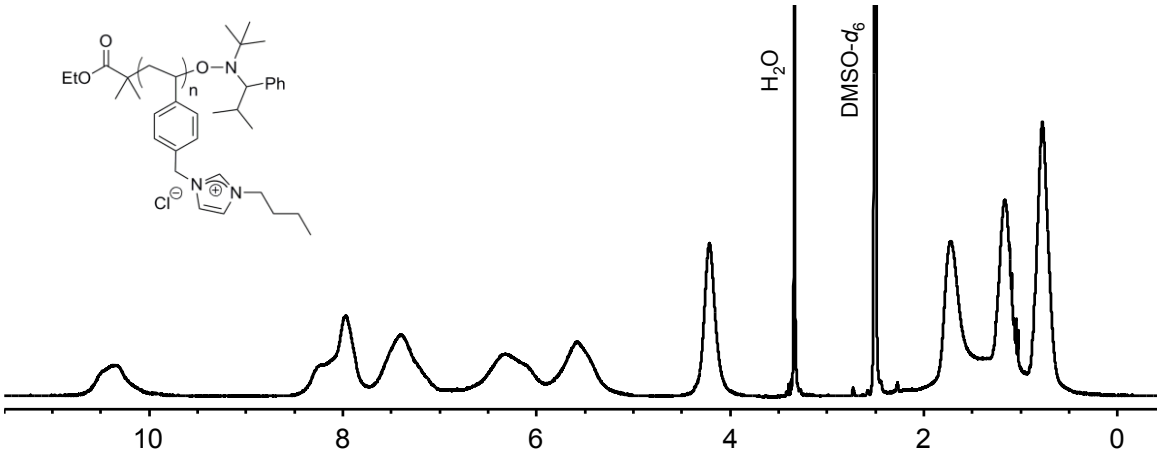

d) PVBnHexImCl (300 MHz, DMSO-d_6, 22°C)

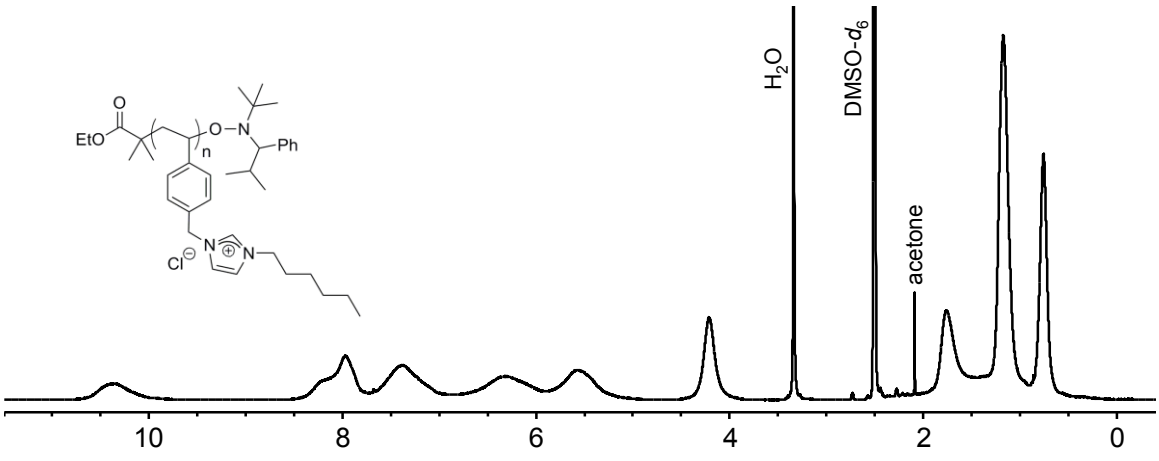

Figure A1.2 (contd). ^{1}H NMR spectra of (*a*) PVBCl, (*b*) PVBnMeImCl, (*c*) PVBnBuImCl, (*d*) PVBnHexImCl, (*e*) PVBnHexImPF_6, (*f*) PVBnHexImBF_4, and (*g*) PVBnHexImTFSI.

e) PVBnHexImPF$_6$ (300 MHz, DMSO-d_6, 22°C)

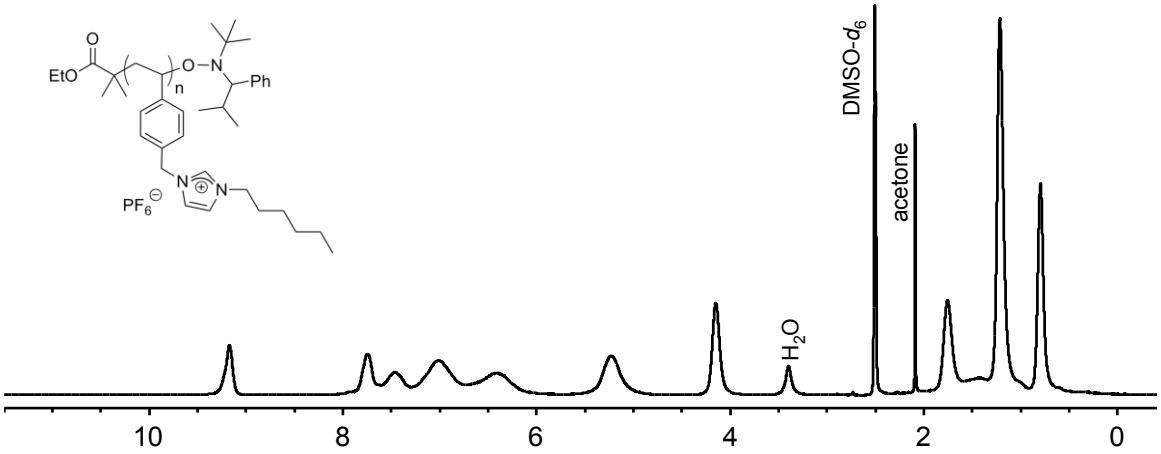

f) PVBnHexImBF$_4$ (300 MHz, DMSO-d_6, 22°C)

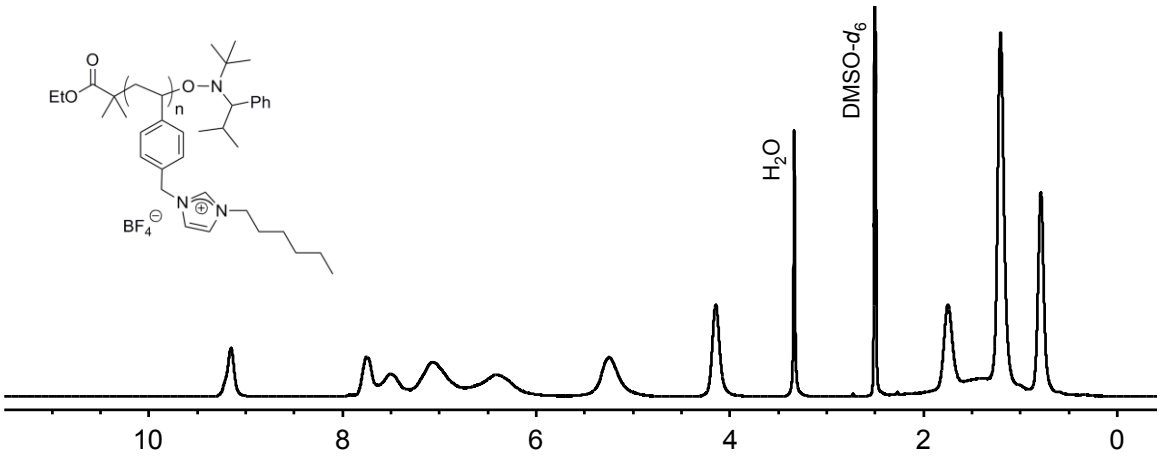

Figure A1.2 (contd). ^{1}H NMR spectra of (*a*) PVBCl, (*b*) PVBnMeImCl, (*c*) PVBnBuImCl, (*d*) PVBnHexImCl, (*e*) PVBnHexImPF$_6$, (*f*) PVBnHexImBF$_4$, and (*g*) PVBnHexImTFSI.

g) PVBnHexImTFSI (300 MHz, DMSO-d_6, 22°C)

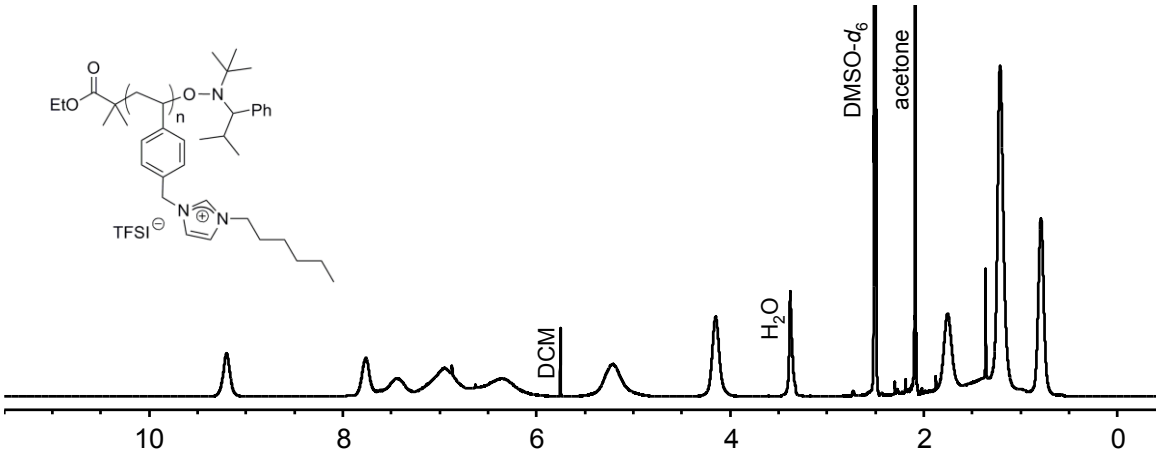

Figure A1.2 (contd). ^{1}H NMR spectra of (*a*) PVBCl, (*b*) PVBnMeImCl, (*c*) PVBnBuImCl, (*d*) PVBnHexImCl, (*e*) PVBnHexImPF_6, (*f*) PVBnHexImBF_4, and (*g*) PVBnHexImTFSI.

We regressed the temperature-dependent conductivity according the two-parameter VFT equation and performed a least-squares fit of the data to minimize error. These fits are shown below for both the styrenic and methacrylate-based POILs. In the range of $0 < T_0 < T_g$, only the TFSI POILs produced reliable VFT fitting parameters with high confidence. The VFT fitting parameters of the BF_4 and PF_6 POILs could not be reliably regressed with high confidence due to the limited temperature range over which the ionic conductivity could be measured for these POILs.

a) PVBnHexImTFSI ($0 < T_0 < T_g$)

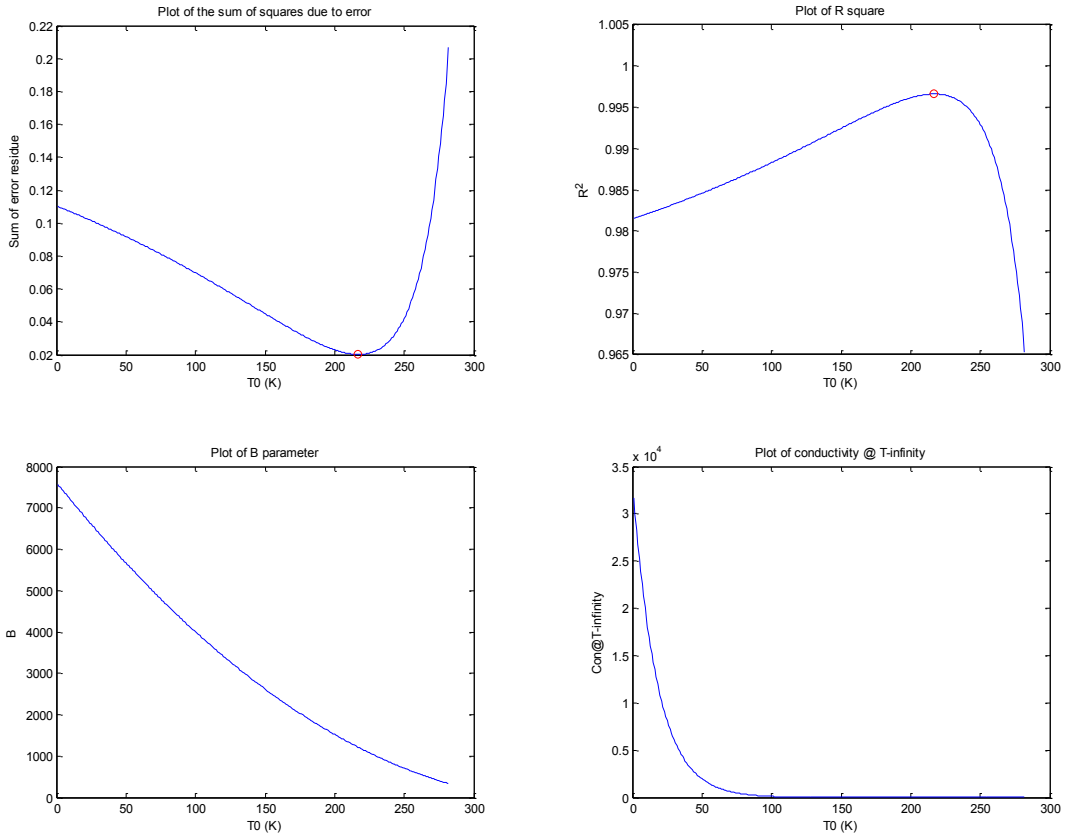

Figure A1.3. Plots of sum of squares due to error for (*a*) PVBnHexImTFSI, (*b*) PMEBImTFSI.

b) PMEBImTFSI ($0 < T_0 < T_g$)

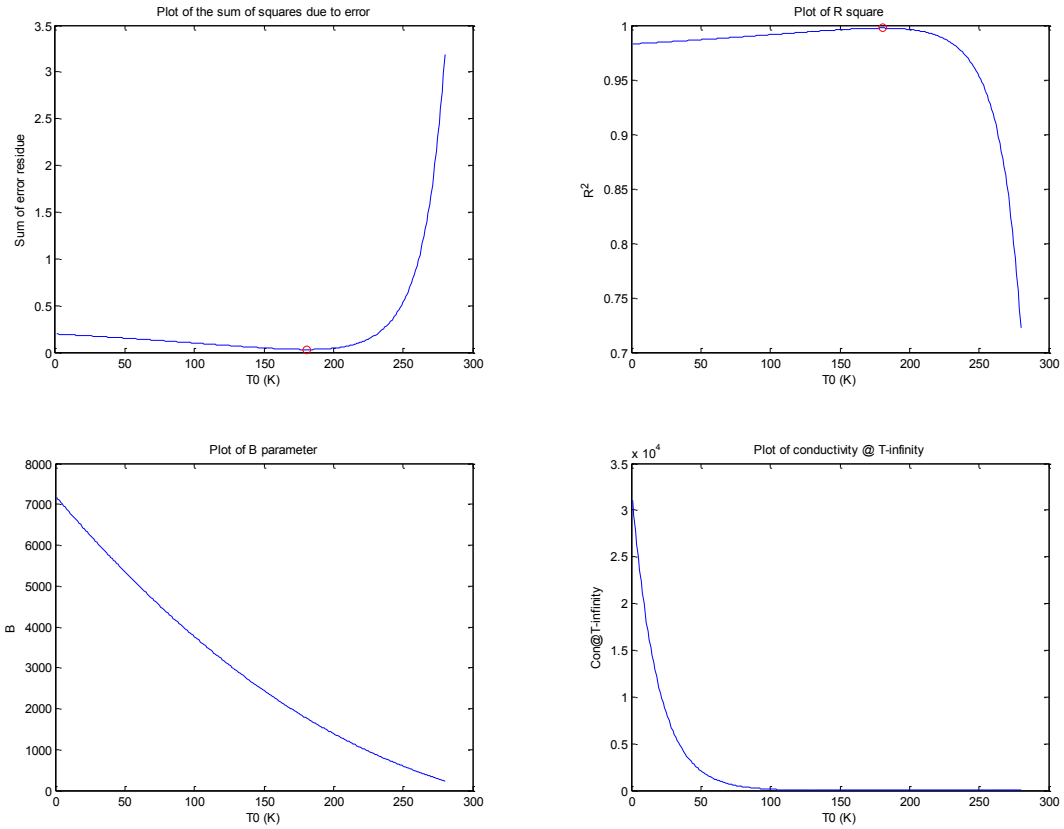

Figure A1.3 (contd). Plots of sum of squares due to error for (*a*) PVBnHexImTFSI, (*b*) PMEBImTFSI.

APPENDIX 2

SUPPORTING INFORMATION FOR CHAPTER 3: EFFECT OF NANOSCALE MORPHOLOGY ON THE CONDUCTIVITY OF POLYMERIZED IONIC LIQUID BLOCK COPOLYMERS

Table A2.1. Key of Experimental Sample Names to Chapter 3 Sample Names

Chapter 3 Sample Name	Experimental Sample Name
Alkoxyamine 1	RLW-III-188
PS-TIPNO	RLW-IV-027
PS-*b*-PVBCl-4.8	RLW-IV-080
PS-*b*-PVBCl-8.3	RLW-IV-082-B
PS-*b*-PVBCl-10.5	RLW-IV-082-A
PS-*b*-PVBCl-17.6	RLW-IV-088
PS-*b*-PVBnMeImTFSI-15.6	RLW-IV-099-C
PS-*b*-PVBnBuImTFSI-16.7	RLW-IV-104
PS-*b*-PVBnHexImTFSI-2.7	RLW-IV-099-A
PS-*b*-PVBnHexImTFSI-7.1	RLW-IV-108
PS-*b*-PVBnHexImTFSI-8.6	RLW-IV-099-B
PS-*b*-PVBnHexImTFSI-17.0	RLW-IV-145
PVBnHexImTFSI	RLW-IV-030-C

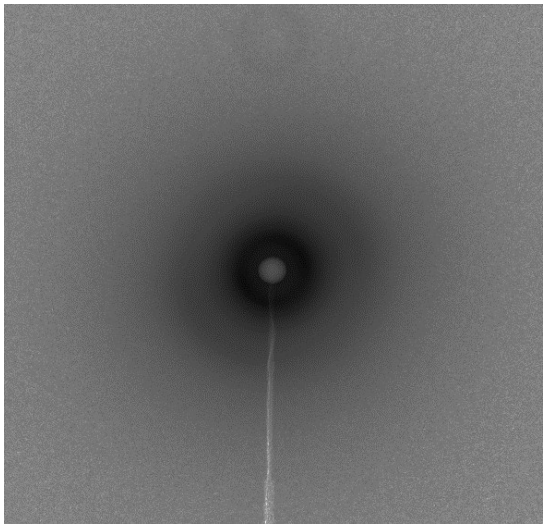

PS-*b*-PVBnHexImTFSI-2.7

(melt pressed)

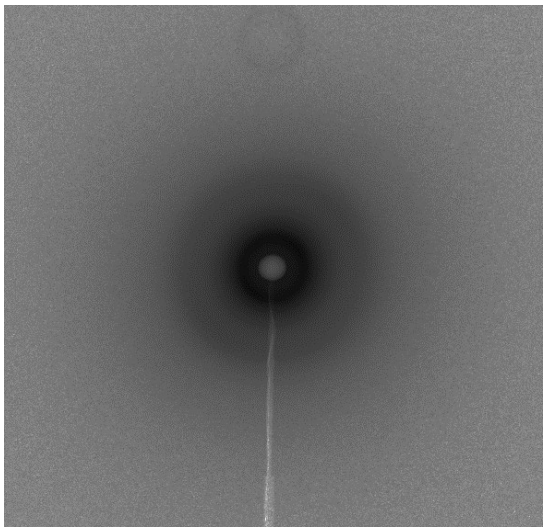

PS-*b*-PVBnHexImTFSI -7.1

(melt pressed)

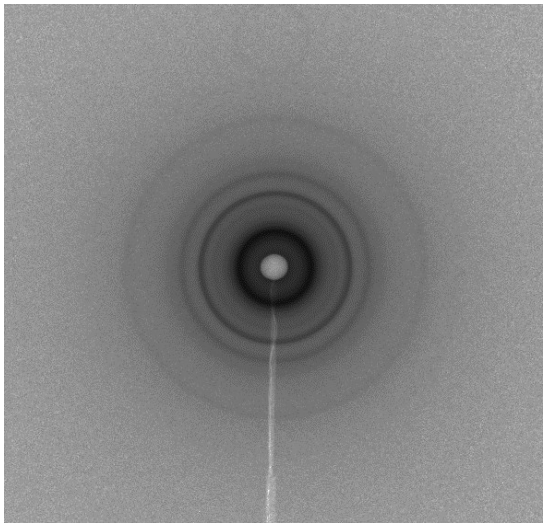

PS-*b*-PVBnHexImTFSI -8.6

(solvent cast)

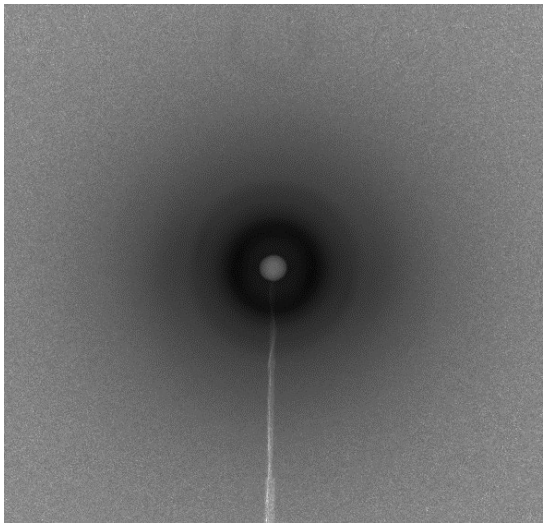

PS-*b*-PVBnHexImTFSI -8.6

(melt-pressed)

Figure A2.1. 2D SAXS patterns of PS-b-PVBn(alkyl)ImTFSI block copolymers films (*continued on next page*).

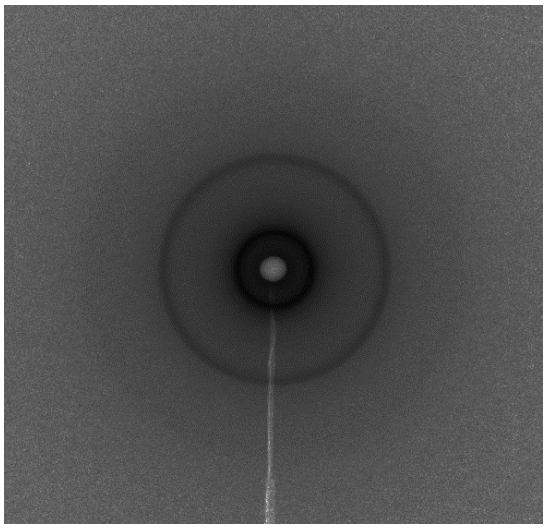

PS-*b*-PVBnHexImTFSI -17.0

(solvent cast)

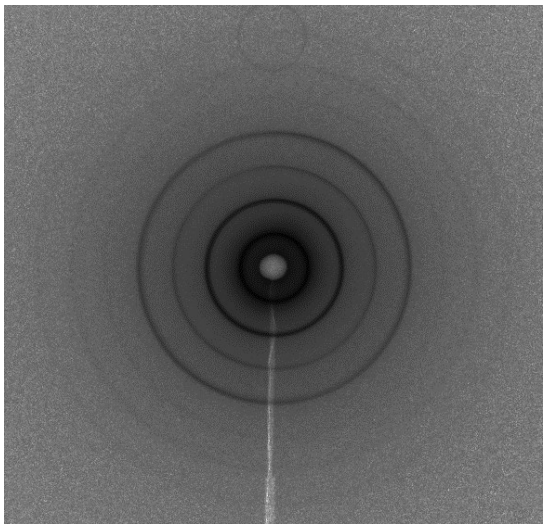

PS-*b*-PVBnMeImTFSI -15.6

(solvent cast)

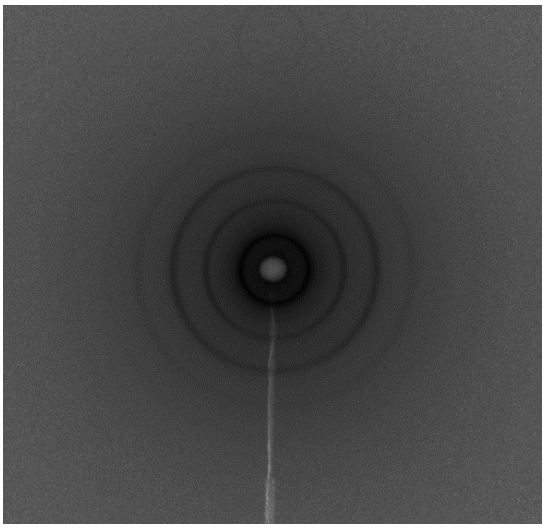

PS-*b*-PVBnBuImTFSI -16.7

(solvent cast)

Figure A2.1. 2D SAXS patterns of PS-*b*-PVBn(alkyl)ImTFSI block copolymers films.

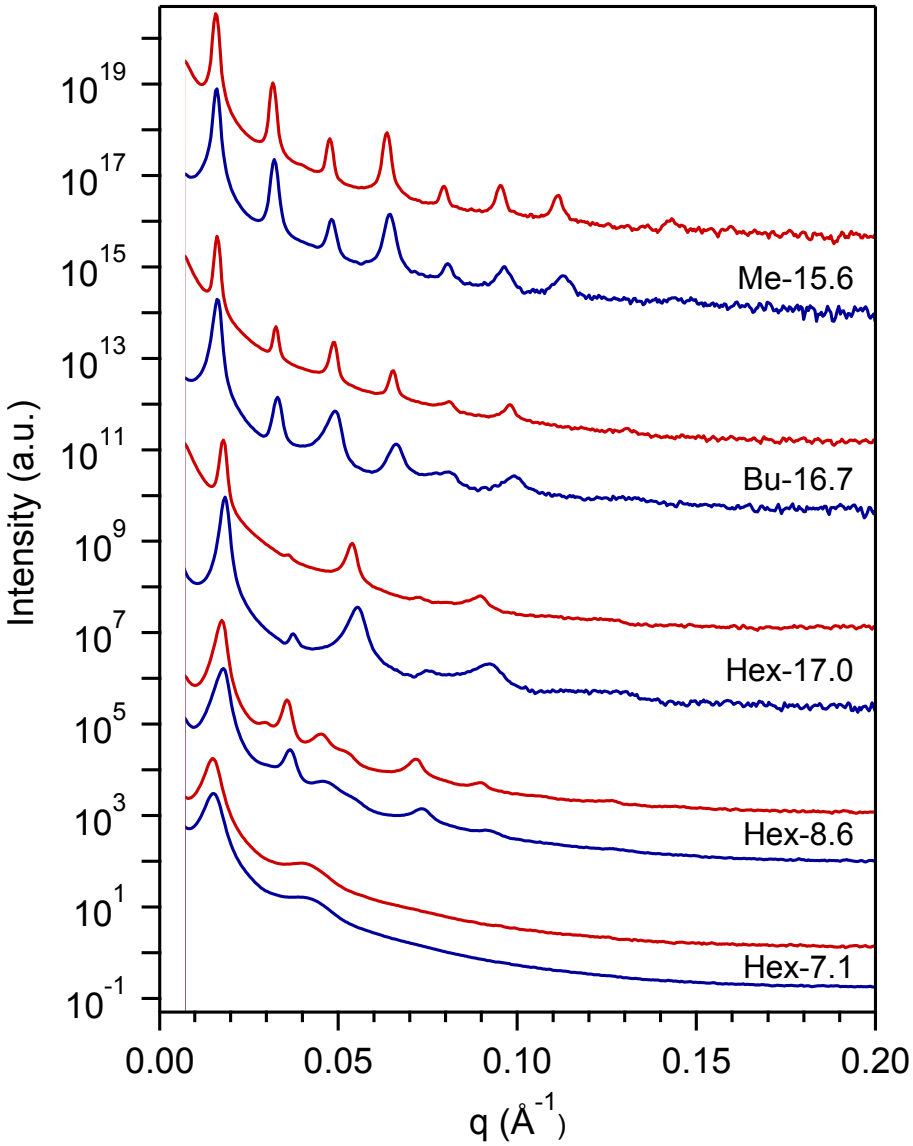

Figure A2.2. Azimuthally integrated SAXS profiles of PS-*b*-PVBn(alkyl)ImTFSI block copolymer melts at 25 °C (bottom, blue) and at 150 °C (top, red) for each sample.

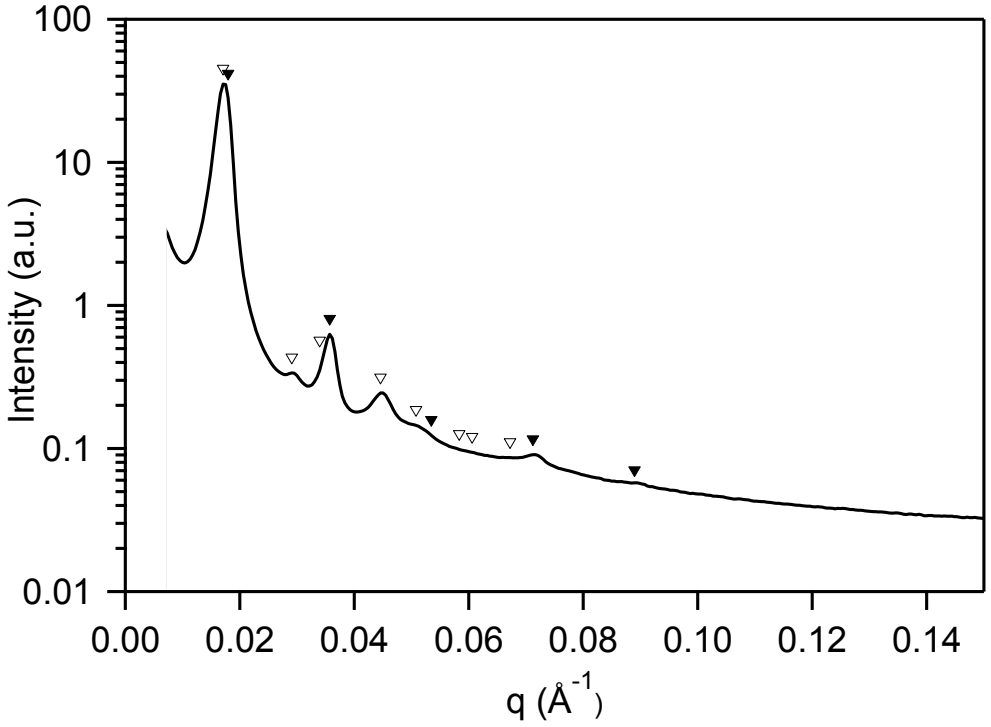

Figure A2.3. Azimuthally integrated SAXS profile of PS-*b*-PVBnHexImTFSI-8.6 (solvent cast) exhibiting coexistence of lamellar and hexagonally packed cylindrical morphologies.

Determination of PS-*b*-PVBnHexImTFSI diblock copolymer volume fractions

In the synchrotron small angle x-ray scattering of PS-*b*-PVBnHexImTFSI-17.0, we observed a structure factor extinction of scattering maxima at 2q* and 4q*, which is consistent with apparent symmetric volume fractions of each block ($\phi_{POIL} = \phi_{PS}$).[1] On this basis, we estimated the PVBnHexImTFSI homopolymer density by setting the volume-normalized degree of polymerization of each block (N_{POIL}, equation A2.1; N_{PS}, equation A2.2) equal to one another and solving for ρ_{POIL} as shown in equation A2.3

$$N_{POIL} = \frac{M_{n(POIL)}}{71.1 \times \rho_{(POIL)}} \qquad \text{A2.1}$$

$$N_{PS} = \frac{M_{n(PS)}}{71.1 \times \rho_{(PS)}} \qquad \text{A2.2}$$

$$\frac{M_{n(POIL)}}{71.1 \times \rho_{(POIL)}} = \frac{M_{n(PS)}}{71.1 \times \rho_{(PS)}} \qquad \text{A2.3}$$

where $M_{n(POIL)}$ (g mol^{-1}) and $M_{n(PS)}$ (g mol^{-1}) are the number average molecular weights of PVBnHexImTFSI and PS, respectively, 71.1 (Å^3) is the somewhat arbitrary monomer reference volume occupied by a 4-carbon unit, and $\rho_{(POIL)}$ (g cm^{-3}) and $\rho_{(PS)}$ = 0.969 g cm^{-3} are the bulk homopolymer densities of PVBnHexImTFSI and PS at 150 °C, respectively. Equation A2.3 is solved for $\rho_{(POIL)}$ = 1.096 g/cm^3 , from which the volume fractions of the series of the PS-*b*-PVBnHexImTFSI diblock copolymers were calculated using equation A2.4

$$\phi_{(POIL)} = \frac{N_{(POIL)}}{N_{(PS)} + N_{(POIL)}} \qquad \text{A2.4}$$

where $\phi_{(POIL)}$ is the volume fraction of PVBnHexImTFSI and N_{POIL} and N_{PS} are the volume-normalized degree of polymerization for PVBnHexImTFSI and PS, respectively. The volume fractions of the PS-*b*-PVBnHexImTFSI block copolymers are tabulated below.

Table A2.2. Copolymer Compositions of PS-*b*-PVBnHexImTFSI Diblock Copolymers.

Diblock Copolymer	POIL mol%[a]	POIL wt%[a]	ϕ_{POIL}[b]
PS-*b*-PVBnHexImTFSI-17.0	17.0	51.9	0.50
PS-*b*-PVBnHexImTFSI-8.6	8.6	33.2	0.34
PS-*b*-PVBnHexImTFSI-7.1	7.1	28.7	0.29
PS-*b*-PVBnHexImTFSI-2.7	2.7	12.8	0.19

[a] Determined by quantitative ^{1}H NMR of PS-*b*-POILs. [b] Determined from polymer compositions and homopolymer densities calculated as described above from equations A2.4.

References

(1) Roe, R. J. *Methods of X-ray and neutron scattering in polymer science*; Oxford University Press: New York, 2000.

APPENDIX 3

SUPPORTING INFORMATION FOR CHAPTER 4: DESIGN AND SYNTHESIS OF LINEAR CHAIN POLYMERIC LITHIUM SINGLE ION CONDUCTORS FOR USE AS LITHIUM ION BATTERY ELECTROLYTES

Table A3.1. Key of Experimental Sample Names to Chapter 4 Sample Names

Chapter 4 Sample Name	Experimental Sample Name
Non-8-enyl-malonic acid	RLW-V-107
Non-8-enyl-malonic acid TMS ester	RLW-V-111
LiBNMB	RLW-V-114
Poly(LiBNMB)	RLW-VI-033 / RLW-VI-075
poly(LiBNMB-co-HDT)	RLW-VI-071 / RLW-VII-151
poly(LiBNMB-co-DEGDT)	RLW-VII-178

Alternative Isolation / Purification Procedure for LiBNMB: After reaction of non-8-enyl-malonic acid trimethylsilyl ester (2.1 equivalents) with lithium tetrafluoroborate (1.0 equivalent) in acetonitrile, the solvent is removed under reduced pressure to furnish a beige/white solid. Under a purge of nitrogen, a spatula is used to grind the solid into a powder and then the flask is sealed with a septum. Dry heptane (distilled from CaH_2) is added to the flask via cannula and then refluxed for 5-10 minutes with vigorous stirring in an oil bath thermostatted at 110 °C. The hot heptane is removed via cannula filtration then fresh heptane is added via cannula and the trituration process is repeated three more times. After removal of the fourth heptane rinse, residual solvent is removed under reduced pressure and then the solid is freeze-dried twice from benzene. (95% yield) See RLW-VII-130.

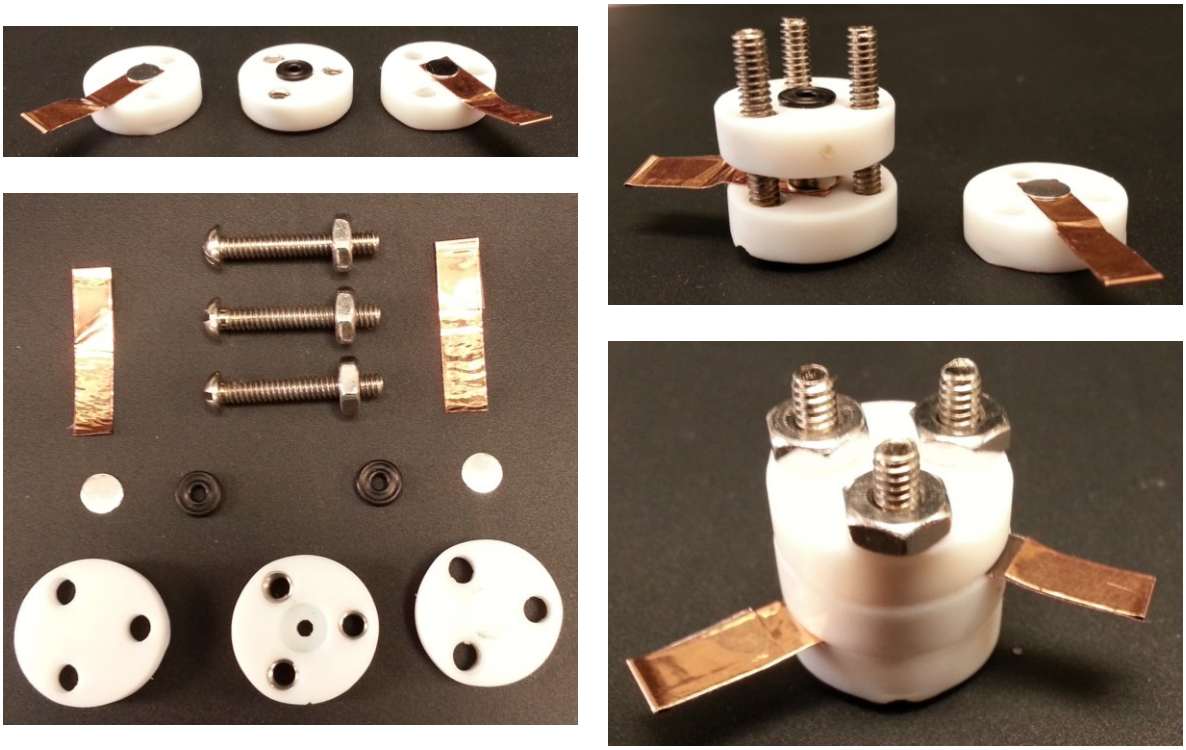

Figure A3.1. Images of cell used to measure conductivity of poly(LiBNMB) and LiTFSI in propylene carbonate.

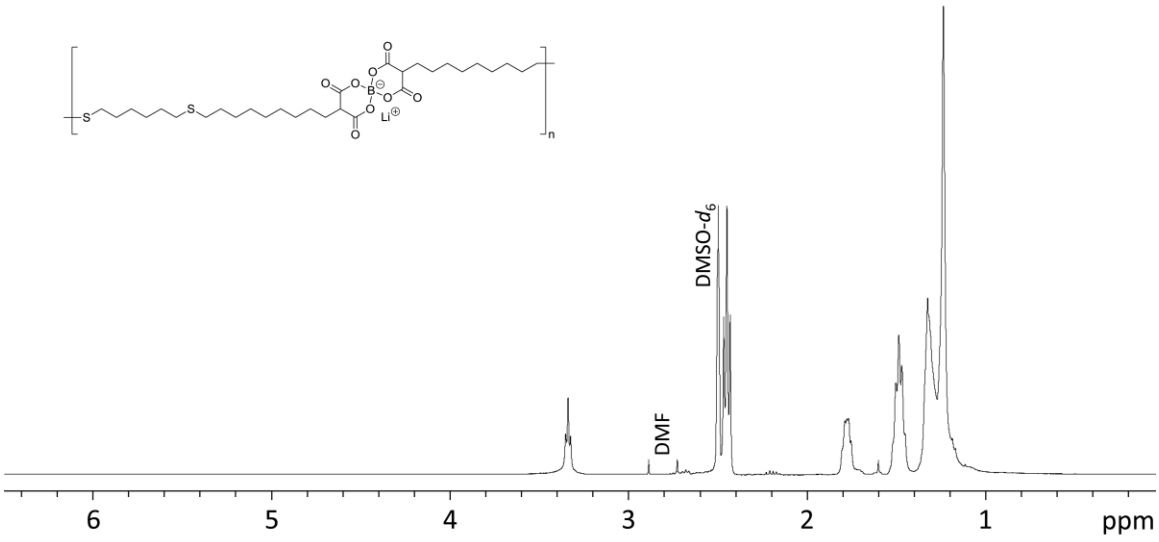

Figure A3.2. ^{1}H NMR spectrum (400 MHz, DMSO-d_6, 22°C) of poly(lithium bis(non-8-enyl-malonato)borate-*co*-1,6-hexanedithiol) (poly(LiBNMB-co-HDT)).

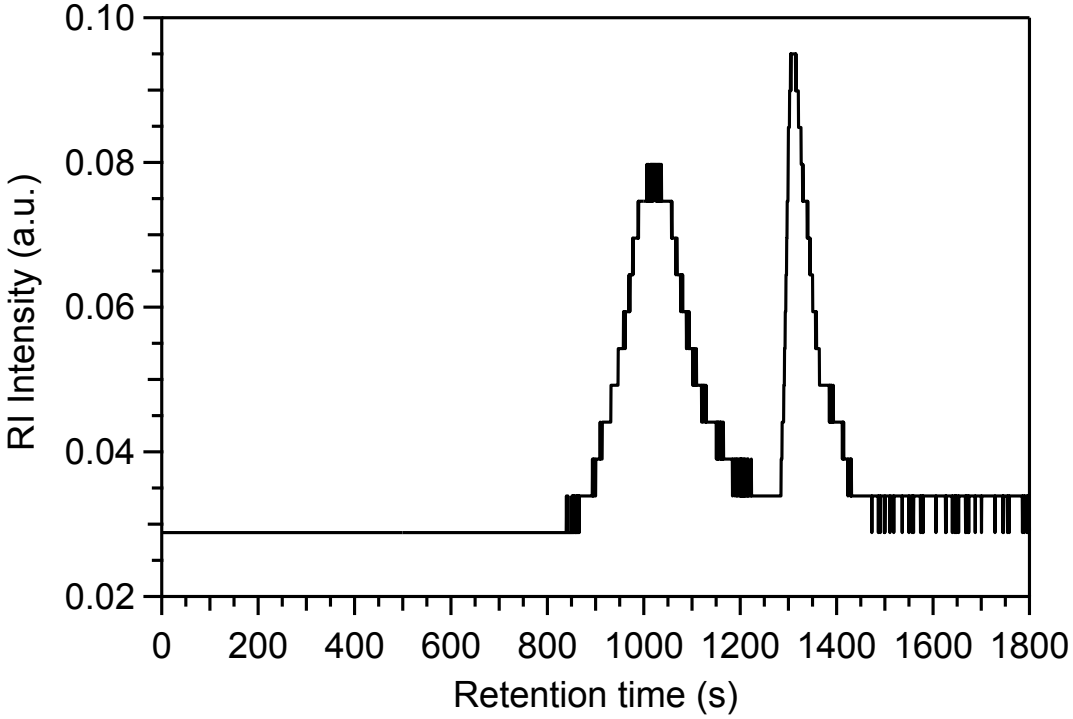

Figure A3.3. Size exclusion chromatography (SEC) refractive index trace of poly(lithium bis(non-8-enyl-malonato)borate-*co*-hexanedithiol) (poly(LiBNMB-*co*-HDT)) in DMF + 0.1 M LiBr.

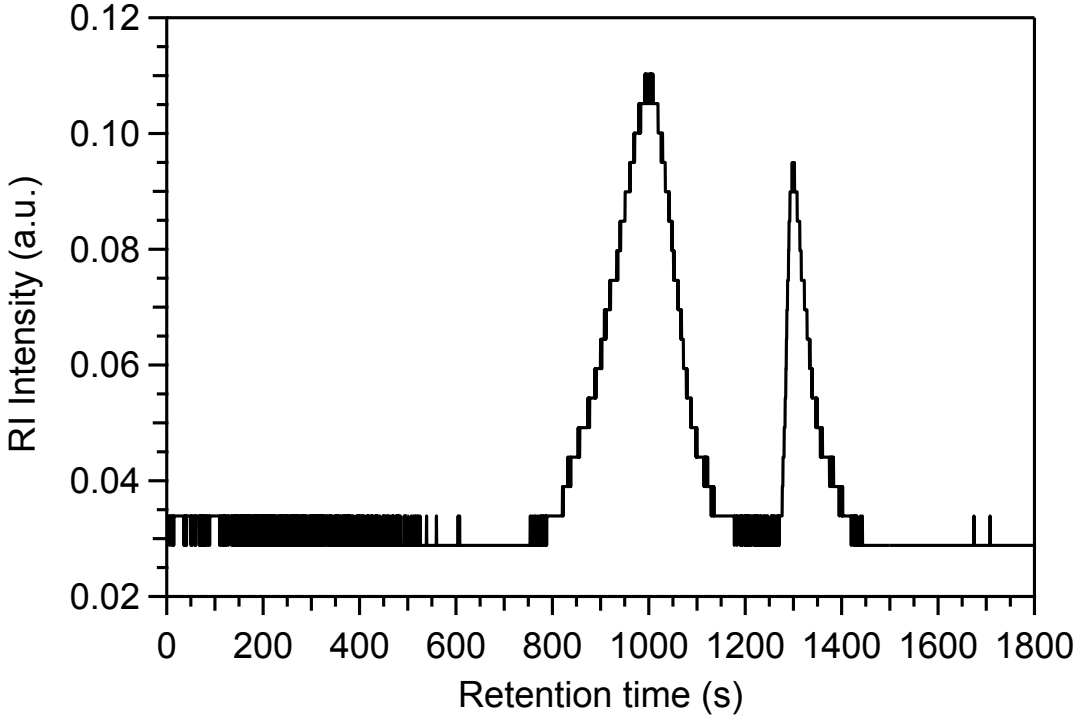

Figure A3.4. Size exclusion chromatography (SEC) refractive index trace of poly(lithium bis(non-8-enyl-malonato)borate-*co*-triethyleneglycol-dithiol) (poly(LiBNMB-*co*-TEGDT)) in DMF + 0.1 M LiBr.

APPENDIX 4

SUPPORTING INFORMATION FOR CHAPTER 5: RHEOLOGICAL AND ION TRANSPORT PROPERTIES OF NETWORK LITHIUM SINGLE-ION CONDUCTING GELS SYNTHESIZED BY THIOL-ENE CHEMISTRY

Table A4.1. Key of Experimental Sample Names to Chapter 5 Sample Names

Chapter 5 Sample Name	Experimental Sample Name
100CL, 69CL, 48CL, 26CL	RLW-VII-170

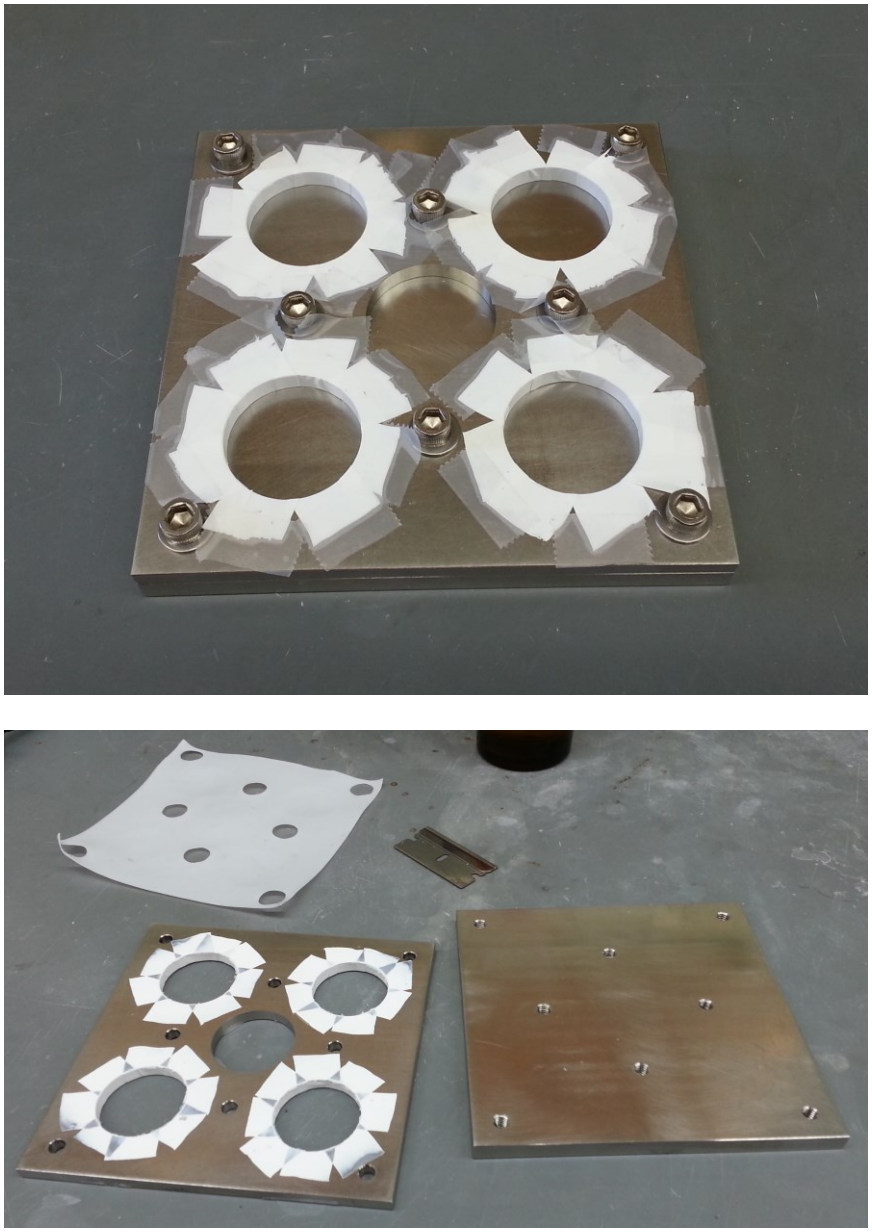

Figure A4.1. Stainless steel mold used to cure gels. (a) Fully assembled mold with Teflon tape used to coat the walls of the mold and (b) disassembled mold after removal of gels from the bottom plate.

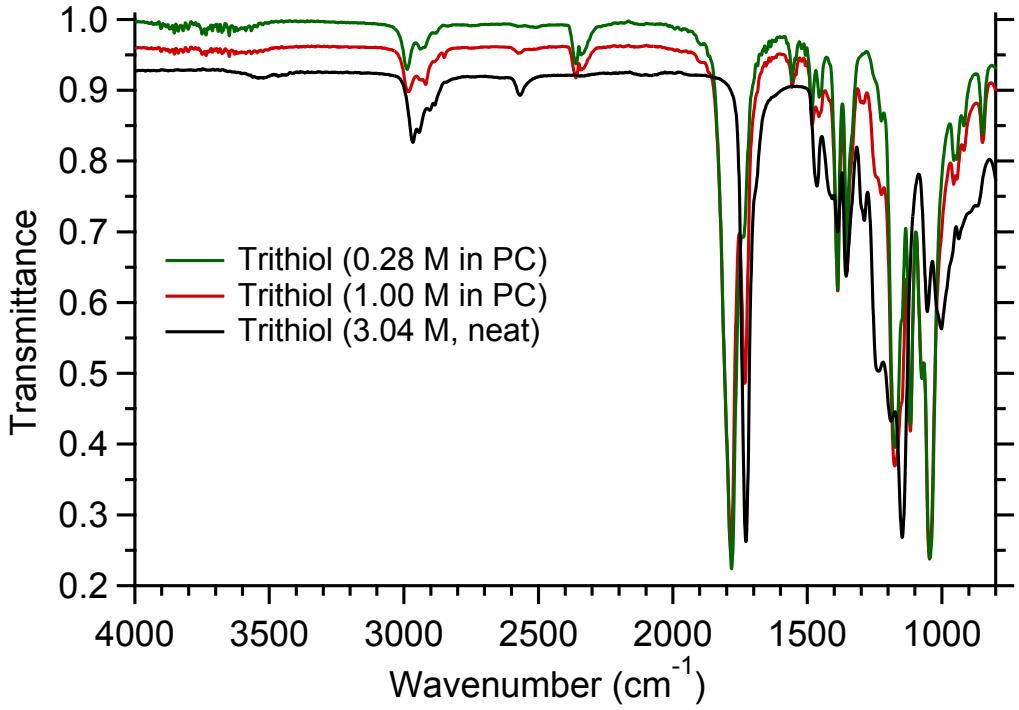

Figure A4.2. FT-IR spectra of neat trimethylpropane tris(3-mercaptopropionate) (trithiol), 1.00 M trithiol in propylene carbonate, and 0.28 M trithiol in propylene carbonate. The thiol S-H stretch is seen at 2570 cm^{-1}. Spectra are vertically offset for clarity.

Figure A4.3. Images of cell used to measure conductivity of crosslinked gels. (top left) unassembled components including PEEK housing, Kalrez O-rings, stainless steel top and bottom electrodes, and brass bolts; (top right) cell with O-rings in place; (middle left) cell with bottom electrode in place; (middle center) fully assembled cell; (middle right) adapted cell for variable temperature EIS allowing motion of top electrode; (bottom) cell connected to potentiostat leads.

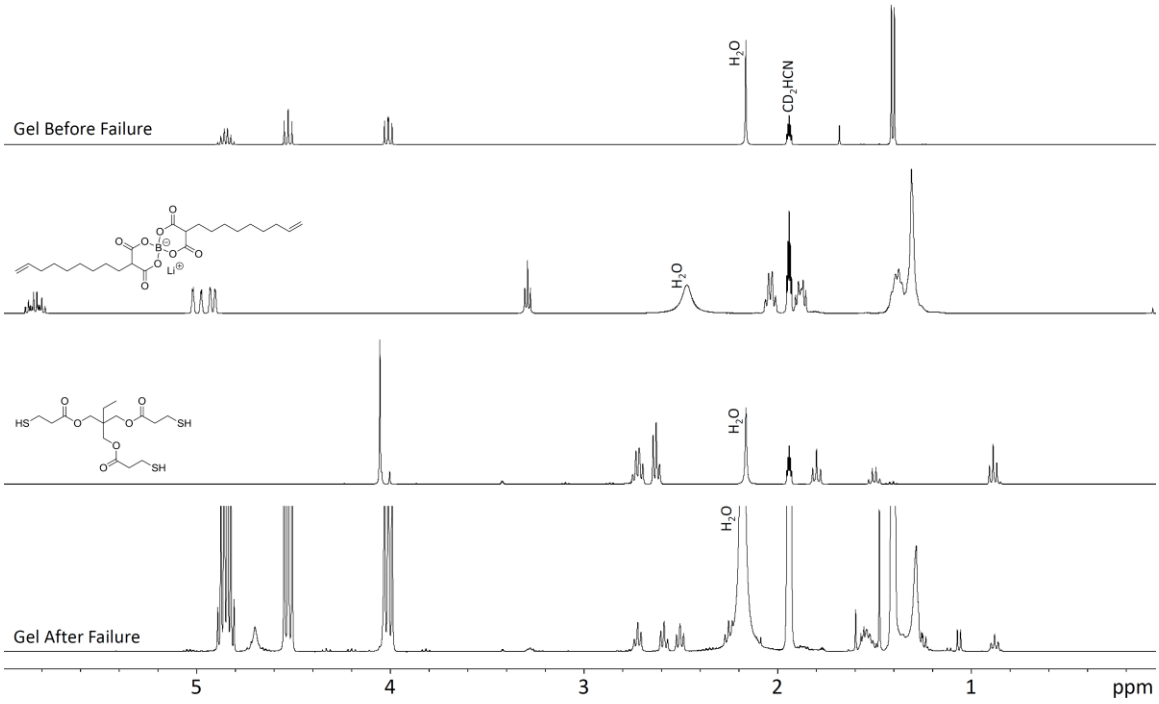

Figure A4.4. ^{1}H NMR spectra (400 MHz, CD_3CN, 22 °C) of the soluble fraction of a disk of 100CL before failure (top) and after failure (bottom) along with spectra of reagents used to make the gel for comparison.